Practical Realisation of Multiband Planar Filters on Multilayer Substrates

Leokadia Ndeapo Popyeni Nepaya

University of Cape Town

This dissertation is submitted for the degree of
Doctor of Philosophy

Faculty of Engineering and the Built Environment

June 2019

I would like to dedicate this thesis to my loving parents ...

Declaration

I hereby declare that, except where specific reference is made to the work of others, the contents of this dissertation are original and have not been submitted in whole or in part for consideration for any other degree or qualification in this, or any other, university. This dissertation is my own work and contains nothing which is the outcome of work done in collaboration with others, except as specified in the text and Acknowledgements.

Signed by candidate

Leokadia Ndeapo Popyeni Nepaya

13 June 2019

Acknowledgements

I would like to thank a number of people who made this dissertation a reality. First and foremost, I would like to thank and show appreciation to my supervisor, Prof. Riana Helena Geschke, for her patience and readiness to provide me with the opportunity to conduct the study and for her guidance, motivation, encouragement and positive attitude that gave me the courage to complete the dissertation.

I would like to thank my colleague, Titus Oyedokun, who has made his support available in a number of ways; furthermore during the completion and writing of this dissertation, his encouraging words were always: 'Everything is going to be alright at the end'. Thank you for your time, generosity and for the jokes we shared.

I must express appreciation to my mother and my brother, Gabriel Nepaya, for being the backbone and foundation that enabled me to further my studies until the culmination in this dissertation. This accomplishment would not have been realizable without your caring and support.

My sincere gratitude goes to my sister, Jomo Kenyata Nepaya, for her continued love, help and support. She took care of my little boys when I spent long hours away from home. I am grateful to my sister's son, Leonard Ketu, for allowing his mother to share his time when looking after his nephews, even when he needed her.

I owe appreciation and thanks to my husband, Likius Ndjuluwa, for his special love and friendship, support and understanding during all the years of my pursuing this PhD. He contributed in several ways towards the completion of this dissertation. I thank my little boys, Josef and Likius, for surviving my being distant during my dissertation writing. I am thankful and cannot find enough words to show my appreciation.

This work would not have been possible without the financial support of the University of Namibia (UNAM), National Research Fund (NRF), Namibia Student Financial Assistance Fund (NSFAF), Namibia Commission for Research, Science and Technology (NCRST) and, last but not least, the National Commission for Higher Education (NCHE).

Abstract

This research presents the design of planar microwave filters implemented on microstrip multi-layer technology. These should be able to attain and realize specified essential requirements such as multi-band operation, compact size, and without significant deteriorated filter performance in comparison with single-band filters. The focus is placed on new synthesis and design procedures for multiband responses. In some cases, the possibility to include re-configurable characteristics of these filters is required. The focus of the research is entirely on examining the properties and implications of a previously proposed reactance transform method for multiband filter synthesis.

The research commences with reviews of multi-band filter synthesis methods. The research specifically examines a full analytical synthesis approach based on reactance transforms method and the implications for practical design approaches Investigations on narrow-band with coupled resonator filters representation and wide-band with quasi-lumped element filters representation of up to quad-bands based on reactance transform method are undertaken. With the emphasis on practical aspects such as losses and selectivity, which are related to the physical implementation on multi-layer substrate, the key differences between multiband and single-band filters based on a reactance transform are highlighted. It is illustrated that, in addition to the order of the basis filter, selectivity is influenced by the number of bands, the spacing of the bands and the relative bandwidths. It is also shown that loss has a significant effect on multiband filter responses, in a somewhat different way from that for single-band filters.

Physical designs of narrow- band coupled resonators filters are implemented with the aim of examining the degrees of design freedom for multi-layer substrate design, considering the resonance properties and couplings between resonators and considering loss for resonators on different layers. Mercurywave 9350, a low-cost multi-layer substrate is chosen and deemed suitable for a number of reasons, including relatively constant permittivity over frequency. The designs consist of novel topologies: parallel connected multi-path referred to as transversal and also all-pole topologies. A transversal topology includes a dual-band dual-path design as well as a dual-band triple-path design while the all-pole topology is a quad-band design.

The research explores re-configurable characteristics of narrow-band coupled resonators of a dual-band dual-path design. A process to obtain a re-configurable multi-band filter with electronically selected pass-bands, based on a reactance transform method for coupled resonator filters, is described. A dual-band multi-band filter realized on multi-layer substrate is designed for passive space applications and reconfigurability is demonstrated using a pre-selection method.

For wide-band, quasi-lumped element filters are realized on multi-layer substrate, the inductors are implemented as rectangular spiral inductors and Capacitors as broadside coupling plates connected from two different layers through metallic vias. Parasitic that may influence the relative bandwidths.

Table of contents

List of figures **xv**

List of tables **xxxi**

1 Introduction **1**
1.1 Motivation 2
1.2 Research objectives 3
1.3 Dissertation contributions 4
1.4 Dissertation outline 5
1.5 List of publications 6

2 Background of microwave filters **7**
2.1 Single band Basics 7
2.1.1 Resonant properties of coupled resonators 7
2.2 Multi-band filters 15
2.2.1 Multi- modes resonators for multi-band filters 19
2.2.2 Optimization Multiband filters 23
2.2.3 Reactance transformed method for multi-band filters 24
2.3 Summary 30

3 Properties of multi-band filters based on narrow-band and wide-band reactance transformation **31**
3.1 Introduction 31
3.2 Narrow band implementation 32
3.2.1 Frequency selectivity of reactance transformed multi-band filter . . 32
3.2.2 Effect of resonator loss on multi-band narrow-band filters with identical resonator Q_u. 55
3.2.3 Group-delay responses 63
3.3 Wide-band implementation 65

3.3.1 Lumped-element circuit values 72
3.3.2 Selection of a multi-band topology for implementation 78
3.4 Narrow-band and wide-band transform comparisons 82
3.5 Summary 84

4 Implementation of narrow-band multi-band filters on multi-layer substrates 85
4.1 Introduction 85
4.2 Multi-and single-path filters 87
4.2.1 Multi-path topologies 88
4.2.2 Single-path all pole topology 89
4.3 Coupled resonators on multi-layer substrates 89
4.3.1 Input/output couplings 90
4.3.2 Inter-resonator couplings 98
4.4 Port tuning 99
4.5 Implementation of coupled resonators microstrip planars on multi-layer substrates 105
4.5.1 Dual-path dual-band filter 105
4.5.2 Triple-path dual-band filter 108
4.5.3 All poles quad band filters 110
4.6 Construction and measured results 112
4.6.1 S-parameter measurements 112
4.6.2 Group delay measurements 118
4.7 Summary 130

5 Switchable Coupled Resonators Dual band Filters 131
5.1 Introduction 131
5.2 Coupled resonator dual-band filter 135
5.3 Pre-selection non-resonant circuit theory 138
5.3.1 One stage pre-selection non-resonant circuit 139
5.3.2 Cascaded two stages pre-selection non-resonant circuit 139
5.4 Design of a pre-selection non-resonant circuit 142
5.5 Construction and measurement of the pre-selection, non-resonant circuit . . 142
5.6 Switchable filter designs 142
5.6.1 5.6.1 The implementation and analysis of the switchable dual-band filter 150
5.6.2 Performance analysis 150
5.7 Construction and measurements of the filter 164

5.8 Summary 164

6 Tunable quasi-lumped element dual band Filters 173
6.1 Introduction 173
6.2 Synthesis based on a wide-band Reactance Transform 175
6.3 Circuit analysis of filter topologies 177
6.4 Practical design and implementation 180
6.4.1 Capacitor and inductor models 180
6.4.2 Via holes 181
6.4.3 Design of a dual-band filter 184
6.5 Construction and measurements 186
6.5.1 Effect of Q on Filter response 189
6.6 The Influence of non-idealities on the realisation of filters 192
6.7 Tunable Dual- band filters 193
6.7.1 Implementation and analysis of the tunable dual-band filter 208
6.8 Summary 212

7 Conclusion and Future Works 213
7.0.1 Conclusion 213
7.0.2 Future work 214

References 215

Appendix A Dimensions of the Coupled resonators filters 221

Appendix B Dimensions of the coupled switchable filter 243

Appendix C Dimensions of the dual band quasi lumped element filters 249

List of figures

1.1 Block diagram for an RF communication system [32]. 2

2.1 LC resonator (a) parallel and (b) series connections. 7
2.2 Lumped constants (a) series capacitive couplings (b) inductive couplings (c) mutual inductive couplings [20] 8
2.3 Lowpass prototype filters for all-pole filters with (a) a ladder network structure and (b) its dual [35]. 9
2.4 (a). Admittance inverter, (b) impedance inverter. 9
2.5 (a). A π network admittance inverter, (b) a T network impedance inverter. . 9
2.6 (a) Capacitance and (c) inductance representation of admittance inverter, (b) capacitance and (d) inductance representation of impedance inverter [35] . . 10
2.7 (a) Immittance inverters convert a series inductance into an equivalent circuit with shunt capacitance. (b) Immittance inverters to convert a shunt capacitance into an equivalent circuit with series inductance. 11
2.8 Low pass ladder networks in (a) is transformed through ideal inverter placement in (b) and (c) which end up with one type of reactance elements, capacitors only in (d) that is transformed into a single-band band-pass filter in (e). 11
2.9 Band pass filter prototype [1]. 12
2.10 Low pass distributed prototype circuits. 13
2.11 Coupling matrix 13
2.12 N + 2 Coupling matrix for the extended form. 16
2.13 N + 2 Coupling matrix for the extended form. 17
2.14 Input coupling and the first resonator equivalent circuit [10]. 17
2.15 Phase response of S_{11} for the circuit in Fig 2.14 [35]. 18
2.16 Measurement of inter-resonator coupling using (a) two port (b) one port network [10] 18
2.17 The return loss of the circuits shown in Fig 2.16 [10] 19

2.18 (a) Coupling configuration of the multi-band BPFs, (b) Schematic diagram arrangement of the microstrip five-band filter based on the SL-SIRs and (c) Frequency response [18] 20
2.19 Source/load and coupling configuration, (a) at the first and third resonant frequencies, (b) at the fourth resonant frequency, and (c) at the second and fifth resonant frequencies, (d) layout of the proposed quint-band band-pass filter structure, and (e) frequency response of the quint-band band-pass filter [28]. 21
2.20 (a) Coupling scheme of (b): (b) Layout of the designed quad-band HTS filter with the pseudo-interdigital structure, and (c) simulated and measured frequency responses of the constructed, quad-band HTS filter [44]. 21
2.21 (a) Coupling arrangement of the quad-band band-pass filter based on parallel-path transmission; (b) Coupling diagram at frequencies f_{B1}^{I} and f_{B2}^{I}. (c) Coupling arrangement at frequencies f_{B1}^{II} and f_{B2}^{II} (grey solid line: ignorable coupling, black solid line: main coupling, dashed line: nonadjacent coupling), (d) constructed filter and (e) simulated and measured frequency response [43]. 22
2.22 Quad-band BPF: (a) filter configuration (b) simulated and measured frequency response [44] 22
2.23 (a) Coupling scheme of the triple pass-bands quasi-elliptic filter (b) Schematic layout. Measured and simulated performance of the filter(c) Insertion and return loss. (d) Wider spurious rejection band [19]. 23
2.24 Circuit topology and symmetrical dual-band response with CST simulation and the measurement after tuning [66]. 25
2.25 Dual-band filter utilizing six open-loop resonators (a) Coupling-matrix theory (dashed lines) are compared with Ansoft Designer (solid lines). (b) Prototype measurements (solid lines) and photograph (Ansoft Designer data (dashed lines) for comparison). [49]. 26
2.26 Low-pass to multi-band response transformation utilizing an unsymmetrical intermediate response [7]. 27
2.27 Cauer I forms of the low-pass to multi-band mapping function [7]. 28
2.28 Reactance transformation function. [7]. 29

3.1 A low-pass prototype basis filter for the reactance transform. 32

3.2 (a) A fourth order, dual-path, transversal, single-band basis filter transformed to (b) a multi-band filter; (c) a sixth order, triple-path, transversal, single-band basis filter transformed to (d) a multi-band filter; (e) an eighth order, quad-path, transversal, single-band basis filter transformed to (e) a multi-band filter; (g) a fourth-order, all-poles, single-band basis filter transformed to (h) a multi-band filter. 33
3.3 A single-band to quad-band transformed prototype. 41
3.4 The filter topologies are (a) 4th order transversal single band coupling topology, (b) a 4th order single-band basis dual-path transversal filter. The multi-band filter in (c) a dual-band filter (d) a triple-band filter (e) a quad-band filter reactance transformed filters. 42
3.5 The ideal lossless response of (a) single-band fourth basis filter of Fig 3.4(b), and (b) dual-band response of the filter of Fig 3.4(c). It is notable that appended resonators add transmission zeros between bands. 43
3.6 The ideal lossless response of (a) triple-band response of the filter of Fig 3.4 (d), and (b) quad-band response of the filter of Fig 3.4(e). It is notable that appended resonators add transmission zeros between bands. 44
3.7 The filter topologies are (a) a 6th order transversal single-band coupling topology. (b) a 6th order single-band basis triple-path transversal filter. The multiband filter in (c) a dual-band filter (d) a triple-band filter (e) a quad-band filter reactance transformed filters. 45
3.8 The ideal lossless response of (a) single-band six order basis filter of Fig 3.7 (b), and (b) dual-band response of the filter of Fig 3.7 (c). It is notable that appended resonators add transmission zeros between bands. 46
3.9 The ideal lossless response of a (a) triple-band response of the filter of Fig 3.7 (d), and (b) quad-band response of the filter of Fig 3.7 (e). It is notable that appended resonators add transmission zeros between bands. 47
3.10 The filter topologies are (a) an 8th order transversal single-band coupling topology. (b) an 8th order single-band basis quad-path transversal filter. The multi-band filter in (c) a dual-band filter (d) a triple-band filter (e) a quad-band filter reactance transformed filter. 48
3.11 The ideal lossless response of (a) single-band eight order basis filter of Fig 3.10 (b), and (b) dual-band response of the filter of Fig 3.10 (c). It is notable that appended resonators add transmission zeros between bands. 49

3.12 The ideal lossless response of a (a) triple-band response of the filter of Fig 3.10 (d), and (b) quad-band response of the filter of Fig 3.10 (e). It is notable that appended resonators add transmission zeros between bands. 50
3.13 The filter topologies are (a) a 10th order transversal single-band coupling topology. (b) a 10th order single-band basis quad-path transversal filter. The multi-band filter in (c) a dual-band filter (d) a triple-band filter (e) a quad-band filter reactance transformed filters. 51
3.14 The ideal lossless response of (a) a single-band tenth order basis filter of Fig 3.13 (b), and (b) dual-band response of the filter of Fig 3.13(c). It is notable that appended resonators add transmission zeros between bands. 52
3.15 The ideal lossless response of (a) a triple-band response of the filter of Fig 3.13 (d), and (b) quad-band response of the filter of Fig 3.13 (e). It is notable that appended resonators add transmission zeros between bands. 53
3.16 The ideal lossless frequency response comparisons of a dual, triple-band of $N = 4, N = 6, N = 8, N = 10$. 54
3.17 The ideal lossless frequency response comparisons of a quad-band of $N = 4$, $N = 6, N = 8, N = 10$. 55
3.18 Parallel RLC resonant circuit model. 56
3.19 Dual-band filter pass-bands for order $N = 4$ and $N = 6$ are affected by various levels of resonator loss. 57
3.20 Dual-band filter pass-bands for order $N = 8$ and $N = 10$ are affected by various levels of resonator loss. 58
3.21 Triple-band filter pass-bands for order $N = 4$ and $N = 6$ are affected by various levels of resonator loss. 59
3.22 Triple-band filter pass-bands for order $N = 8$ and $N = 10$ are affected by various levels of resonator loss. 60
3.23 Quad-band filter pass-bands for order $N = 4$ and $N = 6$ are affected by various levels of resonator loss. 61
3.24 Quad-band filter pass-bands for order $N = 8$ and $N = 10$ are affected by various levels of resonator loss. 62
3.25 A fourth order, all-pole, quad-band filter topology. 64
3.26 A fourth order, all pole, quad-band filter topology. Options in a tuning sequence from A to D, tune the single band basis resonators. In option tuning E to F, resonators are tuned in horizontal plane relative to the single band basis resonators. In option G to J resonators are tuned in a vertical plane. Options K to L tune some resonators in both vertical and horizontal planes. 66

3.27 Group delay response of a fourth order, all pole, quad-band filter topology. Options in a tuning sequence from A to D, tune the single band basis resonators. In option tuning E to F, resonators are tuned in horizontal plane relative to the single band basis resonators. In option G to J resonators are tuned in a vertical plane. Options K to L tune some resonators in both vertical and horizontal plane. 67
3.28 Dual-path, dual-band options in a tuning sequence from A to C allow numerical tuning; the tuning sequence from D to F is not suitable. 68
3.29 Dual-path dual-band group delay responses for the tuning sequence A to F . 69
3.30 Options in a tuning sequence from A to D that allows numerical tuning are shown, options in a tuning sequence from E to G are not suitable. 70
3.31 Triple-path dual-band group delay responses corresponding to the tuning sequence A to H in Fig 3.30. 71
3.32 A quasi-lumped, low-pass prototype circuit as the basis for the transform. . 72
3.33 (a) A Foster expansion (b) Cauer I expansion of the multi-band circuit topology based on lowpass prototype in Fig 3.32. 73
3.34 (a) Cauer II expansion (b mixed Cauer I and II expansion of the multi-band circuit topology based on lowpass prototype in Fig 3.32. 74
3.35 A third order, quasi-lumped, low-pass, prototype circuit as the basis for the transform. 75
3.36 Dual-band, lumped element topologies: (a) Foster; (b) Cauer I; (c) Cauer II; (c) mixed Cauer I and II. 76
3.37 The frequency response for all four topologies. The four are indistinguishable. 3.36. 77
3.38 Inductor values of all topologies in the case of a dual-band, uniform bandwidth 77
3.39 Capacitor values of all topologies in the case of a dual-band, uniform bandwidth. 78
3.40 Triple-band, lumped-element topologies: (a) Foster; (b) Cauer I; (c) Cauer II; (c) mixed Cauer I and II. 79
3.41 A Foster expansion of the triple band circuit topology. 80
3.42 A Foster response of the equal triple band circuit topology as shown in Fig. 3.40. 80
3.43 Inductor values of all topologies for a dual-band, uniform bandwidth. . . . 81
3.44 Capacitor values of all topologies for a dual-band, uniform bandwidth . . . 81
3.45 Comparison of a coupled resonator and lumped-element, dual-band frequency. 83
3.46 Comparison of a coupled resonator and lumped-element, quad-band frequency. 83

4.1 The configuration of split ring resonators in single (a) and stacked (b) layers [13] 89
4.2 Filter A (a) dual-path single-band basis fourth order filter transformed to (b) dual-band dual-path filter. Filter B (c) triple-path single-band basis sixth order filter transformed to (d) dual-band triple-path filter. 90
4.3 (a) Schematic circuit of a dual-path single-band basis filter representing coupling scheme of Fig 4.2(a) and (b) dual-path dual-band filter representing coupling scheme of Fig 4.2(b) (Filter A). 91
4.4 (a) Schematic circuit of a triple-path single-band basis filter representing the coupling scheme of Fig 4.2(c) and (b) a triple-path dual-band filter representing the coupling scheme of Fig 4.2(d) (Filter B). 92
4.5 Frequency response of a 4th order dual-path single-band basis filter of the schematic circuit in Fig4.3(a) and a dual-path dual-band filter in Fig4.3(b) (Filter A). 93
4.6 Frequency response of a 4th order triple-path single-band basis filter of the schematic circuit in Fig4.4(a) and dual-path dual-band filter in Fig4.4(b) (Filter B). 94
4.7 (a) Single-band basis, 4th order, all pole topology and (b) quad-band, all pole topology. 95
4.8 A schematic circuit of a (a) fourth-order, single-band basis filter and (b) a quad-band filter 95
4.9 Frequency response of a 4th order single-band basis filter of the schematic circuit in Fig 4.8 (a) and quad-band of the schematic circuit in Fig 4.8 (b). . 96
4.10 Input/output coupling structures of coupled-line structure: (a) Layout; (b) 3-D view. This coupling topology allows for stronger coupling between feed and resonator than single layer does. 97
4.11 Resonant responses of coupled resonator structures' as shown in Fig. 4.10(b). 98
4.12 Coupling structures of coupled resonators (a) and (b) are mixed coupling, (c) top view of resonators in (b) weakly coupled to the input/output ports and its (d) 3-D view. 98
4.13 Resonant responses of coupled resonator structures in Fig 4.12(c). 99
4.14 Coupling structures of nested coupled resonators. 100
4.15 Resonant responses of nested coupled resonator structures. 100
4.16 The EM layout representing the schematic circuit as shown in Fig. 4.3 (a) is subdivided into three divisions. Each subdivision is analysed separately. . . 102
4.17 16 internal ports are inserted in the EM model to allow port tuning. 102

4.18 The sub-circuits are put together in AWR to fast-tune the length of the resonators. 103
4.19 Single band frequency response of the circuit theory versus simulation of the initial design before length-tuning. 103
4.20 Single band frequency response of the circuit theory versus simulation after length-tuning. 104
4.21 The EM layout representing the schematic circuit in Fig 4.3 (b) is subdivided into three divisions. Each subdivision was analysed separately. 104
4.22 44 internal ports are inserted in the EM model to allow port-tuning 105
4.23 The sub-circuits are put together in AWR to fast tune the length of the resonators. 106
4.24 Dual-band frequency response of the circuit theory versus simulation of the initial design before length-tuning. 106
4.25 Dual-band, frequency response of the circuit theory versus simulation after length-tuning. 107
4.26 The dual-path dual-band filter layout (a) layers stack up (indicated by different colors) of the topology corresponding to a dual-path dual-band Filter A (b) detailed micro-strip open loop resonators layout (c) top view, and (d) 3-D view. 109
4.27 The dual-path dual-band filter layout (a) layers stack up (indicated by different colors) of the topology corresponding to a dual-path dual-band Filter B (b) detailed micro-strip open loop resonator layout (c) top view, and (d) 3-D view. 111
4.28 A chain link, and a chain link like coupling realization. 112
4.29 The single-path quad- band filter layout (a) layers stack up (indicated by different colors) of the topology corresponding to a dual-path dual-band (Filter C) (b) detailed micro-strip open loop resonator layout (c) top view, and (d) 3-D view. 113
4.30 The single-path quad-band filter layout (a) layers stack up (indicated by different colors) of the topology corresponding to a singlel-path quadl-band (Filter D) (b) detailed micro-strip open loop resonators layout (c) top view, and (d) 3-D view. 114
4.31 Photographs of constructed filters: (a) Filter A: dual-path, dual-band filter; (b) Filter B: triple-path, dual-band filter; (c) Filter C: all-poles, quad-band, unchamfered filte; (d) all-poles, quad-band, chamfered filter. 115

4.32 The frequency response of the (a) ideal lossless dual-path dual-band filter versus a simulation of a lossy Filter A; (b) simulation versus measured data of Filter A. 119
4.33 The frequency response of the circuit theory and simulation for a dual-band, triple- path Filter B; the frequency response of the measured and simulation for a dual-band, triple-path Filter B. 120
4.34 S-parameters for Filter C lossless circuit response compared to the lossy simulation. 121
4.35 S-parameters of the measured data for Filter C, compared to the lossy simulation 122
4.36 Image6k 123
4.37 Image6k 124
4.38 Group delay for (a) quad-band filter with inserted cuts except for a single band, basis filter; (b) all-pole topology representing circuit in (a); (c) simulated data against measured data (Filter C). 125
4.39 Group delay for: (a) quad-band filter with inserted cuts except for single band, basis filter and the first line of the appended resonator in a horizontal plane; (b) all-pole topology representing the circuit in (a); (c) simulated data against measured data (Filter C). 125
4.40 Group delay for: (a) quad-band filter with the rest of the resonator removed except for the single band basis filter; (b) all-pole topology representing circuit in (a); (c) simulated data versus measured data (Filter C). 126
4.41 Group delay for: (a) quad-band filter with the rest of the resonator removed except for the single band basis filter; (b) all-pole topology representing circuit in (a); (c) simulated data versus measured data (Filter C). 126
4.42 Group delay for: (a) quad-band filter with the rest of the resonator removed except for the single band basis filter; (b) all-pole topology representing circuit in (a); (c) simulated data versus measured data (Filter C) 127
4.43 Group delay for: (a) quad-band filter with inserted cuts except for single band basis filter and the first line of appended resonator in a horizontal plane; (b) all-pole topology representing circuit in (a); (c) simulated data against measured data (Filter D). 127
4.44 Group delay for: (a) quad-band filter with inserted cuts except for single band basis filter and the first line of appended resonator in a horizontal plane; (b) all-pole topology representing circuit in (a); (c) simulated data against measured data (Filter D). 128

4.45 Group delay for: (a) quad-band filter with inserted cuts except for single band basis filter and the first line of appended resonator in a horizontal plane; (b) all-pole topology representing circuit in (a); (c) simulated data against measured data (Filter D). 128
4.46 Group delay for: (a) quad-band filter with inserted cuts except for single band basis filter and the first line of appended resonator in a horizontal plane; (b) all-pole topology representing circuit in (a); (c) simulated data against measured data (Filter D)). 129

5.1 Filter bank [47]. 133
5.2 Combline filter (a) equivalent circuit (b) layout [36]. 133
5.3 Configuration of switchable filter and its frequency responses [21] 134
5.4 Layout and circuit topology of switchable filter in [15] 135
5.5 Layout and circuit topology of switchable filter in [25]. 136
5.6 Topology of a fourth order parallel connected single band prototype transformed to a dual band filter and its frequency response. 137
5.7 (a) Conceptual illustration of the selected and prohibited bands. 137
5.8 Transmission line (TLIN) model 139
5.9 Pre selection operation circuit (a) two pin diodes are inserted (b) On and (c) Off states 140
5.10 Frequency responses of the pre selection non-resonant circuit operation OFF and ON states. 141
5.11 (a) Two stage pre-selection non-resonant circuit topology (b) On and (c) Off states 143
5.12 Frequency responses of the two stages pre-selection non-resonant circuit topology. 144
5.13 One-stage pre-selection circuit layout. 145
5.14 The design of the pre-selection non-resonant circuit (a) 3 D view, (b) Top View. 145
5.15 Two-stages pre-selection non-resonant circuit layout. 146
5.16 The design of the two-stages pre selection non-resonant circuit (a) 3 D view, (b) Top View. 146
5.17 The photographs of the fabricated pre-select non-resonant circuit (a) one stage (b) two stages. 147
5.18 The simulation versus measured plot of one stage pre-select non-resonant circuit (a) OFF state (b) ON state. 148

5.19 The simulation versus measured plot of two stages pre-select non-resonant circuit (a) OFF state (b) ON state. 149
5.20 Layer stack up of switchable filters A, B, and C. 151
5.21 Proposed switchable dual-band filter topology (Filter A). 151
5.22 The proposed pin-diode-based switchable dual-band filter layout (Filter A). 152
5.23 Switchable filter (a) 3 D view, and (b) Top View of Filter A 153
5.24 Proposed switchable dual-band filter topology (Filter B) with two stages pre-select non-resonant circuit (Symmetric arrangement). 154
5.25 The proposed pin-diode-based switchable dual-band filter layout (Filter B) with two stages pre-select non-resonant circuit (Symmetric arrangement). . 154
5.26 Switchable filter (a) 3 D view, and (b) Top View of Filter B 155
5.27 Proposed switchable dual-band filter topology (Filter C) with two stages pre-select non-resonant circuit. 156
5.28 The proposed pin-diode-based switchable dual-band filter layout (Filter C) with two stages pre-select non-resonant circuit. 156
5.29 Switchable filter (a) 3 D view, and (b) Top View of Filter C 157
5.30 Lossless frequency response of ON and OFF state of Filter A versus fixed dual-band (These are circuit models). 158
5.31 Lossless frequency response of ON and OFF state of Filter A circuit model versus simulation 159
5.32 Lossless frequency response of ON and OFF state of Filter B versus fixed dual-band (These are circuit models.) 160
5.33 Lossless frequency response of ON and OFF state of Filter B circuit model versus simulation. 161
5.34 Lossless frequency response of ON and OFF state of Filter C versus fixed dual-band. (These are circuit models) 162
5.35 Lossless frequency response of ON and OFF state of Filter C circuit model versus simulation. 163
5.36 Lossy frequency response of a switchable Filter A circuit model versus Filter A simulation versus fixed dual-band circuit model. 165
5.37 Lossy frequency response of a switchable Filter B circuit model versus Filter B simulation versus fixed dual-band circuit model. 166
5.38 Lossy frequency response of a switchable Filter C circuit model versus Filter C simulation versus fixed dual-band circuit model. 167
5.39 Frequency response of the switchable Filter A. 168
5.40 Frequency response of the switchable Filter B. 168

5.41 Frequency response of the switchable Filter C. 169
5.42 Photograph of the fabricated Filter A switchable filter. 169
5.43 Photograph of the fabricated Filter B switchable filter. 170
5.44 Measured (solid line) and simulated (dash line) S-parameters of the proposed switchable filter A, (a) is the OFF state where lower band is selected and the upper band is prohibted, (b) is the ON state, the upper band is selected and the lower band is prohibited. 171
5.45 Measured (solid line) and simulated (dash line) S-parameters of the proposed switchable filter B, (a) is the OFF state where lower band is selected and the upper band is prohibted, (b) is the ON state, the upper band is selected and the lower band is prohibited. 172

6.1 Symmetry of the wide-band dual-band filter. 176
6.2 A third order quasi-elliptic lowpass prototype is the basis for two dual-band filter implementations. This filter's cutoff frequency is 1 rad/s and it has one finite transmission zero at 2.5 rad/s. 177
6.3 A dual-band filter results after a transformation from the basis low-pass filter in 6.2. This prototype is created from the (a) Foster expansion and (b) mixed Cauer I and II expansions of the driving point function in the form of a partial fraction expansion. Each inductor and capacitor in the lowpass filter is transformed into its corresponding equivalent reactance for a dual-band filter. This is indicated by the same colour blocks. All capacitors are in units of pF and inductors in nH. 178
6.4 The responses of the lowpass in Fig 6.2 and dual-band filter in Fig 6.3. The dual band filter has finite transmission zeros at zero, 0.238, 0.996,1.085,1.157 and 3.059 GHz. 179
6.5 The ratio of maximum to minimum element value ranges for a wide-band (single) and dual-band Filter with the same overall bandwidth 181
6.6 Layout of inductor models (a) a single turn and (b) spiral inductor. 182
6.7 3-D view of of inductor models (a) a single turn and (b) spiral inductor. . . 182
6.8 Layout of multi-plate capacitor comprising *n* plates [2]. 183
6.9 3-D view of of the capacitor 183
6.10 Blind via hole connecting two layers and a through via hole (top to ground) [2]. 184

6.11 (a) A side view of a rectangular via connecting two strip-lines on different levels in a multi-layer circuit board con- figuration. The strip-lines are 0.25 mm by 1.25 mm, the via is 0.5 by 0.75 mm, and the reference planes are separated from the via by 0.25 mm. (b) The equivalent circuit chosen to represent the rectangular via discontinuity. The transmission lines represent the strip-line portions and the inductors and capacitors represent various parts of the via. (c) The geometry of the cylindrical via discontinuity. (d) An equivalent circuit of the cylindrical via discontinuity [4]. 185
6.12 The layout of Design A (Foster) implementation 186
6.13 The layout of Design B (mixed Cauer I and II) implementation 187
6.14 Layer stack-up based on Park Electrocomp's Mercurywave 9350 and 106 prepreg layers. 187
6.15 Inductor implementation for the filter of Fig 6.3. 188
6.16 The 3-D view of Design A of the Foster expansion corresponding to the circuit diagram of Fig. 6.2 (a) 188
6.17 The 3-D view of Design B of mixed Cauer I and II corresponding to the circuit diagram of Fig. 6.2 (b) 189
6.18 Top view; (b) Photographs of the constructed filter design A of the Foster expansion corresponding to the circuit diagram of Fig. 6.2 (a). 190
6.19 Top view; (b) Photographs of constructed filters of Design B of mixed Cauer I and II corresponding to the circuit diagram of 6.2 (b). 190
6.20 S-parameters for (a) Ideal lumped element filter compared to Design A simulated data, (b) Design A simulated against measured data, (c) Design B simulated against measured data and (d) A comparison of design A and design B measured data. 191
6.21 Q-factors estimated by Sonnet for selected inductors as labelled in Fig. 4.2. 191
6.22 Equivalent circuit with the parasitic elements for an inductor of the filter of Fig. 6.3. L_s is the desired inductance and the other elements are spurious elements. 193
6.23 The ideal circuit model in which the highlighted inductor L_{1a} is replaced by the corresponding circuit in (b) with parasitic elements (refer to Fig. 6.22). 194
6.24 The ideal circuit model in which the highlighted inductor L_{1b} is replaced by the corresponding circuit in (b) with parasitic elements (refer to Fig. 6.22). 195
6.25 The ideal circuit model in which the highlighted inductor L_{3a} is replaced by the corresponding circuit in (b) with parasitic elements (refer to Fig. 6.22). 196

6.26 The ideal circuit model in which the highlighted inductor L_{3b} is replaced by the corresponding circuit in (b) with parasitic elements (refer to Fig. 6.22). 197
6.27 The ideal circuit model in which the highlighted inductor L_{1b} and L_{3b} is replaced by the corresponding circuit in (b) with parasitic elements (refer to Fig. 6.22). 198
6.28 The ideal circuit model in which the highlighted inductor L_{2a} is replaced by the corresponding circuit in (b) with parasitic elements (refer to Fig. 6.22). 199
6.29 The ideal circuit model in which the highlighted inductor L_{2b} is replaced by the corresponding circuit in (b) with parasitic elements (refer to Fig. 6.22). 200
6.30 The ideal circuit model in which the highlighted inductor L_{4a} is replaced by the corresponding circuit in (b) with parasitic elements (refer to Fig. 6.22). 201
6.31 The ideal circuit model in which the highlighted inductor L_{4b} is replaced by the corresponding circuit in (b) with parasitic elements (referto Fig. 6.22). . 202
6.32 The effect of the spurious components of the inductor L_{1a} and L_{1b}, detailed in Fig. 6.23 and Fig. 6.24 on the ideal lumped-element filter response. The bandwidth of band two is affected most dramatically 203
6.33 The effect of the spurious components of the inductor L_{3a} and L_{3b}, detailed in Fig. 6.25 and Fig. 6.26 on the ideal lumped-element filter response. The bandwidth of band two is affected most dramatically 204
6.34 The effect of the spurious components of the inductor L_{1b}, L_{3b}, detailed in Fig. 6.27 on the ideal lumped-element filter response. The bandwidth of band two is affected most dramatically 205
6.35 The effect of the spurious components of the inductor L_{2a} and L_{2b}, detailed in Fig. 6.28 and Fig. 6.29 on the ideal lumped-element filter response. The bandwidth of band two is affected most dramatically 206
6.36 The effect of the spurious components of the inductor L_{4a} and L_{4b}, detailed in Fig. 6.30 and Fig. 6.31 on the ideal lumped-element filter response. The bandwidth of band two is affected most dramatically 207
6.37 Resonator Circuit [46] 208
6.38 Tunable mixed Cauer I and II dua- band prototype filters (a) mixed Cauer I and II circuit model, and its (b) its physical layout. 209
6.39 Fixed ideal response of the circuit in Fig. 6.3 versus tunable response of the circuit and simulated prototypes of Fig 6.38 210
6.40 Fixed ideal response of the circuit in Fig. 6.3 versus tunable response of the circuit and simulated prototypes of Fig 6.38 211

A.1 Length of the Feeds on the top layer: filter A 222

A.2 Length of resonator 1 to 4: filter A 223
A.3 Length of the resonators 5 to 8: filter A 224
A.4 Overlaps between feeds and resonator 1 to 4: filter A 225
A.5 Spacing and gaps of resonators 1 to 4: filter A 226
A.6 Gaps and spacing between Resonators 1 to 4 and the appended resonators 5 to 8: filter A 227
A.7 Length of the Feeds on the top layer: filter B 228
A.8 Length of resonator 1 to 6: filter B 228
A.9 Length of the resonators 7 to 12: filter B 229
A.10 Overlaps between feeds and resonator 1 to 6: filter B 229
A.11 Spacing and gaps of resonators 1 to 6: filter B 230
A.12 Gaps and spacing between Resonators 1 to 6 and the appended resonators 7 to 12: filter B 231
A.13 Length of the Feeds on the top layer: filter C 232
A.14 Length of resonator 1 to 4 and resonators 9 to 12: filter C 232
A.15 Length of the resonators 5 to 8 and resonators 13 to 16 : filter C 233
A.16 Width of the feeds: filter C 233
A.17 Gaps and spacing and overlaps : filter C 234
A.18 Gaps of resonators 5 to 8 and resonators 13 to 16: filter C 234
A.19 Length of the Feeds on the top layer: filter D 235
A.20 Length of resonator 1 to 4 and resonators 9 to 12: filter D 236
A.21 Length of the resonators 5 to 8 and resonators 13 to 16 : filter D 237
A.22 Width of the feeds: filter D 238
A.23 Widths of resonators 1 to 4 and resonators 9 to 12: filter D 239
A.24 Widths of resonators 5 to 8 and resonators 13 to 16: filter D 240
A.25 Gaps for resonators 1 to 4 and resonators 9 to 12 , spacing and overlaps : filter D 241
A.26 Gaps of resonators 5 to 8 and resonators 13 to 16: filter D 242

B.1 Length of one stage non-resonant circuit 243
B.2 Length of one-stage non-resonant circuit 244
B.3 Length of one-stage non-resonant circuit 244
B.4 Width of one-stage non-resonat circuit 245
B.5 Length of two stages non-resonant circuit 245
B.6 Width of two stages non-resonant circuit 246
B.7 Length of one-stage switchable filter 247
B.8 Length of the two-stages switchable 248

C.1 Length of Design B (Mixed cauer I and II) top layer 249
C.2 Length of Design B (Mixed cauer I and II) next layer 250
C.3 Width of Design B (Mixed cauer I and II) top layer 250
C.4 Width of Design B (Mixed cauer I and II) next layer 251
C.5 The numbered inductors are enlarge in Fig C.6 to C.9 251
C.6 This inductor represent inductors number 3 and 4 in Fig C.5. 252
C.7 This inductor represent inductors number 2 and 5 in Fig C.5. 252
C.8 This inductor represent inductors number 1 and 6 in Fig C.5. 252
C.9 This inductor represent inductors number 7 and 8 in Fig C.5. 252
C.10 Length of Design A (Foster topology) top layer. 253
C.11 Length of Design A (Foster topology) next layer. 253
C.12 Width of Design A (Foster topology) top layer. 254
C.13 Width of Design A (Foster topology) next layer. 254
C.14 The numbered inductors are enlarge in Fig C.6 to C.9 255

List of tables

3.1 Frequency specification of the dual-, triple- and quad-band prototypes . . . 34
3.2 Coupling matrix for $N = 10$ transversal topology of Fig. 3.13(b) 36
3.3 Frequency transformation variables of a dual-band, multi-band filter with specification in Table 3.1. 37
3.4 Frequency transformation variables triple band multiband filter with specification in Table 3.1. 39
3.5 Frequency transformation variables quad-band, multi-band filter with specification in Table 3.1. 40
3.6 Element values of Foster, Cauer I, Cauer II and mixed Cauer I and II topology of dual-band circuits. 75
3.7 Element values of the Foster, Cauer I, Cauer II and mixed Cauer I and II topology of triple-band circuits. 80

5.1 Impedance and electrical values of the circuit in Fig 5.9 (a) 139

6.1 The g-values found from the Table in [35] of the circuit in Fig 6.2 177
6.2 The calculation of the lumped-element values calculation based on [6] of the circuit in Fig 6.3 180
6.3 Comparison of element value ranges for a wide-band and dual-band filter with the same overall bandwidth. This factor is a measure of the challenge level to design a dual-band filter as compared to a single band filter with the same bandwidth. Units of inductors are in (nH) and capacitors in (pF). . . . 180
6.4 Extracted element Values of Fig. 6.22 for each inductor. The units of the extracted elements: inductors in nH, capacitors in pF, and resistors in Ω . . 205

A.1 Length of Filter A for Fig A.1, Fig A.2 and Fig A.3 221
A.2 Layer overlapping of Filter A shown in Fig A.4 222
A.3 Spacing and gaps of Filter A shown in Fig A.5 and Fig A.6 222
A.4 Length of Filter B for Fig A.7, Fig A.8 and Fig A.9 223

A.5 Layer overlapping of Filter B shown in Fig A.10 223
A.6 Spacing and gaps of Filter B shown in Fig A.12 and Fig A.12 224
A.7 Length of Filter C for Fig A.13, Fig A.14 and Fig A.15 225
A.8 Width of Filter C shown in Fig A.16 226
A.9 Gaps, spacing and overlaps of Filter C shown in Fig A.17 and Fig A.18 . . 226
A.10 Length of Filter D for Fig A.19, Fig A.20 and Fig A.21 227
A.11 Width of Filter D shown in Fig A.22, Fig A.23, Fig A.24 230
A.12 Gaps, spacing and overlaps of Filter D shown in Fig A.25 and Fig A.26 . . 231

B.1 Lengths of the one-stage non-resonant circuit in Fig B.1, Fig B.2 and Fig B.3.246
B.2 Lengths of the two-stage non-resonant circuit in Fig B.5. 247

C.1 Lengths of Design B (mixed Cauer I and II) for Fig C.1, and Fig C.2 255
C.2 Lengths of the inductors indicated in Fig C.5, are represented by enlarge inductors where inductor in Fig C.6 represents inductor 3 and 4, and inductor in Fig C.7 represents inductor 2 and 5, inductor in Fig C.8 represents inductor 1 and 6, and inductor in Fig C.9 represents inductor 7 and 8. 256
C.3 Width of the lines of design B in Fig C.3 and Fig C.4. Width of the enlarged inductors and spacing between turns. 256
C.4 Lengths and widths of the lines) of Design A (Foster topology) for Fig C.10, and Fig C.11 257

Chapter 1

Introduction

A microwave filter is an analog component that blocks or allows signals of certain frequencies. The performance of the filter depends on its electrical features, specified as insertion loss, return loss and frequency selectivity. Efficient power delivery is related to return and insertion loss. High return loss and low insertion loss are the most vital features that describe the performance of the filter. Frequency selectivity is a significant feature for spectrum utilization, providing a clear pass or stop-band edge of the selected frequency. It is beneficial to have the physical dimension of the filter small in terms of size, weight and volume. The applications of microwave filters have been expanded and upgraded from telecommunications to wireless systems [68, 76, 65, 72, 16, 73] which include radar, navigation, remote sensing, radio astronomy and, in general, any systems that operate in the microwave band. It therefore makes the filter one of the most important devices in the RF chain. Figure 1.1, a representative block diagram for an RF communication system, shows that microwave filters are essential components of any transceiver.

The design of microwave wave filters generally begins with a low pass prototype that can be converted to a high-pass, band-pass or band-stop prototype [35] by utilizing frequency transformations. The response is approximate to the ideal LC resonators, known as the approximation problem. There are different methods of filter approximation, for example, the Butterworth, Chebyshev and Elliptic approximations. All these methods exhibit different characteristics and have unique advantages which depend on their application. The Butterworth approximation presents a flat response through pass-band to stop-band. This approximation is commonly known as a maximally flat approximation. It is of great advantage to implement maximally flat filters when low phase distortion is highly required. The Chebyshev approximation shows equal ripple characteristics in the pass band. It has a steeper transition which is sometimes referred as skirt, and enables high frequency selectivity. Elliptic approximation also shows equal-ripple characteristics but this appears both in the

in-band and out-of-band (rejection) region. It provides high frequency selectivity for a low order of filter.

The approximation functions synthesize the filter by employing the circuit theory. For microwave resonators, the design involves transmission lines. These are distributed networks, networks, whose magnitude and phase of voltages and currents differ along their physical dimensions. It is not the case for lumped elements, as the magnitude and phase of the voltages and currents are the same for every individual element. The wave propagation concept in distributed networks extends from the circuit theory through a mathematical equation, known as telegraphic equation [56]. This equation can also be obtained from Maxwell's equations. The telegraphic equation serves as a bridge between the circuit and electromagnetic theories. The resonant frequency of the LC resonators is obtained in terms of inductances and capacitances. For electromagnetic circuits, the resonant frequency is obtained in terms of the physical dimension of the structure. When the frequency response of an EM structure matches the response of the filter synthesis, by utilizing the circuit theory, this phenomenon is refer as realization.

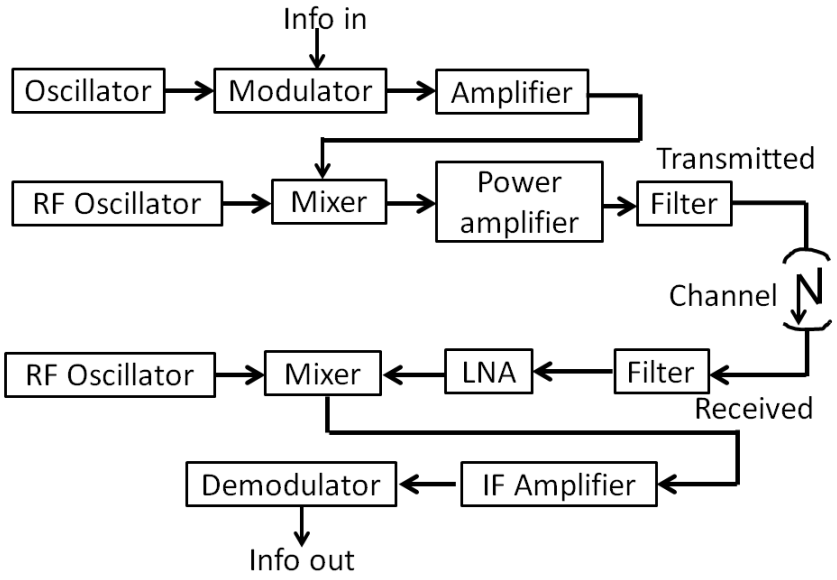

Fig. 1.1 Block diagram for an RF communication system [32].

1.1 Motivation

In every RF and microwave system, a filter is a central and important component which provides the clear pass or stop band edge of the desired frequency, filtering signals transmitted or received. Microwave band ranges from 300 MHz to 30 GHz while the millimeter band

starts from 30 GHz and goes 300 GHz. There are various applications, such as satellite communication, navigation and, the most popular, the wireless communication industry. The invention of new wireless communication devices which include features, such as WiFi, are widely employed all over world. The demand for network connections increases daily as many users make use of voicemail, emails and short text messages, which require high data transfer. It is a challenge for filter and other RF hardware designers to meet users' requirements when taking into consideration the loss, frequency selectivity and size of the hardware. In the past, microwave systems operated over a single frequency band, but the growing wireless industry requires that millions of users around the globe share the frequency spectrum at the same time. This has led engineers to conduct research into multi-band filters. Multi-band, band-pass filters have been a subject of interest for the past decade. Significant progress has been made on the design techniques of multi-band filters. They have enhanced features over diplexers/multiplexers. A multi-band filter as a single device can operate at multiple frequencies and can have symmetric or asymmetric characteristics as well as transmission zeros which offer great frequency selectivity. Multi-band filters eliminate the need of impedance matching between the source and the load, can achieve pass band gain and stop-band rejection as these are critical for filter performance.

1.2 Research objectives

The objectives of the research are to investigate the design of multi-band-narrow-band-coupled resonator filters and wide-band-lumped-elements filters. The realization of prototypes is limited to microstrip and these are constructed and packaged on a Mercury-wave, 9350 multilayer substrate.

The objectives of the research are summarized as follows.

- To determine multi-band synthesis methods based on a systematic synthesis procedure;
- To effect the realization of filters by employing new topologies that are compact yet reduce spurious coupling between elements;
- To include electronic tuning and/or reconfigurability, depending on the application;
- To provide filter responses that satisfy the design specifications, such as passband positions and bandwidths, selectivity and insertion loss.

These objectives are accomplished by finding network topologies suitable to implement multi-band filters based on symmetric or asymmetric prototypes while requiring the least

number of cross-couplings; to find possible methods that manipulate the minimum number of couplings and resonator center frequencies to reconfigure the multiple bands, such as shifting these bands in frequency or eliminating certain pass bands utilizing electronic switching; to evaluate how these filter-coupling structures plus electronic reconfigurable circuit elements are incorporated in multi-layer substrates.

1.3 Dissertation contributions

The main contributions of the thesis are:

- The practical aspects of multi-band filter prototypes, based on the reactance transform method.

The prime focus is on filters realized by employing reactance transforms for narrow-band, based on coupled resonators and wide-band, based on lumped elements. A designer's concerns, when considering a new method of realization, are related to filter order to meet specifications. Factors influencing selectivity, sensitivity, as well the effects of Q-factors when using low Q technologies, are also of importance and to be considered. This work investigated the properties of the multi-band transform filters as affected by (1) number of bands, (2) spacing of bands, (3) resonator loss, (4) direct comparison of the narrow-band and wide-band general mapping function for a narrow band filter example.

- Design approach for coupled-resonator, multi-band filters based on de-tuning methods, group delay and port tuning.

The tasks undertaken were concerned with the linearity of response and effort on numerical tuning by employing group delay methods. Numerical tuning of a design in software to fit the prototype response is generally based on S_{11} group delay, much in the same manner as physical filters are tuned by employing tuning screws. An interesting case is the numerical tuning procedure followed for planar multi-band filters where resonator unloaded Q's are in the range of 100 to 200, much lower than those of wave-guide resonators. To determine a practical order of structures with expanding complication is more challenging than single-band filters. Port-tuning is essential for design closure. Port-tuning for filters on different layers and with novel transversal topologies (involving two or more parallel connected main paths) is a concern for designers.

- A switchable dual-band filter based on a pre-selection network of low orders

A process to obtain a switchable, dual-band filter with electronically selected pass-bands, based on a reactance transform method for coupled resonator filters, is described. A dual-band filter realized on a multi-layer substrate was designed for passive space applications and reconfigurability, and demonstrated by employing a pre-selection method. Relevant practical aspects related to modelling, simulation and measurement for these type of filters are presented.

- Design and effect of parasitic on quasi-lumped element wide-band dual-band filter.

The design of a quasi-lumped element, dual-band filter is implemented on a multi-layer substrate. The effect of main parasitic elements in the quasi-lumped element implementation, as well as the controlled suppression between the two bands, are described and demonstrated.

1.4 Dissertation outline

The aim of this section is to outline the content of the chapters discussed.

Chapter 2 presents presents the background and fundamental concepts of coupled resonators, namely inverter coupling and resonant frequency. Multi-band synthesis methods, which include optimization, multi-modes and reactance transform, are introduced.

Chapter 3 presents an investigation of the representation regarding the properties of multi-band, narrow-band, coupled resonators and wide-band, lumped element by considering the number of bands, spacing of bands, selectivity, losses, effects of Q factor and numerical-group-delay tuning.

Chapter 4 presents the implementation of multi-band, narrow-band, coupled resonators. Three filters were designed, constructed and measured. Two are dual-band, connected in parallel, with dual and triple main paths and a quad-band, all-poles filter.

Chapter 5 presents a coupled resonator with two, switchable bands. A pre-select, non-resonant network is proposed to enable switching. Pin diodes were employed as switching elements.

Chapter 6 presents a wide-band, quasi-lumped element, dual-band filter. The effects of parasitic on the response are discussed. The prototypes were further extended to include tunability in the design. Tunable filters are related to shifting the filter's center frequencies and bandwidths, which requires a varactor diode as a tuning element.

Chapter 7 presents conclusion and suggestions for future work.

1.5 List of publications

- Nepaya, L. N. P., Geschke R, H. (2018). Quasi-lumped element implementation of a wide-band dual-band filter based on reactance transformations. RADIOENGINEERING, (Provisionally accepted).
- Geschke, R. H. and Nepaya, L. (2017). Lossy multiband filters and ghost passbands. In European Microwave Conference (EuMC), 2017 47th, pages 648–651. IEEE.
- Geschke, R. and Nepaya, L. (2016). Practical realisation of multiband planar filters based on a reactance transform method. In Microwave Conference (EuMC), 2016 46th European, pages 134–137. IEEE.

Chapter 2

Background of microwave filters

2.1 Single band Basics

Microwave filters are constructed and designed based on equivalent resonator circuits. A resonator is described as an element which stores both electric and magnetic energy that are frequency dependent. Microwave resonators consist of inductance (L) and capacitance (C) which can either be connected in series or parallel configuration, as depicted in in Fig. 2.1.Inductance is for magnetic energy storage while capacitance is for electric energy storage. Resonators resonate at their resonance frequencies, which is a frequency where electric energy, stored in electric fields, equals magnetic energy, stored in magnetic fields. LC resonators are the basis of filters, and are mathematical models that lead to the realization of the actual device. Next follows a discussion of the critical resonant property of coupled resonators, namely couplings.

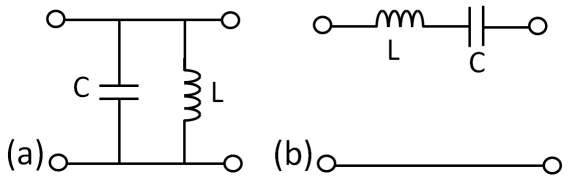

Fig. 2.1 LC resonator (a) parallel and (b) series connections.

2.1.1 Resonant properties of coupled resonators

Coupling of coupled resonators

Single-band, coupled, resonator prototypes consist of multi-coupled LC resonator circuits. The couplings can be capacitive, inductive or mutually inductive [20]. In Fig. 2.2(a), the

resonators are coupled with series capacitors and in (b) shunt inductors and in (c) the coupling is mutual. These are frequency dependent reactances known as real inverters. Additionally, Cohn introduced frequency independent reactances referred to as ideal inverters. Ideal inverters are commonly employed for narrow band filters, while real inverters are mostly utilized in wide-band designs.

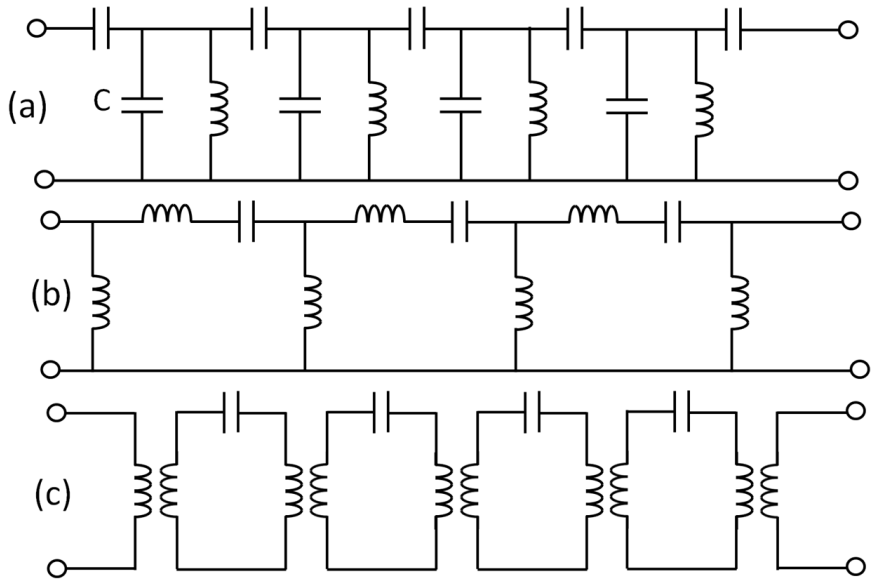

Fig. 2.2 Lumped constants (a) series capacitive couplings (b) inductive couplings (c) mutual inductive couplings [20]

Coupled resonators are designed based on two approaches namely: (1) lowpass ladder networks and (2) mutual-inductively coupled networks.Filters designed on ladder networks are directly coupled resonators; inter-coupling is between adjacent resonators [46, 35, 20] while filter design based on mutual-inductive networks allows cross couplings [10]. Cross coupling is couplings between non-adjacent resonators.

Coupled resonators based on lowpass ladder networks

The design began with a lowpass ladder network which can be even or odd, and is presented in Fig. 2.3. The values of the elements (g values) are generalized and available in the Tables [46, 35, 10]. The ladder networks in Fig. 2.3 can be transformed to have one type of reactance element, either capacitor or inductance. This is possible through the use of two port-idealized immittance inverter network (see Fig. 2.4).

If the load admittance J_L or the load impedance K_L is attached at one terminal, the impedance seen looking in the opposite terminal is described by

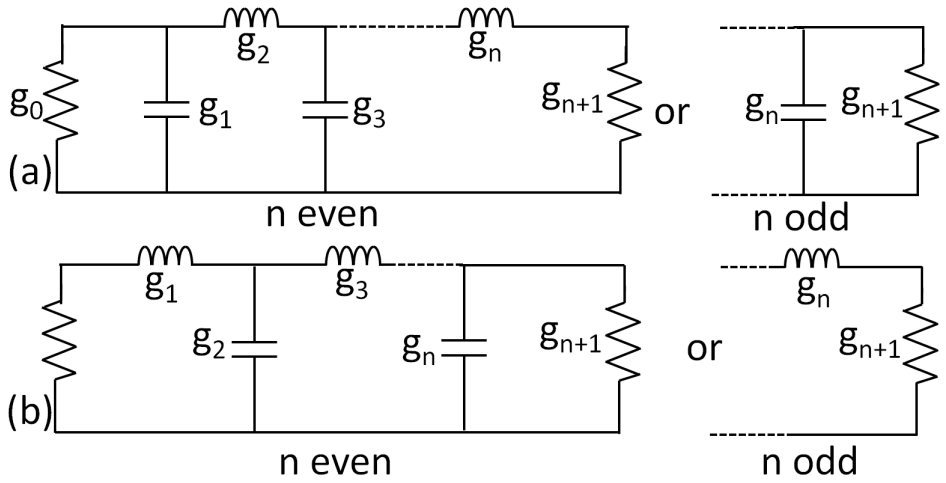

Fig. 2.3 Lowpass prototype filters for all-pole filters with (a) a ladder network structure and (b) its dual [35].

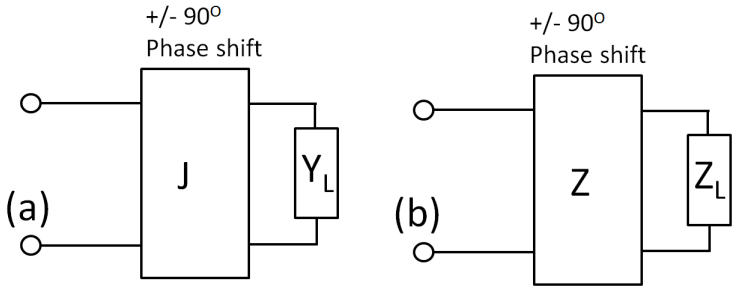

Fig. 2.4 (a). Admittance inverter, (b) impedance inverter.

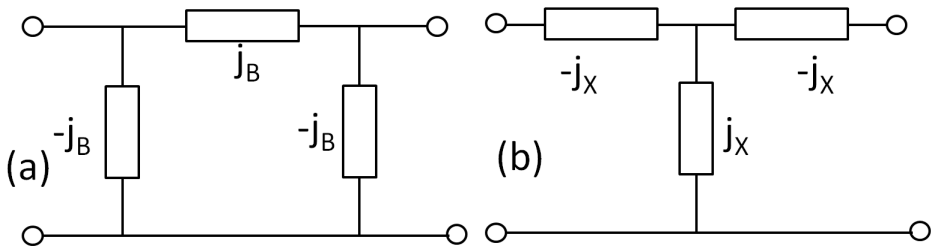

Fig. 2.5 (a). A π network admittance inverter, (b) a T network impedance inverter.

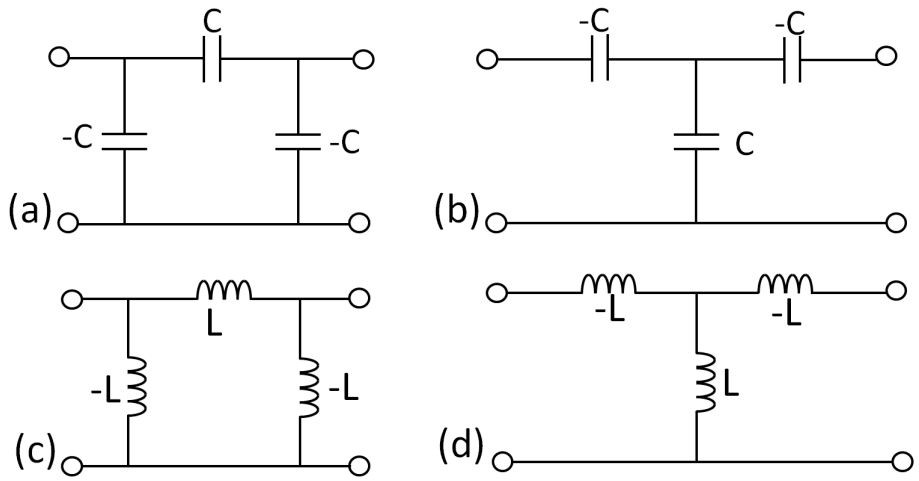

Fig. 2.6 (a) Capacitance and (c) inductance representation of admittance inverter, (b) capacitance and (d) inductance representation of impedance inverter [35]

.

$$Z_{in} = \frac{K^2}{Z_L} \tag{2.1}$$

$$Y_{in} = \frac{J^2}{ZJ_L} \tag{2.2}$$

Immittance inverters are constructed with T or π networks (see Fig. 2.5) and implemented by lumped elements (see Fig. 2.6).

The series inductances with an inverter on each side looks like a shunt capacitance from its exterior terminals. Furthermore, a shunt capacitance with an inverter on both sides look like a series inductance (Fig. 2.7).

With immittance inverters defined in Fig. 2.4 and 2.5, the transformation of the low-pass ladder network in Fig. 2.3(a) to one type of reactance element is detailed in Fig. 2.8. As indicated in Fig. 2.8(b) an inverter inserted in front of the (capacitor) first element, causes the other elements to alternate from inductor to capacitor and vice-versa until all elements are transformed. Inserting another inverter into (c) the elements alternate again, as shown in (b), and (d) shows all elements transformed to a shunt capacitor. The network consisting of one type or reactance element is transformed into a single-band, coupled resonator bandpass filter (See Fig. 2.8(e)).

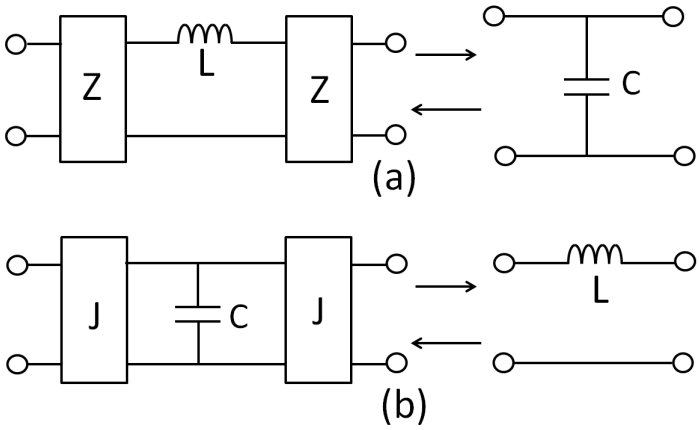

Fig. 2.7 (a) Immittance inverters convert a series inductance into an equivalent circuit with shunt capacitance. (b) Immittance inverters to convert a shunt capacitance into an equivalent circuit with series inductance.

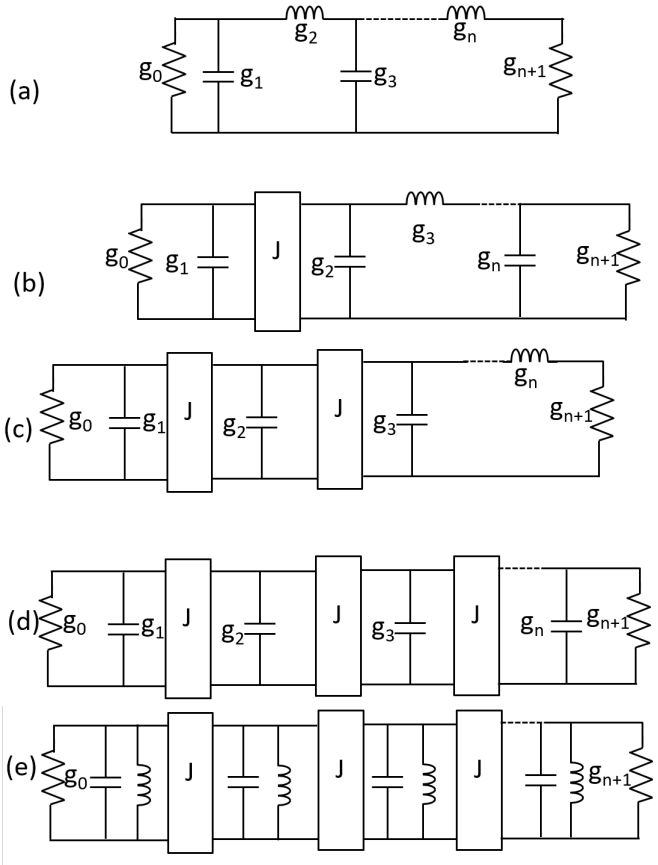

Fig. 2.8 Low pass ladder networks in (a) is transformed through ideal inverter placement in (b) and (c) which end up with one type of reactance elements, capacitors only in (d) that is transformed into a single-band band-pass filter in (e).

Coupled resonator based on coupling matrix

The coupled resonator bandpass prototype (BPP) resembles the circuit in Fig 2.2 (c) and consists of lumped element series resonators inter-connected by transformers (mutual inductive). The cross-coupling version [1] is presented in Fig. 2.9.

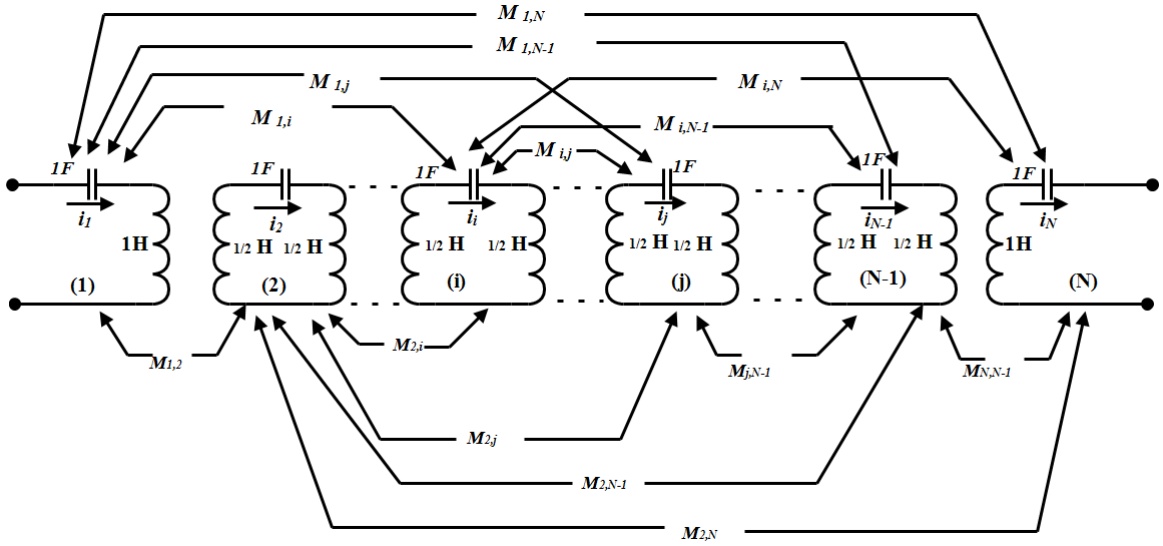

Fig. 2.9 Band pass filter prototype [1].

On the distributed model Fig.2.10,the inverters substitute mutual inductive couplings, as indicated in Fig. 2.9, with the same value as the mutual couplings of the transformers.The inverters provide equal quantities of coupling energy between the resonators in a similar way as transformers and with an identical phase change of 90°.

The synthesis techniques for a popular, coupling matrix [8] are formulated from a two-port, short circuit admittance matrix. The admittance matrix is synthesized directly from the co-efficients of the polynomials. The coupling matrix is a mathematical characterization of filter topologies in the design of coupled resonators. The coupling matrix is computed from the transmission and reflection filtering functions S_{21} and S_{11}. The coupling matrix is represented in Fig. 2.11.

The coupling matrix depicted in Fig. 2.11, represents the network of the $N \times N$ coupling matrix. The letter (X) represents elements (nodes) which are interconnected. It is difficult to implement this network practically, as all elements are interconnected. The technique, known as similarity transform or rotation [10] is employed to transform the $N \times N$ matrix to its simple form by eliminating some elements. The simplified matrix results in topologies which implement single-band band-pass filters.

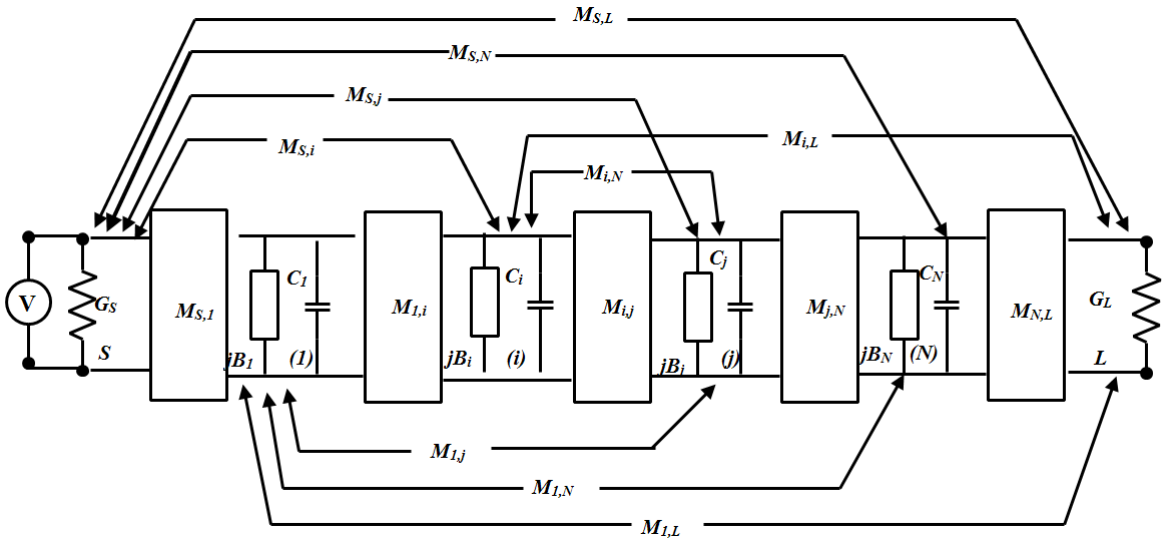

Fig. 2.10 Low pass distributed prototype circuits.

	1	2	....	k	....	N-1	N
1	X	X	X	X	X	X	X
2	X	X	X	X	X	X	X
⋮	X	X	X	X	X	X	X
k	X	X	X	X	X	X	X
⋮	X	X	X	X	X	X	X
N-1	X	X	X	X	X	X	X
N	X	X	X	X	X	X	X

Fig. 2.11 Coupling matrix

Inter-resonator and external coupling calculations

Coupling parameters of coupled resonators consist of resonant frequencies, inter-resonator coupling coefficients and input/output coupling, known as the external quality factor. Resonant frequency provides a primary interpretation of the filter performance, and coupling coefficients are determined from it. Inter-resonator coupling is coupling between resonators. For two resonators coupled by ideal admittance or impedance inverters, the inter-resonator can be calculated by employing electric and magnetic wall symmetry [10, 35]. Figure 2.12(a) consists of two resonators separated by an inductive coupling element of a T network, as defined in Fig. 2.6 (d). The coupling element has a shunt inductance L_m and two series inductance values of $-L_m$. The coupling coefficient is determined by evaluating the resonant frequency of the even f_m and odd f_e mode of Fig. 2.12 (b) and (c) written as [10]

$$f_m = \frac{1}{2\pi\sqrt{(L-L_m)C}} \tag{2.3}$$

$$f_e = \frac{1}{2\pi\sqrt{(L+L_m)C}} \tag{2.4}$$

Equations 2.3 and 2.4 give the inductive coupling coefficient k_M as

$$k_M = \frac{L_m}{L} = \frac{f_e^2 - f_m^2}{f_e^2 + f_m^2} \tag{2.5}$$

The coupling element M between two adjacent resonators is given by

$$M = \frac{F_0}{BW}\frac{f_e^2 - f_m^2}{f_e^2 + f_m^2} \tag{2.6}$$

where f_0 and BW are the filter's centre frequency and bandwidths.

Figure 2.13 presents a π network capacitively coupling of an admittance inverter J as defined in Fig. 2.6 (a). The resonant frequencies f_m and f_e of the two circuits in Fig. 2.13 (b) and (c) are written as [10]

$$f_m = \frac{1}{2\pi\sqrt{(C-C_m)L}} \tag{2.7}$$

$$f_e = \frac{1}{2\pi\sqrt{(C+C_m)L}} \tag{2.8}$$

Equations 2.7 and 2.8 give a capacitive coupling coefficient k_e as

$$k_e = \frac{C_m}{C} = \frac{f_m^2 - f_e^2}{f_m^2 + f_e^2} \tag{2.9}$$

The coupling element M between two adjacent resonators is given by

$$M = \frac{F_0}{BW} \frac{f_m^2 - f_e^2}{f_m^2 + f_e^2} \tag{2.10}$$

The external quality factor is deduced from the input coupling and the first resonator. The representation of the equivalent circuit of the input/output coupling includes conductance G in Fig 2.14. When frequency offsets from the resonance, it constitutes

$$\Delta_{\omega\pm} = \pm \frac{\omega_0}{2Q_e} \tag{2.11}$$

the phase of S_{11} in Fig. 2.15 and takes $\pm 90°$. Thus the Q_e is related to the $\pm 90°$ bandwidth in the phase of S_{11} by $\Delta\omega_{\pm 90} = \Delta\omega_+ - \Delta\omega_- = \frac{\omega_0}{Q_e}$

$$Q_e = \frac{\omega_0}{\Delta\omega_{\pm 90}} \tag{2.12}$$

Calculating inter-resonator coupling by electric and magnetic walls is a major challenge to implement. Another option to calculate inter-resonator coupling is to use electromagnetic (EM) simulation. The resonant frequency f_m and f_e are evaluated from the two resonators coupled in a two or one port network as presented in Fig 2.16 . The requirement for this approach is weak coupling of the ports . For a one port network, the two resonators present two peaks of S_{11} (Fig 2.17) that represent two frequencies f_e and f_m.

2.2 Multi-band filters

A multi-band filter presents pass-bands at different frequencies, and bandwidth generally can be equal or unequal. The filter separates and refines the frequency components of a signal, by allowing certain frequencies to pass through a band while stopping or rejecting frequencies that are out of band by keeping the frequency within their spectral limits. There are different approaches involved in the network synthesis of multi-band filters which include (i) utilizing the multiple harmonic resonating modes of resonators, (ii) a single filter structure realization based on the coupling matrix synthesis, (iii) optimization and (iv) reactance transform methods. The latter produces a number of passbands, all with the same shape of response but with different bandwidths.

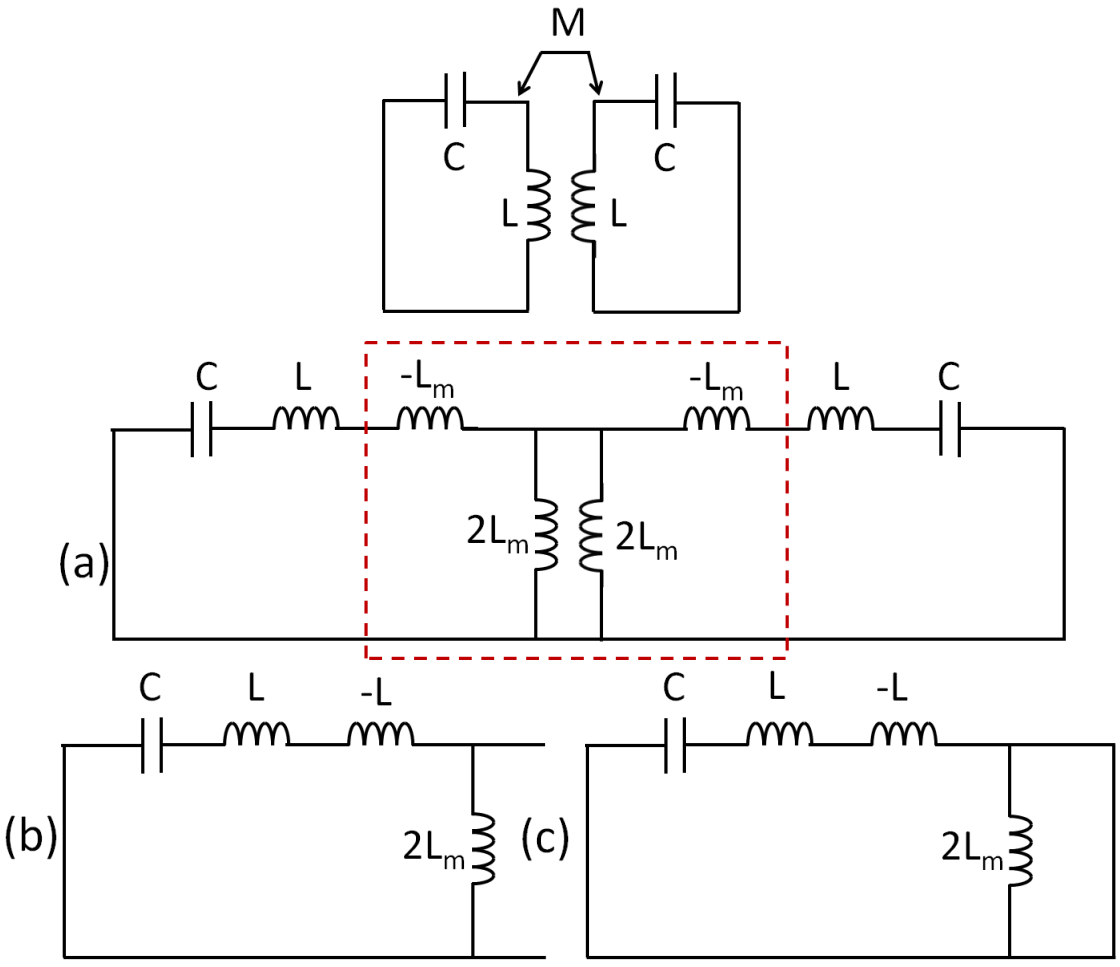

Fig. 2.12 N + 2 Coupling matrix for the extended form.

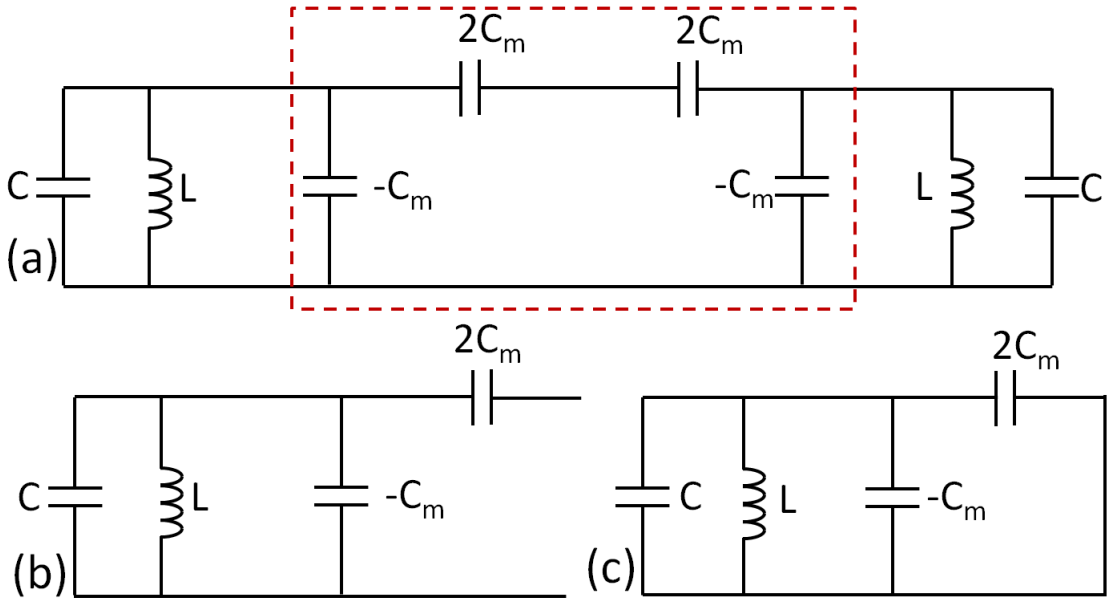

Fig. 2.13 N + 2 Coupling matrix for the extended form.

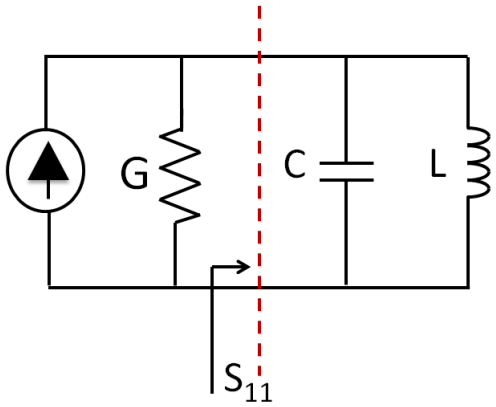

Fig. 2.14 Input coupling and the first resonator equivalent circuit [10].

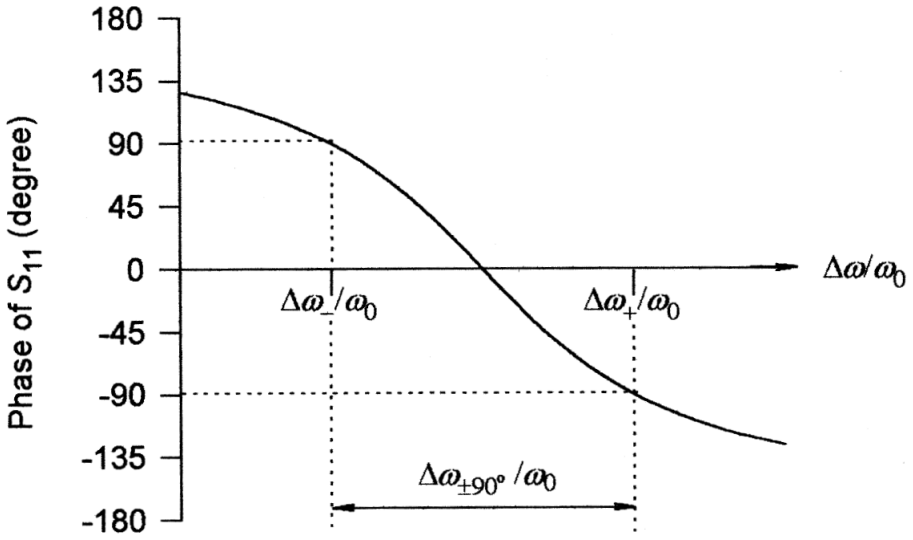

Fig. 2.15 Phase response of S_{11} for the circuit in Fig 2.14 [35].

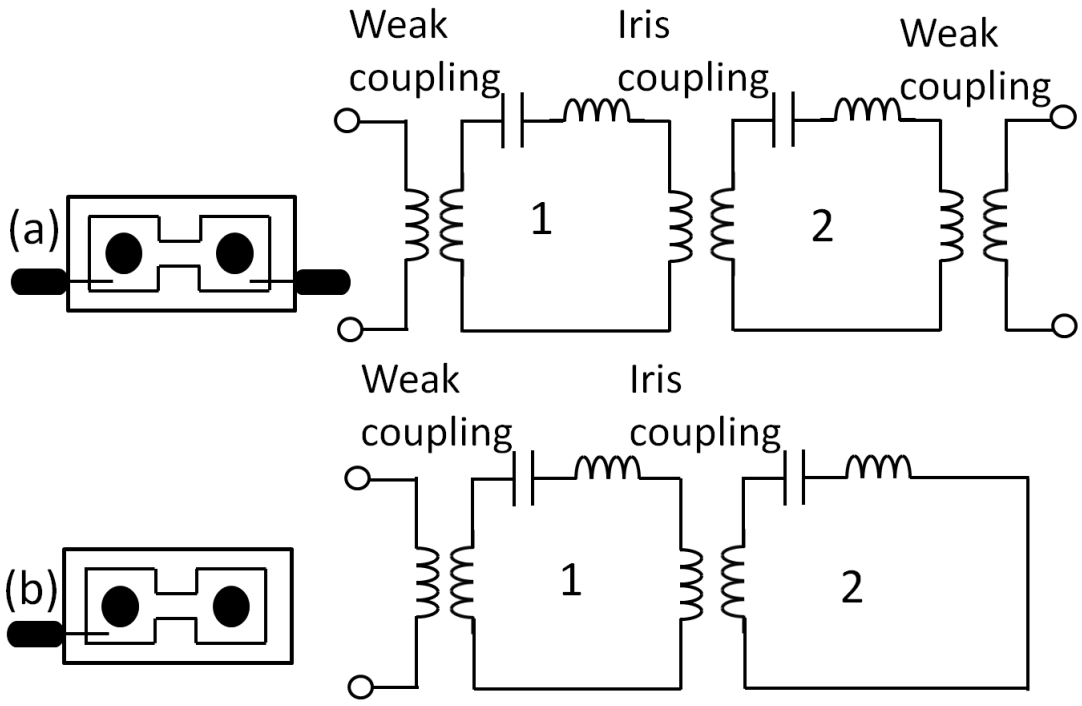

Fig. 2.16 Measurement of inter-resonator coupling using (a) two port (b) one port network [10]

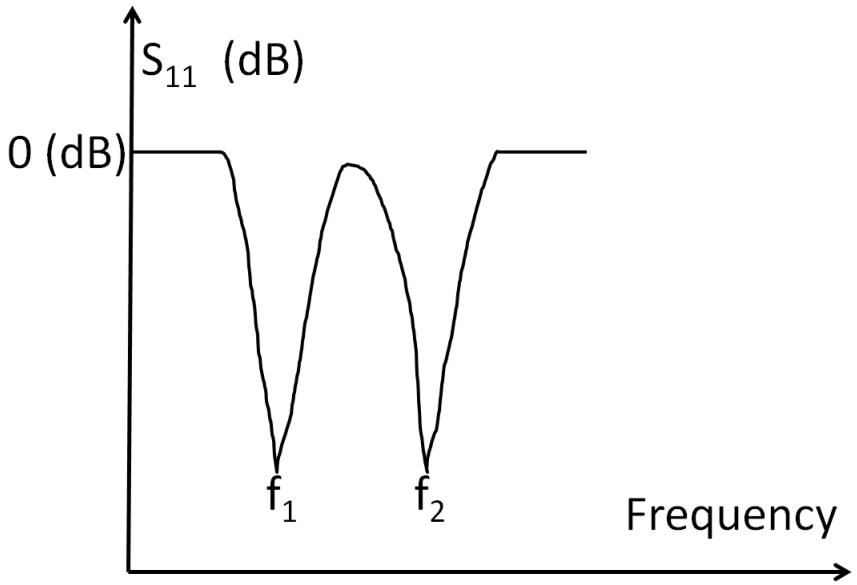

Fig. 2.17 The return loss of the circuits shown in Fig 2.16 [10] .

2.2.1 Multi- modes resonators for multi-band filters

As far as microwave resonators are concerned, a single resonator may consist of a single resonant mode or degenerate modes. Degenerate modes are created when a single physical resonator allows the realization of two electric resonators (dual-modes) or three electric resonators (triple-modes) or multi-electric resonators (multi-modes). It is of great advantage to realize multi-modes in terms of the reduction of the physical size of the filter, but spurious, performance degrades. The spurious performance is determined from the proximity [10] of a neighboring resonant to the operating mode. Spurious frequencies are undesirable, and it is important to have spurious-free stop-band to increase filter performance.

The operating (fundamental) resonant mode and degenerate modes are measured or calculated with EM tools by utilising (1) eigen-values analysis or (2) s-parameters analysis. In the s-parameters analysis approach, a resonator is weakly coupled to the feed by employing one port to measure the s_{11} response. The response shows all the modes that a feed excites inside a resonator, by showing s_{11} dips, as depicted in Fig. 2.17. The width of the dips represents the losses of a resonator: the wider the dips, the higher the losses.

Multi-modes resonators for multi-band filters can be implemented for narrow, wide, as well as ultra-wideband, applications. In comparison with other multi-band design approaches, filters designed, based on multi-modes, are compact in size and have simple structures that are easy to construct. Multi-modes resonators can be implemented on different configurations which include coupled resonators, stepped impedance resonators, as well as stub loaded resonators.

Stepped impedance and stub-loaded resonators for multi-modes multi-band filters

Multi-mode networks that are connected in parallel, are commonly employed for multi-band filters. Two configurations reported in [18, 28] are based on a parallel-connected coupling scheme that realizes quint-bands. Two of the five bands in [18] have an equal bandwidth and the remaining three each have different bandwidths. The coupling scheme is shown in Fig 2.18 (a), (b) is the filter layout and (c) shows the frequency response of the five bands. For the filter in [28] coupling scheme, the layout and frequency response are shown in Fig 2.19.

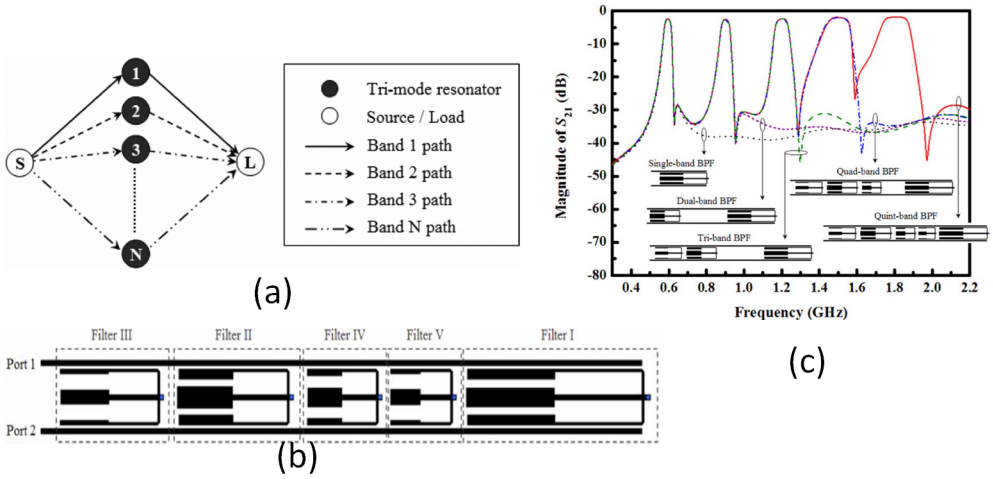

Fig. 2.18 (a) Coupling configuration of the multi-band BPFs, (b) Schematic diagram arrangement of the microstrip five-band filter based on the SL-SIRs and (c) Frequency response [18]

A quad-band, as designed in [44], is based on an even and odd mode of analysis. The conventional multi-mode, ring-loaded resonator (RLR) is modified to include a transmission line model (TLM). The filter layout consists of a meander, coupled-line for resonant frequency adjustments. The filter is centered at 2.44, 3.53, 5.18 and 5.79 GHz with unequal bands. The coupling scheme, layout and frequency response are detailed in Fig. 2.20.

Other quad-band designs are detailed in [43, 63, 74], a microstrip filter in [43] is centered at 1.55, 2.79, 3.29 and 4.47 GHz with fractional bandwidth equal to 3.1%, 3.22%, 2.79% and 2.23%. The frequency response in Fig. 2.21 (e) shows that the out-of-band rejection is about 40 dB and the filter achieves high selectivity, influenced by transmission zeros which are created by the input/output couplings. The coupling scheme, constructed filter and frequency response are detailed in Fig. 2.21.

A quad-mode, stub loaded resonator in [44], employs the mode-division characteristic of the quad-mode resonator, which creates double-band behavior. When the two, four modes are cascaded, they produce the quad-band response shown in Fig. 2.22

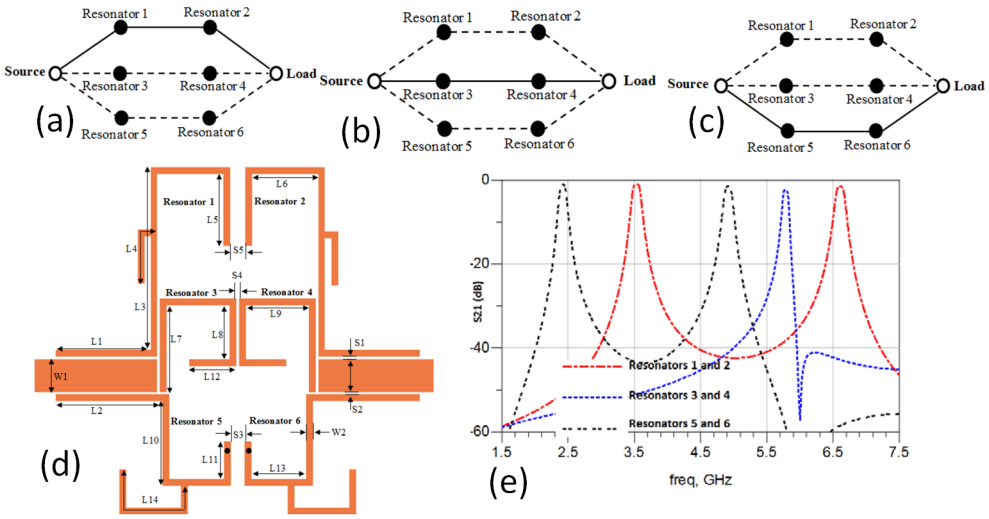

Fig. 2.19 Source/load and coupling configuration, (a) at the first and third resonant frequencies, (b) at the fourth resonant frequency, and (c) at the second and fifth resonant frequencies, (d) layout of the proposed quint-band band-pass filter structure, and (e) frequency response of the quint-band band-pass filter [28].

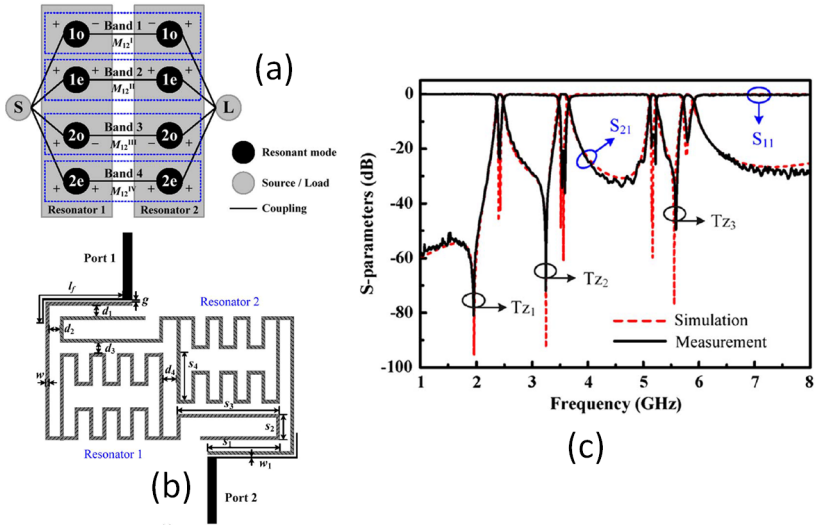

Fig. 2.20 (a) Coupling scheme of (b): (b) Layout of the designed quad-band HTS filter with the pseudo-interdigital structure, and (c) simulated and measured frequency responses of the constructed, quad-band HTS filter [44].

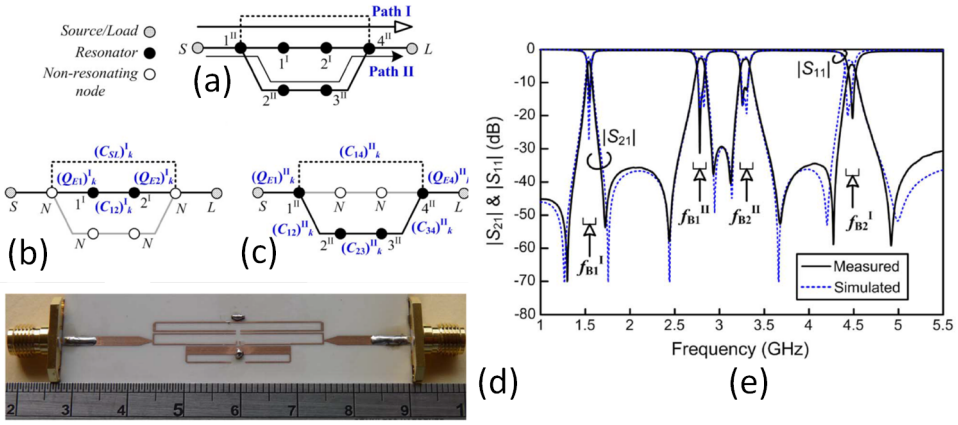

Fig. 2.21 (a) Coupling arrangement of the quad-band band-pass filter based on parallel-path transmission; (b) Coupling diagram at frequencies f_{B1}^{I} and f_{B2}^{I}. (c) Coupling arrangement at frequencies f_{B1}^{II} and f_{B2}^{II} (grey solid line: ignorable coupling, black solid line: main coupling, dashed line: nonadjacent coupling), (d) constructed filter and (e) simulated and measured frequency response [43].

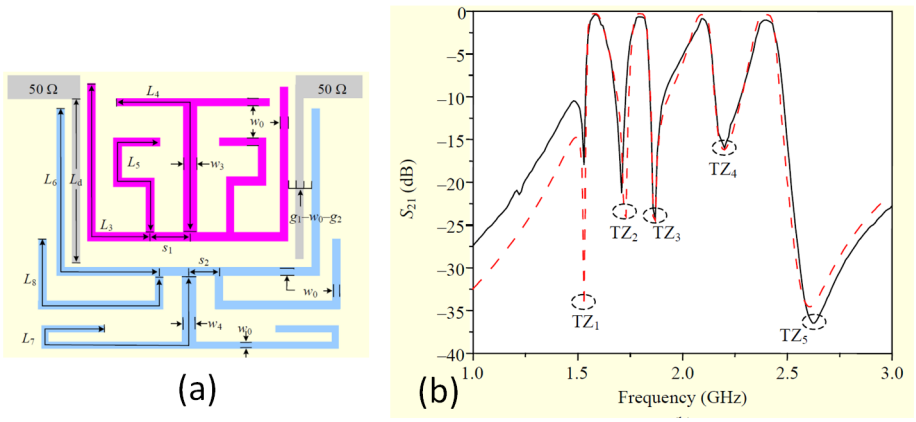

Fig. 2.22 Quad-band BPF: (a) filter configuration (b) simulated and measured frequency response [44] .

Multi-band filters utilising parallel connected topology, are introduced in [17]. The advantages of this topology are that pass-bands are design separately and there is freedom to choose the frequency of each band center. The inclusion of transmission zeros is possible with the introduction of source-load couplings, and the suppression of harmonics between adjacent bands is achieved.

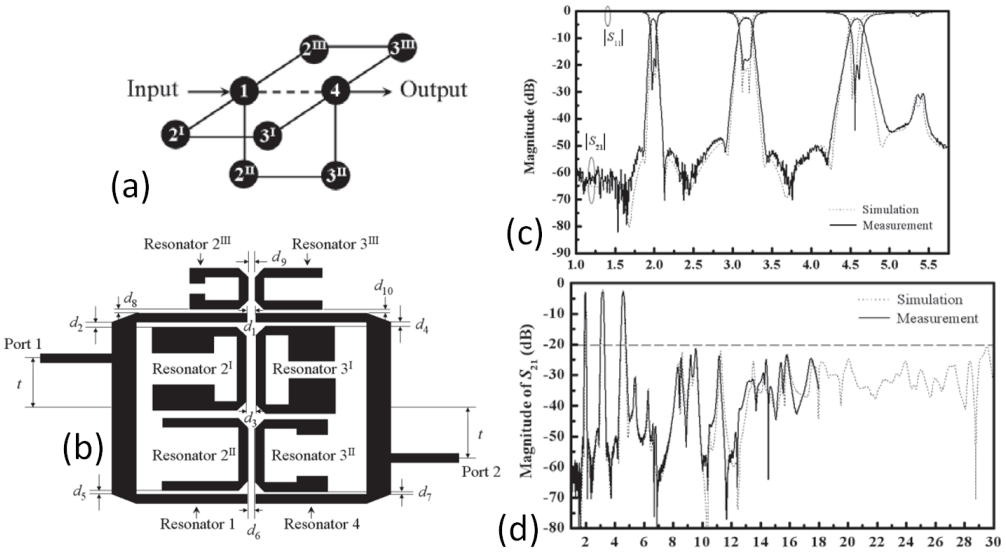

Fig. 2.23 (a) Coupling scheme of the triple pass-bands quasi-elliptic filter (b) Schematic layout. Measured and simulated performance of the filter(c) Insertion and return loss. (d) Wider spurious rejection band [19].

A multi-band example or spurious suppression is presented in [19] with multi-order, spurious mode suppression that was proposed. A triple, pass-bands, quasi-elliptic filter with folded, stepped-impedance resonators (SIRs) and U-shaped, unit-impedance resonators (UIRs) was designed and implemented. A wider upper stop-band can be attained by selecting constitutive resonators with staggered, higher-order, resonant frequencies over the stop-band. The coupling scheme and the layout and frequency responses with a wide stop-band are detailed in Fig. 2.23.

2.2.2 Optimization Multiband filters

The approach in [66, 52] presents the design of multi-band filters based on the coupling matrix. The characteristics polynomial transfer functions is first computed, followed by optimization of coupling matrix. The optimization problem utilized a hybrid technique, a combination of a genetic algorithm (GA) and a local, sequential, quadratic, programming (SQP) search. The reason for the hybrid was to speed up convergence in GA to improve

accuracy in the solutions. GA alone suffers from slow convergence, although it has the ability to place initial values close enough to the global minimum. The example in [66] presents computed responses with equal and unequal bandwidths and different return losses. The coupling scheme and frequency response of a dual-band filter is presented in Fig. 2.24. Another coupling matrix synthesis approach is reported in [49] where the single, wide-band filter was designed. The transmission zeros were placed within a wider band to divide them into individual bands. The entries of the coupling matrix were adjusted through optimization.

The benefits of employing this approach are the capability to control the coupling topology, flexibility to achieve different filter topologies and the inclusion of higher-order, mode effects. The coupling scheme and its constructed filter, based on [49], is presented in Fig. 2.25. Another optimization method utilized for dual-band filter synthesis was based on Zolotarev functions introduced in [42] and [5]. Additionally, Remez algorithm-like functions can be employed to synthesize polynomial characteristics, which results in an equal-ripples response in all bands. The downside of this approach is the lack of control over the attenuation level in the stop-band. Some alterations to the pass-band and stop-band frequency were necessary to solve the attenuation-level problem.

2.2.3 Reactance transformed method for multi-band filters

Rational mapping functions were employed to synthesize multi-band filters. The method [7]] is valid for narrow band, coupled resonators, as well as wide band designs for lumped elements at any frequencies and for any number of bands. For narrow band applications, rational mapping functions relate lowpass frequencies to multi-band frequencies, as shown in Fig. 2.26; the mapping rational functions are given as polynomial functions of the form [7]

$$\Omega_s(\Omega_m) = \frac{P(\Omega_m)}{Q(\Omega_m)} = \frac{\alpha_N \Omega_n^N + \alpha_{N-1}\Omega_m^{N-1} + \cdots + \alpha_1 \Omega_m + \alpha_0}{\beta_{N-1}\Omega_m^{N-1} + \cdots + \beta_1 \Omega_m + 1} \tag{2.13}$$

The coefficients Ω_m^N, α_m^N, and β_{N-1} were computed from the specifications of multi-band filters which were followed by another transformation which transformed intermediate frequencies to final, actual multi-band frequencies. This equation (see Fig 2.13) works for narrow-band multi-band coupled-resonators.

Narrow band reactance transformed filters

This step involved a reactance function for a passive, lossless, LC network transformed through a well-known lowpass to bandpass transformations.

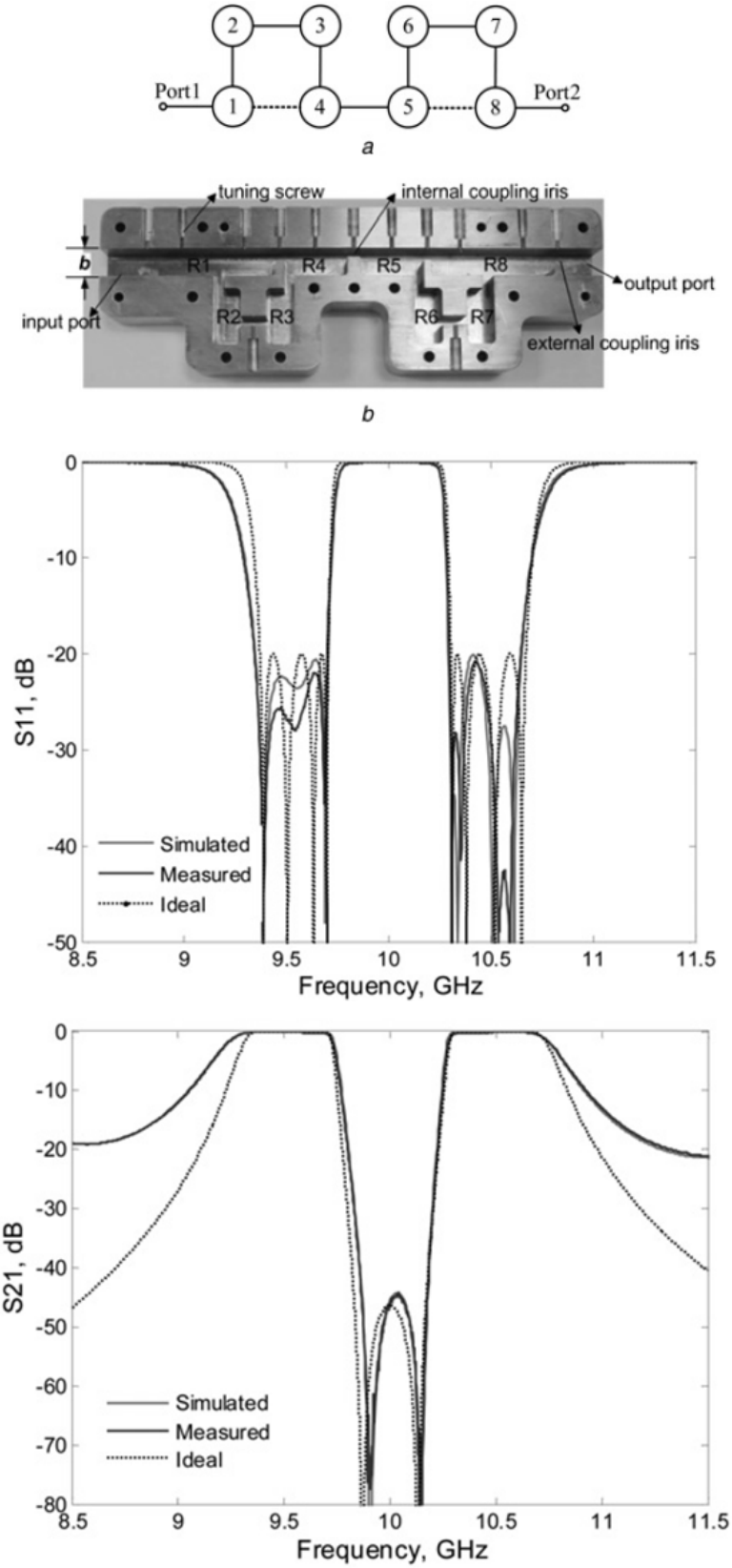

Fig. 2.24 Circuit topology and symmetrical dual-band response with CST simulation and the measurement after tuning [66].

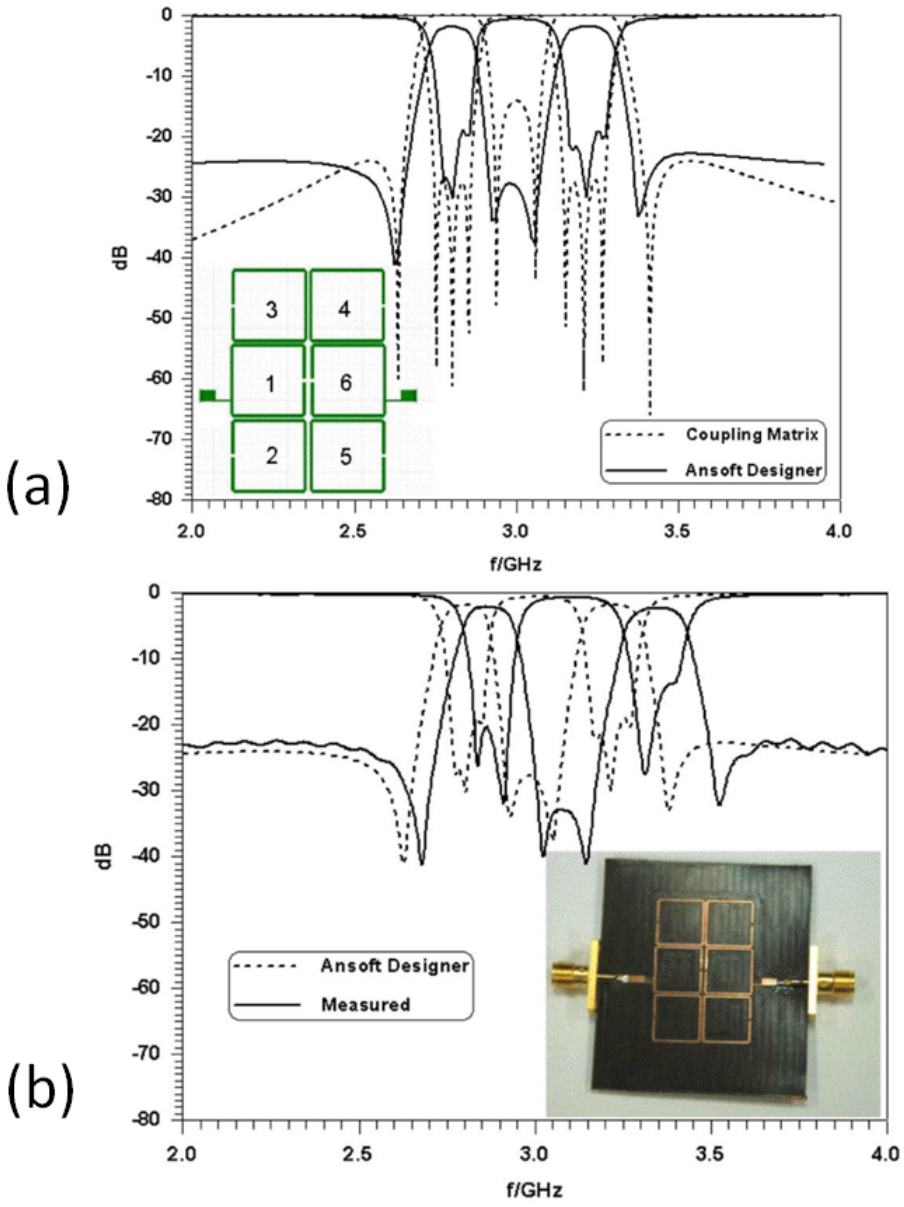

Fig. 2.25 Dual-band filter utilizing six open-loop resonators (a) Coupling-matrix theory (dashed lines) are compared with Ansoft Designer (solid lines). (b) Prototype measurements (solid lines) and photograph (Ansoft Designer data (dashed lines) for comparison). [49].

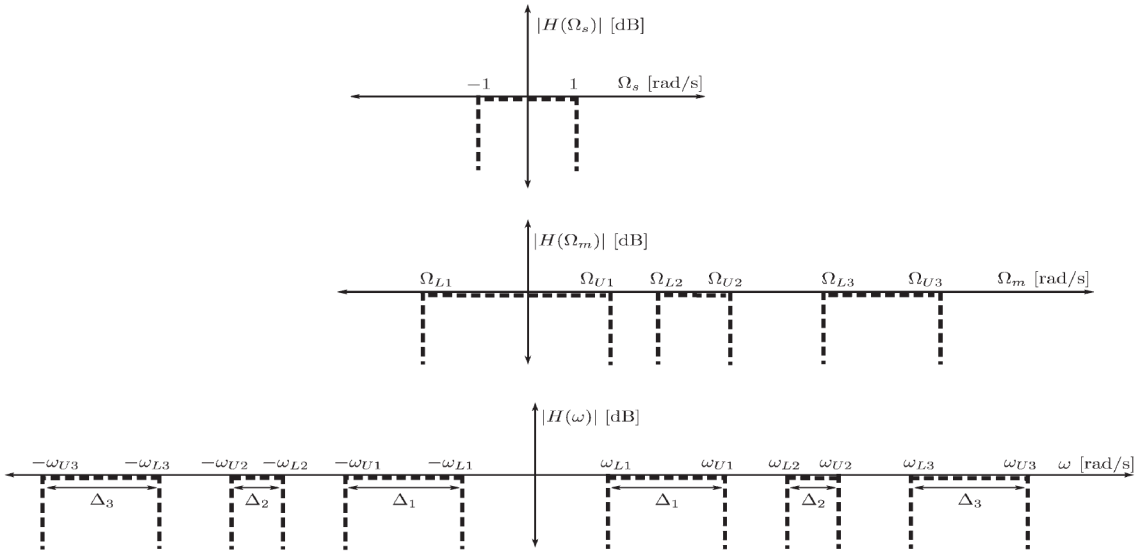

Fig. 2.26 Low-pass to multi-band response transformation utilizing an unsymmetrical intermediate response [7].

$$\Omega_m = \frac{1}{\Delta}\left(\frac{\omega}{\omega_0} - \frac{\omega_0}{\omega}\right) \tag{2.14}$$

Once the transformation was completed, a single-band coupled resonator could be designed by employing existing techniques with or without transmission zeros or other requirements, including return loss; the filter order should also be specified. Each reactive element in a single-band coupled filter was replaced by a multi-band, reactive sub-circuit (see 2.27). The reactive, LC transformations were computed through Cauer I or Cauer II expansions. The Cauer I expansion had the following form:

$$j\Omega_s(\omega_m) = j\Omega_m k_1 + jh_1 + \cfrac{1}{j\Omega_m k_2 + jh_2 + \cfrac{1}{\ddots}} \tag{2.15}$$

Wide-band reactance transformed filters

For wide-band requirements, the rational mapping functions were computed, followed by a linear frequency transformation which utilized only positive inductors and capacitors, instead of frequency-invariant, reactive elements. As in the case of narrow band, the rational mapping functions in the form of polynomial were given as [6]

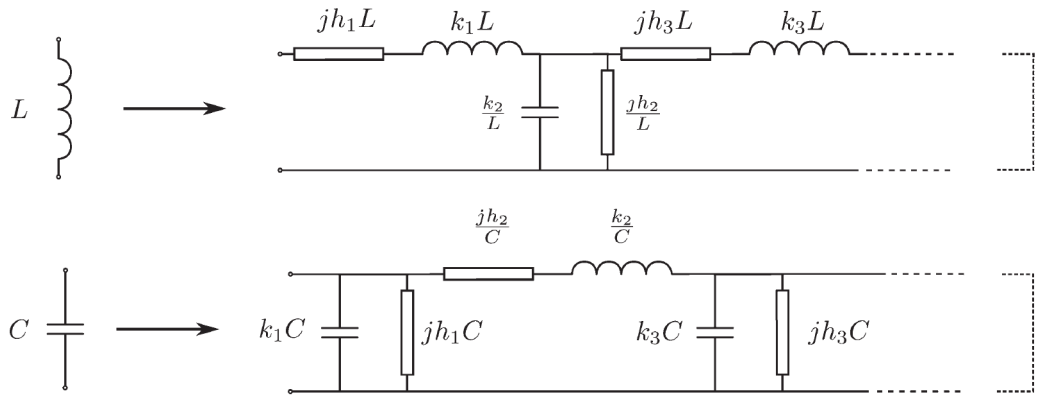

Fig. 2.27 Cauer I forms of the low-pass to multi-band mapping function [7].

$$\Omega'(\Omega) = \frac{\alpha_{2N}\Omega^{2N} + \alpha_{2N-1}\Omega^{2N-1} + \alpha_{2N-2}\Omega^{2N-2} + \cdots + \alpha_2\Omega^2 + \alpha_1\Omega + 1}{\beta_{2N-1}\Omega^{2N-1} + \beta_{2N-2}\Omega^{2N-2} + \beta_{2N-3}\Omega^{2N-3} + \cdots + \beta_1\Omega + \beta_0} \tag{2.16}$$

The coefficients Ω_m^N, α_m^N, and β_{N-1} were computed from the specifications of multi-band filters; this was followed by another transformation transforming intermediate frequencies to final, actual, multi-band frequencies. This step involved a reactance function for passive, lossless, LC network transformed through a linear frequency transformation of the form

$$\Omega = \frac{\omega}{\omega_{UN}} \tag{2.17}$$

which is the de-normalization function that relates the multi-band prototype frequency variable (Ω) and the actual frequency variable (ω).

The main difference between the equations 2.13) and 2.16 is that for narrow band the rational function maps to N pass-bands while for wide-band it maps to $2N$. For example, in a narrow case, if specified to synthesize 2 bands, it means a set of $2N$ pass-band cut-off frequencies in the actual frequency domain ($1N$ on the positive and $1N$ on the negative axis). Wide band will have a set of $4N$ pass-bands, $2N$ on the positive and $2N$ on the negative frequency axis as shown in Fig 2.28.

Similar to narrow band requirements, each reactive element in a low-pass prototype was replaced by a multi-band reactive sub-circuit. The reactive LC transformations were computed through Foster, Cauer I, Cauer II and mixed Cauer I and II expansions. The frequency transformation, sub-circuit of Foster expansions had the following form:

$$H(S)=\frac{k_0}{S}+\frac{k_1}{S-j\omega_1}+\frac{k_1^*}{S+j\omega_1}+\frac{k_2}{S-j\omega_2}+\frac{k_2^*}{S+j\omega_2}+\cdots+k_\infty=\frac{k_0}{S}+\sum_{i=1}^{N-1}(\frac{2k_iS}{S^2+\omega_i^2})+k_\infty S \tag{2.18}$$

The frequency transformation, sub-circuit of the Cauer I expansions had the following form:

$$H(S)=\frac{a_{2N}S^{2N}+a_{2N-2}S^{2N-2}+\cdots+1}{b_{2N-1}S^{2N-1}+b_{2N-3}S^{2N-3}+\cdots+b_1S}=Sk_0+\frac{1}{Sk_1+\frac{1}{Sk_2+\frac{1}{Sk_3+\cdots}}} \tag{2.19}$$

The frequency transformation, sub-circuit of Cauer II expansions had the following form:

$$H(S)=\frac{1+a_2S^2+a_4S^4+\cdots+a_{2N}S^{2N}}{Bb_1S+b_3S^3+\cdots+b_{2N-1}S^{2N-1}}=\frac{k_0}{S}+\frac{1}{\frac{k_1}{S}+\frac{1}{\frac{k_2}{S\cdots}}} \tag{2.20}$$

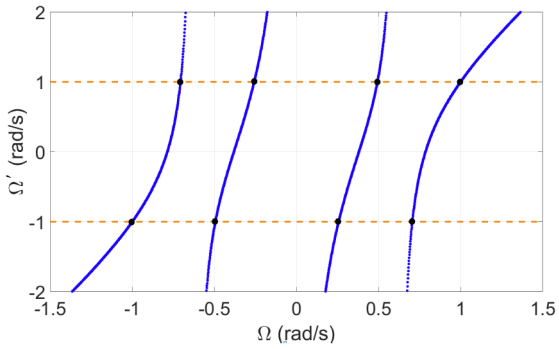

Fig. 2.28 Reactance transformation function. [7].

Cauer I and Cauer II expansions were mixed by extracting one pole at zero and one pole at infinity at each level inside the continued fraction expansion to form a new expansion called the mixed Cauer I and II expansions. The continued fraction expansion can again be found through a series of polynomial divisions and inversion steps. It should be noted that two components must be extracted between inversions. The continued fraction expansion had the following form:

$$H(S)=k_0S+\frac{k_1}{S}+\frac{1}{k_2S+\frac{k_3}{S}+\frac{1}{k_3S+\frac{k_4}{S}+\cdots}} \tag{2.21}$$

2.3 Summary

This chapter focused on the background of microwave filters, and covered fundamental concepts, including low-pass prototypes T and π immitance, inverter networks, ladder networks, band pass filter prototypes and their coupling matrices. The chapter subsequently covered multi-band filters, designs based on multi-mode resonators, stepped impedance and stub loaded resonators, as well as multi-band filters constructed based on optimization methods. Lastly, an analytical synthesis technique, based on reactance transformed methods for multi-band filters for both narrow-band and wide-band filters was discussed.

Chapter 3

Properties of multi-band filters based on narrow-band and wide-band reactance transformation

3.1 Introduction

Multi-band filters enable frequency selectivity for the front end of microwave systems that range from communication to navigation. A technique to develop and realize multi-band response by utilizing frequency mapping is reported in [41], [29]. The network for single-band response was first developed. To achieve a multi-band response, additional resonators were connected to each resonator of the single-band network. This provided extra resonances that produced extra pass-bands. The order of a new, multiple pass-band network increased, depending on the desired number of pass-bands. This means that if N is the order of the single-band network, the multiple pass-bands network has the order of nN, where n is the number of the desired pass-bands. The collection of resonators added were connected through admittance inverters, which made the network a shunt topology.

A synthesis method which is completely analytical is introduced in [7], [6] based on reactance transformations. Optimization is not required and is implemented for narrow-band and wide-band cases. Narrow-band implementation is based on the representation of coupled resonators and wide-band on lumped elements and transmission line filters. The transformation converts a single-band basis filter into a multi-band filter with M pass-bands, with no limitations on the number of pass-bands.

This chapter focuses on properties of multiple pass-bands related to their implementation, namely selectivity, losses, group delays and the sensitivity of filters based on reactance

transform. Starting with the narrow band implementation in Section 3.2 followed by wide band discussed in Section 3.3, while the polynomial mapping functions for narrow band only and genereal mapping fucntions for both narrow and wide-band implementation are compared in Section 3.4 with a narrow band example. Section 3.5 is a summary of the chapter.

3.2 Narrow band implementation

A low-pass filter is the basis of a single band filter which is converted through reactance transformation to represent multi-bands. Any low-pass prototype circuit can be the basis for the transform. The example here is an all-pole filter shown in Fig 3.1. For coupled resonators, single-band basis can have any coupling topology with or without cross coupling.

Basis filters can have any order number. For a single-band basis filter of order N transformed into multi-band filter with M bands, the number of resonators equals to NM in the multi-band filter network. Figure 3.2 (a) shows a dual-path, transversal, fourth order, single-band basis filter transformed into (b) multi-band filter, in (c) a triple-path transversal sixth order single-band basis is transformed to (d), in (e) a quad-path transversal eight order single-band basis filter is transformed to a multi-band filter in (f), (g) is a fourth order, all pole basis filter transformed into multi-band in (h). The frequencies f_1's represent a single-band filter basis. Each level of additional resonators creates a pass-band f_2's, f_3's up to f_M's. The benefit is that the additional resonators do not introduce any new cross-couplings apart from those already appearing in the single-band filter which are synchronously tuned resonators.

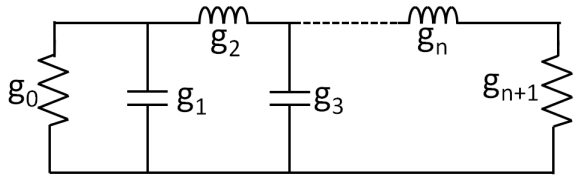

Fig. 3.1 A low-pass prototype basis filter for the reactance transform.

3.2.1 Frequency selectivity of reactance transformed multi-band filter

Filters are preferred to have steep skirt frequency selectivity. High order filters have a high selectivity, although it comes at the cost of high insertion loss. The physical design of high order filters is more challenging than that of low orders. For reactance, transformed filters, the selection between bands has a steeper skirt because the transformation introduces additional transmission zeros without new cross couplings. The examples in this chapter

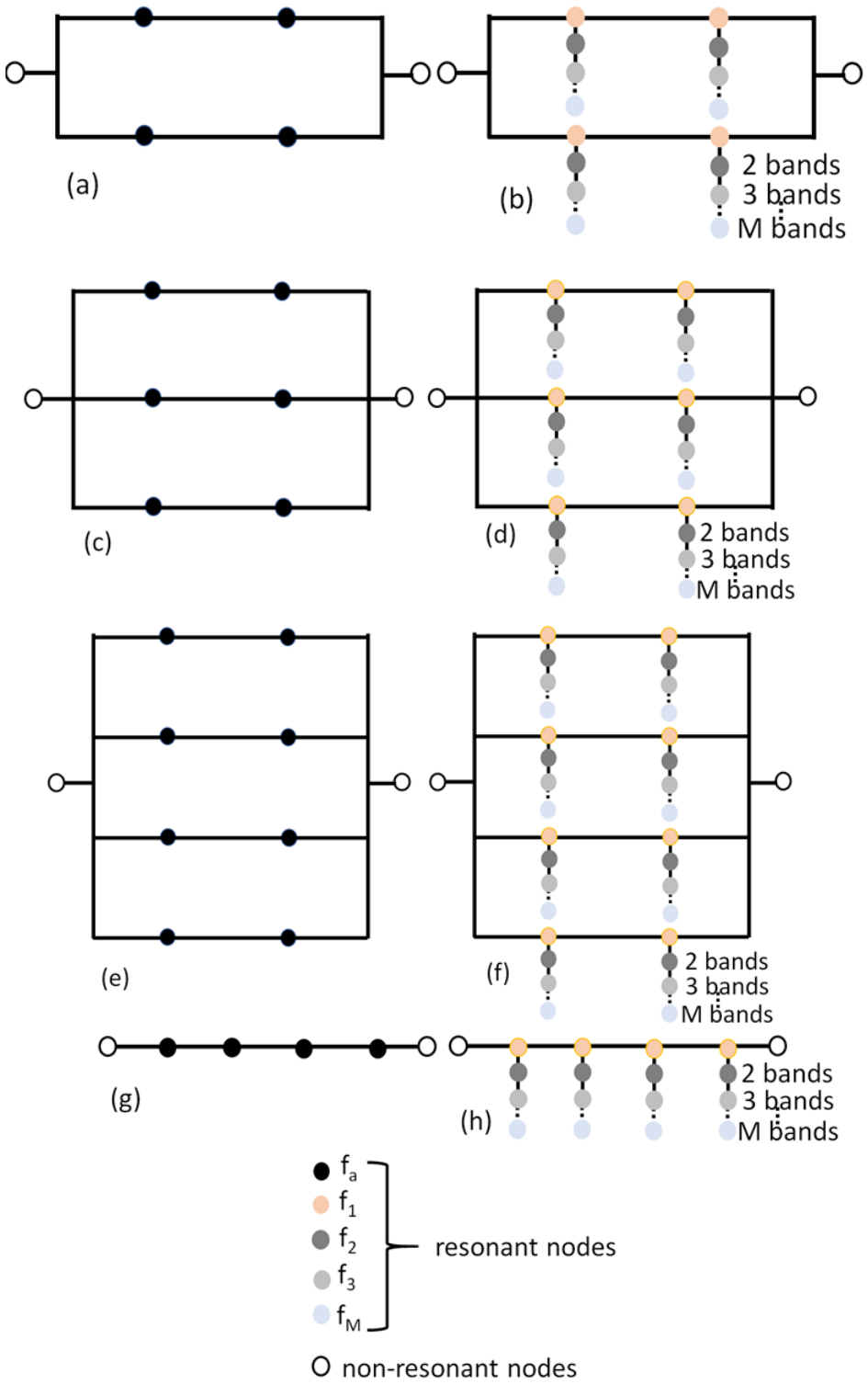

Fig. 3.2 (a) A fourth order, dual-path, transversal, single-band basis filter transformed to (b) a multi-band filter; (c) a sixth order, triple-path, transversal, single-band basis filter transformed to (d) a multi-band filter; (e) an eighth order, quad-path, transversal, single-band basis filter transformed to (e) a multi-band filter; (g) a fourth-order, all-poles, single-band basis filter transformed to (h) a multi-band filter.

Bands	Frequency(GHz)	$f_0(GHz)$	FBW	$BW(MHz)$	Spacing (MHz)
Dual	3.100 to 3.200 3.330 to 3.430	3.2608	0.1012	100	130
Triple	3.000 to 3.080 3.130 to 3.210 3.260 to 3.340	3.1654	0.1074	80	50
Quad	3.000 to 3.050 3.100 to 3.150 3.200 to 3.250 3.300 to 3.350	3.1702	0.1104	50	50

Table 3.1 Frequency specification of the dual-, triple- and quad-band prototypes

have transversal topologies of four, six, eight and ten order as a single band basis filters transformed into dual, triple and quad-bands.Transversal topologies were chosen to provide a wide analysis of filter selectivity and losses depending on the number of resonators. A quad-band response, for example, was analyzed, with a total of 16 resonators, when a fourth order, single band, basis filter was employed; for a ten order basis filter, a quad-band response was produced by 40 resonators in total. The dual, triple and quad-band frequency specifications, with uniform bandwidth and equal spacing between bands, are given in Table 3.1.

Transversal single-band basis filters

Transversal topologies consist of the parallel connection of N single-band resonators, terminated between the source and the load, as detailed in Fig. 3.4(a),3.7(a),3.10(a),3.13(a) for the 4th, 6th, 8th and 10th orders respectively. The synthesis of transversal topologies is presented in [9]. It is shown that the filtering function must be symmetric and of even degree. Similarity transformation was employed to eliminate and reduce coupling elements. The transformation did not affect or reduce the number of resonators. As indicated, the pivot of rotation began at position $[1,N]$, progressing inwards to the center of the matrix to position$[N/2,N/2+1]$. For the 4th order, there were $N/2=2$ rotations while the 6th, 8th and 10th orders had 3, 4 and 5 rotations respectively.

The single-band basis filter of the $N=4$ transversal coupling topology is shown in Fig. 3.4(b). Its coupling matrix was computed as indicated in equation 3.1.

$$M_4 = \begin{bmatrix} 0 & 0.5355 & -0.8744 & 0 & 0 & 0 \\ 0.5355 & 0 & 0 & 0 & 1.2939 & 0 \\ -0.8744 & 0 & 0 & 0.6789 & 0 & 0 \\ 0 & 0 & 0.6789 & 0 & 0 & 0.8744 \\ 0 & 1.239 & 0 & 0 & 0 & 0.5355 \\ 0 & 0 & 0 & 0.8744 & 0.5355 & 0 \end{bmatrix} \tag{3.1}$$

Their corresponding lossless frequency response for a single band basis filter is presented in Fig 3.5(a) .

The single-band basis filter of $N = 6$ transversal coupling topology is shown in Fig 3.7(b). Its coupling matrix was computed as shown in equation 3.2.

$$M_6 = \begin{bmatrix} 0 & -0.4304 & 0.6199 & -0.6548 & 0 & 0 & 0 & 0 \\ -0.4304 & 0 & 0 & 0 & 0 & 0 & 1.1850 & 0 \\ 0.6199 & 0 & 0 & 0 & 0 & 0.9927 & 0 & 0 \\ -06548 & 0 & 0 & 0 & 0.3777 & 0 & 0 & 0 \\ 0 & 0 & 0 & 0.3777 & 0 & 0 & 0 & 0.6548 \\ 0 & 0 & 0.9927 & 0 & 0 & 0 & 0 & 0.6199 \\ 0 & 1.1850 & 0 & 0 & 0 & 0 & 0 & 0.4303 \\ 0 & 0 & 0 & 0 & 0.6548 & 0.6199 & 0.4303 & 0 \end{bmatrix} \tag{3.2}$$

The corresponding lossless frequency response for a single band basis filter is presented in Fig3.8 (a).

The single-band basis filter of $N = 8$ transversal coupling topology is shown in Fig 3.10 (b). Its coupling matrix was computed and is shown in equation 3.3.

0	-0.3869	0.4725	-0.4118	0.4528	-0.4716	0	0	0	0	0	0
-0.3869	0	0	0	0	0	0	0	0	0	1.1135	0
0.4725	0	0	0	0	0	0	0	0	1.0760	0	0
-0.4118	0	0	0	0	0	0	0	0.8534	0	0	0
0.4528	0	0	0	0	0	0	0.5578	0	0	0	0
-0.4716	0	0	0	0	0	0.1940	0	0	0	0	0
0	0	0	0	0	0.1940	0	0	0	0	0	0.4716
0	0	0	0	0.5578	0	0	0	0	0	0	0.4528
0	0	0	0.8534	0	0	0	0	0	0	0	0.4118
0	0	1.0760	0	0	0	0	0	0	0	0	0.4725
0	1.1135	0	0	0	0	0	0	0	0	0	0.3869
0	0	0	0	0	0	0.4716	0.4528	0.4118	0.4725	0.3869	0

Table 3.2 Coupling matrix for $N = 10$ transversal topology of Fig. 3.13(b)

$$M_8 = \begin{bmatrix} 0 & 0.3965 & -0.5218 & 0.5067 & -0.5414 & 0 & 0 & 0 & 0 & 0 \\ 0.3965 & 0 & 0 & 0 & 0 & 0 & 0 & 0 & 1.1384 & 0 \\ -0.5218 & 0 & 0 & 0 & 0 & 0 & 0 & 1.0569 & 0 & 0 \\ 0.5067 & 0 & 0 & 0 & 0 & 0 & 0.7166 & 0 & 0 & 0 \\ 0.5414 & 0 & 0 & 0 & 0 & 0.2564 & 0 & 0 & 0 & 0 \\ 0 & 0 & 0 & 0 & 0.2564 & 0 & 0 & 0 & 0 & 0.5414 \\ 0 & 0 & 0 & 0.7166 & 0 & 0 & 0 & 0 & 0 & 0.5067 \\ 0 & 0 & 1.0569 & 0 & 0 & 0 & 0 & 0 & 0 & 0.5218 \\ 0 & 1.1384 & 0 & 0 & 0 & 0 & 0 & 0 & 0 & 0.3965 \\ 0 & 0 & 0 & 0 & 0 & 0.5414 & 0.5067 & 0.5218 & 0.3965 & 0 \end{bmatrix} \quad (3.3)$$

The single-band basis filter of the $N = 10$ transversal coupling topology is shown in Fig 3.13(b). Its coupling matrix was computed and is shown in Table 3.2.

Creation of multi-band topologies

The narrow-band rational mapping function [7] was employed and the polynomial of the form equation 2.13 was deduced for the specifications listed in Table 3.1.

The band cut-off frequency in the dual-band frequency domain, utilizing Fig. 2.14 was computed as

i	k_i	h_i
1	1.6488	0.0228
2	-1.5431	0.0543

Table 3.3 Frequency transformation variables of a dual-band, multi-band filter with specification in Table 3.1.

$$\Omega'(\Omega) = (-1.000, -1.000); (-0.3722, 1.000); (0.4149, -1.000); (1.000, 1.000) \tag{3.4}$$

Using:

$$\rho_1(\Omega_i) - \Omega'(\Omega) q_1(\Omega_i) = 0, i \in [1, 2N] \tag{3.5}$$

The matrix $AX = B$ is calculated as:

$$A = \begin{bmatrix} 1.000 & -1.000 & 1.000 & 1.000 \\ 0.1385 & -0.3722 & 1.000 & -0.3722 \\ 0.1721 & 0.4149 & 1.000 & -0.4149 \\ 1.000 & 1.000 & 1.000 & 1.000 \end{bmatrix} \tag{3.6}$$

$$B = \begin{bmatrix} -1.000 \\ 1.000 \\ -1.000 \\ 1.000 \end{bmatrix} \tag{3.7}$$

$$X = \begin{bmatrix} -46.8271 \\ 1.000 \\ 18.4271 \\ 28.4000 \end{bmatrix} \tag{3.8}$$

The mapping function is computed as:

$$\Omega'(\Omega) = \frac{-46.8271\Omega^2 + 1.0000\Omega + 18.4271}{-28.4000\Omega + 1.0000} \tag{3.9}$$

This is a representation of the Cauer 1, multi-band expansion equation 2.19. Equation 3.9 was solved to obtained the frequency transformation variables for a dual band filter, as presented in Table 3.3.

When utilizing equations 2.14 and 3.5 for the case of a triple band, the band edge for a triple band prototype in the frequency domain was obtained as:

$$\Omega'(\Omega) = (-1.0000, -1.0000); (-0.5095, 1.0000); (-0.2096, -1.0000); (0.2603, 1.0000); (0.5482, -1.0000); \tag{3.10}$$

The matrix $A_{tri}X_{tri} = B_{tri}$ was calculated as:

$$A_{tri} = \begin{bmatrix} -1.000 & 1.0000 & -1.0000 & 1.0000 & -1.0000 & 1.0000 \\ -0.3230 & 0.2596 & -0.5095 & 1.0000 & 0.2596 & -0.5095 \\ -0.0092 & 0.0439 & -0.2096 & 1.0000 & -0.0439 & 0.2096 \\ 0.0176 & 0.0678 & 0.2603 & 1.0000 & 0.0678 & 0.2603 \\ 0.1647 & 0.3005 & 0.5482 & 1.0000 & -0.3005 & 0.5482 \\ 1.000 & -1.0000 & 1.0000 & 1.0000 & 1.0000 & 1.0000 \end{bmatrix} \tag{3.11}$$

$$B_{tri} = \begin{bmatrix} -1.000 \\ 1.000 \\ -1.000 \\ 1.000 \\ -1.000 \\ 1.000 \end{bmatrix} \tag{3.12}$$

$$X_{tri} = \begin{bmatrix} -8.0788 \\ 0.3607 \\ 3.3743 \\ -0.0716 \\ 5.7046 \\ -0.2891 \end{bmatrix} \tag{3.13}$$

The mapping function was computed as:

$$\Omega'(\Omega) = \frac{-8.0788\Omega^3 + 0.3607\Omega^2 + 3.3743\Omega - 0.00716}{-5.7046\Omega^2 + 0.2891\Omega + 1.0000} \tag{3.14}$$

and the frequency transformation variables for a triple-band are given in Table 3.4

The band edge for a quad- band prototype in the frequency domain was obtained as:

i	k_i	h_i
1	1.4162	0.0085
2	-2.9170	0.0283
3	1.9512	-0.0799

Table 3.4 Frequency transformation variables triple band multiband filter with specification in Table 3.1.

$$\Omega'(\Omega) = (-1.0000, -1.0000); (-0.7002, 1.0000); (-0.4055, -1.0000); (-0.1156, 1.0000); (0.1696, -1.00 \tag{3.15}$$

The matrix $A_{quad}X_{quad} = B_{quad}$ is calculated as

$$A_{quad} = \begin{bmatrix} 1.000 & -1.0000 & 1.0000 & -1.0000 & 1.0000 & 1.0000 & -1.0000 & 1.0000 \\ 0.2404 & -0.3433 & 0.4903 & -0.7002 & 1.0000 & -0.3433 & 0.4903 & -0.7002 \\ 0.0270 & -0.0667 & 0.1645 & -0.45055 & 1.0000 & 0.0667 & -0.1645 & 0.4055 \\ 0.002 & -0.0015 & 0.0134 & -0.1156 & 1.0000 & -0.015 & 0.0134 & -0.1156 \\ 0.008 & 0.0490 & 0.0288 & 0.1696 & 1.0000 & -0.049 & -0.0288 & -0.1696 \\ 0.0412 & 0.0915 & 0.2030 & 0.4505 & 1.0000 & 0.0915 & 0.2030 & 0.4505 \\ 0.2798 & 0.3847 & 0.5289 & 0.7273 & 1.0000 & -0.3847 & -0.5289 & -0.7273 \\ 1.000 & 1.0000 & 1.0000 & -1.0000 & 1.0000 & 1.0000 & -1.0000 & 1.0000 \end{bmatrix} \tag{3.16}$$

$$B_{quad} = \begin{bmatrix} -1.000 \\ 1.000 \\ -1.000 \\ 1.000 \\ -1.000 \\ 1.000 \\ -1.000 \\ 1.000 \end{bmatrix} \tag{3.17}$$

i	k_i	h_i
1	1.7493	0.0118
2	-1.874	0.0043
3	2.1916	-0.0445
4	-3.2131	0.1516

Table 3.5 Frequency transformation variables quad-band, multi-band filter with specification in Table 3.1.

$$X_{quad} = \begin{bmatrix} -147.6269 \\ -9.3045 \\ -102.1343 \\ 4.4150 \\ 6.3862 \\ -84.3897 \\ 5.8895 \\ 32.5109 \end{bmatrix} \tag{3.18}$$

The mapping function is computed as

$$\Omega'(\Omega) = \frac{-147.6269\Omega^4 - 0.93045\Omega^3 - 102.1343\Omega^2 + 4.4150\Omega + 6.3862}{84.3897\Omega^3 - 5.8895\Omega^2 - 32.5109\Omega + 1.000} \tag{3.19}$$

and the frequency transformation variables for a quad band are given in Table 3.5

The next step after obtaining the frequency transformation variables k_i and h_i was to transform each resonator in a single band basis filter to a multi-band sub-division. A fourth order basis filterwas employed as an example to show the transformation from single-band to quad-band filter as depicted in Fig 3.3, where the J_A, J_B and J_C are the coupling in the sub-division, while the $\frac{h_i}{k_1}$ represents the frequencies of the resonant nodes.

The single band prototype filters were created from matrix equations 3.1, 3.2,3.3 and Table 3.2, for order $N = 4, 6, 8, 10$ respectively. The single-band coupling matrices were influenced by the frequency transformation variables listed in Tables 3.3, 3.4, and 3.5. Figure 3.3 defines the single-band to multi-band transfomations in terms of resonant frequency and coupling values.

Figure 3.4(b) shows a fourth order single band basis transversal coupling topology transformed to form multi-band filters in (c) dual, (d) triple and (e) quad-band filters. Their corresponding lossless frequency responses for a dual-band filter are shown in Fig 3.5(b)

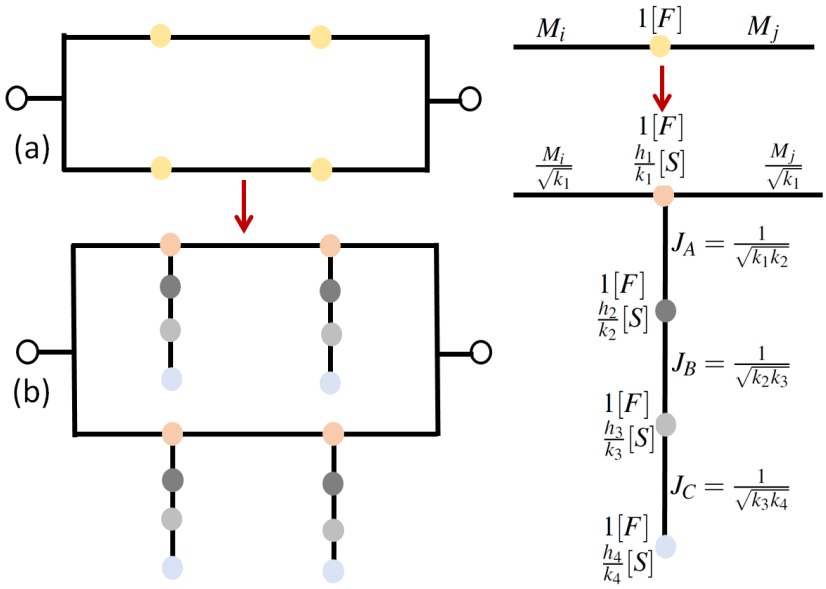

Fig. 3.3 A single-band to quad-band transformed prototype.

whereas triple and quad-bands are shown in Fig. 3.6. It is observed that the dual-band response has five, the triple-band has eight and the quad-band eleven transmission zeros.

Figure 3.7(b) shows a sixth order, single band basis, transversal coupling topology transformed to form multi-band filters in (c) dual, (d) triple and (e) quad band filters. Their corresponding lossless frequency responses for a dual-band filter are shown in Fig 3.8(b) whereas triple and quad-bands are shown in Fig 3.9.

Figure 3.10(b) shows an eight order, single band basis, transversal coupling topology, transformed to form multi-band filters in (c) dual, (d) triple and (e) quad-band filters. Their corresponding lossless frequency responses for a dual-band filter are shown in Fig. 3.11(b) whereas triple and quad-bands are shown in Fig 3.12. It was observed that the dual-band response had nine, triple-band fourteen and quad band nineteen transmission zeros.

Figure 3.13(b) shows a ten order, single band basis, transversal coupling topology, transformed to form multi-band filters in (c) dual, (d) triple and (e) quad-band filters. Their corresponding lossless frequency responses for a dual-band filter are shown in Fig. 3.14 (b) whereas triple and quad-bands are shown in Fig. 3.15.

The comparisons between the filter order for dual and triple band are plotted in in Fig. 3.16 and for quad-bands in Fig 3.17. In summary, the reactance transformed filters have additional transmission zeros (i.e. apart from those introduced by the single band basis filter) between pass-bands without introducing cross-coupling. The consequence of this is that selectivity between pass-bands is increased for filters with more pass-bands.

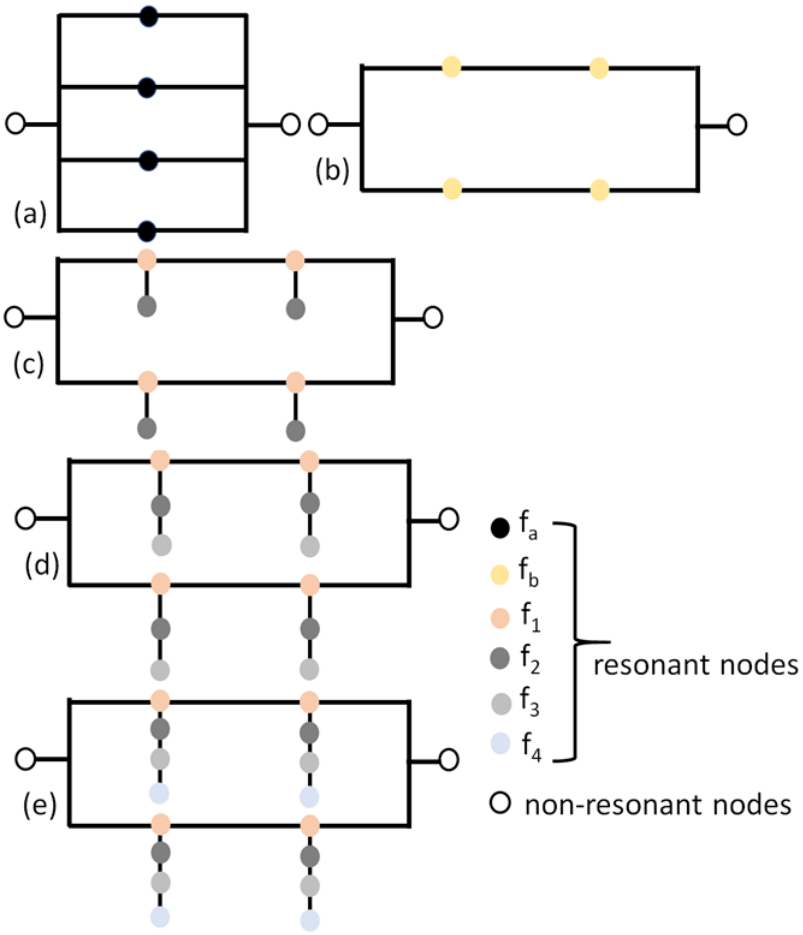

Fig. 3.4 The filter topologies are (a) 4th order transversal single band coupling topology, (b) a 4th order single-band basis dual-path transversal filter. The multi-band filter in (c) a dual-band filter (d) a triple-band filter (e) a quad-band filter reactance transformed filters.

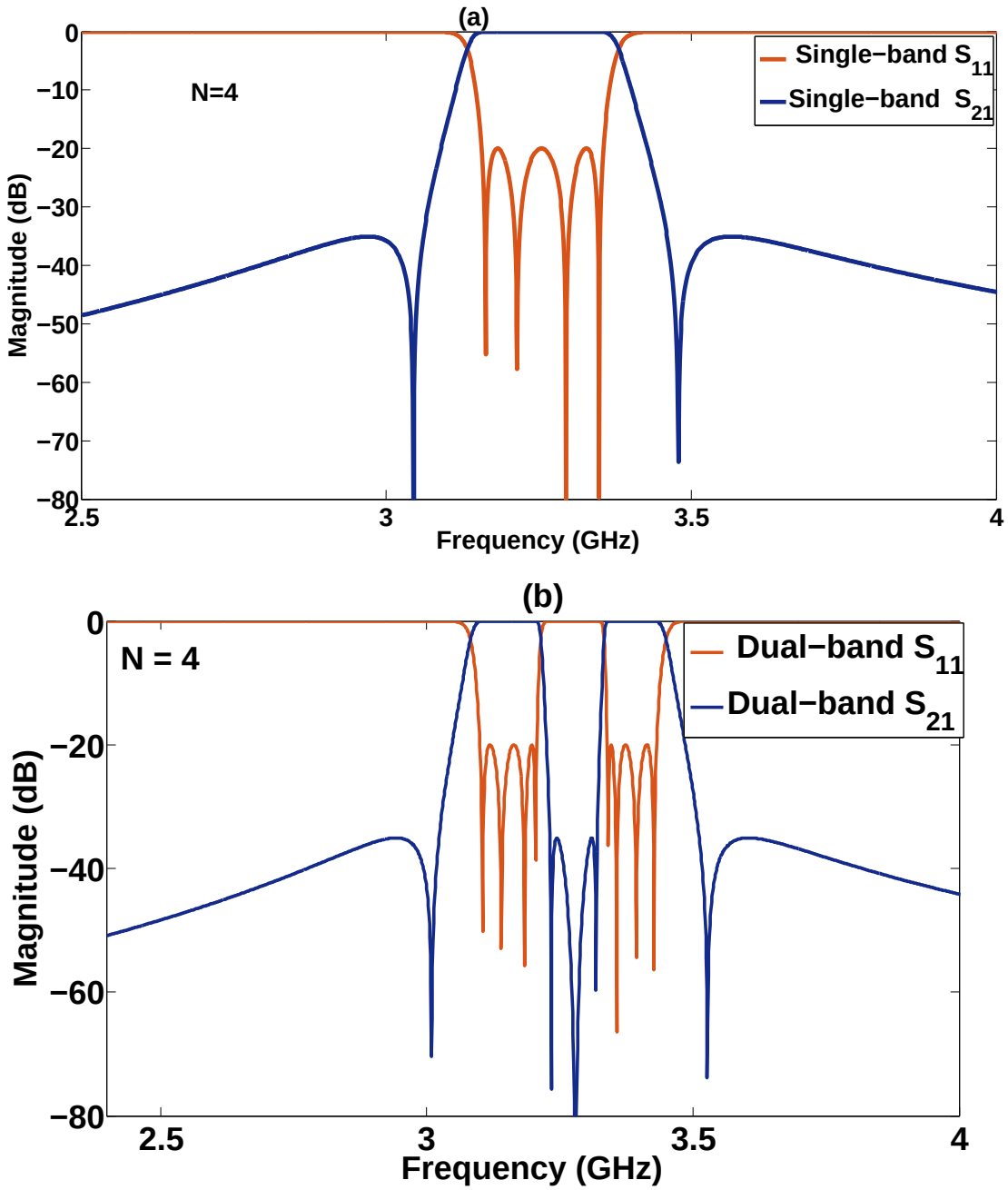

Fig. 3.5 The ideal lossless response of (a) single-band fourth basis filter of Fig 3.4(b), and (b) dual-band response of the filter of Fig 3.4(c). It is notable that appended resonators add transmission zeros between bands.

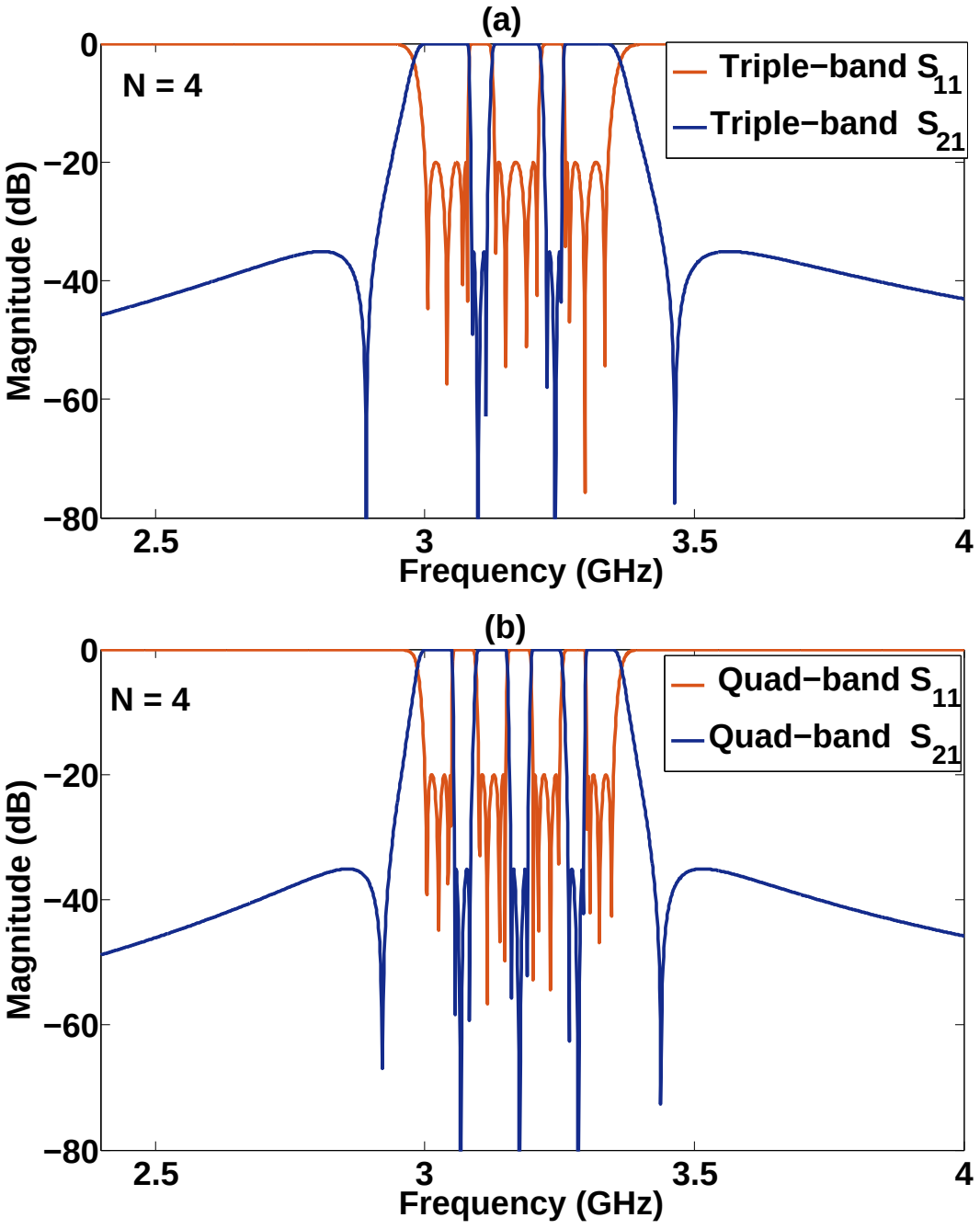

Fig. 3.6 The ideal lossless response of (a) triple-band response of the filter of Fig 3.4 (d), and (b) quad-band response of the filter of Fig 3.4(e). It is notable that appended resonators add transmission zeros between bands.

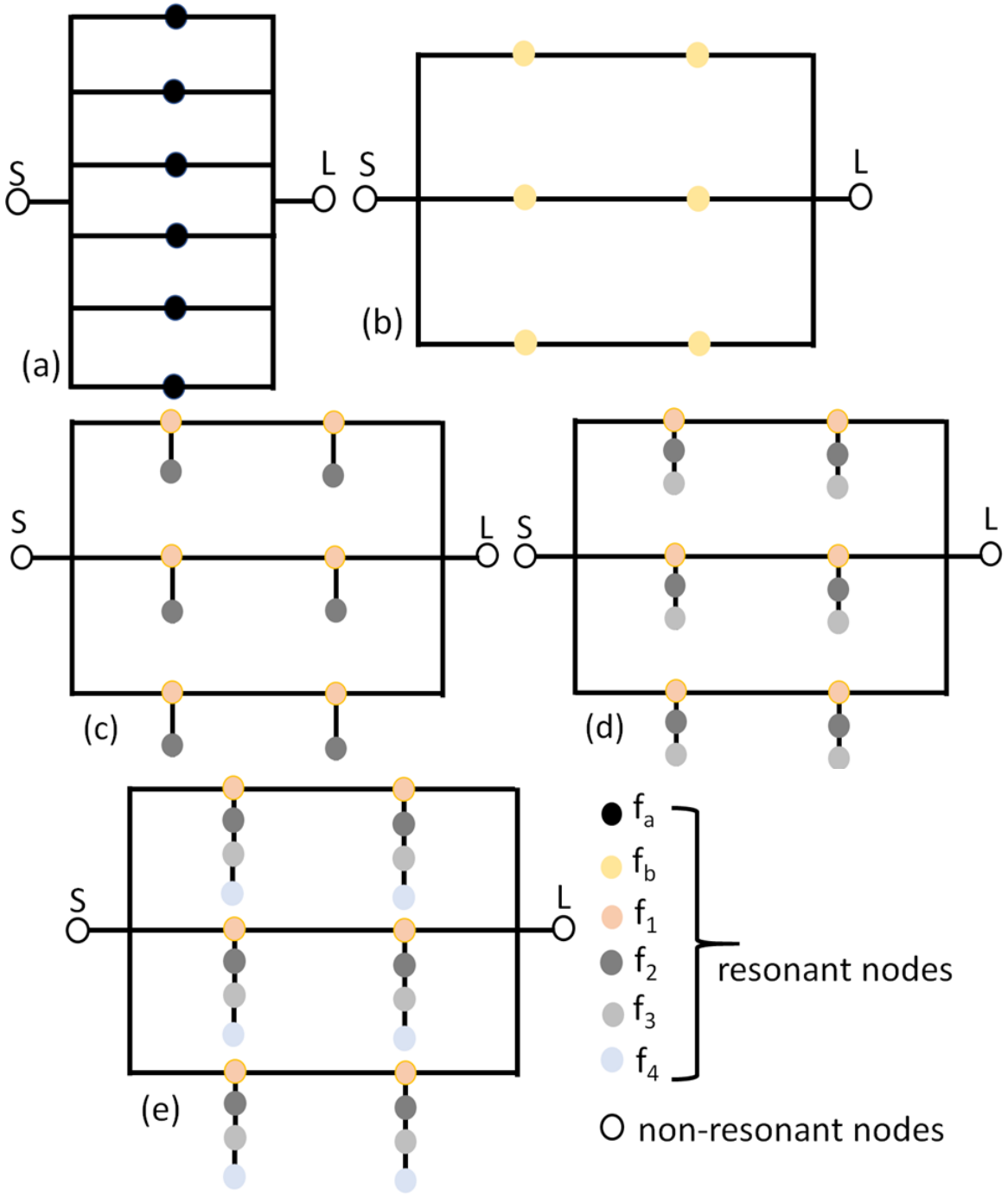

Fig. 3.7 The filter topologies are (a) a 6th order transversal single-band coupling topology. (b) a 6th order single-band basis triple-path transversal filter. The multiband filter in (c) a dual-band filter (d) a triple-band filter (e) a quad-band filter reactance transformed filters.

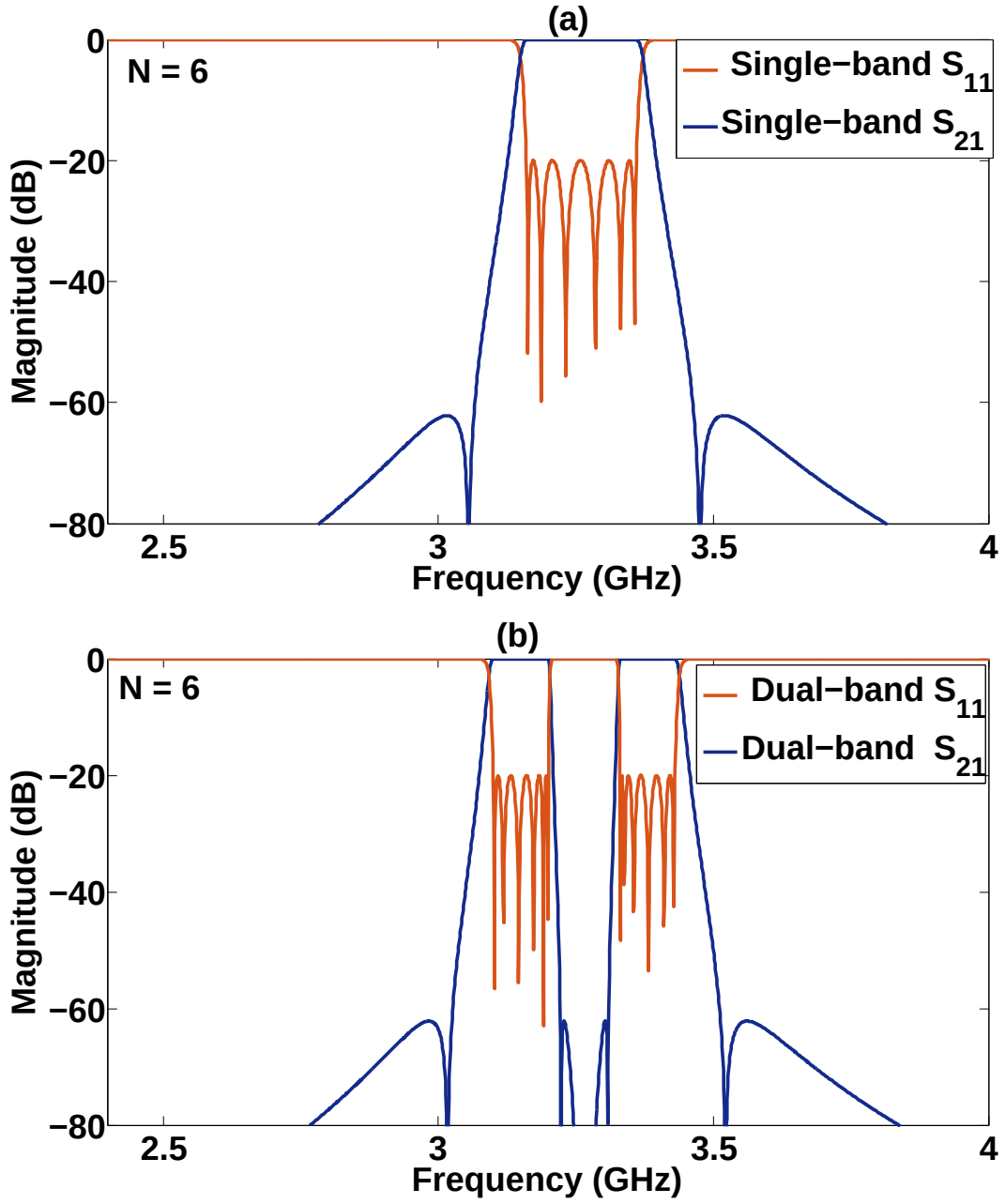

Fig. 3.8 The ideal lossless response of (a) single-band six order basis filter of Fig 3.7 (b), and (b) dual-band response of the filter of Fig 3.7 (c). It is notable that appended resonators add transmission zeros between bands.

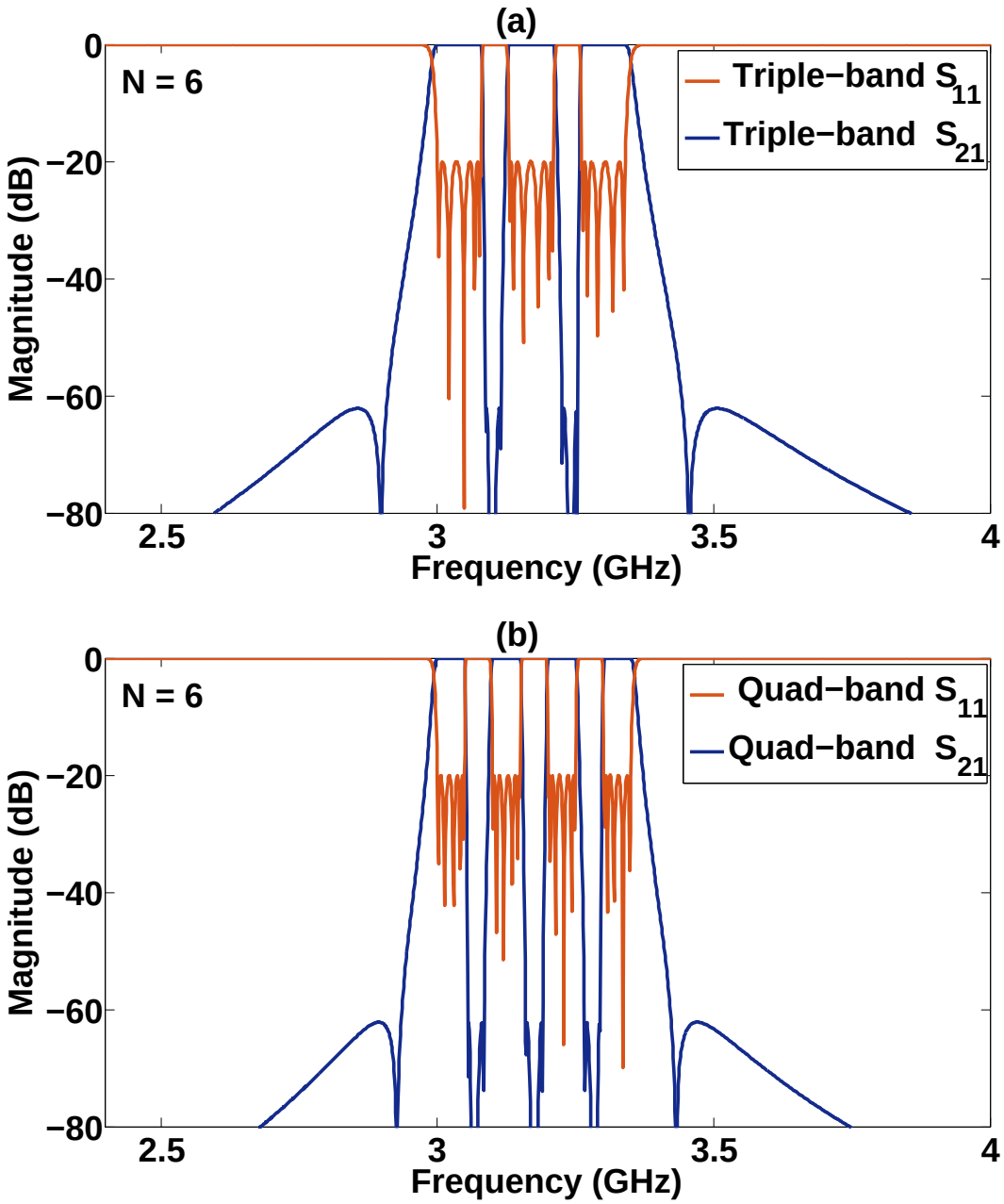

Fig. 3.9 The ideal lossless response of a (a) triple-band response of the filter of Fig 3.7 (d), and (b) quad-band response of the filter of Fig 3.7 (e). It is notable that appended resonators add transmission zeros between bands.

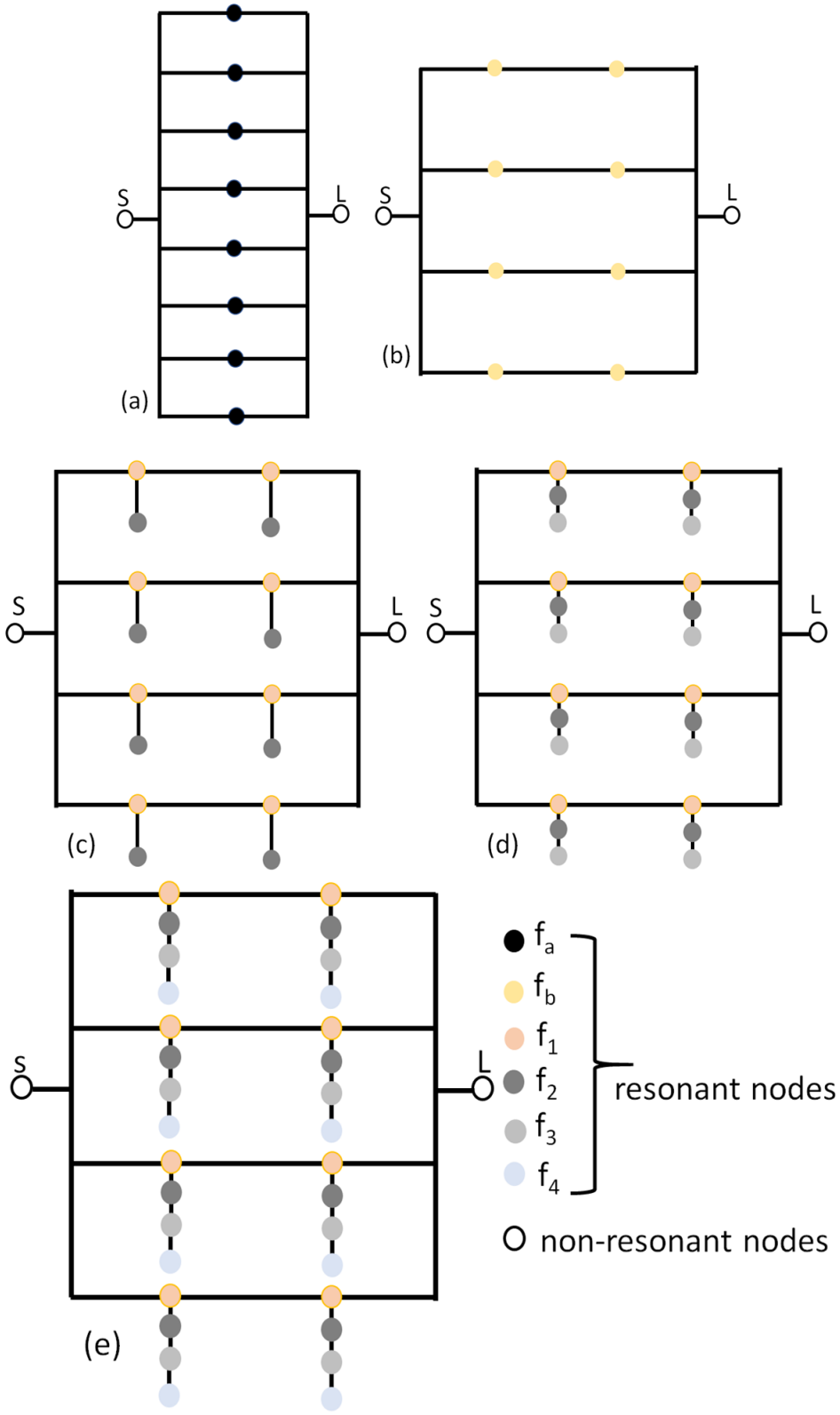

Fig. 3.10 The filter topologies are (a) an 8th order transversal single-band coupling topology. (b) an 8th order single-band basis quad-path transversal filter. The multi-band filter in (c) a dual-band filter (d) a triple-band filter (e) a quad-band filter reactance transformed filter.

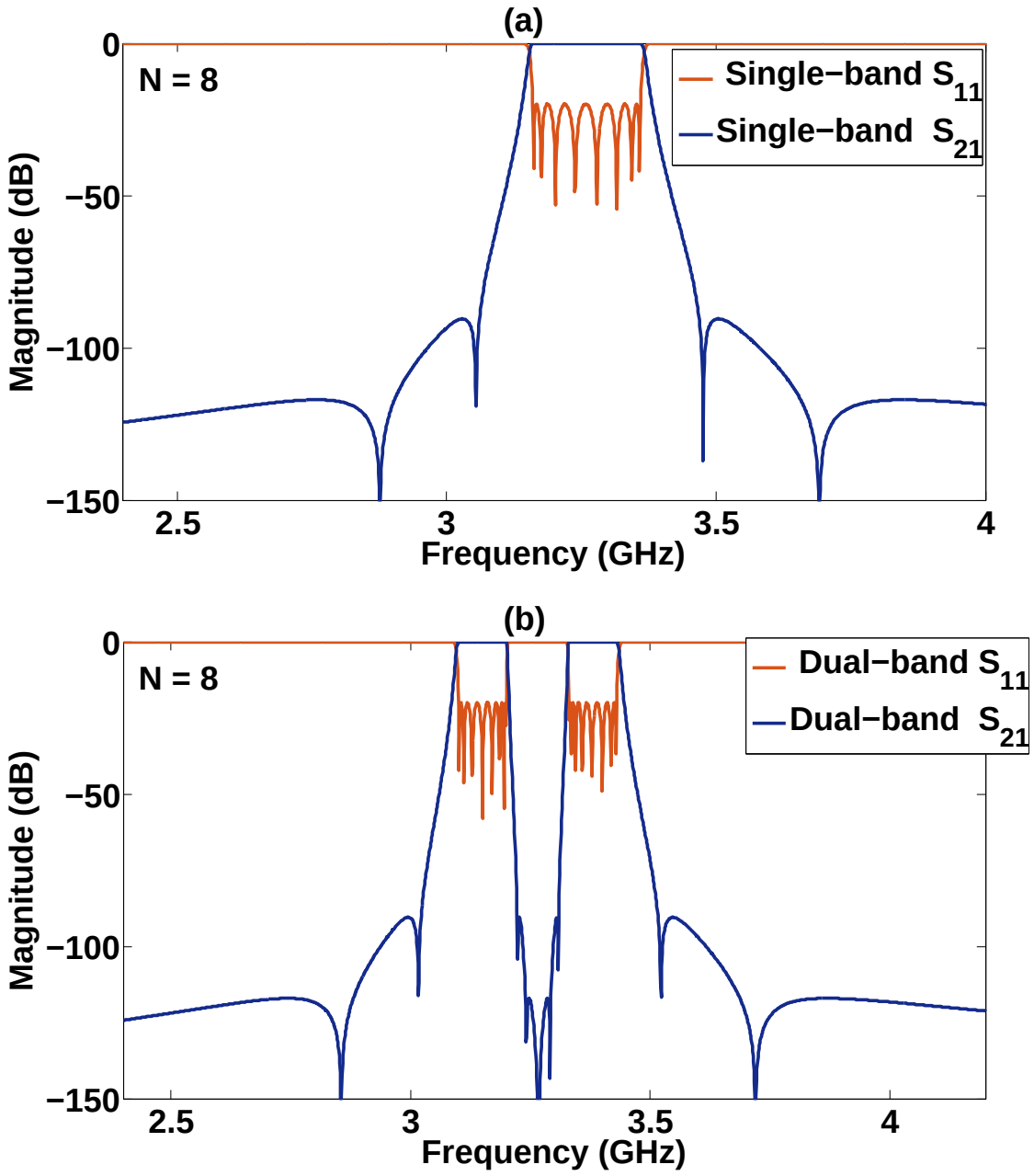

Fig. 3.11 The ideal lossless response of (a) single-band eight order basis filter of Fig 3.10 (b), and (b) dual-band response of the filter of Fig 3.10 (c). It is notable that appended resonators add transmission zeros between bands.

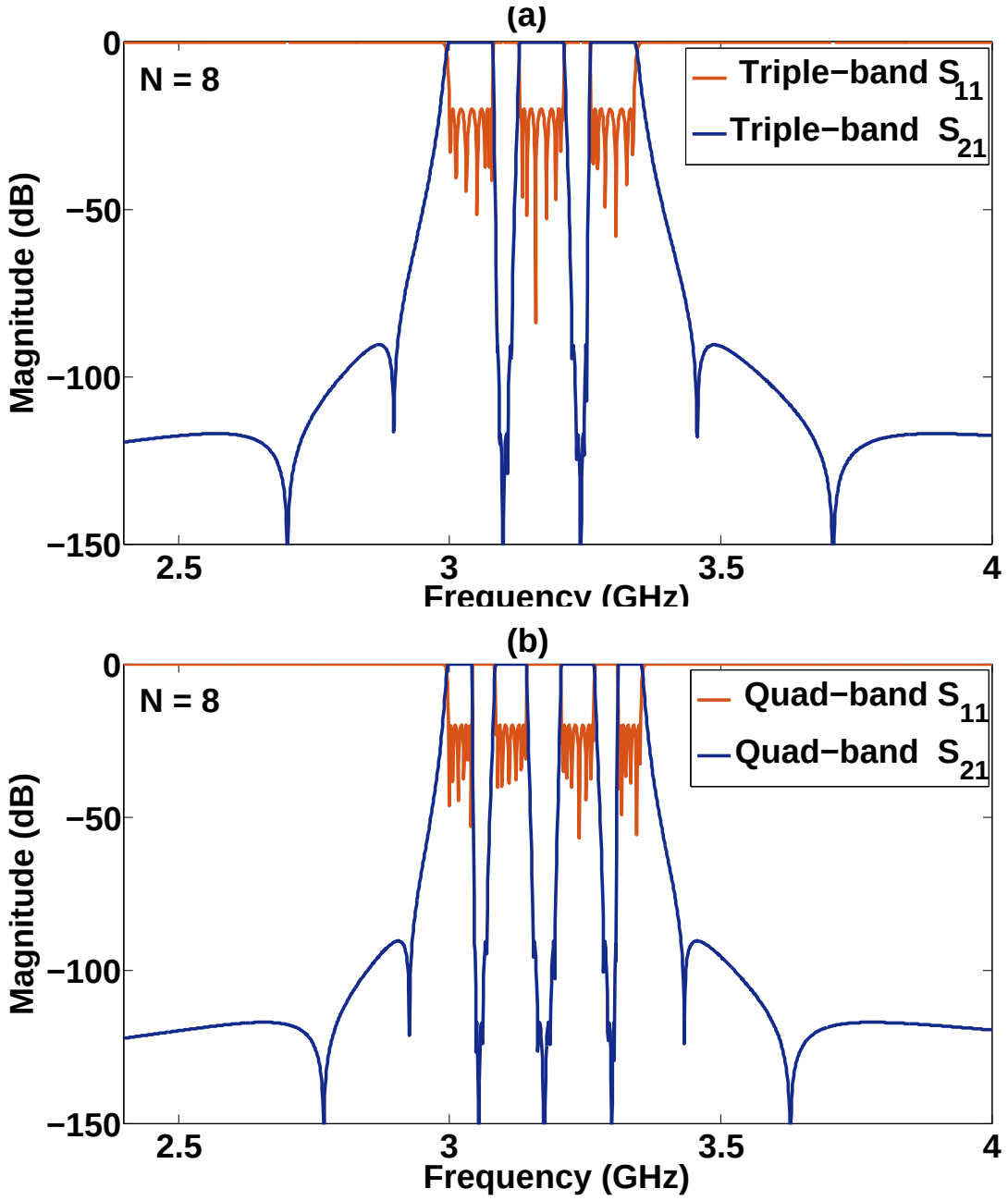

Fig. 3.12 The ideal lossless response of a (a) triple-band response of the filter of Fig 3.10 (d), and (b) quad-band response of the filter of Fig 3.10 (e). It is notable that appended resonators add transmission zeros between bands.

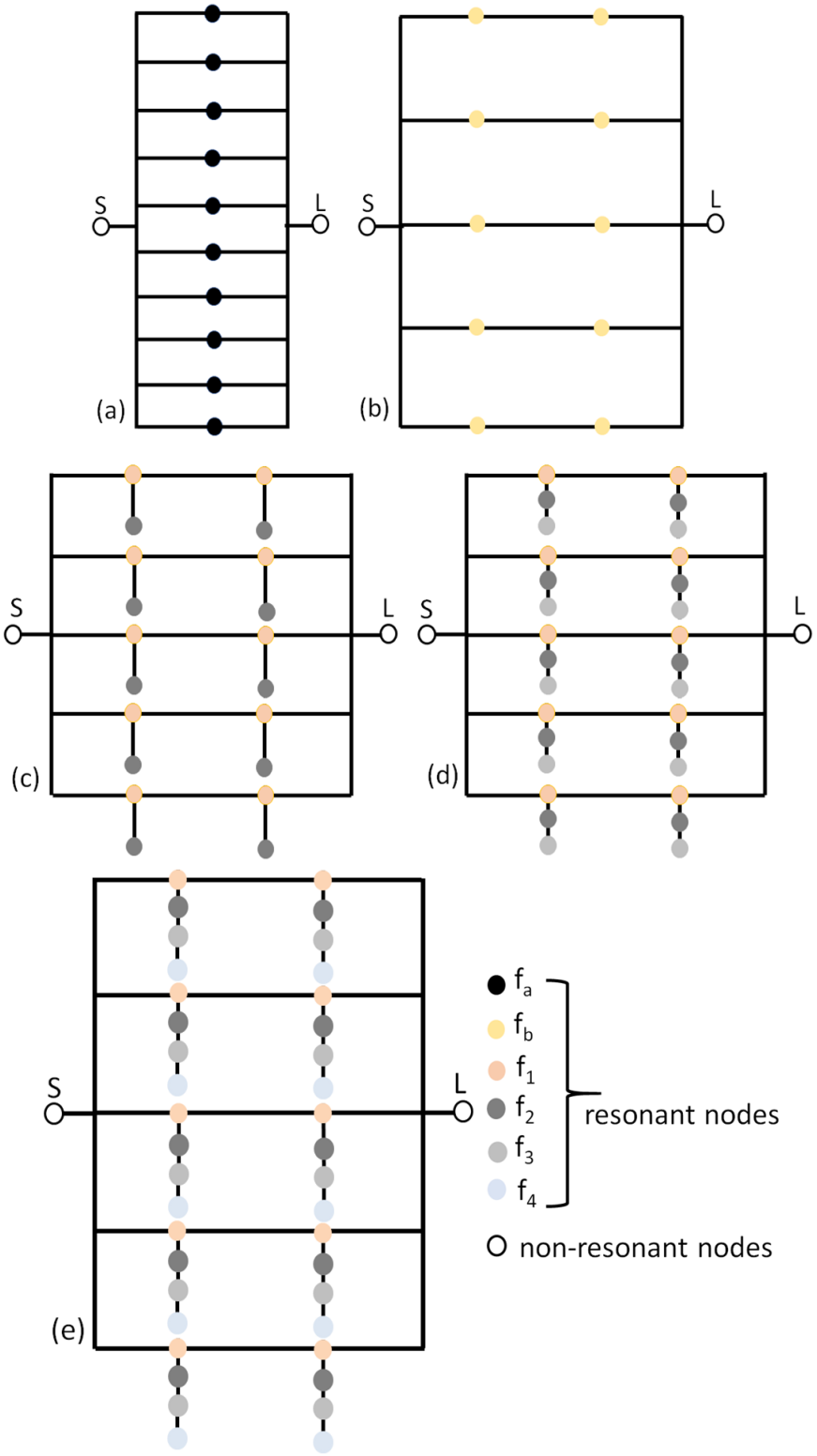

Fig. 3.13 The filter topologies are (a) a 10th order transversal single-band coupling topology. (b) a 10th order single-band basis quad-path transversal filter. The multi-band filter in (c) a dual-band filter (d) a triple-band filter (e) a quad-band filter reactance transformed filters.

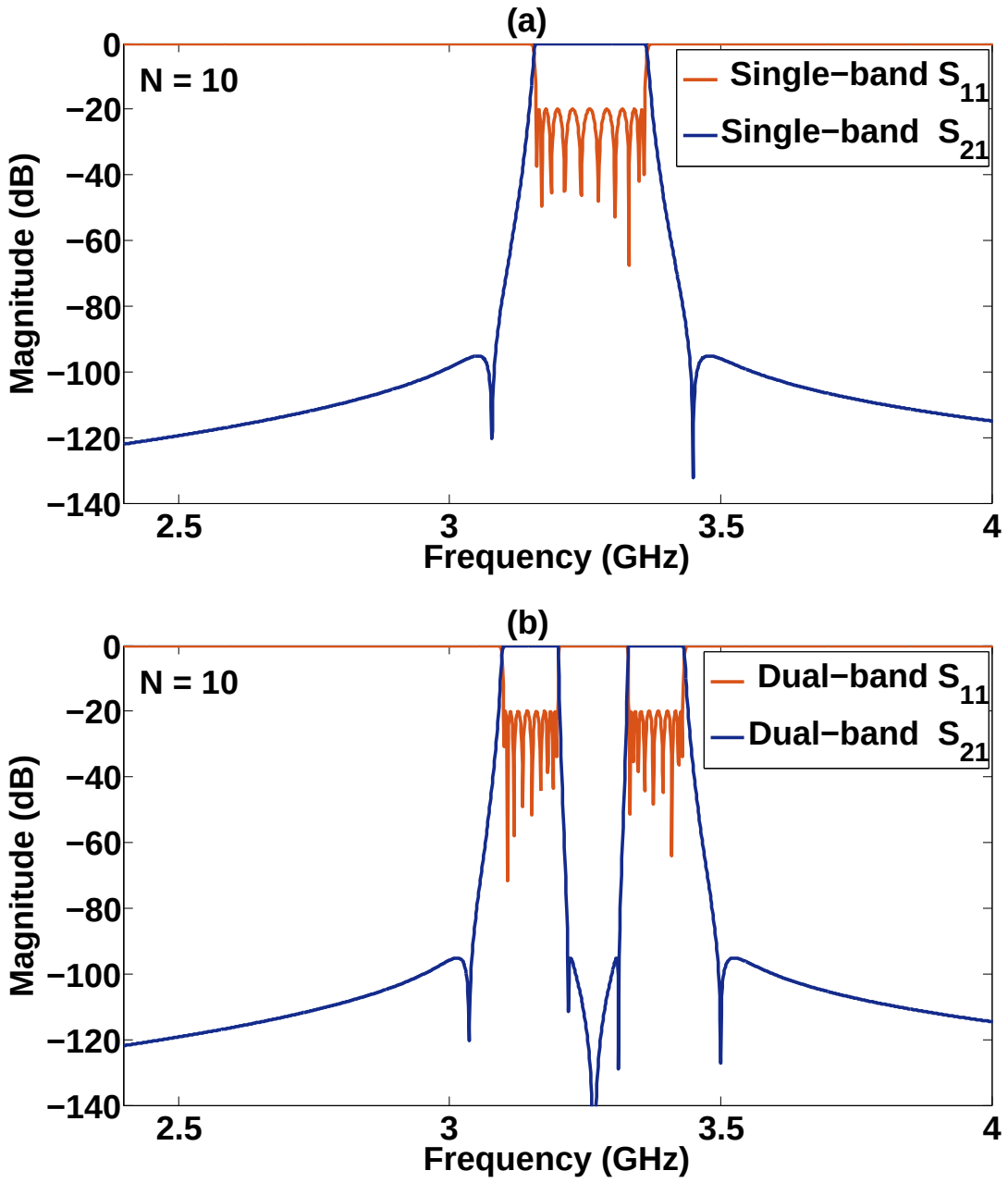

Fig. 3.14 The ideal lossless response of (a) a single-band tenth order basis filter of Fig 3.13 (b), and (b) dual-band response of the filter of Fig 3.13(c). It is notable that appended resonators add transmission zeros between bands.

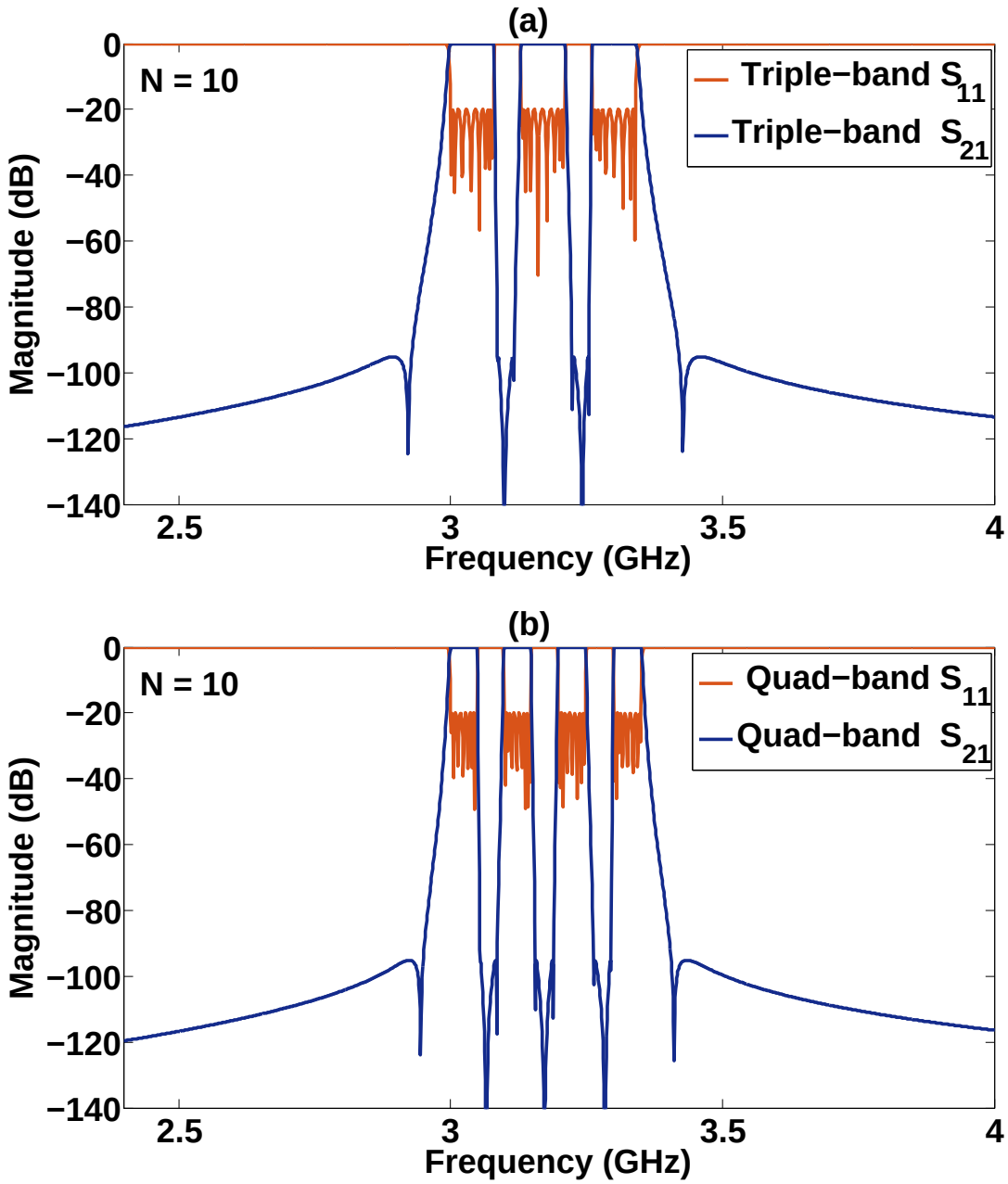

Fig. 3.15 The ideal lossless response of (a) a triple-band response of the filter of Fig 3.13 (d), and (b) quad-band response of the filter of Fig 3.13 (e). It is notable that appended resonators add transmission zeros between bands.

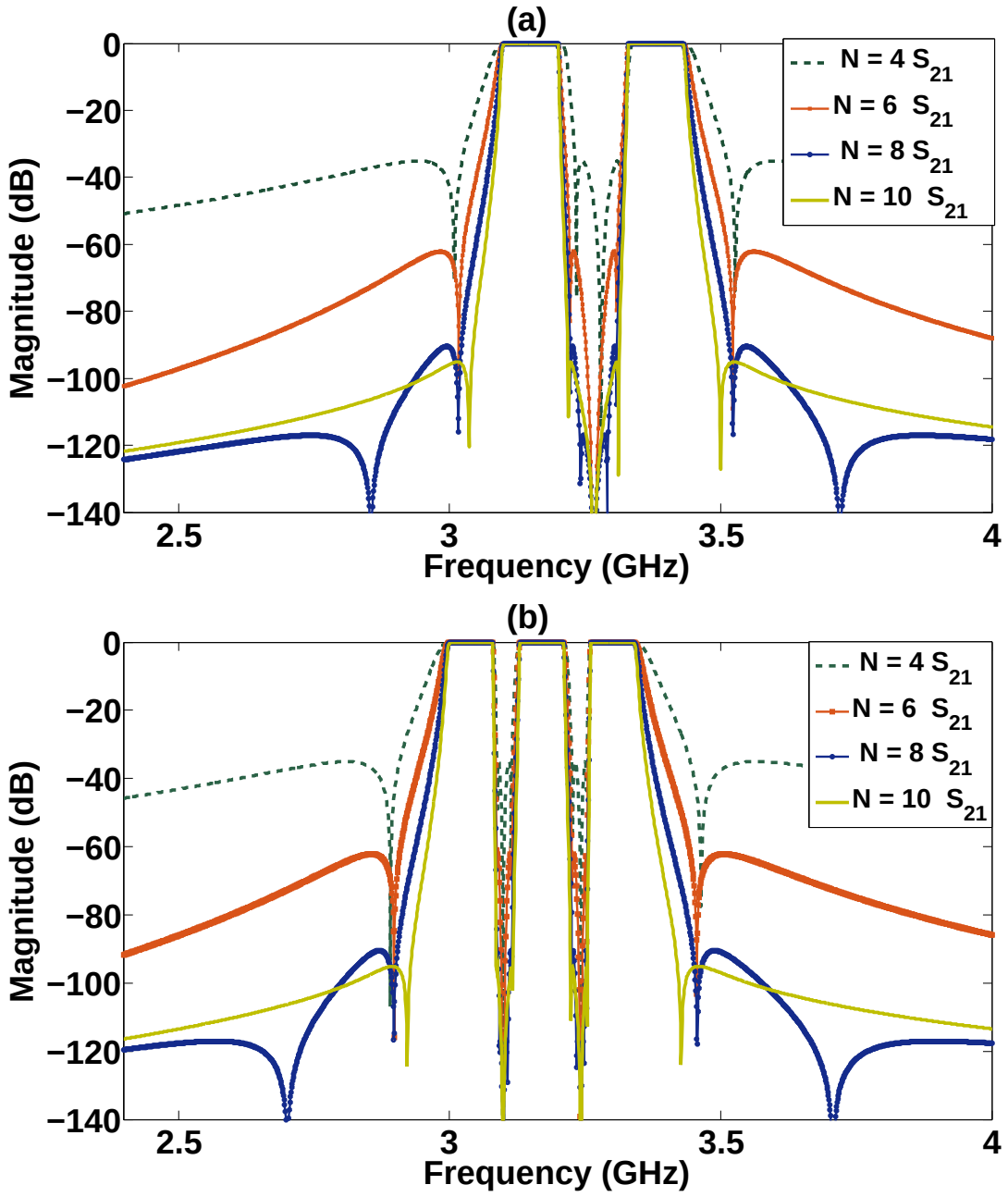

Fig. 3.16 The ideal lossless frequency response comparisons of a dual, triple-band of $N = 4$, $N = 6$, $N = 8$, $N = 10$.

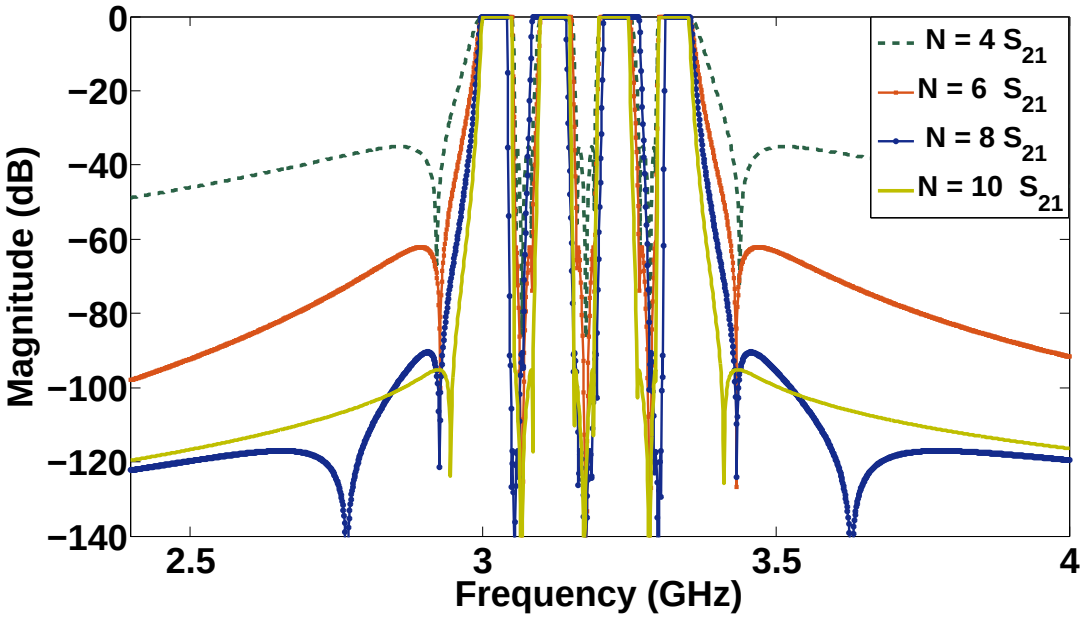

Fig. 3.17 The ideal lossless frequency response comparisons of a quad-band of $N = 4$, $N = 6$, $N = 8$, $N = 10$.

3.2.2 Effect of resonator loss on multi-band narrow-band filters with identical resonator Q_u.

A quality factor notion was employed to describe the coupling of an immitance inverter between a resonator and a non-resonating node, that is, the source or load. When the resonator is not connected to any load, its quality factor is known as an unloaded quality factor Q_u. Lossless resonators are regarded to have an inifinite quality factor. The coupling matrix, which is synthesized based on a generalized Chebyshev technique, models lossless resonators; hence, their unloaded quality factor is regarded to be infinite as well.

In resonant circuits, the unload Q factors (Q_u) determine the loss. High Q_u resonators have low loss while lower Q_u resonators have high loss. The effect of low Q_u is a deviation in insertion loss from the ideal position where the band edge becomes rounded, resulting in poor performance. The number of resonators and the bandwidth are related to the filter insertion loss. Figures 3.19 to 3.24 displays a differing S_{21} for a dual, triple and quad-bands with an equal bandwidth of 100 MHz, 80MHz and 50 MHz respectively.

In all cases, the range of Q_u is from the 2000 maximum to the minimum of 50. The Q_u is modelled by a resistor in parallel with a parallel resonator (see Fig 3.18). The Q_u is described as a ratio of the energy stored in the inductor and capacitor to the power dissipated in the resistor as a function of frequency[56].

The Q_u of the parallel resonant circuits is given as:

$$Q_u = \frac{R}{X} = \frac{R}{\omega_o L} = \omega_0 RC \tag{3.20}$$

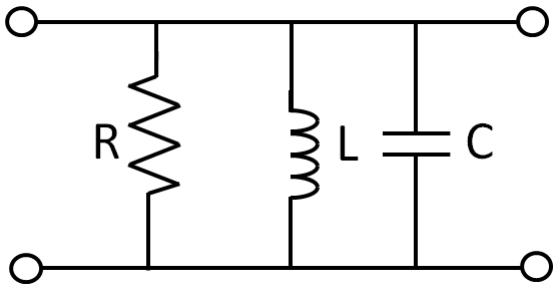

Fig. 3.18 Parallel RLC resonant circuit model.

Effects of Q-factor due to the number of resonators

From the graph plotted for the comparisons of Q-factors, it can be seen that the number of resonators contribute to the loss of the filter. For a dual-band example with a single-band basis of order 4, 6, 8 and 10, the total number of resonators are equal to 8, 12, 16 and 20 respectively. For the triple-bands, the number of resonators are 12, 18, 24 and 30, while in the case of the quad-band, the total number of resonators add up to 16, 24, 32 and 40 respectively. As the Q-factor decreases, the filters with a large number of resonators exhibit large losses. The insertion loss degrading is exactly the same as for single band filters and part of well-established theory. However, as demonstrated in this section and [31], this is also the same for multiband filters, with the difference that not all passbands are affected equally.

Effects of Q- factor on pass-band width

When one considers all single-band basis orders for a dual-band response, it is clear that the second band bandwidth is not the same as the first; it appears to be smaller. With triple band, the mid-band bandwidth appears to be smaller than the outer bands. When one increases the bands to four, the bandwidth of the two inner bands is smaller when compared to the two outer bands. These filters have been specified with equal bandwidth but the size of the bandwidth differs between bands as the losses increases. In all cases, the pass-band levels are different.

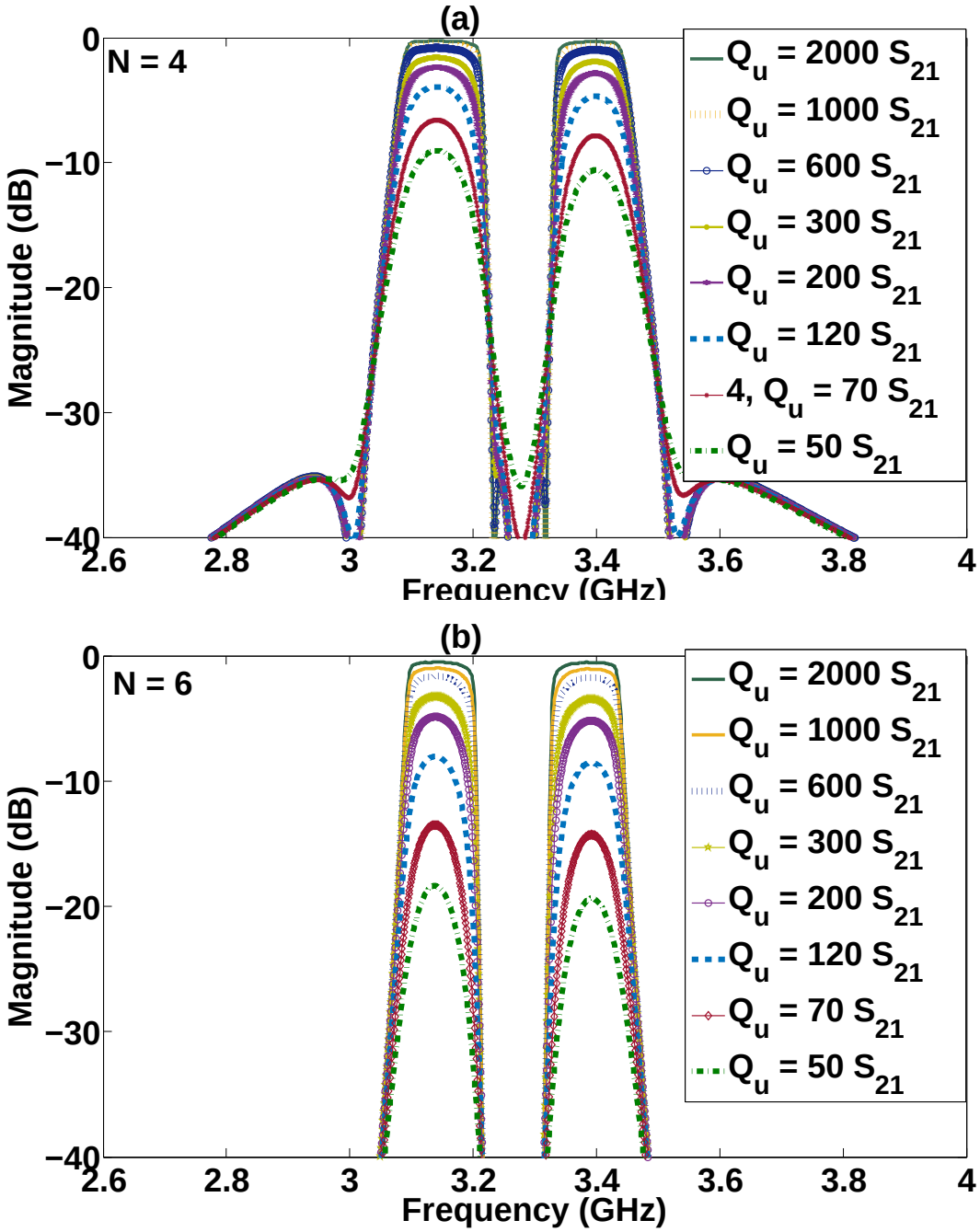

Fig. 3.19 Dual-band filter pass-bands for order $N = 4$ and $N = 6$ are affected by various levels of resonator loss.

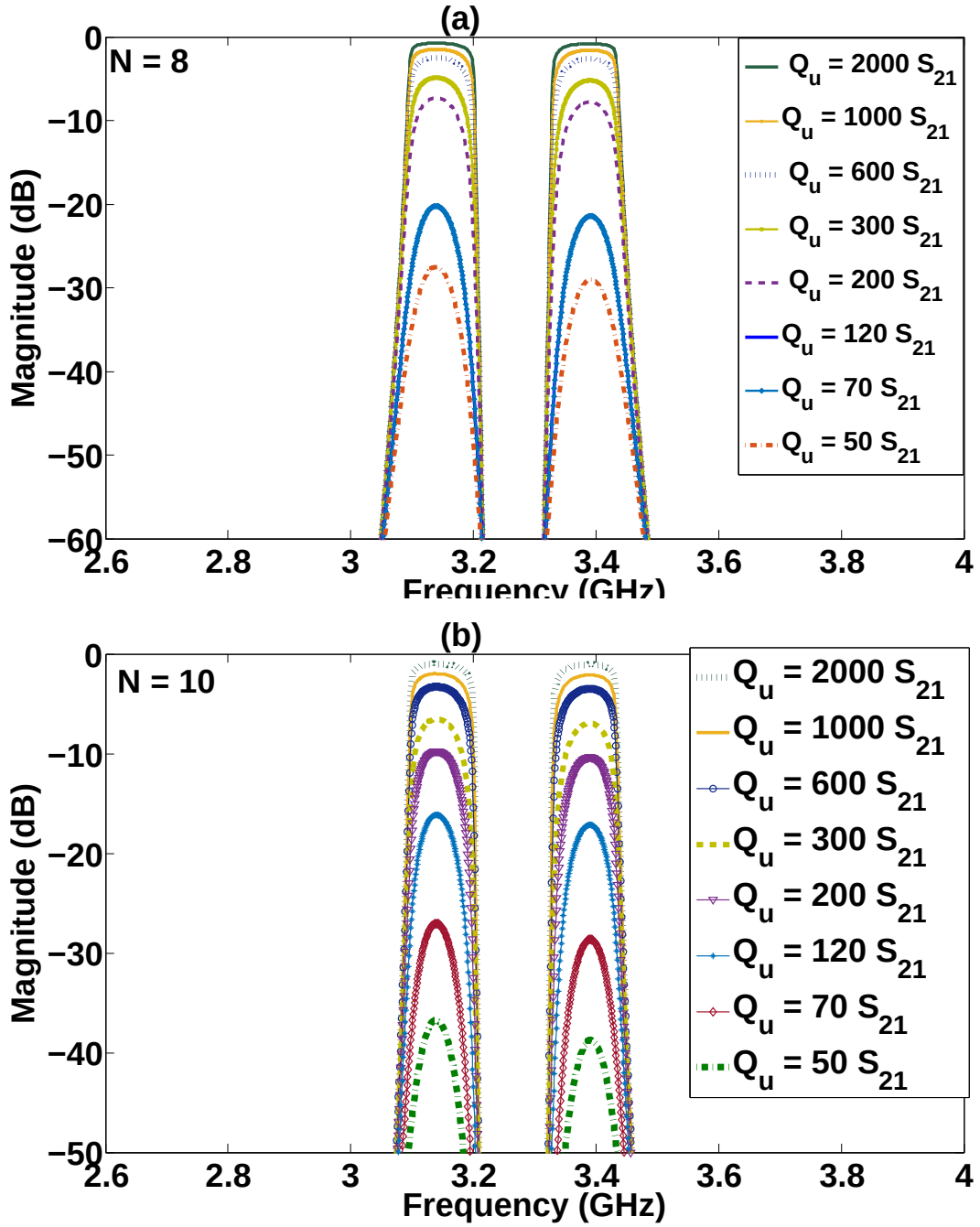

Fig. 3.20 Dual-band filter pass-bands for order $N = 8$ and $N = 10$ are affected by various levels of resonator loss.

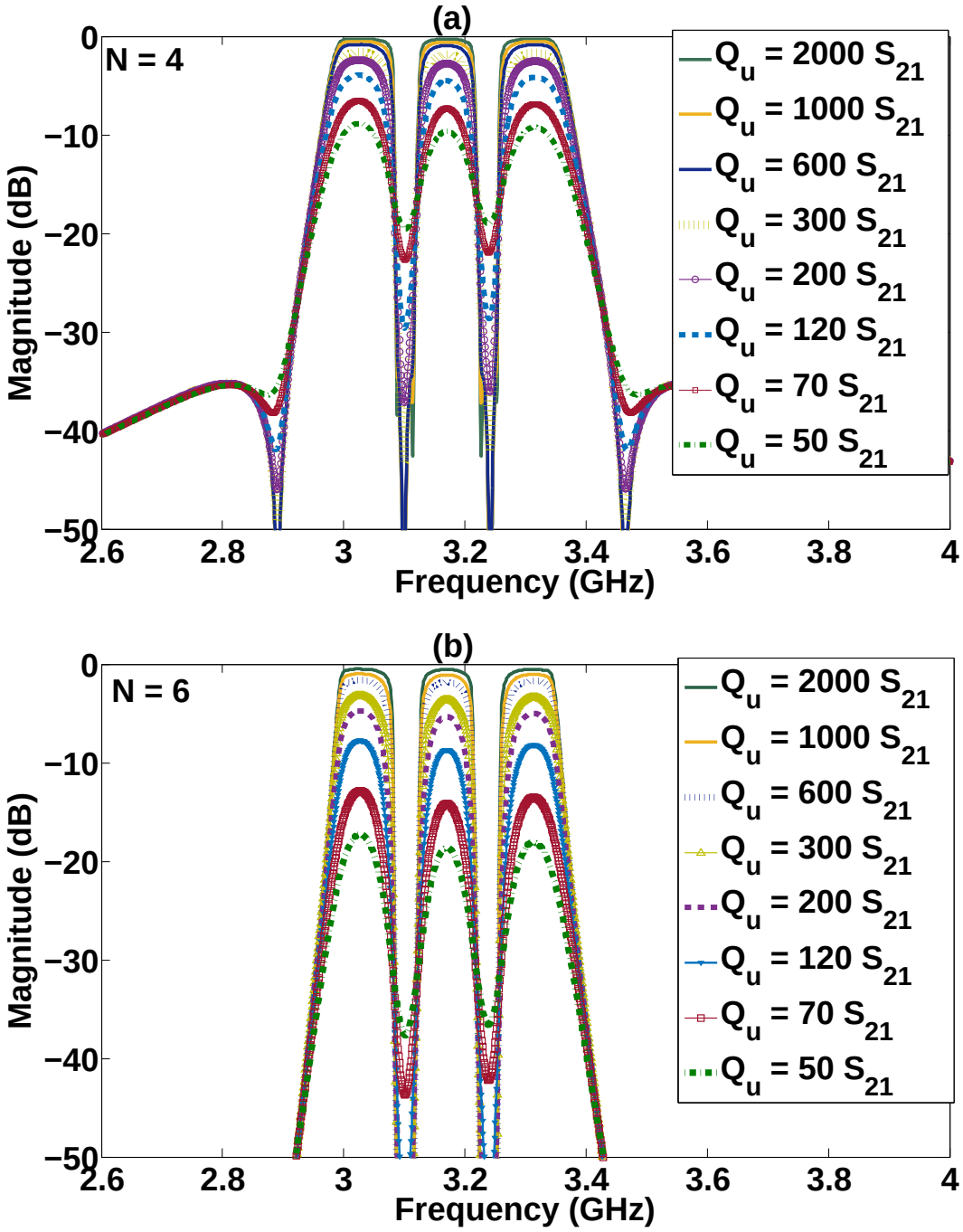

Fig. 3.21 Triple-band filter pass-bands for order $N = 4$ and $N = 6$ are affected by various levels of resonator loss.

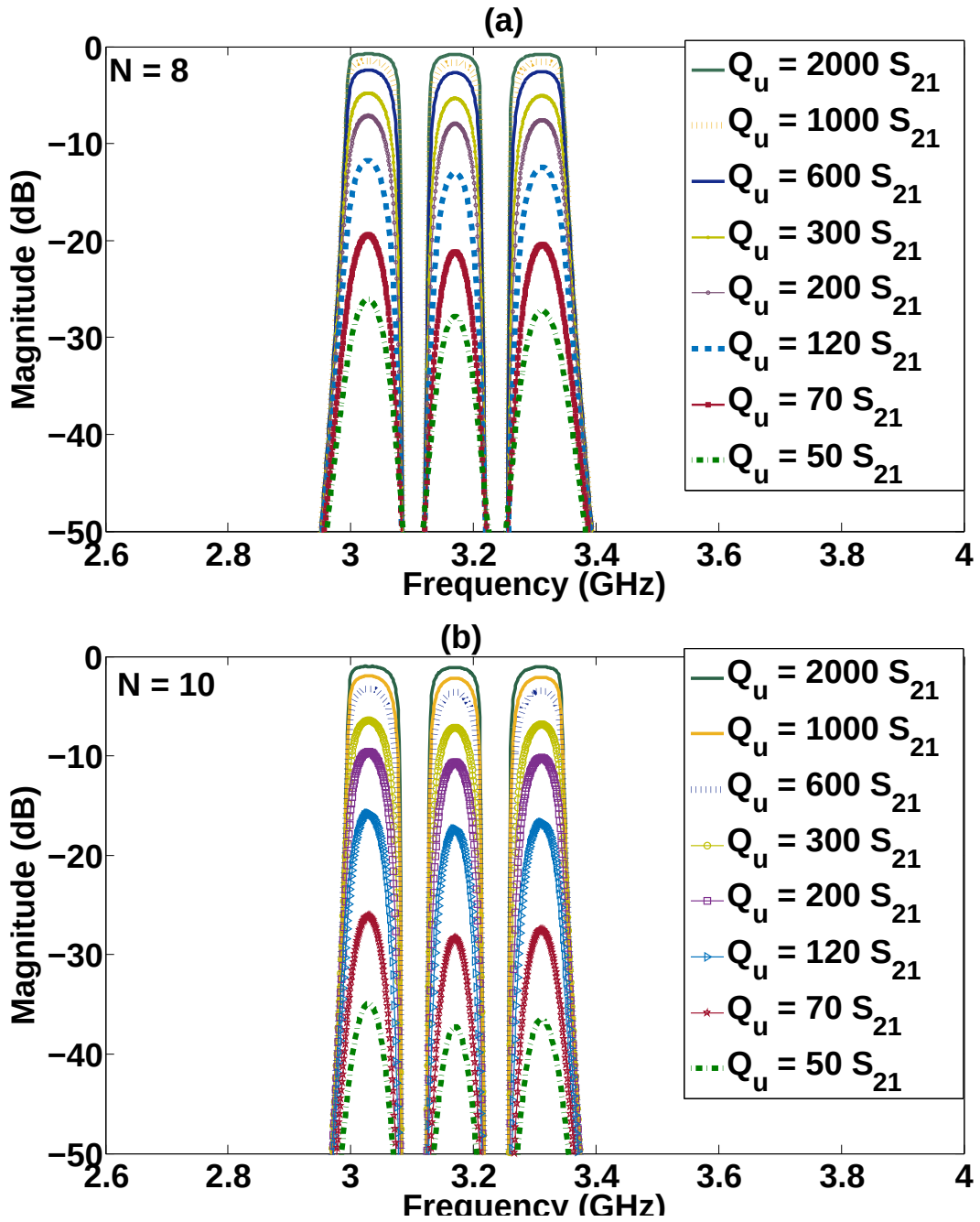

Fig. 3.22 Triple-band filter pass-bands for order $N = 8$ and $N = 10$ are affected by various levels of resonator loss.

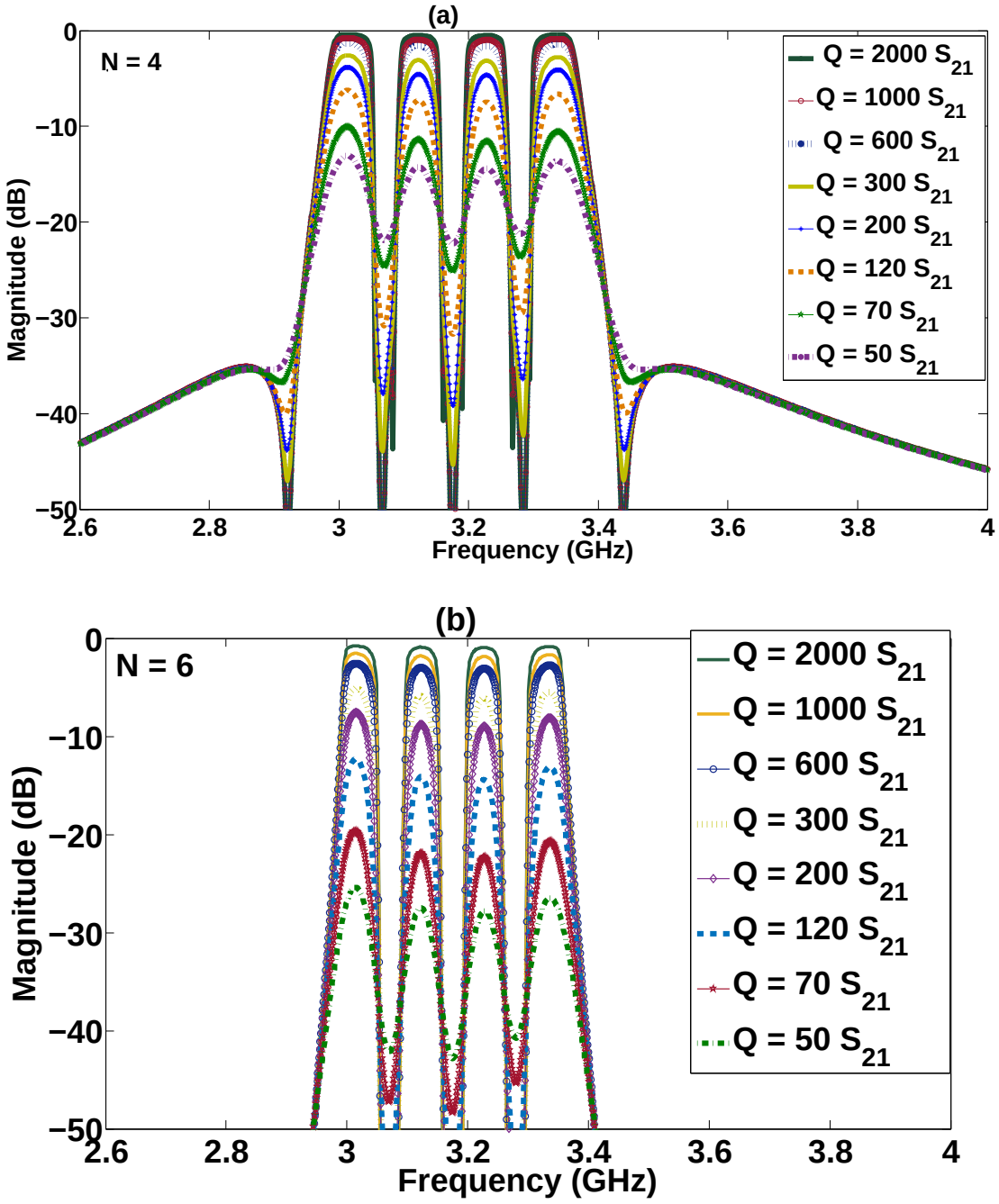

Fig. 3.23 Quad-band filter pass-bands for order $N = 4$ and $N = 6$ are affected by various levels of resonator loss.

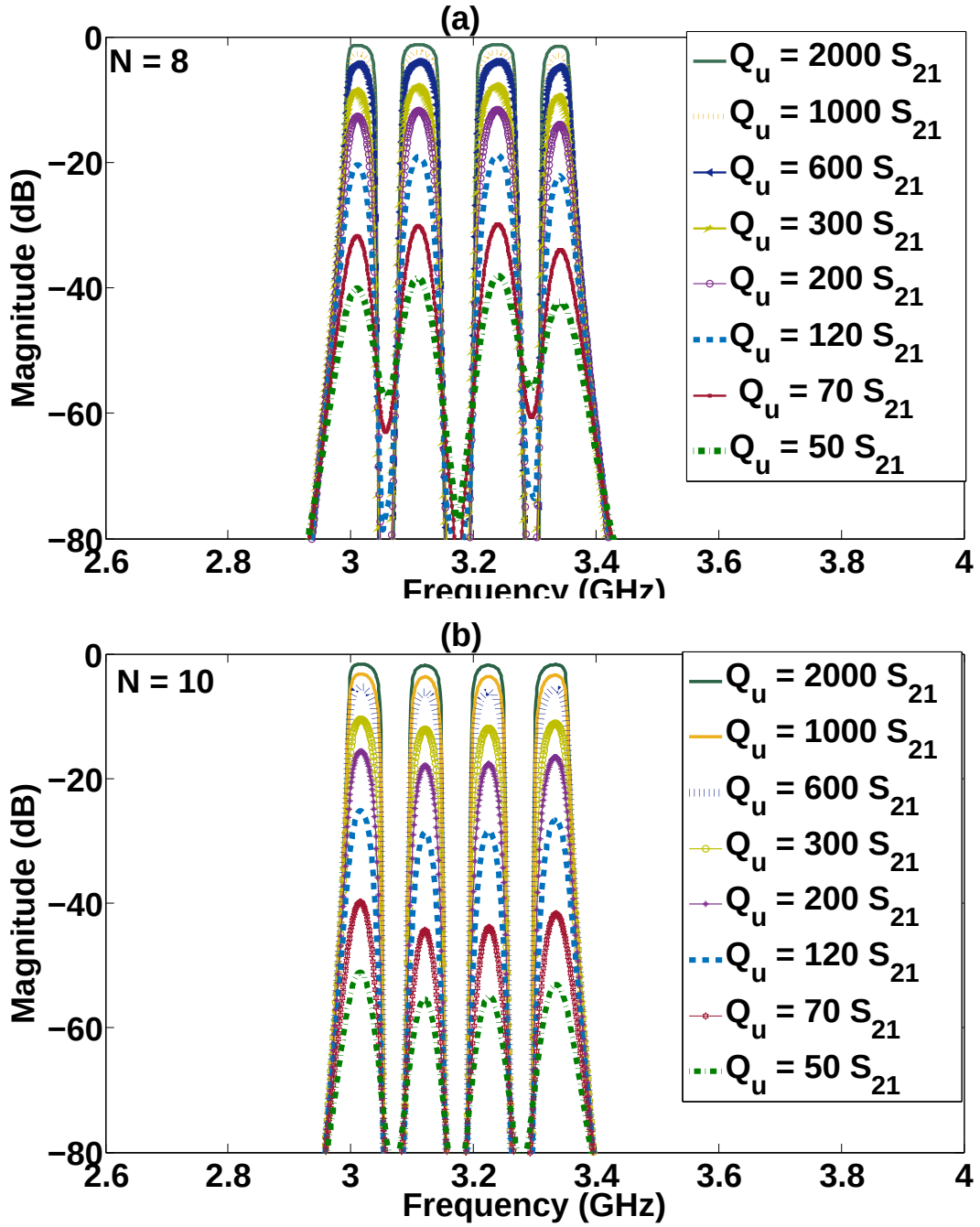

Fig. 3.24 Quad-band filter pass-bands for order $N = 8$ and $N = 10$ are affected by various levels of resonator loss.

Effects of Q- factor on selectivity

The transmission zeros appear to be co-located but the selectivity becomes poorer with the increasing number of bands and decreasing Q-factor.

3.2.3 Group-delay responses

The group-delay, tuning concept was introduced in [51] for direct-coupled resonators. Group-delay tuning involves adjustments to the coupling values of both the external quality factor (Q_E) and inter-resonator couplings k_{ij}. When successive resonators are tuned Q_E and k_{ij} can be obtained from reflected signals S_{11}. According to [51] the group delay of S_{11} is defined as:

$$\Gamma_d(\omega) = -\frac{\delta\phi}{\delta\omega} \tag{3.21}$$

where ϕ is the phase of S_{11} in radians, and ω is the angular frequency. Narrow-band, single-band, coupled resonators utilize a standard low-pass to band-pass frequency transformation; similarly, multi-band, narrow-band, coupled resonators, based on reactance transformed, utilize the same transformation for the single band basis filter, given in equation 2.14. The group delay of S_{11} of a single-band inverter coupled circuit is given by [51]

$$\Gamma_d(\omega) = -\frac{\omega_0}{(\omega_2-\omega_1)}\left(\frac{1}{\omega_0}+\frac{\omega_0}{\omega_2}\right)\frac{\delta\phi}{\delta\omega^1} = -\frac{\omega^2+\omega_0^2}{\omega^2(\omega_2-\omega_1)}\frac{\delta\phi}{\delta\omega^1} \tag{3.22}$$

Now

$S_{11} = \frac{Z_{IN}-Z_0}{Z_{IN}+Z_0}$

Since Z_{IN} is purely imaginary and Z_0 is real then

$S_{11} = \frac{jX_{IN}-Z_0}{jX_{IN}+Z_0}$

Therefore,

$$\phi = -tan^{-1}\frac{X_{IN}(\omega)}{Z_0} - tan^{-1}\frac{X_{IN}(\omega)}{Z_0} = -2tan^{-1}\frac{X_{IN}(\omega)}{Z_0} \tag{3.23}$$

Then

$$\Gamma_d(\omega) = \frac{2(\omega^2+\omega_0^2)}{\omega^2(\omega_2-\omega_1)}\frac{\delta}{\delta\omega_1}tan^{-1}\frac{X_{IN}(\omega)}{Z_0} \tag{3.24}$$

Detailed steps of group-delay tuning of the sixth order, all pole filter are presented in [51]. The resonators are adjusted in a sequence, that is, when the first resonator is tuned; others are shorted to allow adjustment of the input coupling until the specified group delay is set. The second resonator can be tuned while others remain shorted; the coupling between the first and the second resonator is adjusted to the desired group delay. The procedure continues until all the resonators are tuned to the specified group delay.

A numerical group-delay tuning procedure similar to that followed in [51] was developed for reactance transformed filters. For multi-band filters the structures are more complex with the increasing number of bands. The sequence of tuning and shorting resonators is complex than single-band filters. The major characteristic of the reactance transform filters is the negative group delay. Negative group delays usually appear when the simulation frequency points are under-sampled. For these filters, negative group delays arise, depending on the number of pass-bands and resonators. An example of the theoretical group-delay tuning for a fourth order, single band, basis filter of the quad-band, shown in Fig. 3.25 is presented. The filter has a total of 16 resonators; the basis single band and appended resonators add up to quad-band.

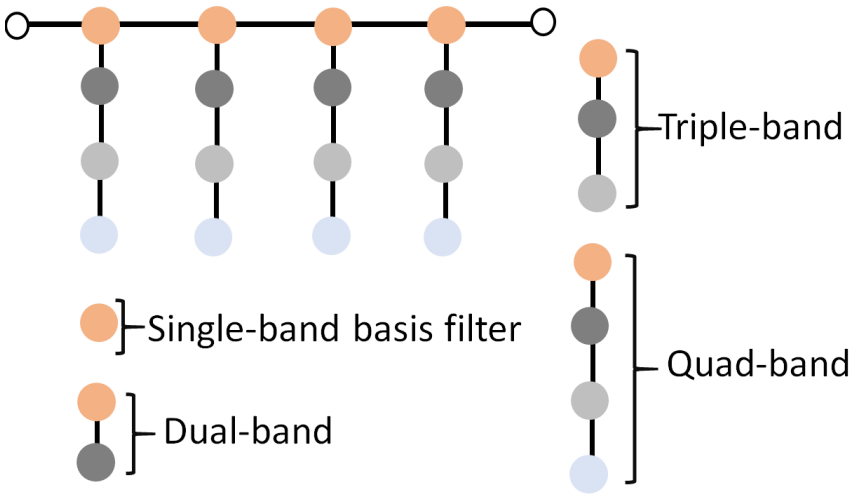

Fig. 3.25 A fourth order, all-pole, quad-band filter topology.

Quad band all poles group-delay tuning

Figure 3.26 shows the numerical tuning sequence of an all-poles, quad-band filter. The first resonator is tuned while the rest are de-tuned. As depicted in tuning A, the resonators are tuned and de-tuned in the sequence until the single band, basis resonators are all tuned, tuning A to D. Resonators may be tuned in a horizontal plane relative to the single-band,

basis tuning E to F, vertical plane tuning G to J or tuning some resonators in both horizontal and vertical planes simultaneously. It was observed that for this topology option K to L was not suitable for numerical tuning as negative group delay and sharp spike responses arose. The group delay responses of tuning A to L are shown in Fig. 3.27.

Dual-band dual-path group-delay tuning

The method for tuning group delay is extended to include cross-coupled resonators in [50] where the process for group-delay tuning is summarized for a tenth order, cross-coupled resonator. The numerical tuning is examined for the dual-path, dual-band topology for a fourth order, single band basis filter. The best sequence is tuning symmetric, horizontal or vertical planes. The coupling topology sequence and responses of the dual-path, dual-band filter are detailed in Fig. 3.28 and Fig. 3.29 respectively.

Dual-band triple-path group-delay tuning

The numerical tuning was examined for the triple path, dual-band topology. An example is a sixth order, single band basis filter; the network coupling matrix is rotated N/2 rotations and for $N = 6$ the resultant network has three parallel coupled paths. Figure 3.30 shows a representation of the coupling topology with possible numerical tuning. For a three-path topology tuning, A to E do not have a negative group delay, while tuning sequences F to H show negative, group-delay responses, as plotted in Fig. 3.31. From the observations, it was found that the best options for tuning transversal coupled resonator topologies were those with symmetry in the horizontal and vertical planes.

3.3 Wide-band implementation

A wide-band version of the synthesis methods in [6], based on rational functions which utilize reactance transform methods, was employed for wide-band, multi-band, lumped element filters. The well-known, canonical forms of the one-port, reactance functions of the first and second Foster and Cauer forms were transformed into multi-band prototype networks. The reactance transform method is general; it can achieve any number of pass bands with symmetrical or asymmetrical characteristics. The reactance transform has a low pass prototype as a basis filter. This may be an all-pole filter or, as in the case of this section, a quasi-elliptic filter. Each element in a low-pass prototype of the order M transformed to a multi-band prototype of the order NM. M is the number of desired bands. Each element

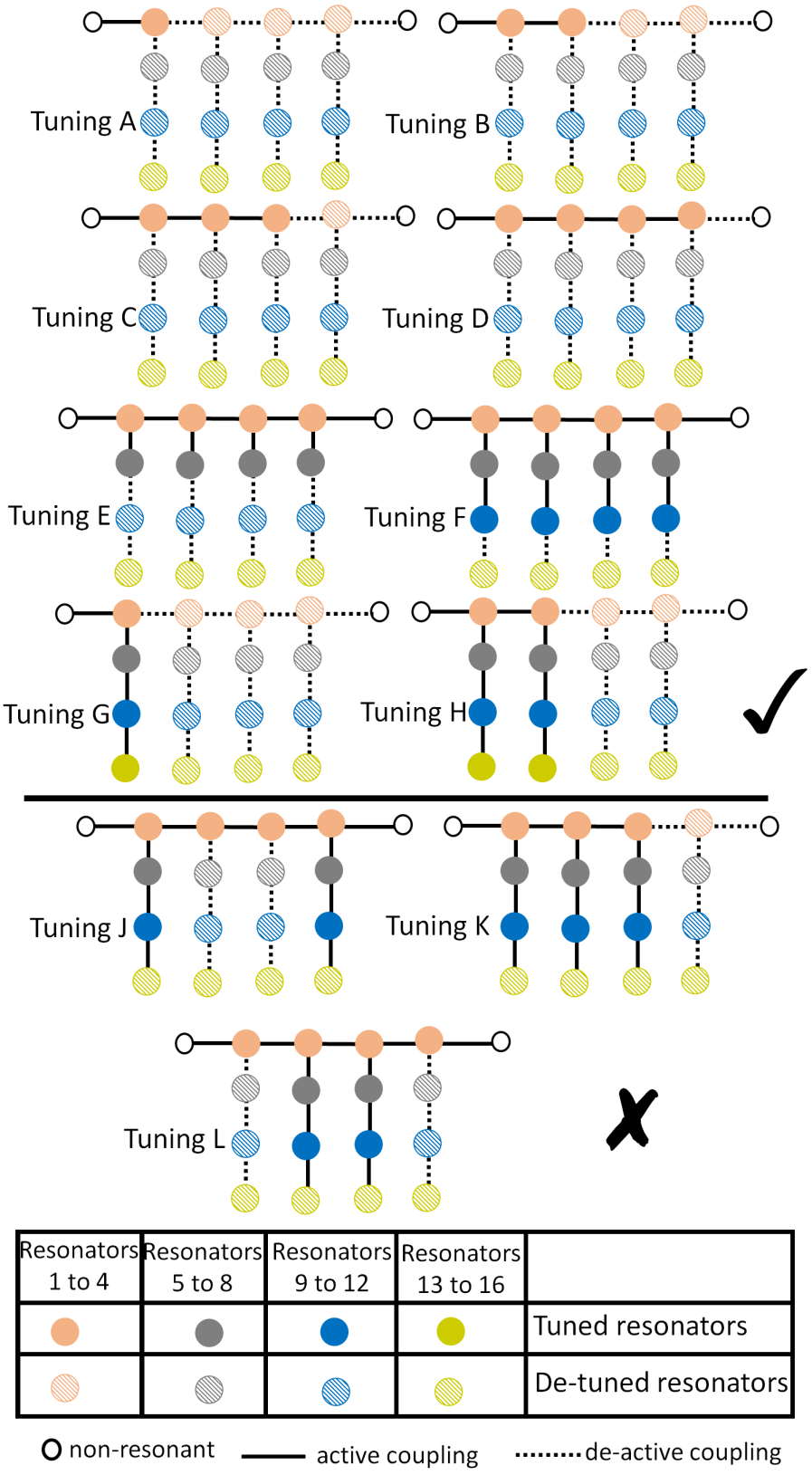

Fig. 3.26 A fourth order, all pole, quad-band filter topology. Options in a tuning sequence from A to D, tune the single band basis resonators. In option tuning E to F, resonators are tuned in horizontal plane relative to the single band basis resonators. In option G to J resonators are tuned in a vertical plane. Options K to L tune some resonators in both vertical and horizontal planes.

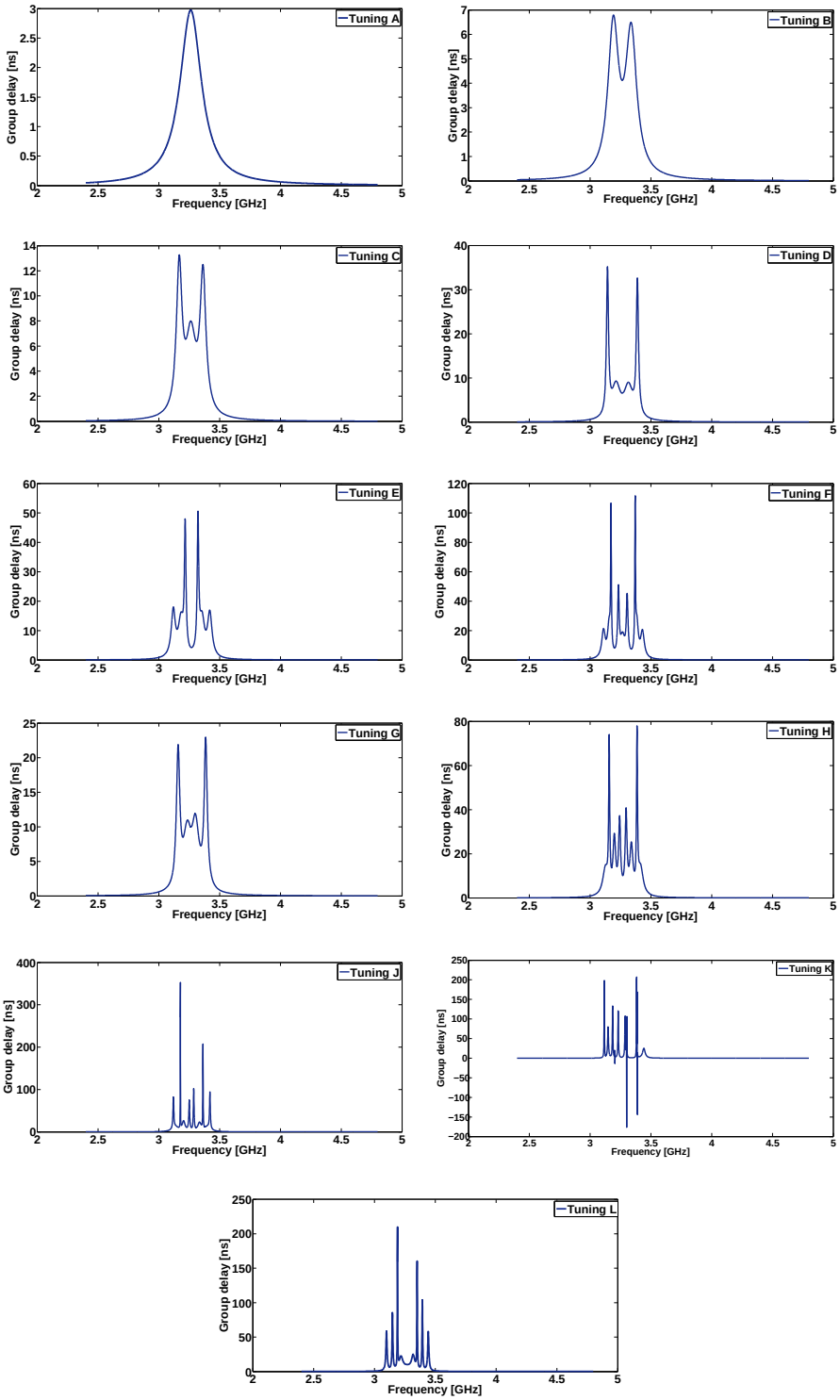

Fig. 3.27 Group delay response of a fourth order, all pole, quad-band filter topology. Options in a tuning sequence from A to D, tune the single band basis resonators. In option tuning E to F, resonators are tuned in horizontal plane relative to the single band basis resonators. In option G to J resonators are tuned in a vertical plane. Options K to L tune some resonators in both vertical and horizontal plane.

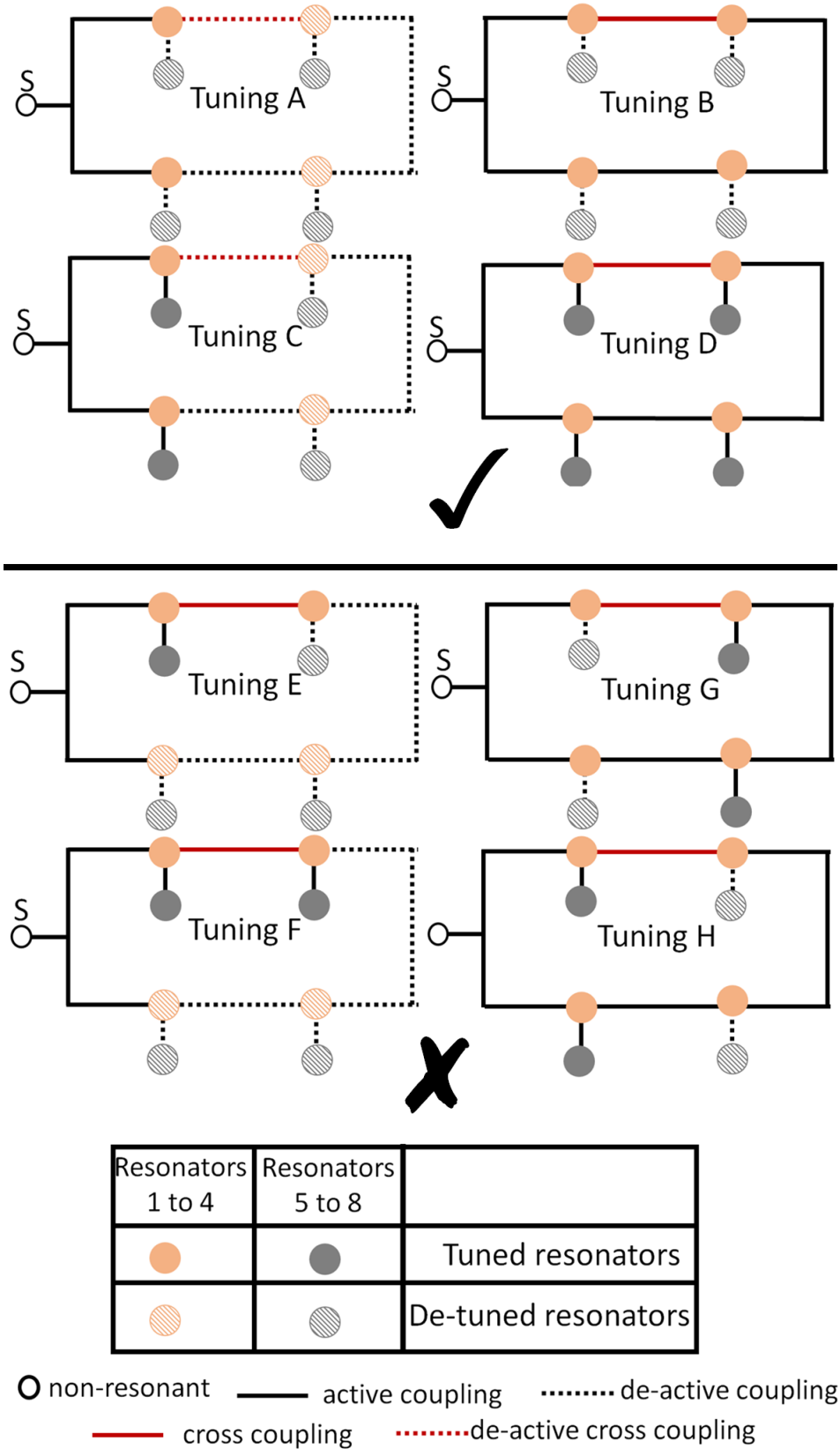

Fig. 3.28 Dual-path, dual-band options in a tuning sequence from A to C allow numerical tuning; the tuning sequence from D to F is not suitable.

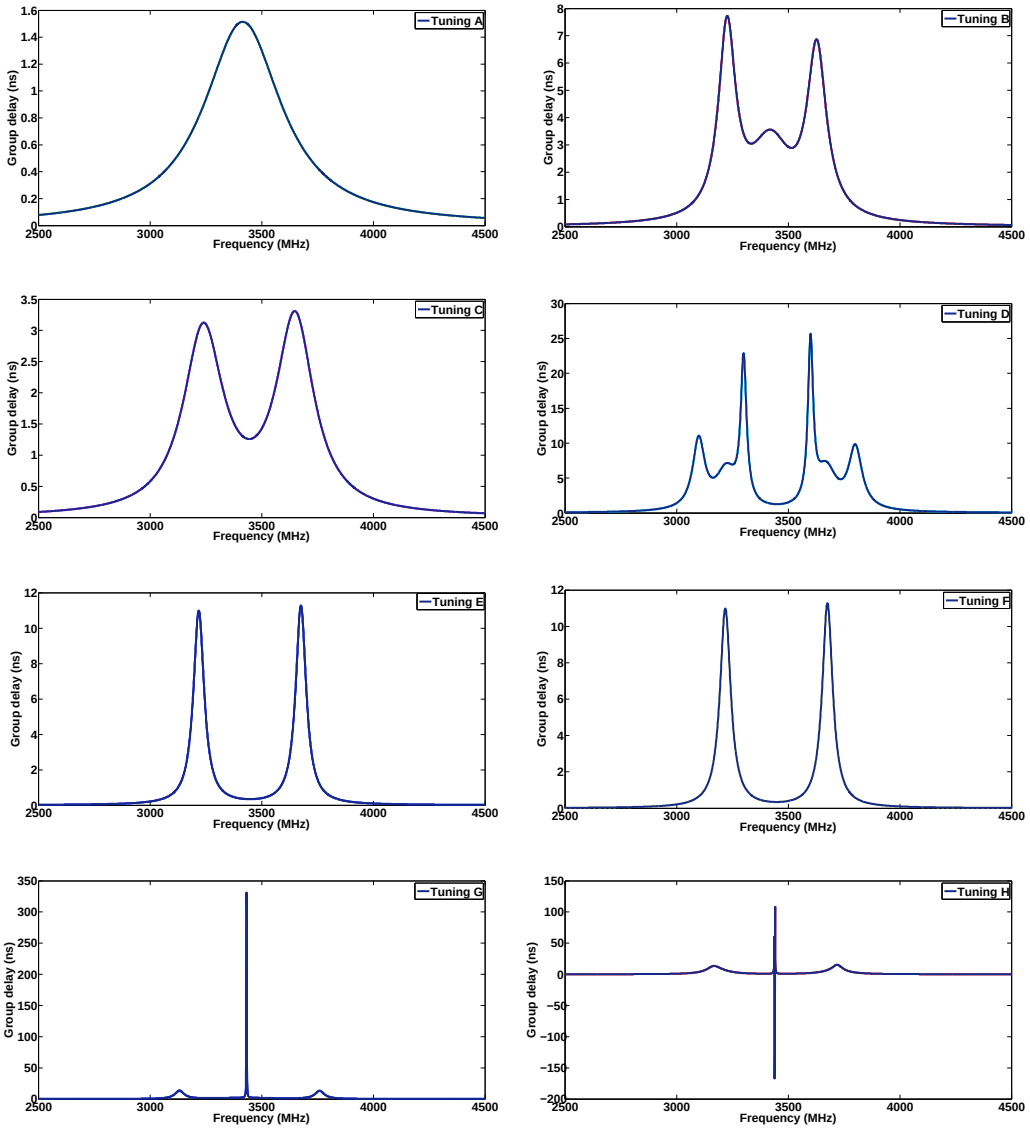

Fig. 3.29 Dual-path dual-band group delay responses for the tuning sequence A to F

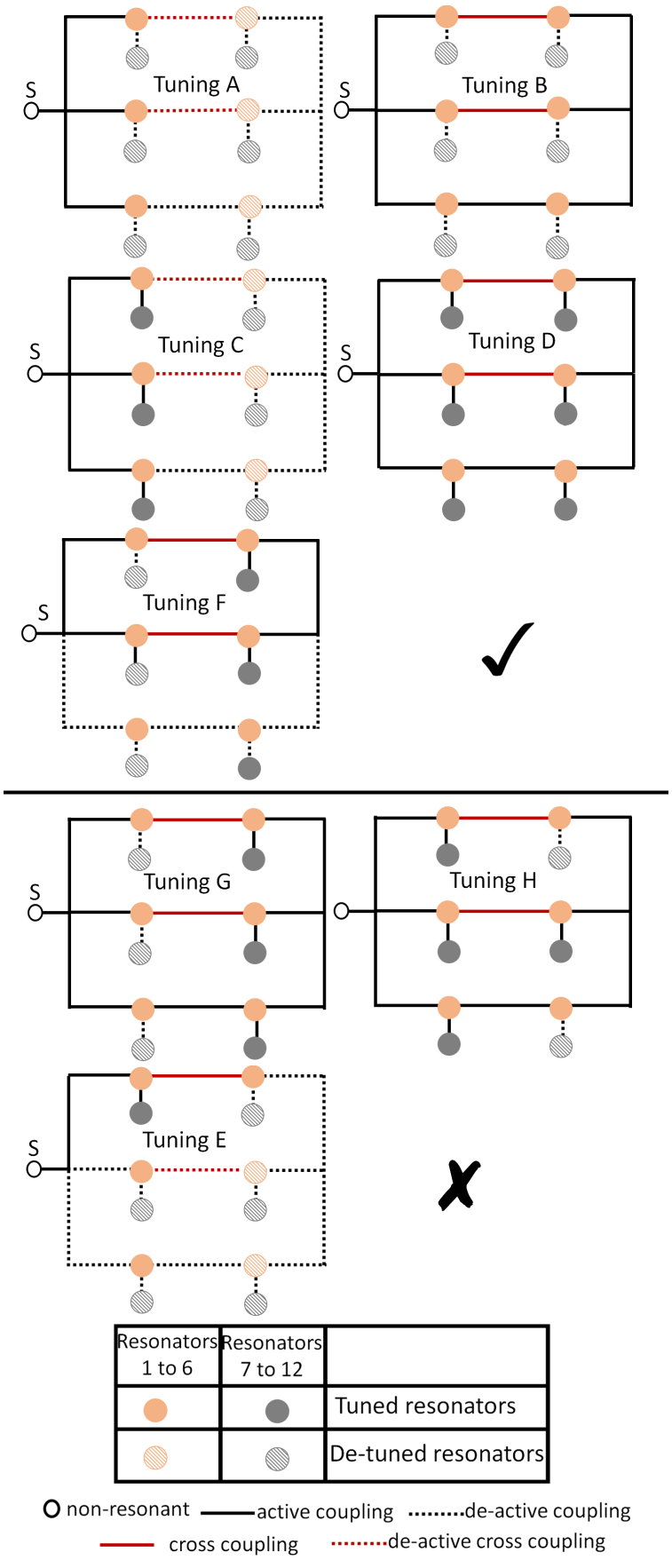

Fig. 3.30 Options in a tuning sequence from A to D that allows numerical tuning are shown, options in a tuning sequence from E to G are not suitable.

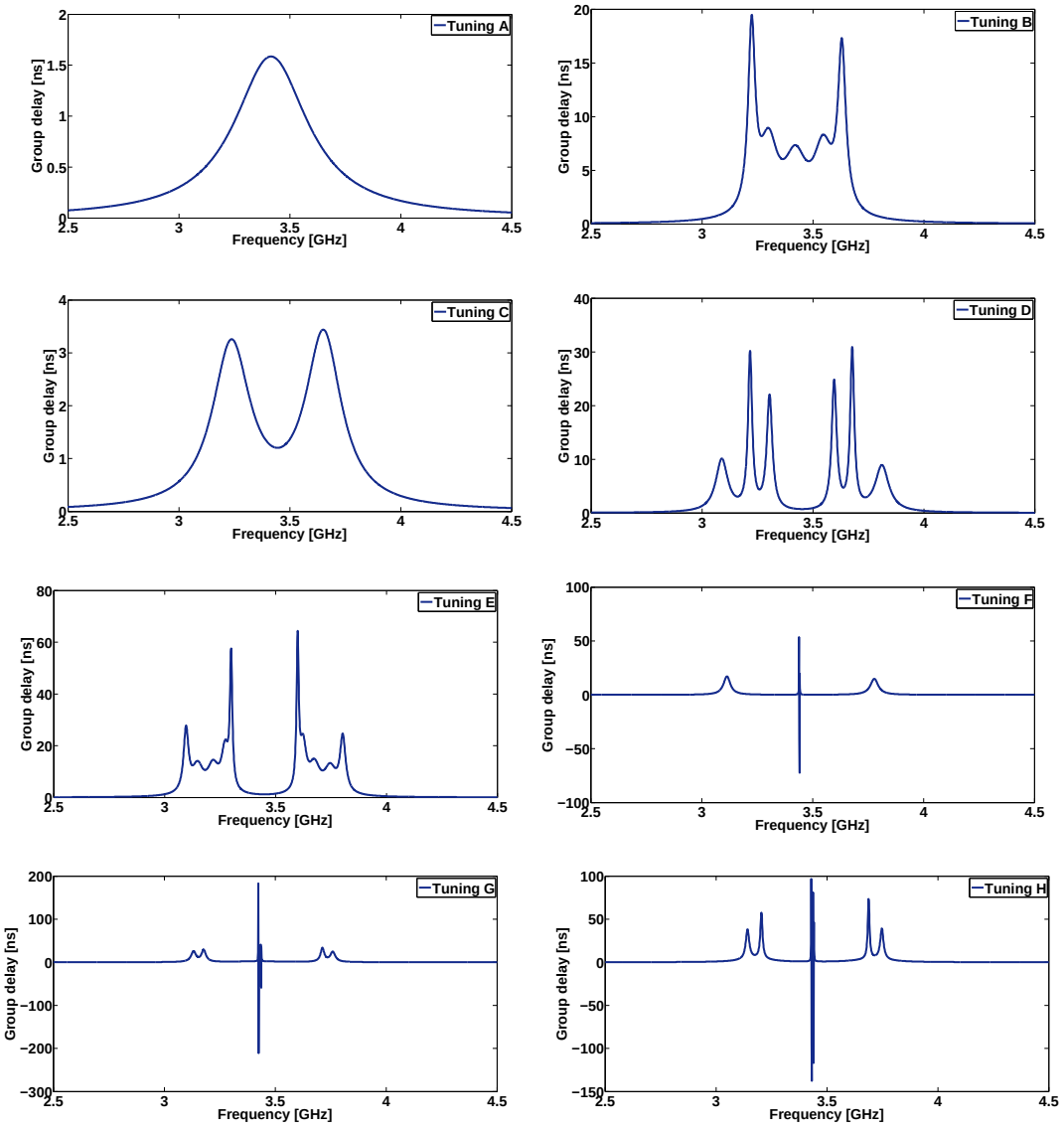

Fig. 3.31 Triple-path dual-band group delay responses corresponding to the tuning sequence A to H in Fig 3.30.

in a low pass prototype transformed to a number of shunt or series elements in a multi-band prototype, depending on the number of the bands required. A network structure for a quasi-elliptic, low-pass prototype is shown in Fig. 3.32. The shunt branches of elements in series are utilized to realize finite, frequency transmission zeros. The quasi-elliptic, low-pass prototype in Fig. 3.32 is transformed to a Foster expansion in Fig 3.33(a) and a Cauer I expansion in (b) Cauer II expansion (see Fig 3.34)(a), and mixed Cauer I and II expansion in (b).

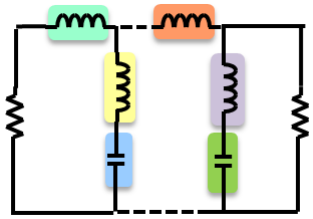

Fig. 3.32 A quasi-lumped, low-pass prototype circuit as the basis for the transform.

3.3.1 Lumped-element circuit values

Lumped-element circuits contain only positive inductor (L) and capacitor (C) elements. These are frequency dependent, reactive elements, and are not limited in terms of bandwidth. The coupled resonators are not valid over wide bands as they contain the frequency invariant reactances that characterize offset in the resonant frequency.

As an example, we set up a theoretical dual and triple-band filters of each of the four expansions (1) Foster, (2) Cauer I, (3) Cauer II and (4) mixed Cauer I and II, to look at the way in which the L's and C's were spread versus the number of bands and bandwidths. The dual-band filter was based on a third order, quasi-lumped element, low-pass filter (see Fig 3.35).

Dual-band filters

The dual-band filter has two pass-bands, extending from 400 to 700 MHz for the first band to 1000 to 1300 MHz for the second band. The bandwidth is uniform at 300 MHz for each band. The spacing between bands is also 300 MHz. The element values for all topologies (see Fig. 3.36) are shown in Table 3.6 for a uniform bandwidth. Inductor $L_{1a} = L_{3a}, L_{1b} = L_{3b}$ and capacitor $C_{1a} = C_{3a}, C_{1b} = C_{3b}$, by symmetry the number of unique elements reduced to six for the capacitors and inductors.

The frequency response for all four topologies are presented in Fig. 3.37.. The four responses are indistinguishable. The values of inductors and capacitor in Table 3.6 are plotted

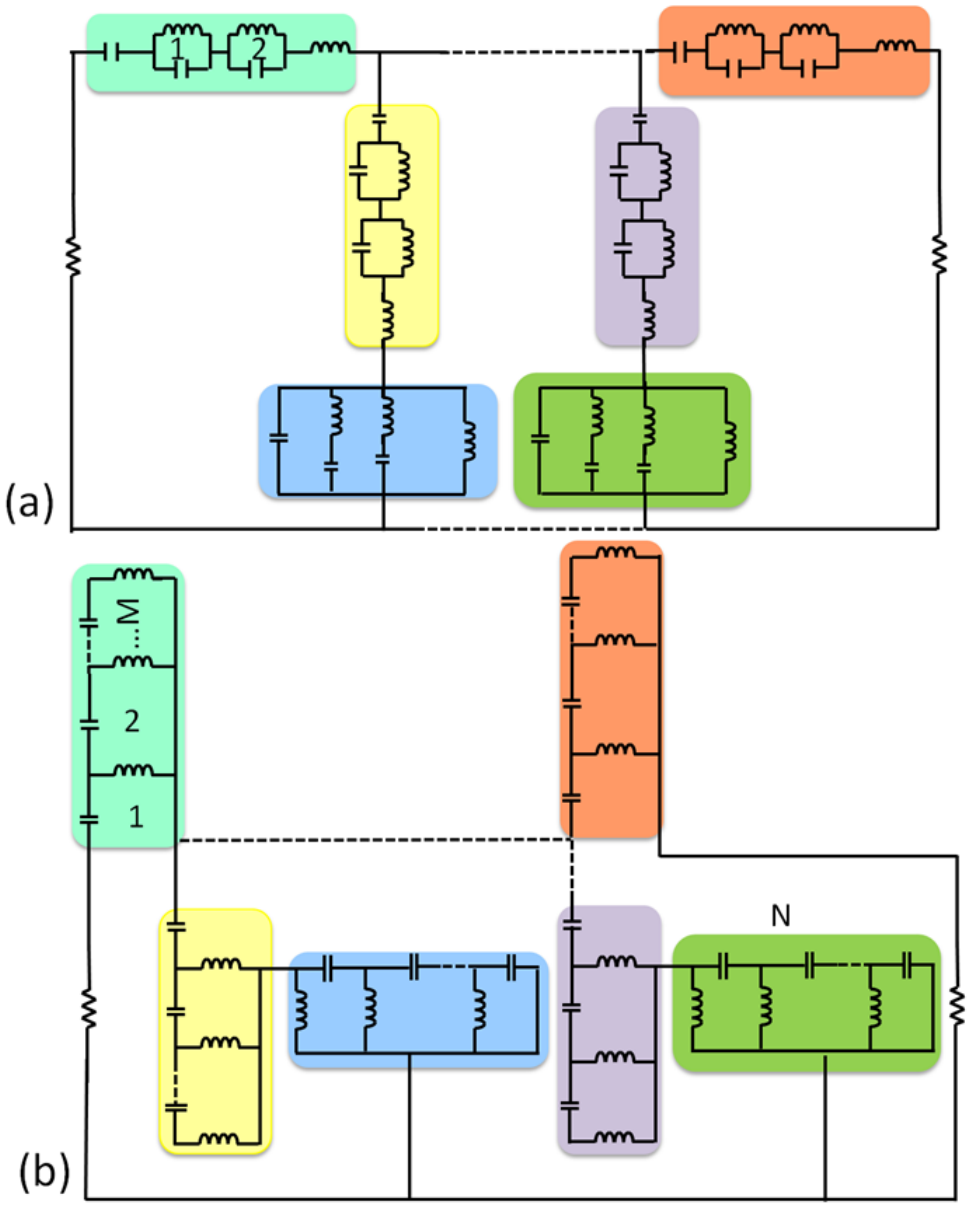

Fig. 3.33 (a) A Foster expansion (b) Cauer I expansion of the multi-band circuit topology based on lowpass prototype in Fig 3.32.

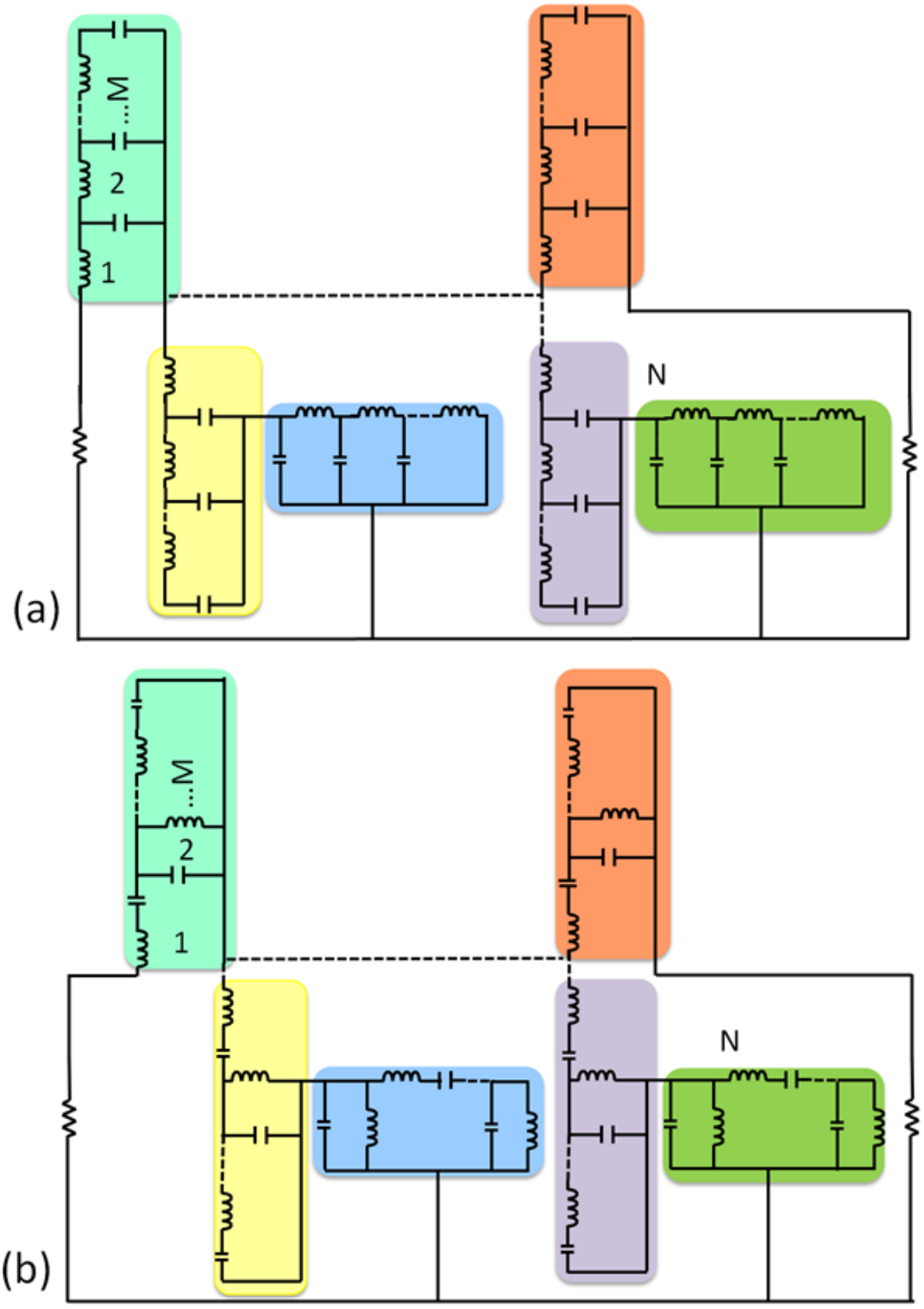

Fig. 3.34 (a) Cauer II expansion (b mixed Cauer I and II expansion of the multi-band circuit topology based on lowpass prototype in Fig 3.32.

Table 3.6 Element values of Foster, Cauer I, Cauer II and mixed Cauer I and II topology of dual-band circuits.

Element values	Foster		Cauer I		Cauer II		mixed Cauer I and II	
	L (nH)	C(pF)	L (nH)	C(pF)	L (nH)	C (pF)	L (nH)	C (pF)
L_{1a} and C_{1a}	3.805	4.377	12.56	2.881	16.36	4.377	12.56	4.377
L_{2a} and C_{2a}	0.4841	34.38	1.598	22.62	2.082	34.38	1.598	34.38
L_{3a} and C_{3a}	3.805	4.377	12.56	2.881	16.36	4.377	12.56	4.377
L_{4a} and C_{4a}	10.23	5.367	6.733	5.374	10.23	7.001	10.23	5.367
L_{1b} and C_{1b}	12.56	8.422	32.57	1.495	54.03	0.4552	3.805	8.422
L_{2b} and C_{2b}	1.598	66.23	4.413	11.75	6.874	3.579	0.4841	66.23
L_{3b} and C_{3b}	12.56	8.422	32.57	1.495	54.03	0.4552	3.085	8.422
L_{4b} and C_{4b}	19.7	1.628	3.496	13.89	1.064	23.10	19.7	1.628

in the chart in Figures 3.38 and 3.39. For the same specifications, the Cauer II topology has the highest inductor value of L_{1b} and L_{3b} = 54.03 nH, and the lowest value is L_{2a} = 2.082 nH. In the Cauer I topology, the highest inductor value is L_{1b} and L_{3b} = 32.57 nH and the lowest L_{2a} = 1.598 nH; in the Foster and mixed Cauer I and II, the highest inductor value is L_{4b} = 19.7 nH and lowest $L_{2a} = L_{2b}$ = 0.4841 nH.

The highest capacitance was observed in the Foster and mixed Cauer I and II topologies, with C_{2b} = 66.23 pF and the lowest values as C_{4b} = 1.628 pF. For the Cauer II the highest capacitor value was C_{2a} = 34.38 pF and the lowest $C_{1b} = C_{3b}$ = 0.4552 pF. For the Cauer I, the highest capacitor value was C_{2a} = 22.62 pF and the lowest $C_{1b} = C_{3b}$ = 1.495 pF.

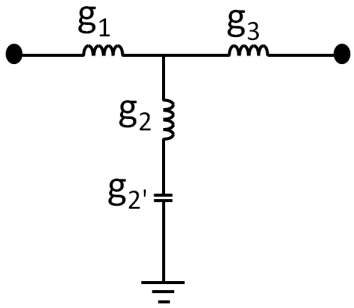

Fig. 3.35 A third order, quasi-lumped, low-pass, prototype circuit as the basis for the transform.

Triple-bands filter

The triple-band filter has three pass-bands, extending from 400-700 MHz. The second pass band is between 1000 - 1300 MHz and the third between 1600-1900 MHz; the bandwidth and spacing between bands are 300 MHz. All expansions have an equal number of elements,

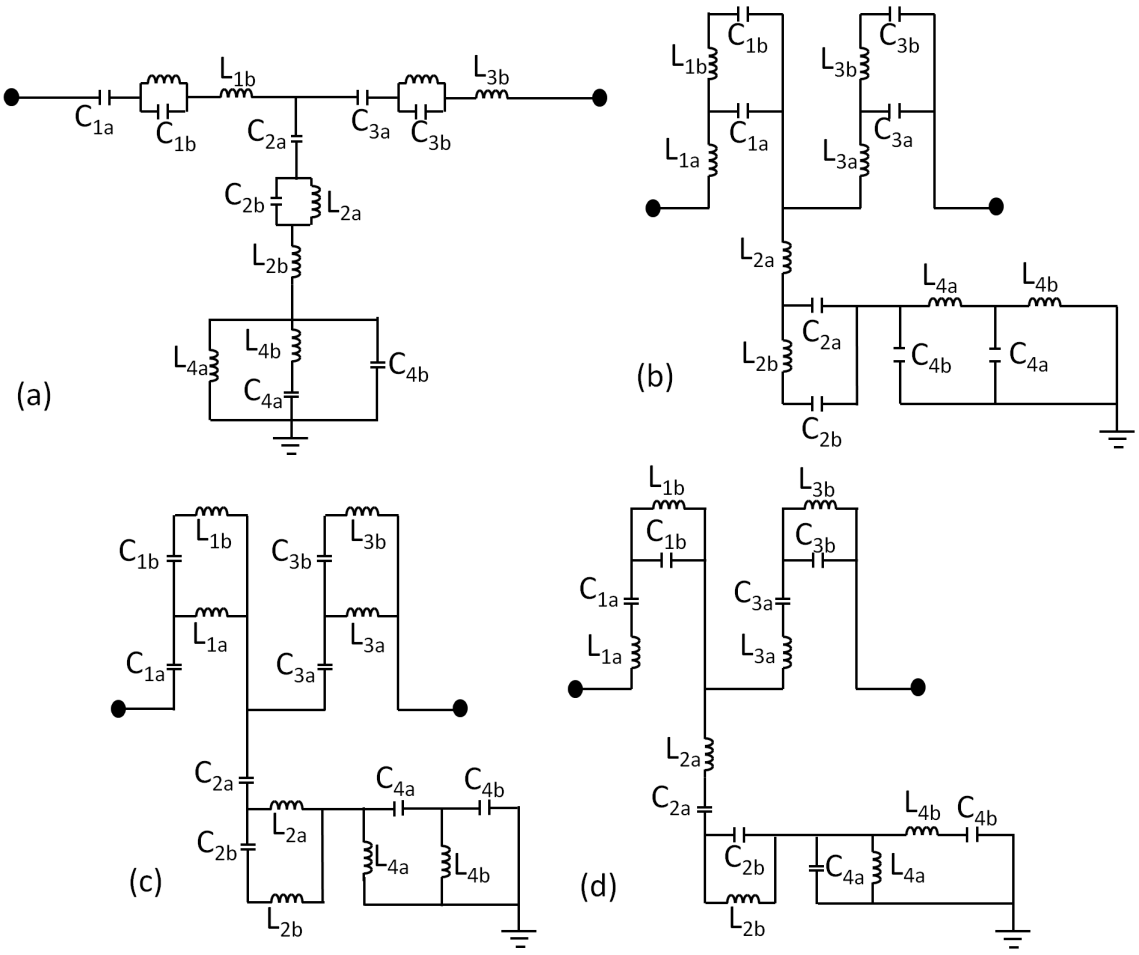

Fig. 3.36 Dual-band, lumped element topologies: (a) Foster; (b) Cauer I; (c) Cauer II; (c) mixed Cauer I and II.

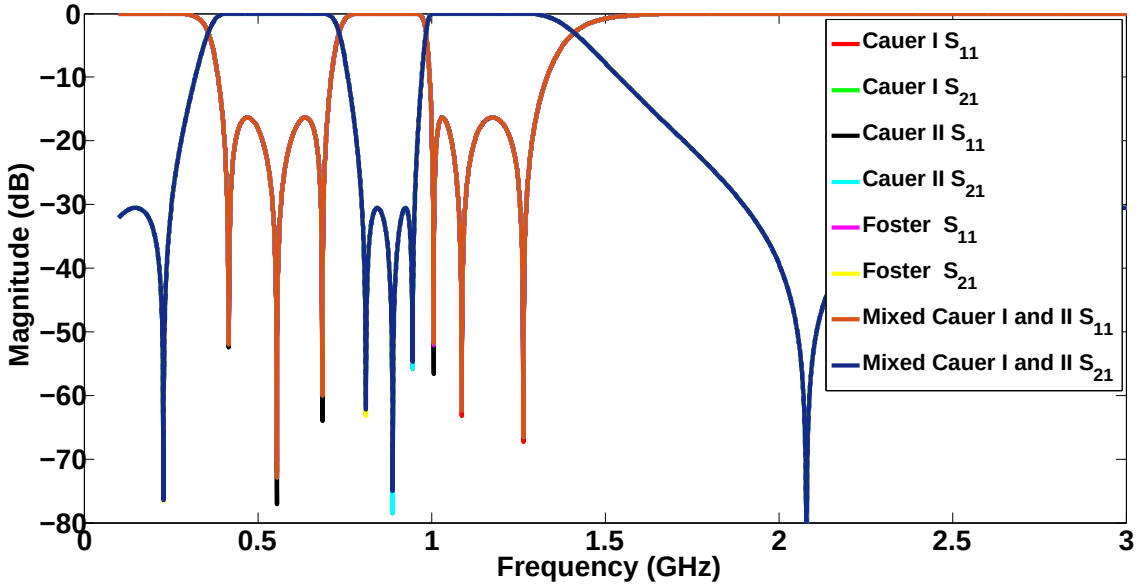

Fig. 3.37 The frequency response for all four topologies. The four are indistinguishable. 3.36.

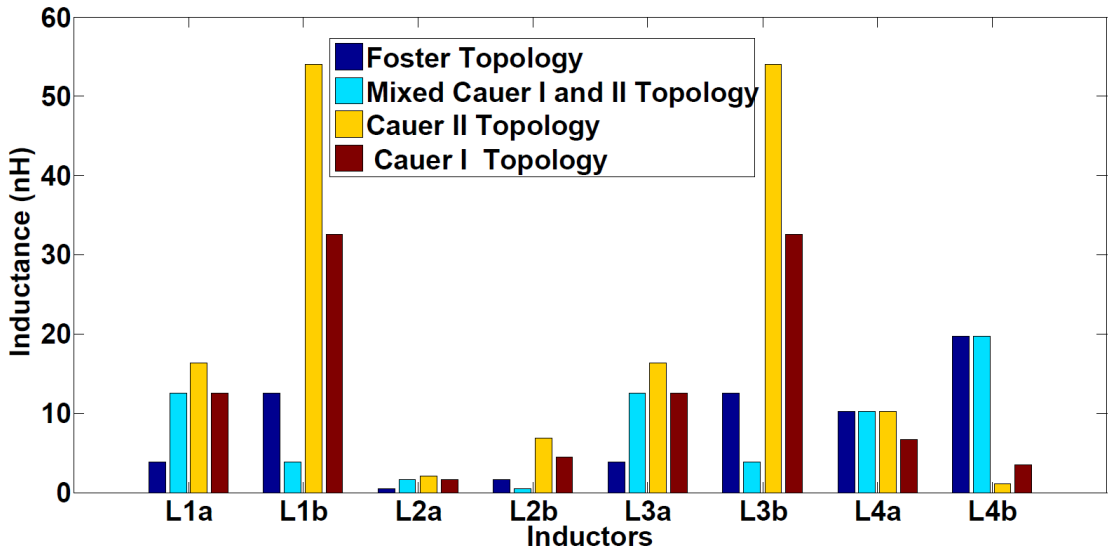

Fig. 3.38 Inductor values of all topologies in the case of a dual-band, uniform bandwidth .

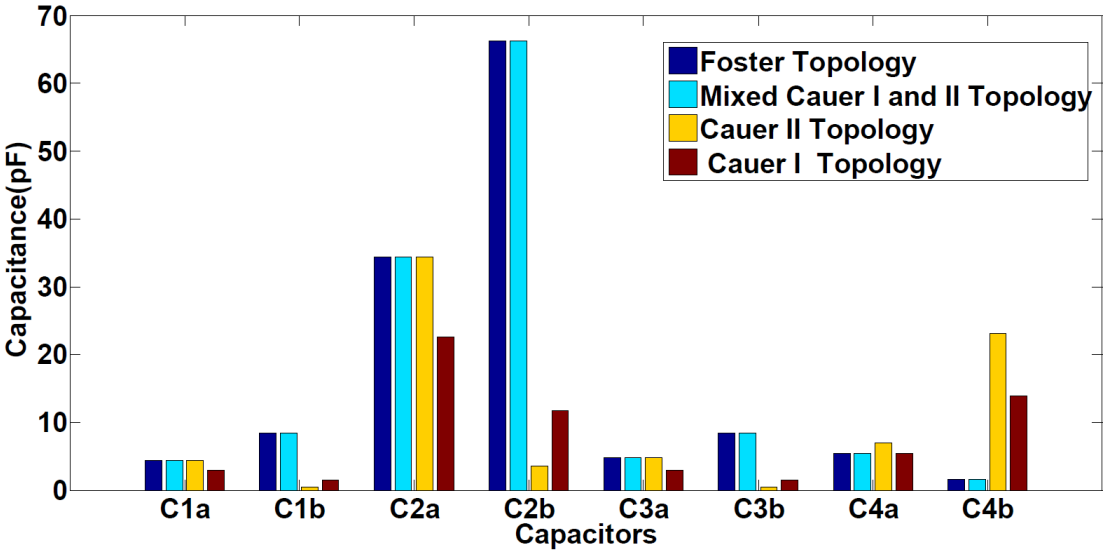

Fig. 3.39 Capacitor values of all topologies in the case of a dual-band, uniform bandwidth.

which means twelve (12) capacitors and twelve (12) inductors in a triple band circuit. The triple band circuits for all topologies are shown in Fig. 3.40. Inductor $L_{1a} = L_{3a}, L_{1b} = L_{3b}, L_{1c} = L_{3c}$ and capacitor $C_{1a} = C_{3a}, C_{1b} = C_{3b}, C_{1c} = C_{3c}$, by symmetry the number of unique elements reduced to nine (9) for capacitors and inductors.

Table 3.7 shows element values of all four topologies. Foster's largest inductor value was 24.73 nH and the smallest 0.1323 nH; for capacitors, the highest value was 83.15 pF and the smallest 1.78 pF. In the Cauer I topology, the largest inductor value was 37.63 nH and the smallest 1.065 nH; for the capacitors, the highest value was 18.29 pF and the smallest 0.8857 pF. In the Cauer II topology, the largest inductor value was 160.6 nH and the smallest 0.1602 nH. For the capacitors, the highest value was 68.71 pF and the smallest 0.0685 pF. The mixed Cauer I and II had the largest inductor value of 15.11 nH and the smallest of 0.6616 nH. For the capacitors, the highest value was 81.03 pF and the smallest 1.031 pF. The frequency response for all four topologies are presented in Fig. 3.42. The four responses are indistinguishable. The values of inductors and capacitors in Table 3.7 are plotted in the chart presented in Fig. 3.43 and Fig. 3.44.

3.3.2 Selection of a multi-band topology for implementation

From the circuit elements of both dual- and triple bands, it was found that the four topologies had different values regarding inductors and capacitors. An inductor is characterized by its inductance value, the unloaded quality factor $Q-$, and its resonant frequency [2]. The knowledge of inductor values helps to determine the inductor model to be employed in the

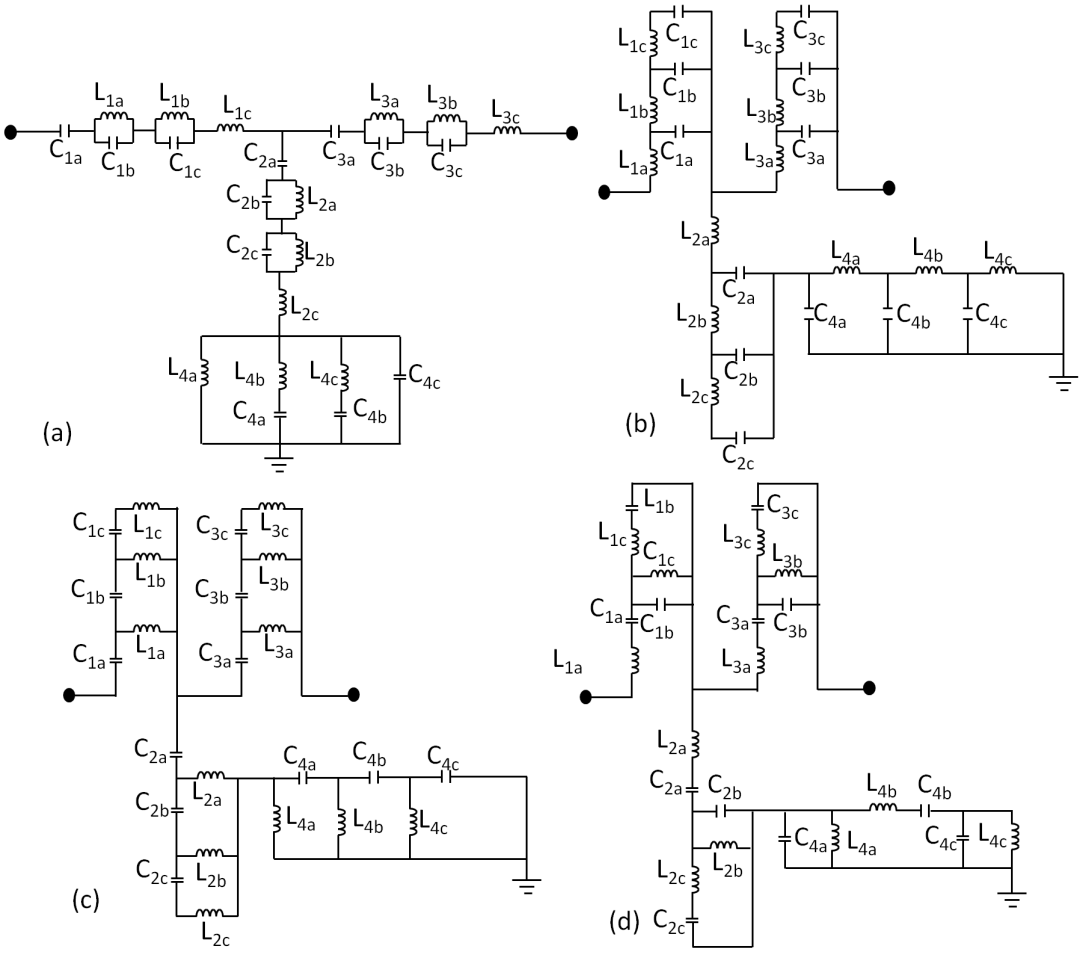

Fig. 3.40 Triple-band, lumped-element topologies: (a) Foster; (b) Cauer I; (c) Cauer II; (c) mixed Cauer I and II.

Table 3.7 Element values of the Foster, Cauer I, Cauer II and mixed Cauer I and II topology of triple-band circuits.

Element values	Foster		Cauer I		Cauer II		mixed Cauer I and II	
	L (nH)	C(pF)	L (nH)	C(pF)	L (nH)	C (pF)	L (nH)	C (pF)
L_{1a} and C_{1a}	1.04	4.708	8.374	2.327	13.58	4.708	8.374	4.708
L_{2a} and C_{2a}	0.1323	37.01	1.065	18.29	1.727	37.01	1.065	37.01
L_{3a} and C_{3a}	1.04	4.708	8.374	2.327	13.58	4.708	8.374	4.708
L_{4a} and C_{4a}	11	3.583	5.439	5.374	11	5.808	11	3.583
L_{1b} and C_{1b}	8.374	10.58	15.12	1.495	25.31	0.8264	5.2	4.6
L_{2b} and C_{2b}	1.065	83.15	1.924	11.76	3.221	6.495	0.6616	36.16
L_{3b} and C_{3b}	8.374	10.58	15.12	25.31	0.8264	0.4552	5.2	4.6
L_{4b} and C_{4b}	24.73	4.45	3.496	6.469	1.931	10.83	10.75	2.225
L_{1c} and C_{1c}	4.16	8.137	37.63	0.8857	160.6	0.06852	15.11	1.031
L_{2c} and C_{2c}	0.5293	63.95	4.788	6.961	20.43	0.5385	1.922	81.03
L_{3c} and C_{3c}	4.16	8.137	37.63	0.8857	160.6	0.06852	15.11	1.031
L_{4c} and C_{4c}	19.02	1.78	2.07	16.1	0.1602	68.71	2.41	6.463

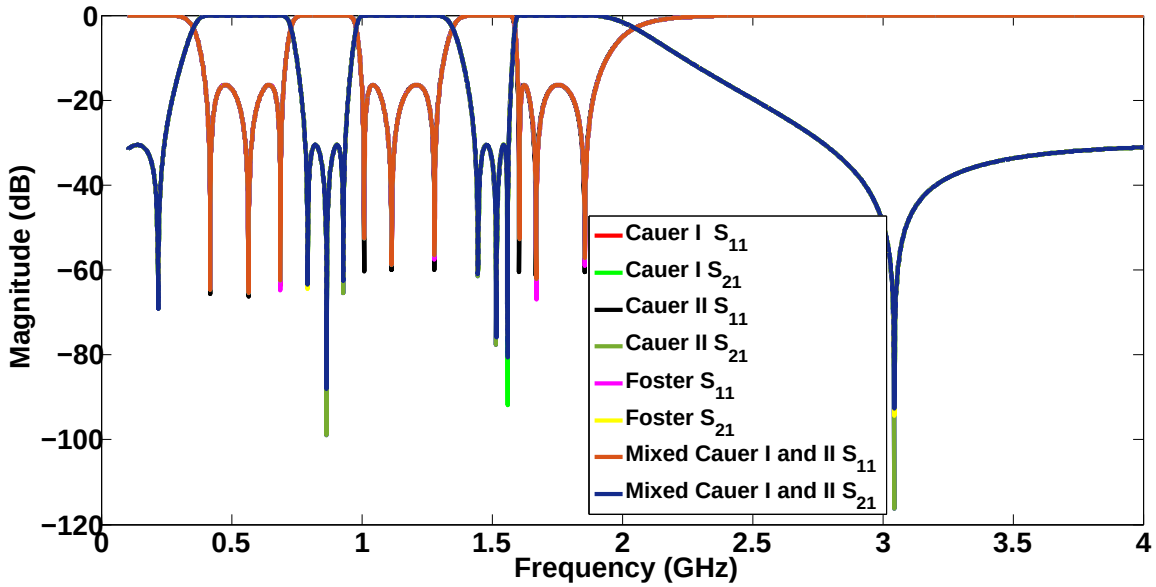

Fig. 3.41 A Foster expansion of the triple band circuit topology.

Fig. 3.42 A Foster response of the equal triple band circuit topology as shown in Fig. 3.40.

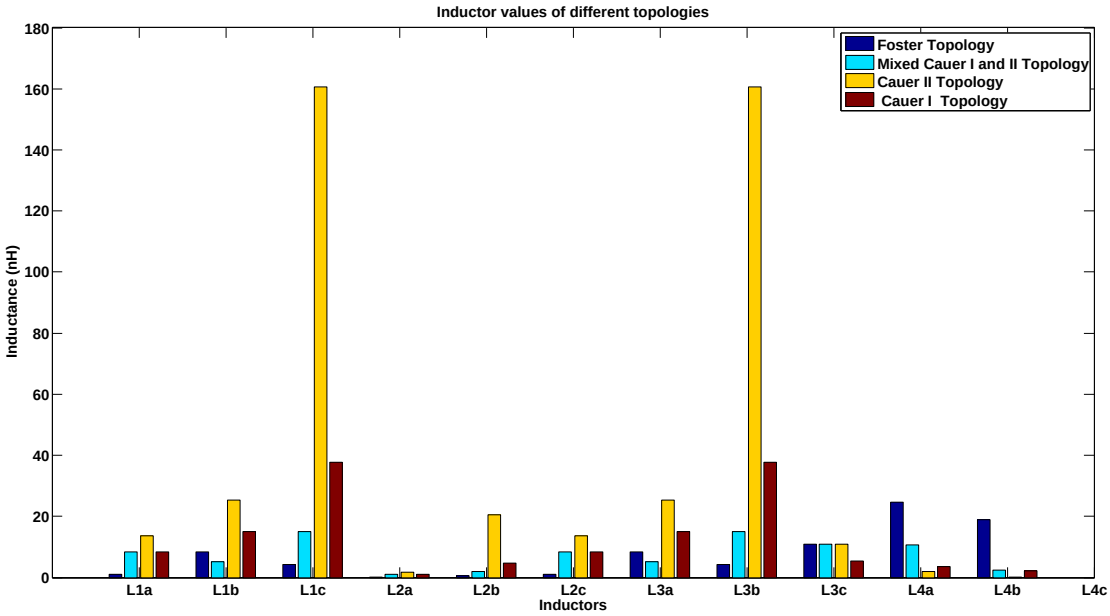

Fig. 3.43 Inductor values of all topologies for a dual-band, uniform bandwidth.

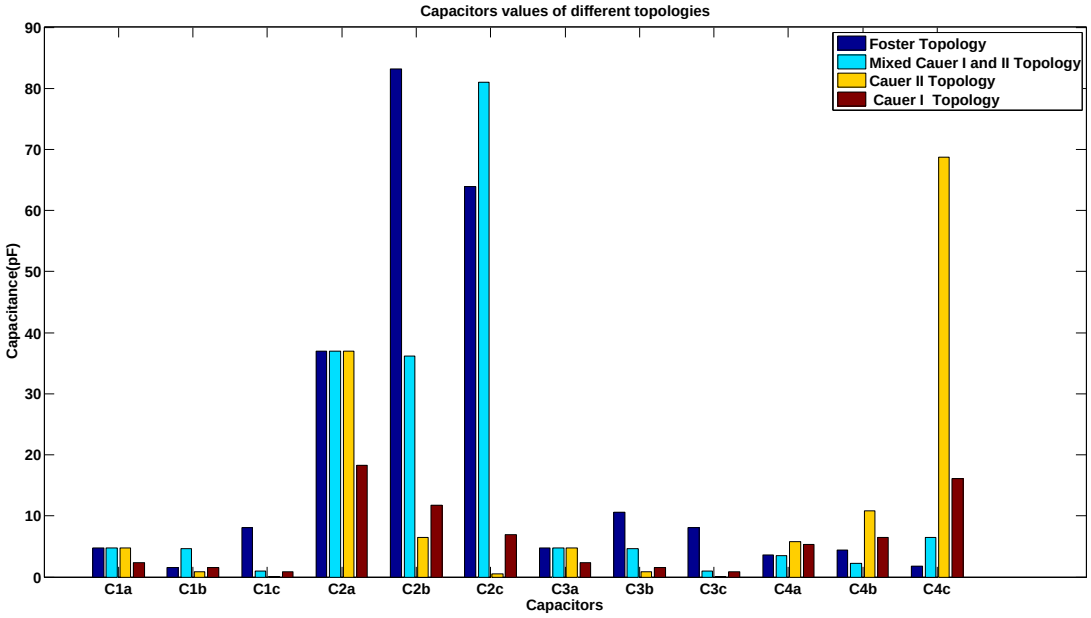

Fig. 3.44 Capacitor values of all topologies for a dual-band, uniform bandwidth

design. Generally, high inductance values are implemented with spiral models while low inductances are implemented with meandered lines. High inductance has a low quality factor and low inductance a high quality factor.

For a dual-band filter, Fig 3.38 and Fig 3.39 show that Cauer I and Cauer II expansions are likely to utilize large inductors to provide high inductance while the mixed Cauer and Foster expansion inductors have lower inductances. Another point to note is that, on the dual-band filter, the circuit values of the Foster and mixed Cauer expansions are similar. This means that the circuits are the same, with the only difference in the sequential arrangement of the elements.

For a triple-band filter, it is observed from the chart shown in Fig. 3.43 and Fig 3.44, that the Cauer II expansion has the highest inductor values, followed by Cauer I. The Foster expansion and mixed Cauer have lower inductances. From this observation, it is clear that the Foster and mixed Cauer expansions can be selected for the design, due to their lower inductances; they are also likely to have a high $Q-$ factor. Inductors are more influential on the filter response than capacitors, due to their dominant parasitic.

3.4 Narrow-band and wide-band transform comparisons

The narrow-band, coupled resonators and wide-band, lumped-element topology (Foster expansions) were compared to observe the frequency response. The comparison was between dual-band, all-pole filters with the following specifications: pass-band 1 extending from 3.100 GHz to 3.200 GHz, and pass-band 2 from 3.330 to 3.430 centered at 3.260 GHz with 20 dB ripple levels and a fractional bandwidth (FBW) of 0.1012. The filters had an equal bandwidth of 100 MHz and spacing between bands of 130 MHz. The compared frequency response is presented in Fig. 3.45 .

For quad-band responses, narrow-band coupled resonators and wide-band lumped elements (Foster expansion) were compared with pass-band 1, extending from 3.000 GHz to 3.050 GHz, pass-band 2, from 3.100 GHz to 3.150 GHz, pass-band 3 from 3.200 GHz to 3.250 GHz and pass-band 4 extended from 3.300 GHz to 3.350 GHz, the filter was centered at 3.170 GHz and the FBW was 0.1104. The filter had an equal bandwidth of 50 MHz and equal spacing between bands of 50 MHz. The compared frequency response is presented in Fig. 3.46. The results of the functions mapped from equation 2.13 and 2.16 agreed and the difference was indistinguishable.

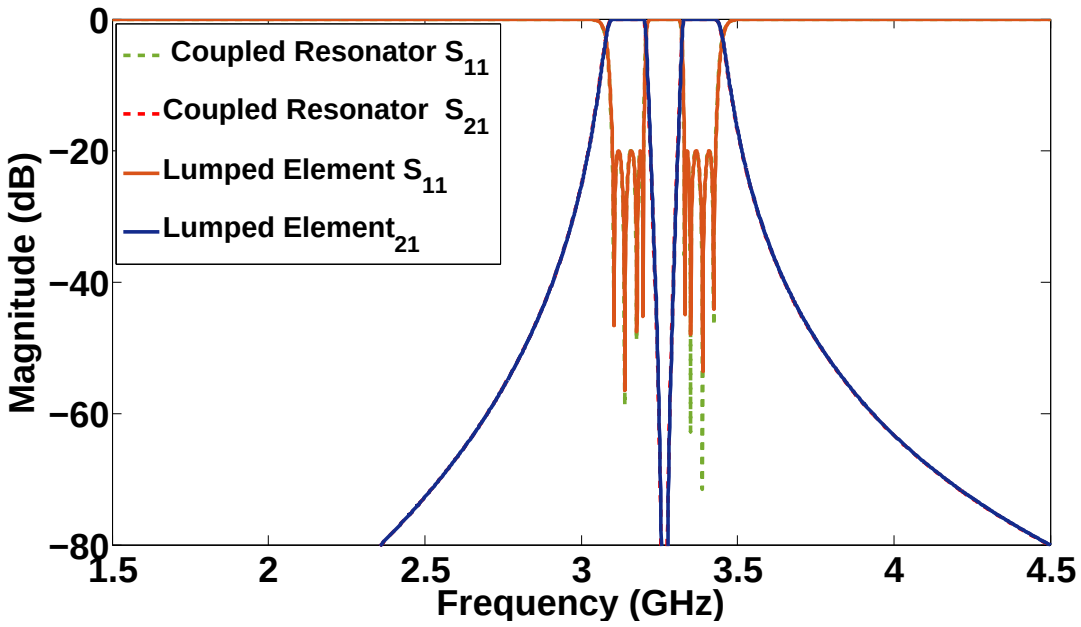

Fig. 3.45 Comparison of a coupled resonator and lumped-element, dual-band frequency.

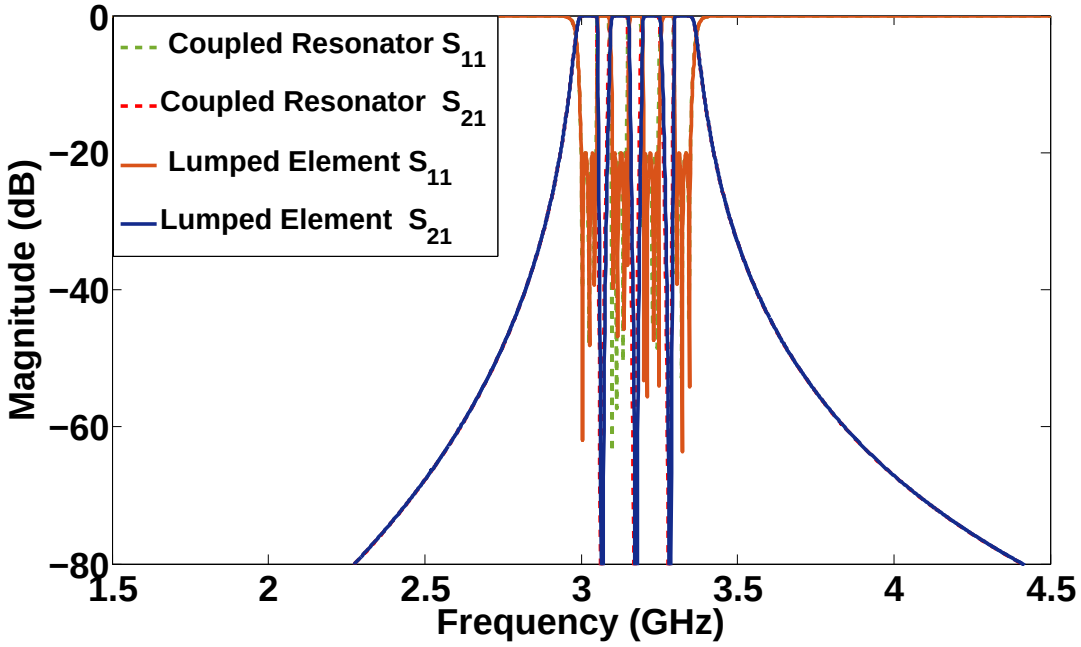

Fig. 3.46 Comparison of a coupled resonator and lumped-element, quad-band frequency.

3.5 Summary

The chapter described a method that translates a single band, basis filter into a multi-band filter with N bands. It can be seen as a transformation from single-band directly to multi-band without any intermediate steps. The resulting coupling topology has the format of appended resonators attached to a single-band basis filter. It is generalized and can be employed for any number of bands; furthermore, it requires no optimization. For narrow-band responses this is implemented by employing coupled resonators, and for wide-band, lumped-elements implementation are utilized.

Lumped elements were implemented with four topologies and the illustration of the selection of topology was presented. Topologies with high inductance are likely to have a lower Q than those with low inductance. As an aspect of selectivity, resonator losses and group-delay methods for multi-band, coupled resonators were detailed. A comparison between the general functions of wide-band and narrow-band mapping functions was given to illustrate agreement between the two mapping functions.

Chapter 4

Implementation of narrow-band multi-band filters on multi-layer substrates

4.1 Introduction

Filters provide frequency selectivity for communication systems. Some application requires narrow bandwidth frequency selection while achieving low in band insertion loss, high out off band attenuation without spurious and harmonics frequencies. A challenging requirement for modern communication system is size; compact sized RF chain devices are desirable. Printed circuit board (PCB) technology is chosen for easy integration with other RF chain devices.

There are various materials suitable for microwave applications, such as glass, ceramics and polymers. Usually, selecting a material depends on the application, since different materials have different permittivity. Permittivity is related to the filter's important parameters, for example, couplings, center frequency and electrical wavelength. For many decades, filters were designed on a single layer. The manufacturing process is simpler, cost is moderate and the performance of the filter is rated high, especially for narrow band applications. The drawback is their large physical dimensions, because the resonators are arranged horizontally, both in a parallel or series configuration, and they are inflexible in design. The solution is to utilize thin substrates that enable three dimensional designs where resonators are placed in different layers rather than in one layer. The resonators are arranged stacked up vertically, as shown in Fig. 4.1. The stacked arrangement miniaturizes the filter and provides a coupling mechanism crucial for frequency selectivity. The popular technologies enabling a multi-layer

design that are commercially available are Low Temperature Co-Fired Ceramic (LTCC) and Liquid Crystal Polymer (LCP). The reports in [39, 54] highlight general information on LCP materials, the manufacturing process, electrical properties and the benefits of LCP substrates. For high frequency applications, LCP substrates have a long list of advantages, ranging from their physical dimensions to electrical characteristics. The LCP substrate is very thin; this results in a lightweight as far as the volume and mass of the filter are concerned. In addition, it has high electric strength and low dissipation. On the other hand, LTCC has similar multi-layer properties but with tape-shrinkage disadvantages that happen during the firing processing [26]; however, shrinkage problems can be controlled. Roger's technologies have some multi-layer substrates, such as RT Duroid 5880 High-Frequency Laminates. LTCC, LCP and Rogers substrates are commonly utilized, and have been widely investigated; however, there is little design knowledge regarding their utilization on the Mercurywave substrate. All the filters in this thesis were designed on the Mercurywave™ 9350 substrate of the Park Electrochemical Corp. Mercurywave is a non-Polytetrafluoroethylene (PTFE) high frequency, low loss, electrical property and has high thermal reliability; Mercurywave™ 9350 offers greater flexibility and freedom to design high performance RF and Microwave circuits.

This chapter presents an analysis and implementation of the multi-band narrow band coupled resonator microstrip filters. The chapter is organized as follows: Section 4.2 discusses multi-path and single path filters coupling matrix and coupling topologies. Two multi-path filters (dual-path dual band and triple-path dual band filters) are designed. For a single path an all pole quad-band filter is designed. Section 4.3 discusses coupling parameters required for the physical implementation of the filter and gives examples of input/output and inter-resonator couplings structure in multi-layer. Section 4.4 presents port and numerical tuning. Port tuning is employed for a quick resonator length tuning. Section 4.5 is an implementation of all three filters. Section 4.6 presents fabrications and measured results. The chapter is summarized in section 4.7.

This chapter presents an analysis and implementation of the multi-band narrow-band coupled-resonator microstrip filters. The chapter is organized as follows: Section 4.2 discusses multi-path and single path filters, coupling matrices and coupling topologies. Two multi-path filters (dual-path, dual-band and triple-path, dual-band filters) were designed. For a single path, an all-pole, quad-band filter was designed. Section 4.3 discusses the coupling parameters required for the physical implementation of the filter, and gives examples of input/output and inter-resonator coupling structures in multi-layer arrangement. Section 4.4 presents port and numerical tuning. Port tuning was employed for a quick resonator length

tuning. Section4.5 comprises the implementation of all three filters. Section 4.6 presents the construction and measured results. The content of the chapter is summarized in Section 4.7.

4.2 Multi-and single-path filters

Multi-path coupling filters were introduced in [64] where the coupling matrix of several topologies were synthesized based on optimization. Many other topologies were analyzed and implemented in planar microstrip circuits in [11, 12, 62]. Multi-path topologies are known as [9] transversal topologies in which resonators are connected in multi-parallel paths between source and load. A multi-path coupling scheme has several advantages over single path coupled resonators which includes [64]

- The filter contains multi-paths (N-paths) for the signal between the source and the load; hence, the source and load are coupled to more than one resonator. The paths start from the source and terminate at the load. One attractive feature of parallel, multi-path resonators is that they can be employed to design dual mode filters without utilizing intra-cavity couplings.
- During the design process, resonators in an individual path can be designed and tuned separately and then interconnected back to complete the filter at the interface port.
- Uwe further explains and demonstrates a zero shifting property. Parallel, multi-path filters exhibit transformation properties, for example, transmission zeros are controlled and shifted from one side of the pass-band to the other by altering the resonant frequencies of the resonators without changing the coupling coefficients.

For single-path couplings, all-poles is the most common filter topology with all its attenuation poles located in infinity frequencies. There are no finite transmission zeros, and attenuation increases monotonically beyond the pass-bands. Critical frequencies for these types of filters were selected via the Chebyshev polynomials [10], to ensure the maximum number of equi-ripple peaks in the pass-band. For this reason, such filters are commonly known as Chebyshev Filters. The advantage of an all-poles topology is that the filter contains a single-path and all its sequential resonators are directly coupled to one another. No cross coupling appear in this topology; hence, the design and construction are less complicated when compared to multi-path circuits. The directly coupled filters were studied in [20], where resonators were directly coupled by either capacitive, inductively or mutual inductive coupling. This coupling arrangement has been upgraded to include inverters.

The goal of this chapter is to present the micro-strip, planar implementation of two, transversal topologies and all-pole topologies. The transversal topologies were implemented as dual-path (Filter A) and triple-path (Filter B) coupling schemes. For the all-poles topology, two filters were implemented, a right angle bends (Filter C) and a chamfered design (Filter D).

4.2.1 Multi-path topologies

Transversal topologies were implemented as a wave-guide, micro-strip hybrid [45], integrated wave-guide [67], and many others were analyzed and implemented in planar micro-strip circuits [55, 11, 12, 62]. Two, multi-path, coupled resonators with dual-band response were implemented as micro-strip planar circuits; their coupling schemes of a dual-path (Filter A) and a triple-path (Filter B) are presented in Fig. 4.2. A dual-path has a fourth order single-band basis filter(as shown in Fig 4.2) (a) transformed to a dual-band filter in (b), and triple-path has a sixth order single-band basis filter and in (c) transformed to a triple-path dual-band in (d).

The design process began with a computation of the coupling matrix of single-band basis filters for Filter A and B to synthesize the frequency response. The procedures presented in [9] were employed to compute the transversal matrix $(N+2)\times(N+2)$. Similarity transformation was applied to reconfigure the matrix from $(N+2)\times(N+2)$ to attain a coupling matrix of the coupling scheme as shown in Fig 4.2 (a) and (c). The coupling matrix of (Filter A) fourth order single band basis and (Filter B) sixth order single band basis filter were computed as $M_{FilterA}$ and $M_{FilterB}$ respectively. Schematic circuits in Fig 4.3 (a) and (b) represent the coupling scheme in Fig 4.2 (a) and (b) (Filter A). Schematic circuits in Fig 4.4 (a) and (b) represent the coupling scheme in Fig 4.2 (c) and (d)(Filter B). The frequency responses are shown in Fig 4.5 (Filter A) and Fig. 4.6 (Filter B) respectively.

$$M_{FilterA} = \begin{pmatrix} 0 & 0.5355 & -0.8744 & 0 & 0 & 0 \\ 0.5355 & 0 & 0 & 0 & 1.2939 & 0 \\ -0.8744 & 0 & 0 & 0.6789 & 0 & 0 \\ 0 & 0 & 0.6789 & 0 & 0 & 0.8744 \\ 0 & 1.239 & 0 & 0 & 0 & 0.5355 \\ 0 & 0 & 0 & 0.8744 & 0.5355 & 0 \end{pmatrix}$$

$$M_{FilterB} = \begin{pmatrix} 0 & -0.4304 & 0.6199 & -0.6548 & 0 & 0 & 0 & 0 \\ -0.4304 & 0 & 0 & 0 & 0 & 0 & 1.1850 & 0 \\ 0.6199 & 0 & 0 & 0 & 0 & 0.9927 & 0 & 0 \\ -0.6548 & 0 & 0 & 0 & 0.3777 & 0 & 0 & 0 \\ 0 & 0 & 0 & 0.3777 & 0 & 0 & 0 & 0.6548 \\ 0 & 0 & 0.9927 & 0 & 0 & 0 & 0 & 0.6199 \\ 0 & 1.1850 & 0 & 0 & 0 & 0 & 0 & 0.4304 \\ 0 & 0 & 0 & 0 & 0.6548 & 0.6199 & 0.4304 & 0 \end{pmatrix}$$

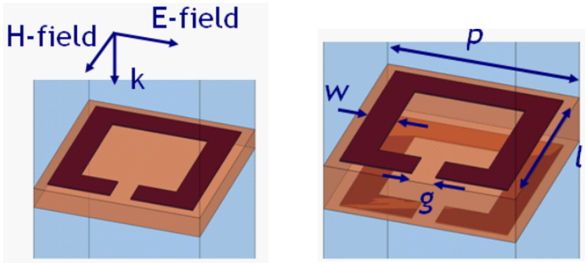

Fig. 4.1 The configuration of split ring resonators in single (a) and stacked (b) layers [13]

4.2.2 Single-path all pole topology

An all pole, single-band, fourth order basis filter and quad-band filter topologies are shown in Fig 4.7(a) and (b). These are represented by schematic circuits in Fig 4.8 (a) and (b) respectively. Frequency responses are shown in Fig 4.9.

4.3 Coupled resonators on multi-layer substrates

This section details the way in which a multi-layer, printed circuit board (PCB) was utilized for an advantage over a single layer in terms of input/output couplings, and inter-resonator couplings extended to the filter designed, based on the reactance transform method. The structures were printed, open loop $\lambda/2$ resonators. Couplings were realized with broad side couplings for the basis filter. The dual band characteristics were realized in a nested coupling. Nested couplings allow all-sides couplings between appended and basis resonators.

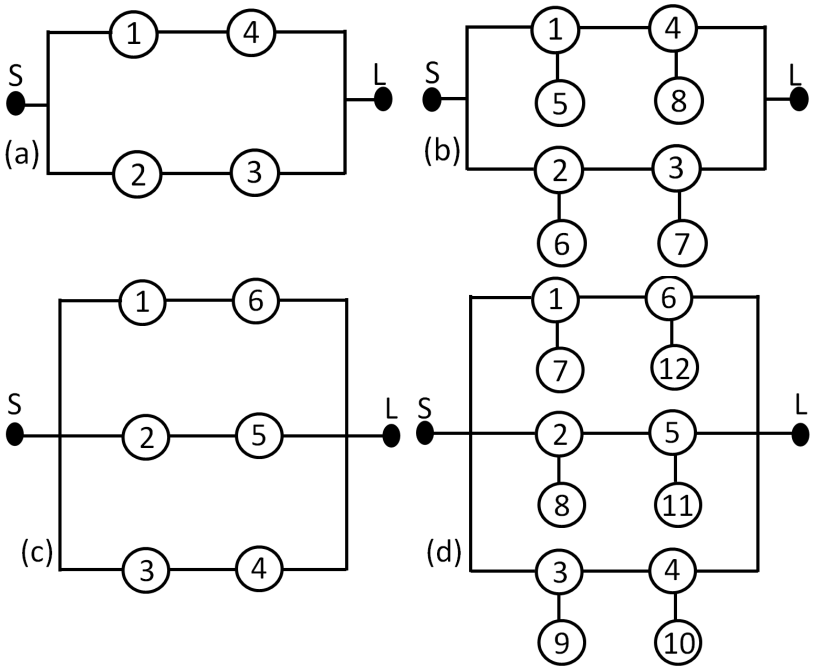

Fig. 4.2 Filter A (a) dual-path single-band basis fourth order filter transformed to (b) dual-band dual-path filter. Filter B (c) triple-path single-band basis sixth order filter transformed to (d) dual-band triple-path filter.

4.3.1 Input/output couplings

The microstrip designs were simulated with Sonnet software, implemented on Mercurywave, a multi-layer substrate. Resonators coupled strongly on vertically stacked up arrangements. The input/output coupling for a multi-layer, microstrip, open loop resonator employed a coupled line structure [35]. The coupling was from the overlap between the dashed lines and the resonator, as shown in Fig. 4.10 (a); a 3-D view is shown in (b). The full overlap between the lines resulted in a strong input/output coupling. The width of the line was equal to the width of the resonator. The coupling line structure was on the top layer while the resonator was on the next layer. The simulated resonant frequency response between the input/output and resonator, shown in Fig 4.10(b) which was weakly coupled between two ports is shown in Fig 4.11. The value of S_{21} had a magnitude given by [35].

$$|S_{21}| = \frac{1}{\sqrt{1+(Q_e\Delta\omega/\omega_0)^2}} \tag{4.1}$$

The external quality factor Q_e which is an immitance inverter coupling between source/load and the resonator is calculated as

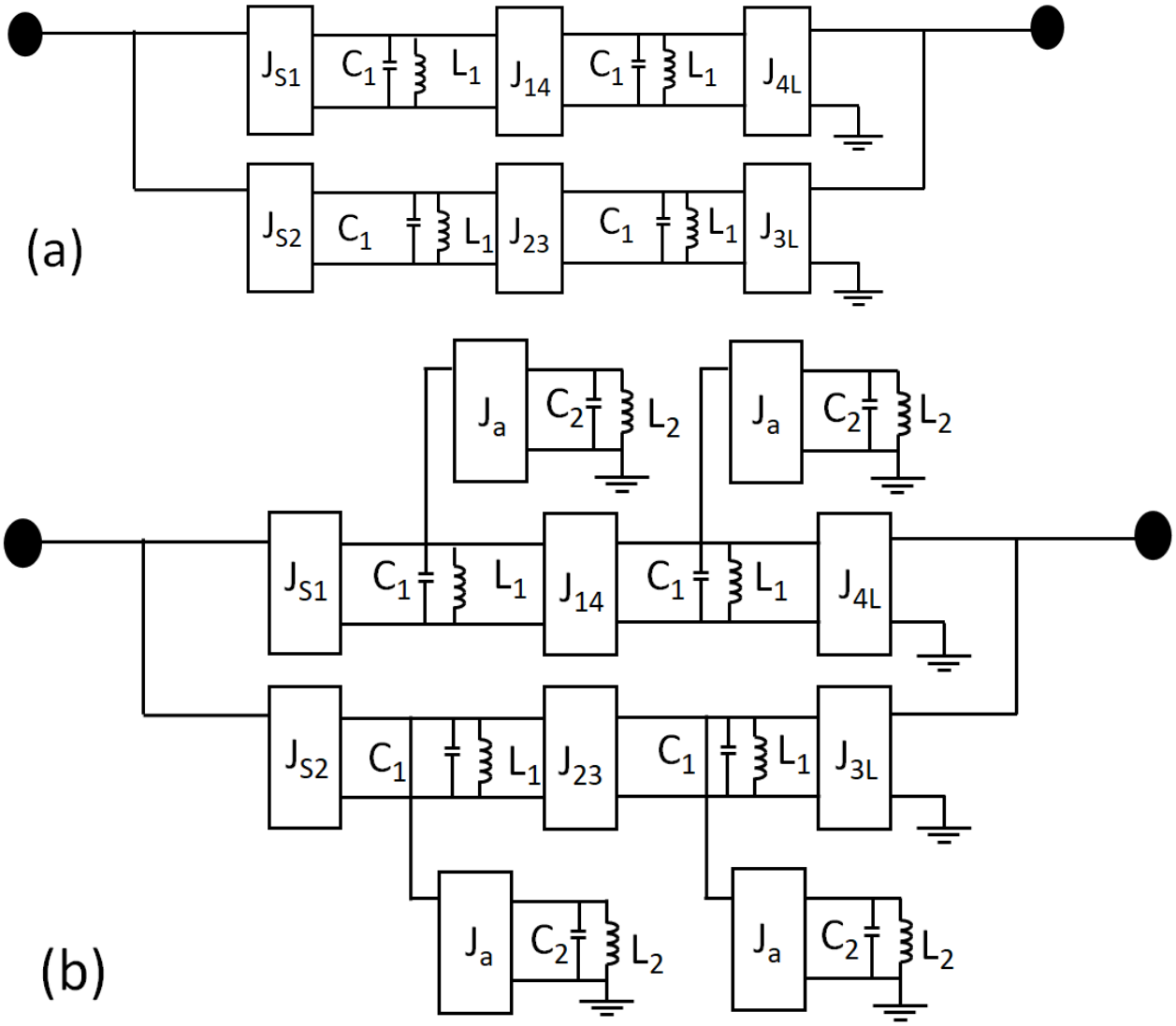

Fig. 4.3 (a) Schematic circuit of a dual-path single-band basis filter representing coupling scheme of Fig 4.2(a) and (b) dual-path dual-band filter representing coupling scheme of Fig 4.2(b) (Filter A).

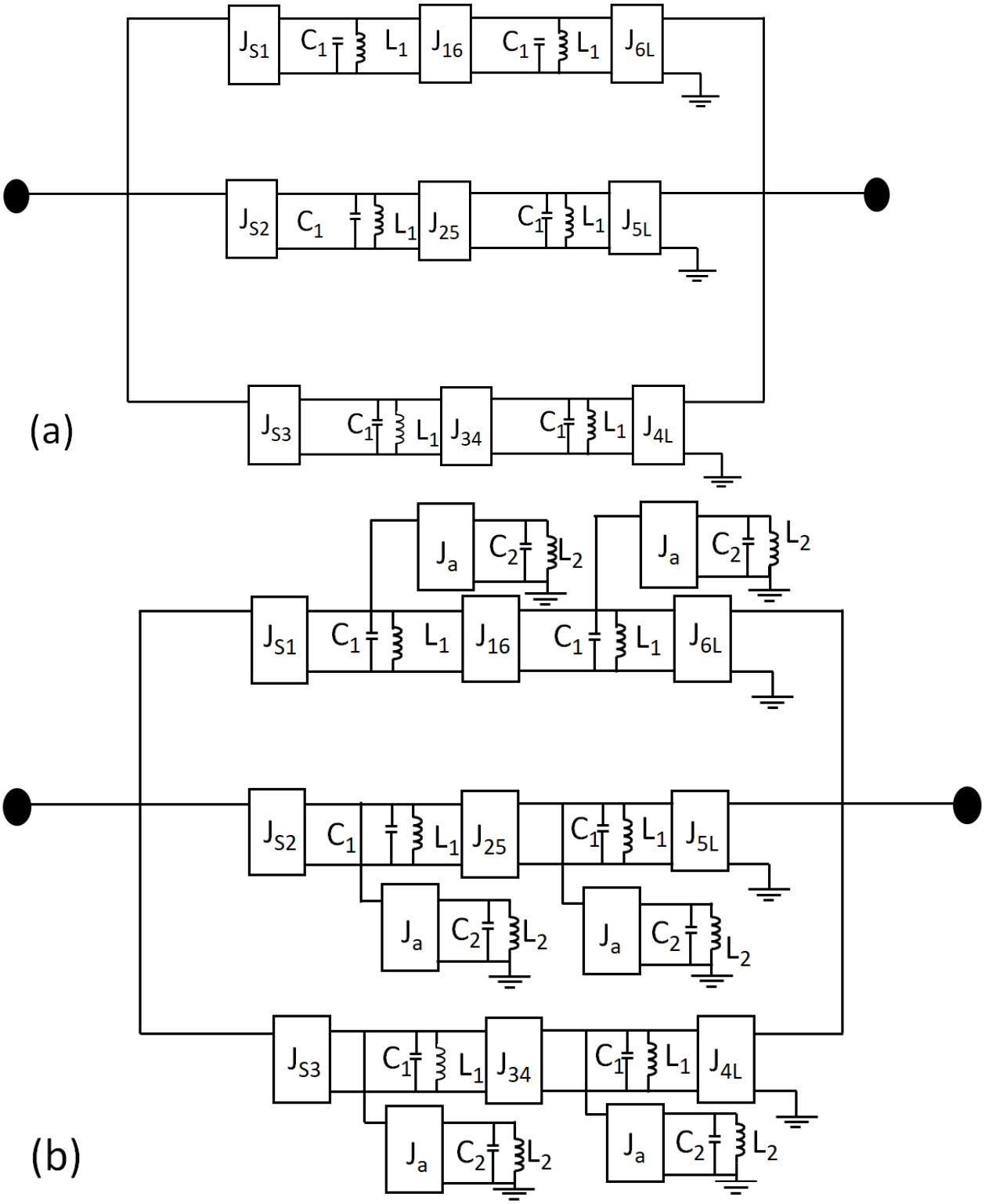

Fig. 4.4 (a) Schematic circuit of a triple-path single-band basis filter representing the coupling scheme of Fig 4.2(c) and (b) a triple-path dual-band filter representing the coupling scheme of Fig 4.2(d) (Filter B).

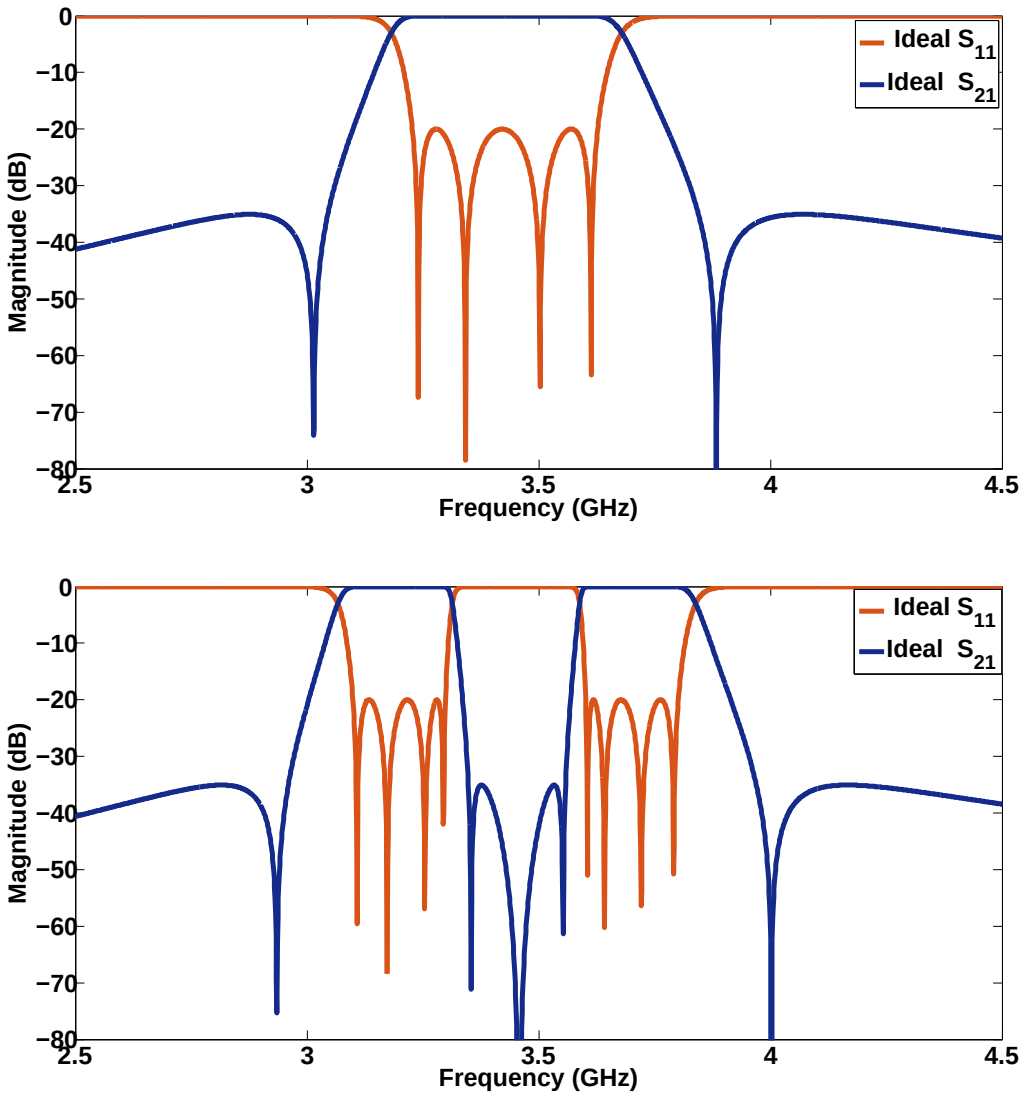

Fig. 4.5 Frequency response of a 4th order dual-path single-band basis filter of the schematic circuit in Fig4.3(a) and a dual-path dual-band filter in Fig4.3(b) (Filter A).

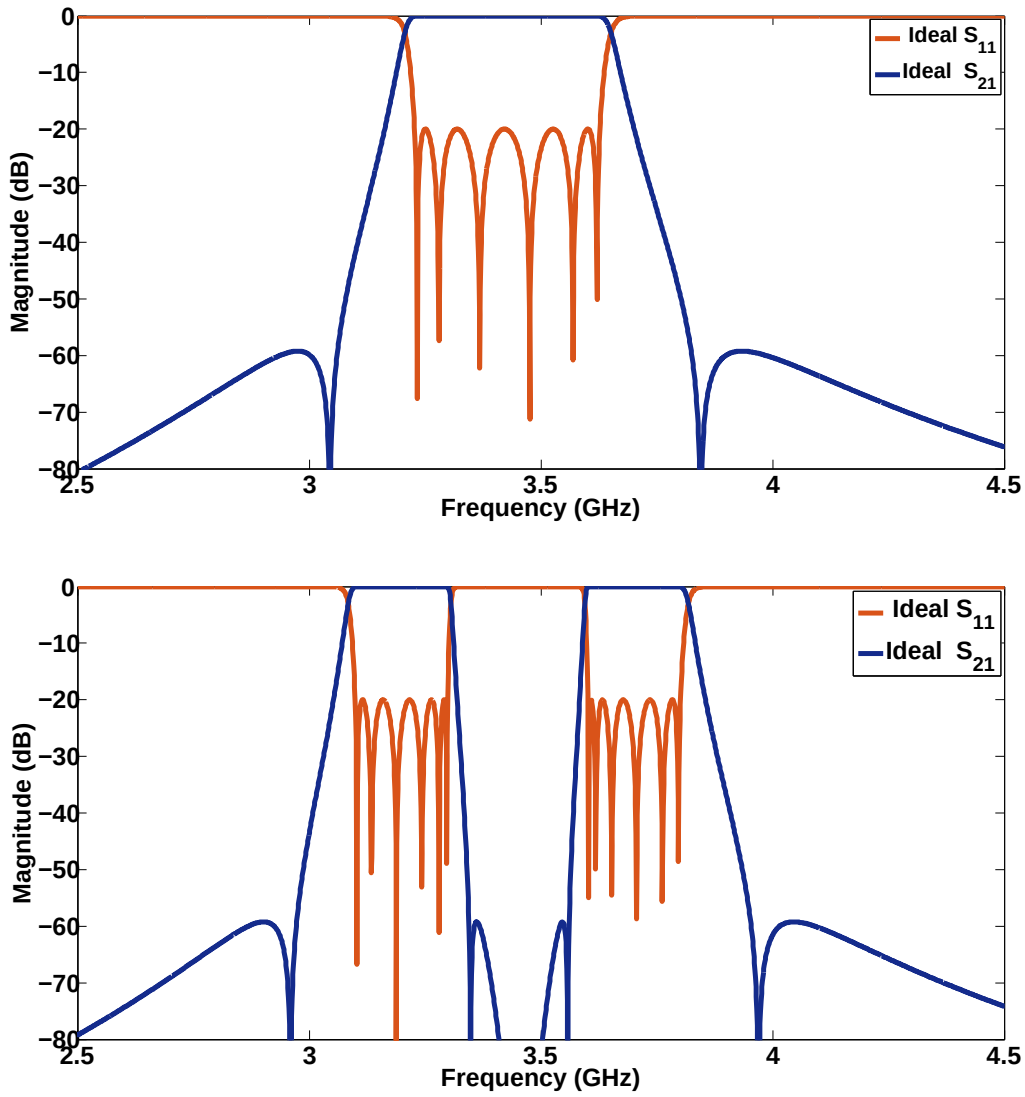

Fig. 4.6 Frequency response of a 4th order triple-path single-band basis filter of the schematic circuit in Fig4.4(a) and dual-path dual-band filter in Fig4.4(b) (Filter B).

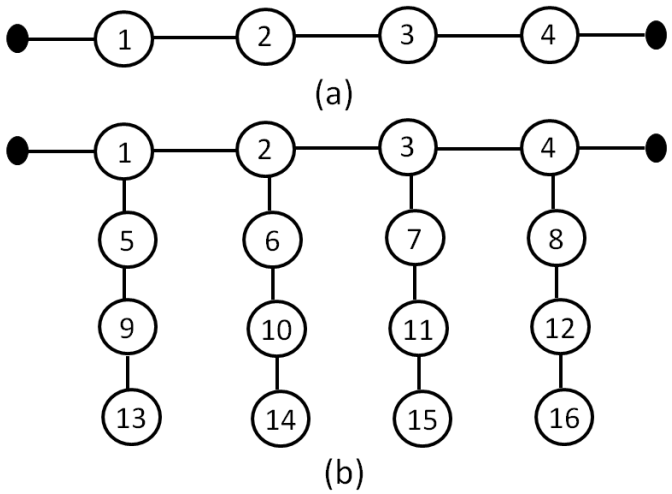

Fig. 4.7 (a) Single-band basis, 4th order, all pole topology and (b) quad-band, all pole topology.

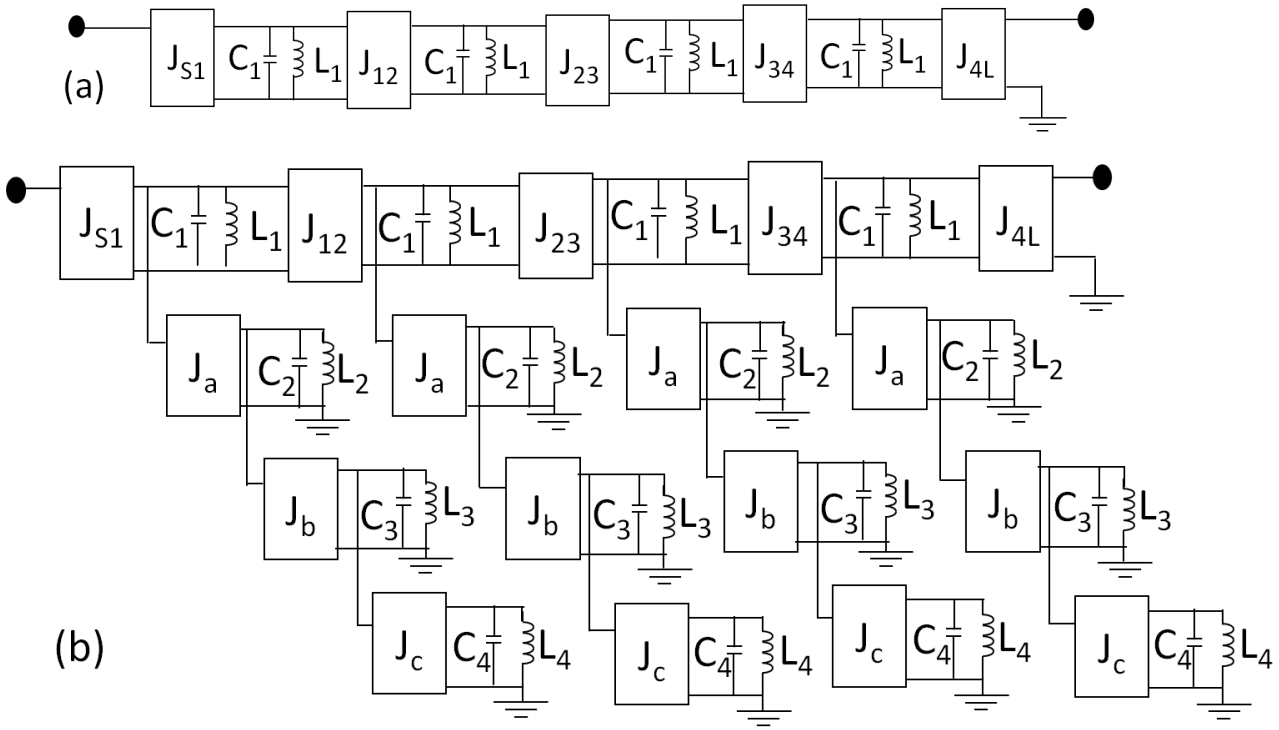

Fig. 4.8 A schematic circuit of a (a) fourth-order, single-band basis filter and (b) a quad-band filter

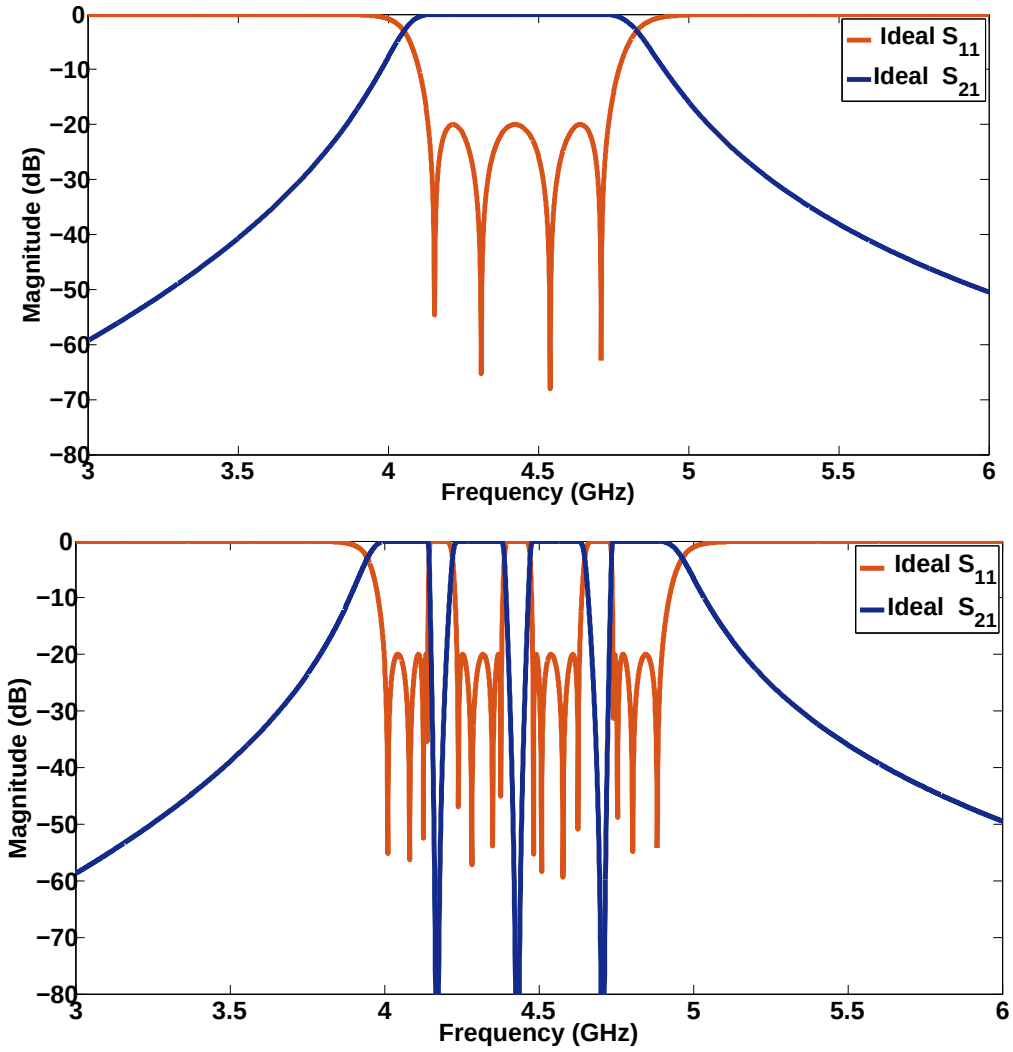

Fig. 4.9 Frequency response of a 4th order single-band basis filter of the schematic circuit in Fig 4.8 (a) and quad-band of the schematic circuit in Fig 4.8 (b).

$$Q_e = \frac{\Delta\omega_{\pm}}{\omega_0} = \pm 1 \tag{4.2}$$

The value of S_{21} falls to 0.707 or $(-3dB)$ of its maximum value according to equation 4.1. The bandwidth is defined based on equation 4.4 as

$$\Delta\omega_{3dB} = \Delta\omega + -\Delta\omega - = \frac{\omega_0}{(Q_e/2)} \tag{4.3}$$

$\Delta\omega_{3dB}$ is the bandwidth for which the attenuation for S_{21} is up $3dB$ from that at resonance. The double terminated loaded external quality factor Q'_e as indicated in Fig 4.11 is computed as

$$Q'_e = \frac{Q_e}{2} = \frac{\omega_0}{\Delta\omega_{3dB}} \tag{4.4}$$

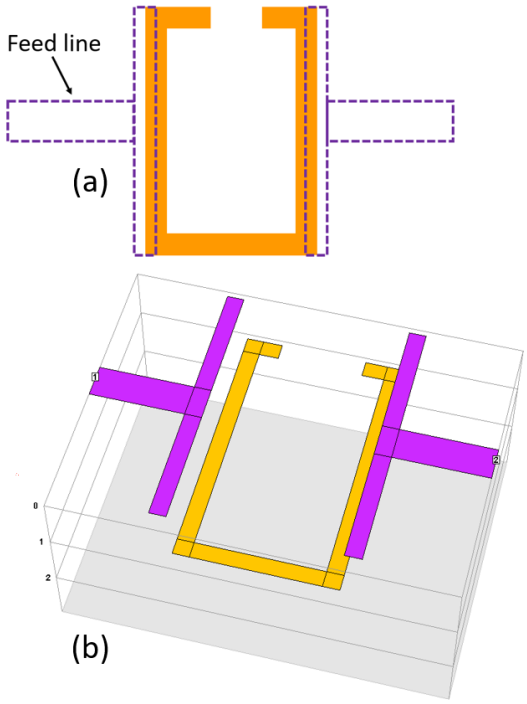

Fig. 4.10 Input/output coupling structures of coupled-line structure: (a) Layout; (b) 3-D view. This coupling topology allows for stronger coupling between feed and resonator than single layer does.

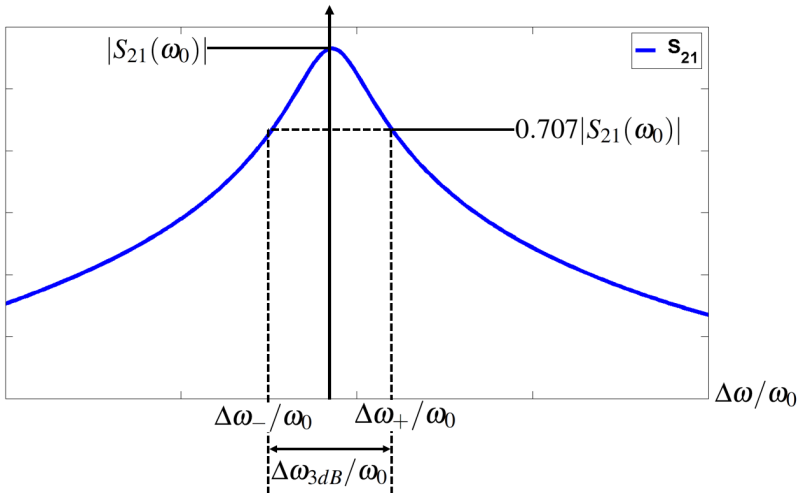

Fig. 4.11 Resonant responses of coupled resonator structures' as shown in Fig. 4.10(b).

4.3.2 Inter-resonator couplings

The reactance transformed multi-band basis filters were synchronously tuned. The resonators employed in the example were for dual-path, dual-band filters. The single band basis filter of order four had two-pairs, coupled resonators similar to the mixed coupling structure [35]. The top path resonators were arranged, as shown in Fig. 4.12(a),), while the bottom path resonator arrangement is shown in (b), Fig 4.12(c) shows the top view of the resonators in (b) weakly coupled to the input/output ports and its 3-D view in (d). The simulated resonant frequency response of the two coupled resonators in Fig 4.12(b) that were weakly coupled between two ports is shown in Fig 4.13.

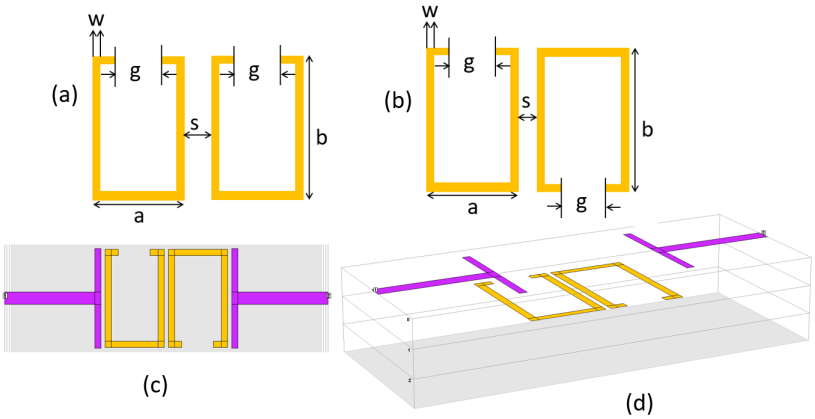

Fig. 4.12 Coupling structures of coupled resonators (a) and (b) are mixed coupling, (c) top view of resonators in (b) weakly coupled to the input/output ports and its (d) 3-D view.

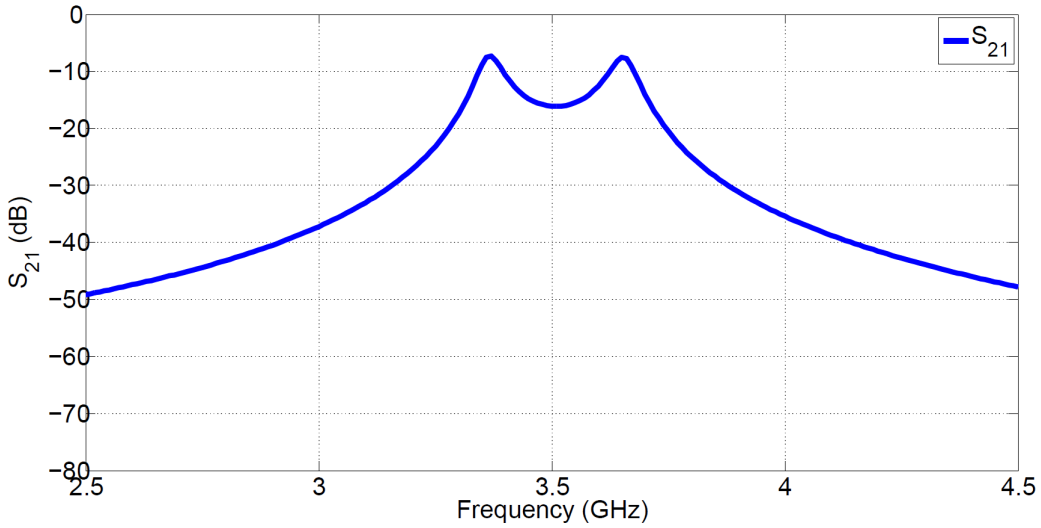

Fig. 4.13 Resonant responses of coupled resonator structures in Fig 4.12(c).

The two resonant frequencies are $f_1 = 3.370$ GHz and $f_2 = 3.650$ GHz. The synchronously tuned coupled resonators was formulated as [35].

$$k = \frac{f_{p2}^2 - f_{p1}^2}{f_{p2}^2 + f_{p1}^2} \tag{4.5}$$

The composite coupling also referred to as nested coupling was for the coupling between single band basis resonators and appended resonators which were positioned on the sequential layers. The appended resonators are nested within the single band basis resonators. This type of coupling was realized from all sides resulting in a strong coupling between levels. The multi-layer composite coupling is illustrated in Fig 4.14, (a) is the layout with dimensions of the nested resonator, (b) top view of resonator weakly coupled to the input/output ports and its 3-D view in (c). The dimensions of the nested arrangement are $a = 0.6mm$, $b = 0.3mm$, $g_1 = 3.1mm$, $g_2 = 0.6mm$, $a = 5.8mm$, $b = 9.6mm$, $c = 1.4mm$, $d = 4.0mm$, $e = 7.8mm$, $f = 2.7mm$ and $g = 1.7mm$. The simulated resonant frequency response of the two coupled resonators that were weakly coupled between two ports are shown in Fig. 4.15. The two resonant frequencies are $f_1 = 3.230$ GHz and $f_2 = 3.740$ GHz.

4.4 Port tuning

Port tuning is a design technique aiming to shorten the design cycle [59]. Ports are defined as two terminal signal and ground. The details of port tuning are presented in [60] where internal ports were inserted in a microstrip hairpin filter. Internal ports are described as ports

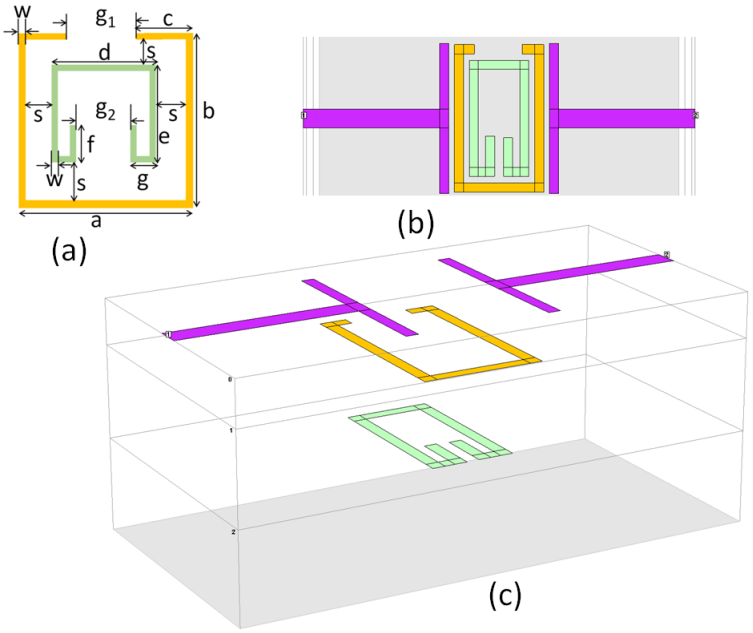

Fig. 4.14 Coupling structures of nested coupled resonators.

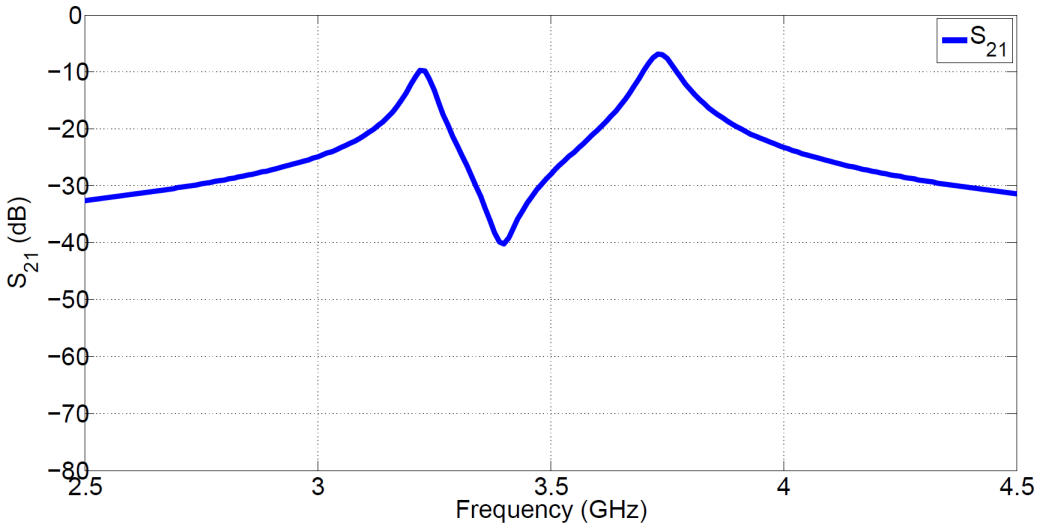

Fig. 4.15 Resonant responses of nested coupled resonator structures.

appearing inside the structure other than those on the edge. The port tuning procedure started with splitting the EM circuit into sections and simulating the circuits in parts. The data were imported into circuit analysis software, such as ADS and AWR, to tune the EM structure at the speed of the circuit analysis level in real time to shorten the design time. The split circuit was reconnected in a circuit analysis tool, before tuning; the response should match the EM analysis response. If the response does not match the EM analysis than the port tuning technique will fail.

The example in [60] details a single path, single band, hairpin filter. The circuit discussed here had more than one path (dual and triple-path), and provided a dual band response. Utilizing the port tuning technique was more challenging than an all-pole, single band filter. The example given here is for a dual-path, dual-band filter.

Port tuning is done in two steps, first resonators 1, 2, 3 and 4 are tuned to provide a single band response and resonators 5,6,7, 8 are completely removed. For the single band response in Fig 4.19 , the EM initial results do not fits the circuit model response. We use and inserted internal ports [59, 58] to tune the lengths of the resonators. The filter is partition or segmented into three sub circuits in the EM simulator as shown in Fig 4.16. As the results the circuit split into three sub-circuits and have 16 internal ports as shown in Fig 4.17. The sub-circuits are connected in AWR circuit simulator software by inserting the TLINP transmission line model between the internal ports of the resonators to tune the length. The sub circuit's blocks connections are illustrated in Fig 4.18. When the length of a transmission line (TLINP) is tuned to -0.1 mm the EM better fits the circuit model response, which means on each resonator the length should be reduced by 0.2 mm as each resonator has two (TLINP) transmission lines. The frequency response before tuning is shown in Fig 4.19 and after tuning in Fig 4.20.

Port tuning was done in two steps. First, resonators 1, 2, 3 and 4 were tuned to provide a single band response, and resonators 5, 6, 7, 8 were completely removed. For the single band response, shown in Fig. 4.19, the EM initial results did not fit the circuit model response. We utilized and inserted internal ports [59, 58] to tune the lengths of the resonators. The filter was partitioned or segmented into three sub-circuits in the EM simulator, as shown in Fig. 4.16. As a result, the circuit split into three sub-circuits and had 16 internal ports, as shown in Fig. 4.17. The sub-circuits were connected in AWR circuit simulator software by inserting the TLINP transmission line model between the internal ports of the resonators to tune the length. The block connections of the sub-circuit are illustrated in Fig. 4.18. When the length of a transmission line (TLINP) is tuned to -0.1mm, the EM fits the circuit model response more effectively; this implies that on each resonator the length should be reduced by 0.2 mm,

as each resonator had two (TLINP) transmission lines. The frequency response before tuning is shown in Fig. 4.19 and after tuning in Fig. 4.20.

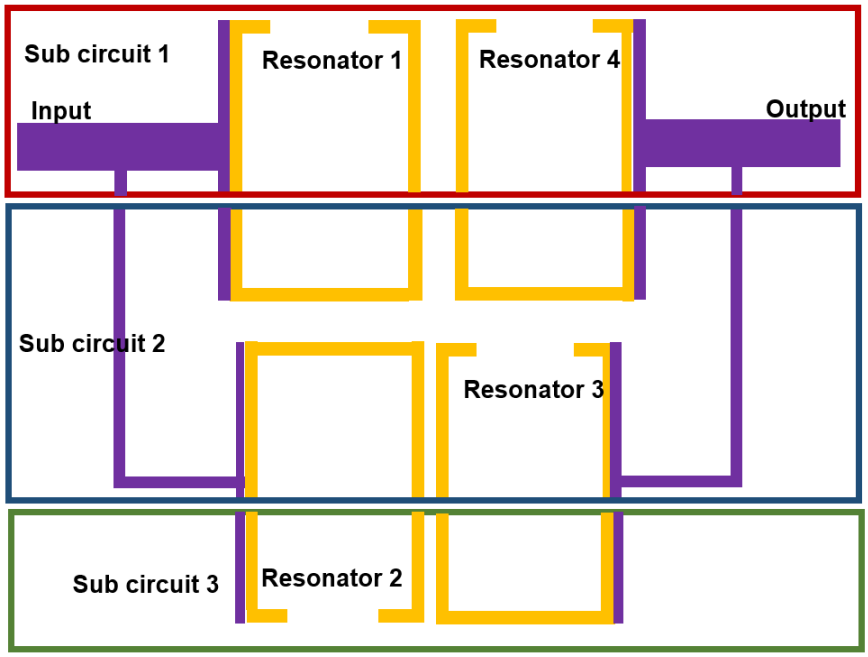

Fig. 4.16 The EM layout representing the schematic circuit as shown in Fig. 4.3 (a) is subdivided into three divisions. Each subdivision is analysed separately.

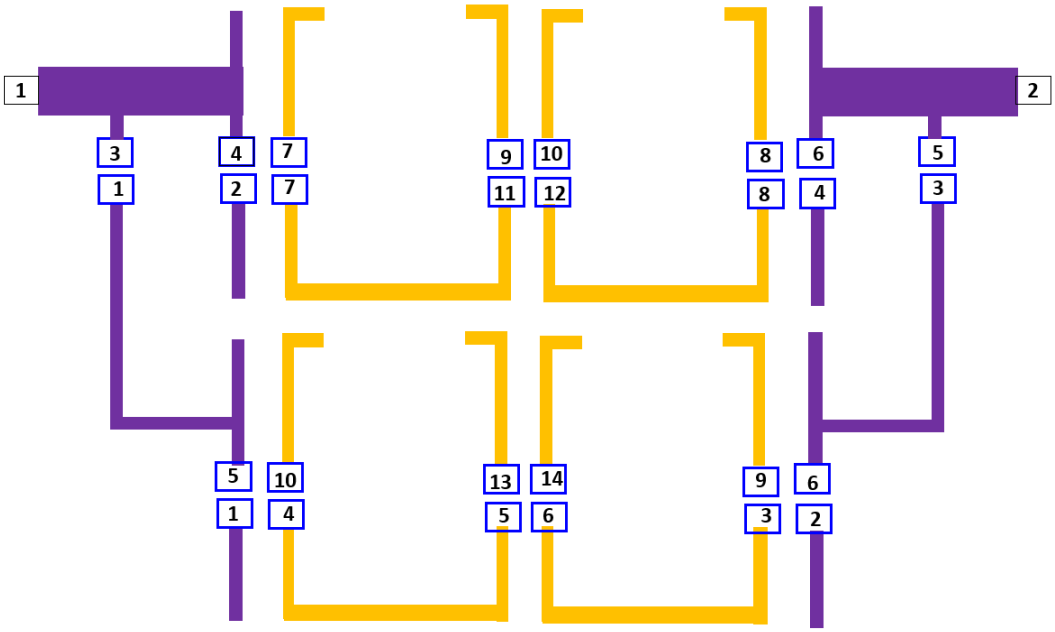

Fig. 4.17 16 internal ports are inserted in the EM model to allow port tuning.

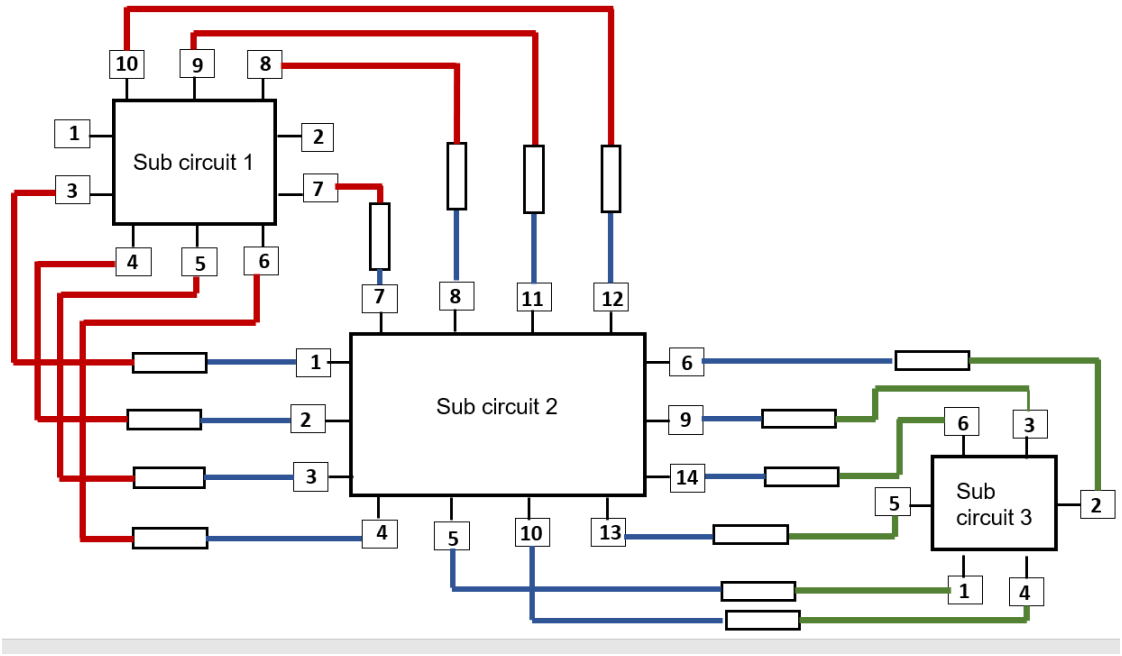

Fig. 4.18 The sub-circuits are put together in AWR to fast-tune the length of the resonators.

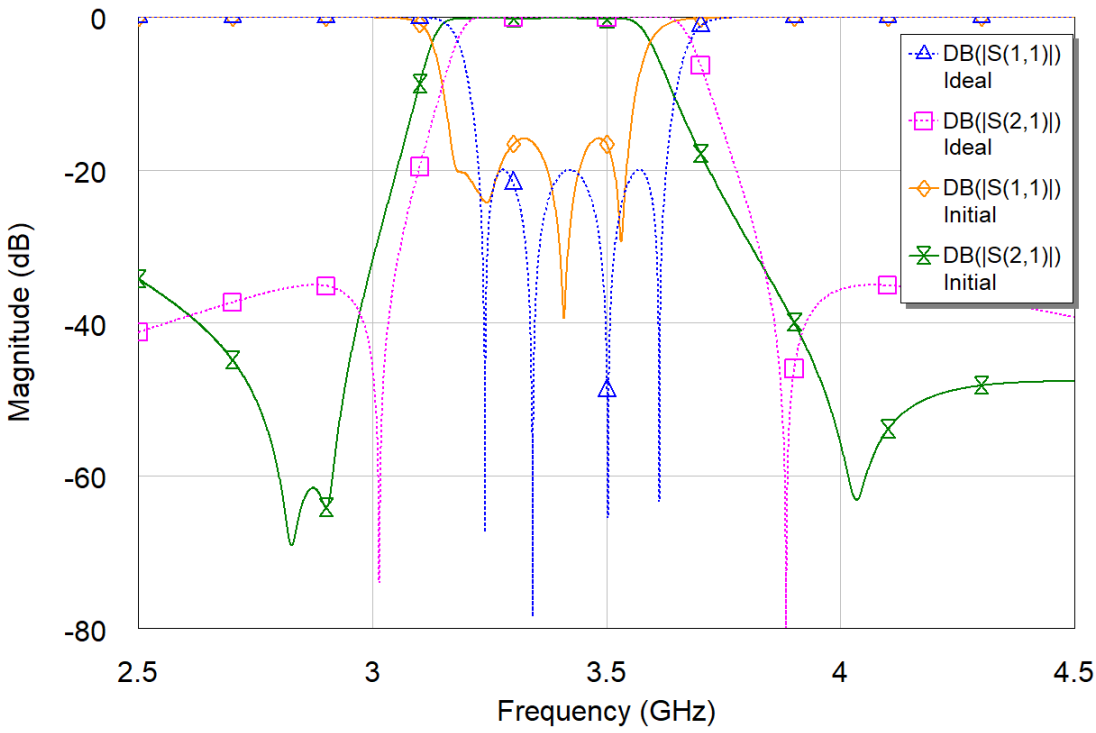

Fig. 4.19 Single band frequency response of the circuit theory versus simulation of the initial design before length-tuning.

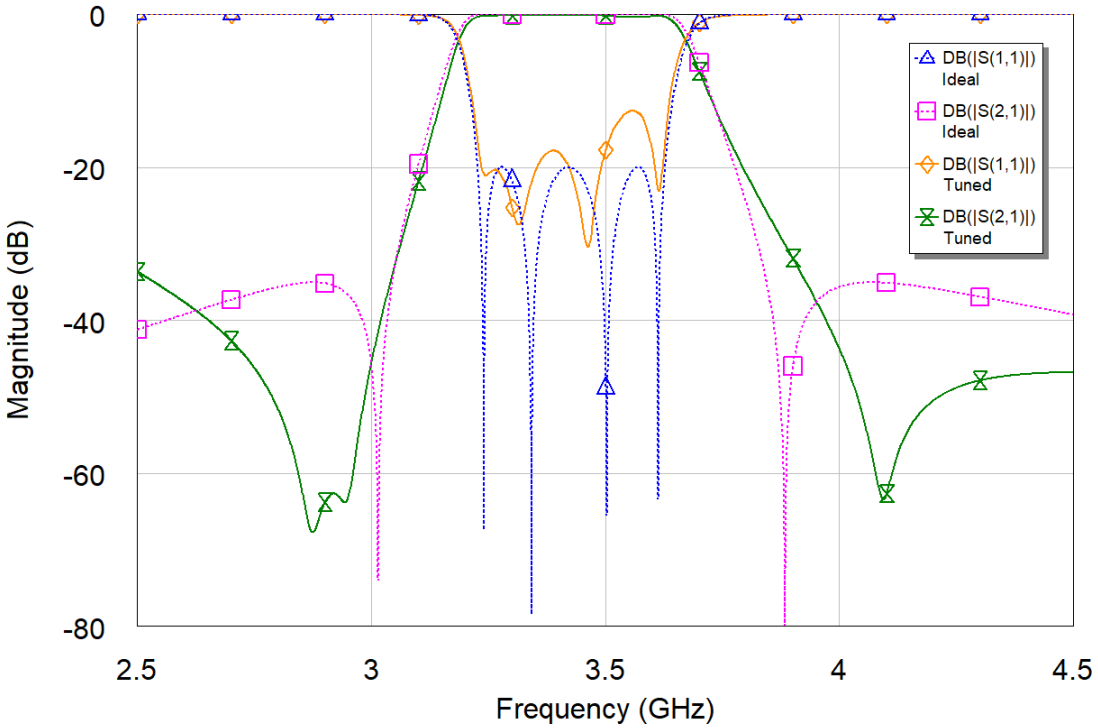

Fig. 4.20 Single band frequency response of the circuit theory versus simulation after length-tuning.

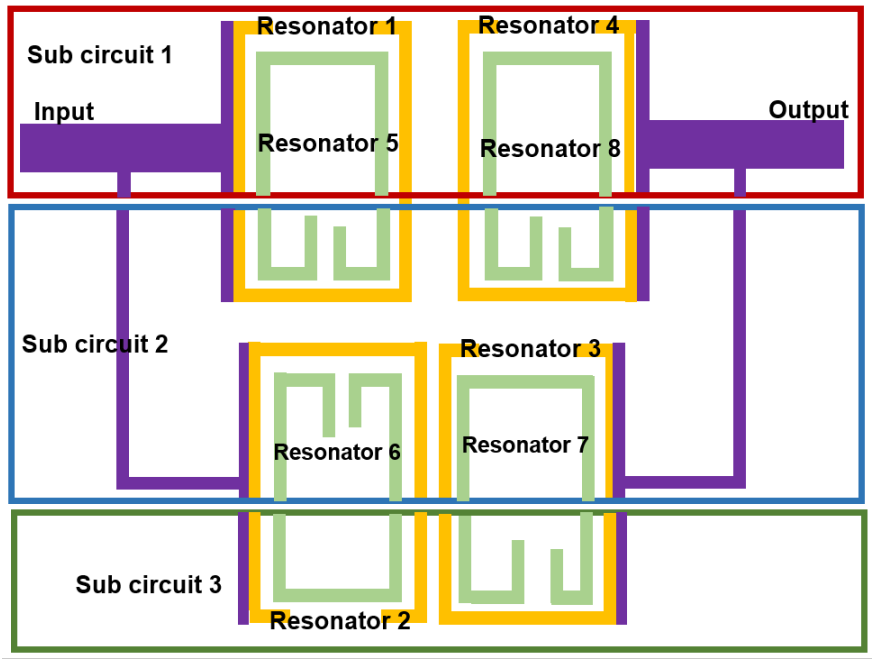

Fig. 4.21 The EM layout representing the schematic circuit in Fig 4.3 (b) is subdivided into three divisions. Each subdivision was analysed separately.

The second step was to add the appended resonators and segment the filter into 3 sub-circuits as depicted in Fig 4.21. These resulted into 44 internal ports illustrated in Fig 4.22. Since the single band basis was already tuned to the correct length in the first step, when assembling the circuit, shown in Fig 4.23, TLINP transmission lines were connected to ports for the single band basis should have zero length (no length tuning required for basis resonators). The only length to be tuned was for the appended resonators. The frequency response before and after length tuning is shown in Fig 4.24 and 4.25 respectively.

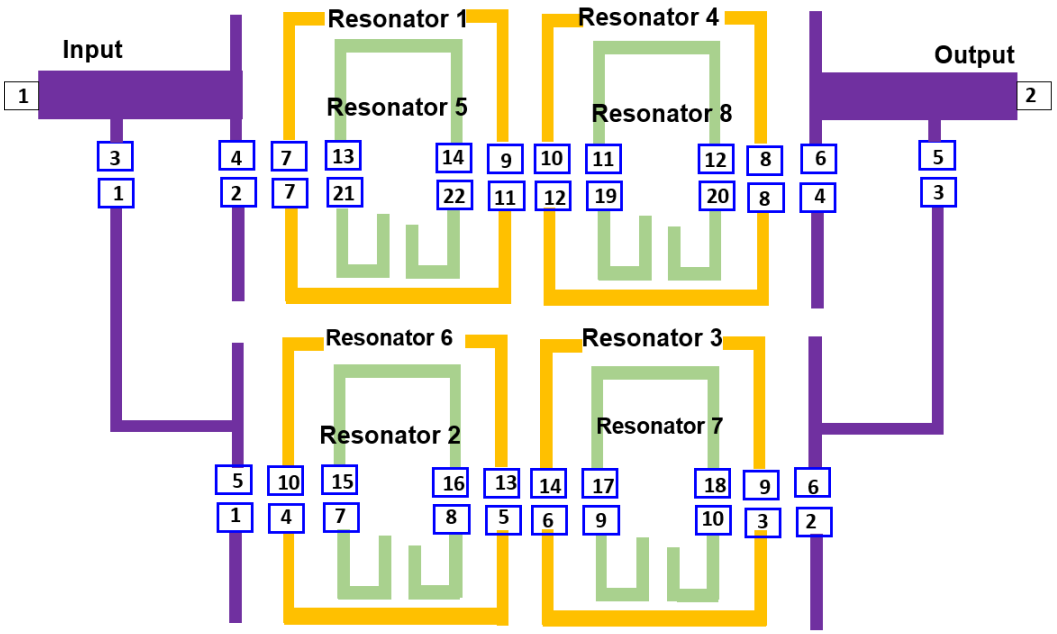

Fig. 4.22 44 internal ports are inserted in the EM model to allow port-tuning .

4.5 Implementation of coupled resonators microstrip planars on multi-layer substrates

This section details the implementation of a multi-layer Mercury wave of multi- and single-path. Mercury wave substrates have a dielectric constant of 3.5 and a loss tangent of 0.004.

4.5.1 Dual-path dual-band filter

The dual-path dual-band filter corresponding to coupling topology as shown in Fig 4.2(b) (Filter A) is represented by a circuit schematic in Fig 4.3 (b). The coupling matrix of a single band basis presented above as $M_{filterA}$ consists of one negative coupling necessary

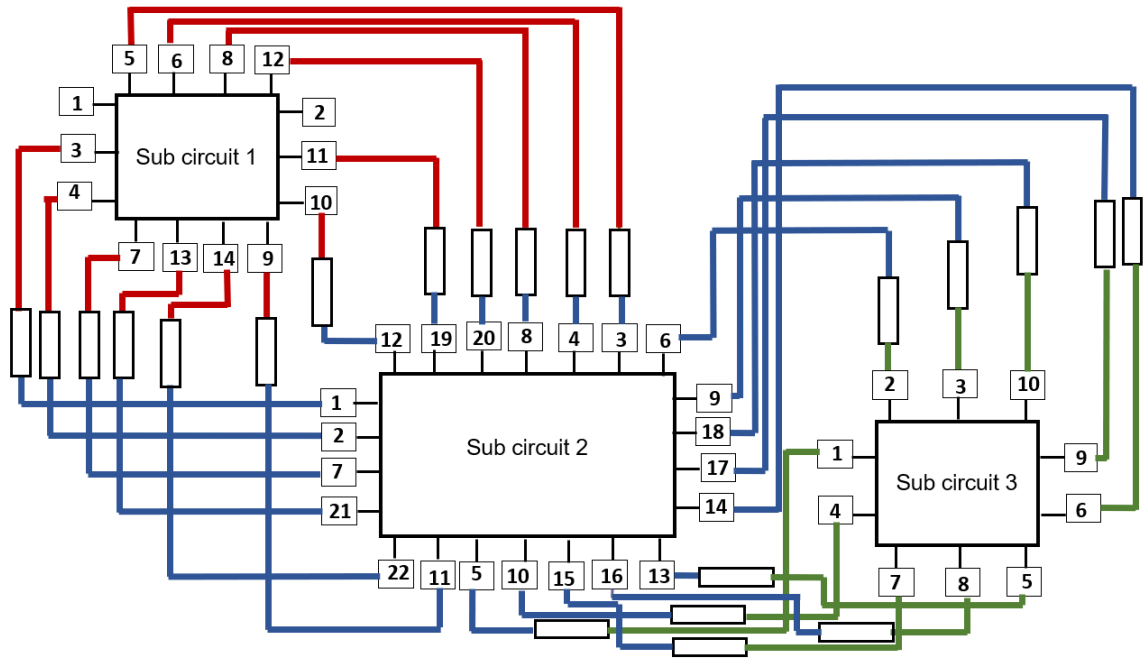

Fig. 4.23 The sub-circuits are put together in AWR to fast tune the length of the resonators.

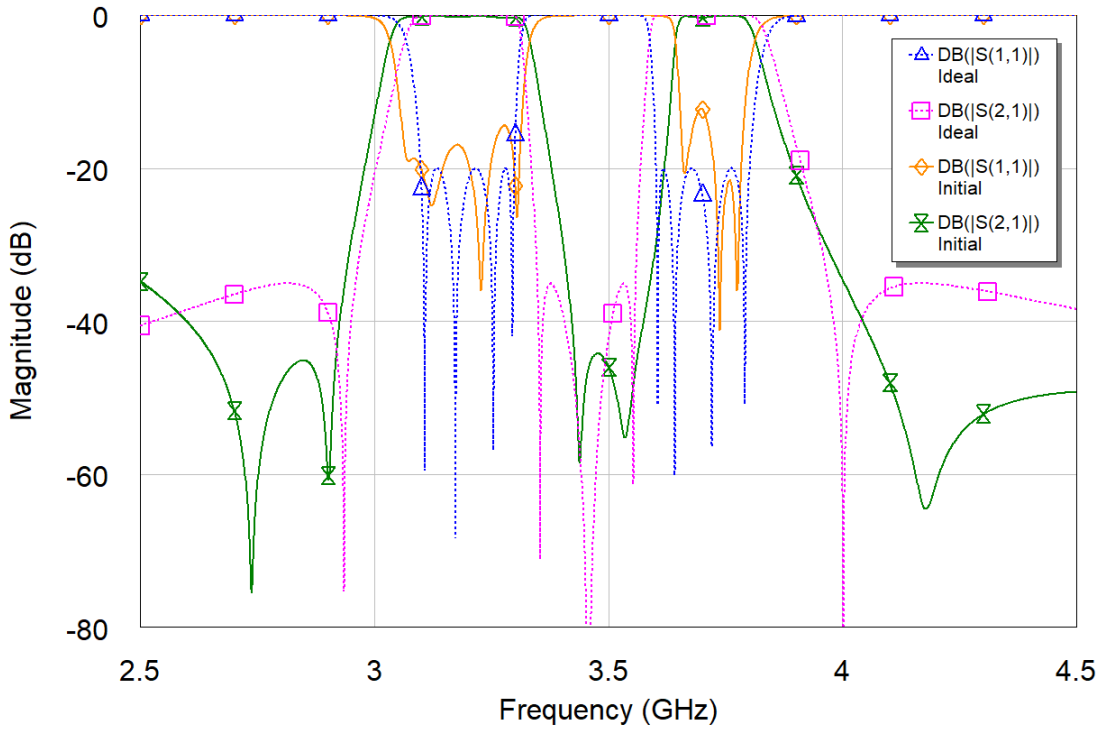

Fig. 4.24 Dual-band frequency response of the circuit theory versus simulation of the initial design before length-tuning.

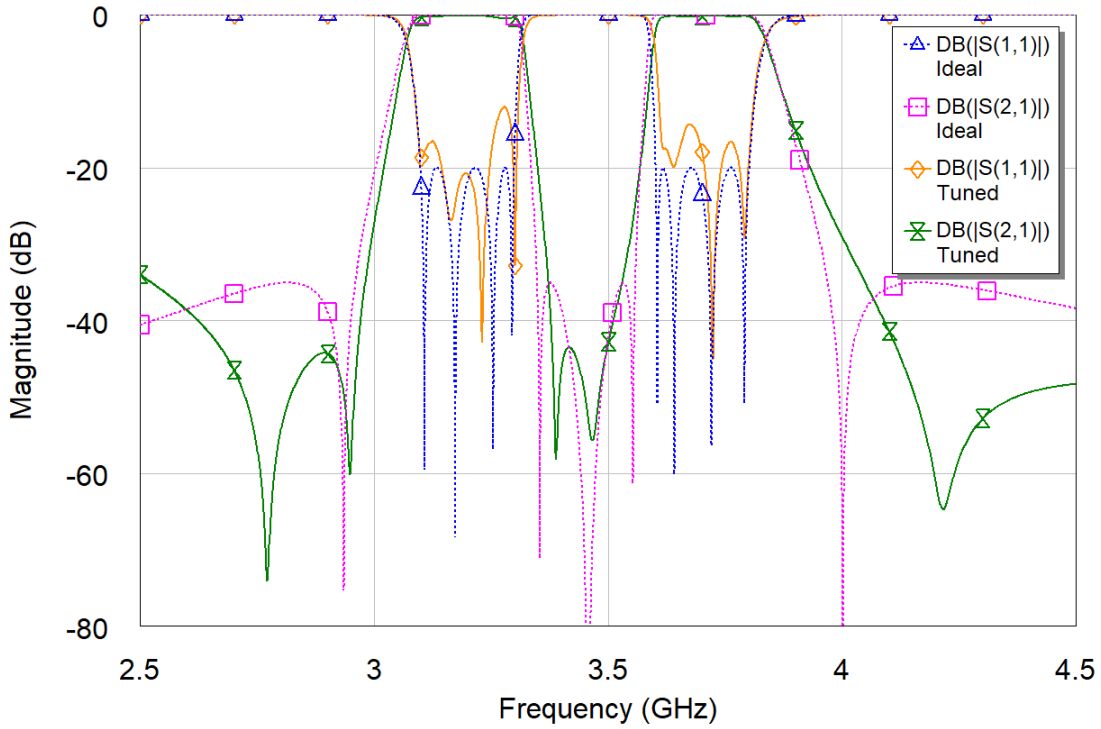

Fig. 4.25 Dual-band, frequency response of the circuit theory versus simulation after length-tuning.

to position one transmission zero on each side of the pass-band. This is illustrated on the frequency response of the single band basis filter in Fig 4.5 (b). The rest of the resonators showed positive couplings.

We subsequently designed a dual-path, dual-band filter with quasi-elliptic response. The filter center frequency was 3.432 Ghz, and the fractional bandwidth equaled 0.204, about 20 % .Each band had a bandwidth of 200 MHz, with a 20 dB (return loss) ripple level. The spacing between two bands was also 200 MHz. Once the coupling matrix $M_{FilterA}$ was obtained the procedures in [7] based on reactance transformation were followed to attain dual-band response. The additional couplings J_a's were obtained from the mapping functions. The multi-band reactance transform method has several advantages [7] which include the following:

- Each band is a replica of the original, low-pass, transfer function. The multi-band results with the same characteristics, for example, the same reflection zeroes, ripple level and transmission characteristics.
- The choice of bandwidth and center frequency is arbitrary.
- No new cross couplings arises, apart from those appearing in a single band basis filter

The dual-path, dual-band filter was implemented as a micro-strip, planar structure on a Mercury wave, multi-layer substrate with four printed metallization layers, detailed in Fig. 4.26(a). On the top (first metallization) layer (shaded purple), only the input/output port lines were printed, with a substrate thickness of 0.1016 mm. Both input and output ports were coupled to two resonators. The input/output ports and resonators couplings were realized by overlap between the layers.

On the next (second metallization from the top) layer (shaded orangish) resonators 1 to 4lay on a substrate thickness of 0.1016 mm plus a pre-preg of 0.104 mm. Inter-resonators appeared between resonator 1 and 4, as well as resonator 2 and 3. These were realized with $\lambda/2$ open loop resonators.Pre-pregs are bonding sheets utilized in multi-layer construction to resin and reinforce the material. The pre-preg utilized in the design had the same electrical property as the Mercury wave substrates. To implement the sign change appearing in $M_{FilterA}$ or phase shift, the arrangement of resonators was changed, as detailed in the layout of the dual-path, dual-band filters in Fig4.26(b) and (c) for resonator 7. The three D- view of filter A is shown in Fig4.26(d).

The appended resonators 5 to 8 lay on the next (third metallization from the top) layer (shaded green) on a substrate thickness of 0.1016 mm plus a pre- preg of 0.104 mm. These were folded inward to attain the required frequency. Coupling between single band basis resonators 1 to 4 and appended resonators 5 to 8 was realized in a nested coupling, in which resonators 5 to 8 appeared as if they were inside the single band basis resonators. The total substrate height of this filter added up to be 0.508 mm.

4.5.2 Triple-path dual-band filter

The triple-path dual-band filter was implemented as a micro-strip planar structure on a Mercury wave multi-layer substrate with four printed metallization layers detailed in Fig 4.27(a). On the top (first metallization) layer (shaded orangish) only the input/output ports lines were printed; with a substrate thickness of 0.1016 mm. Both input and output ports were coupled to three resonators. The input/output ports and resonators couplings were realized by overlap between layers.

On the next (second metallization from the top) layer (shaded greenish) resonators 1 to 6 lies on substrate thickness of 0.1016 mm plus a pre-preg of 0.043 mm. Inter resonators appear between resonator 1 and 6, 2 and 5 as well resonator 3 and 4. To implement the sign change appearing in $M_{FilterB}$ or phase shift, the arrangement of resonators was changed, as detailed in the layout of the triple-path dual-band filters in Fig 4.27(b) and (c) for resonator 1 and 3.

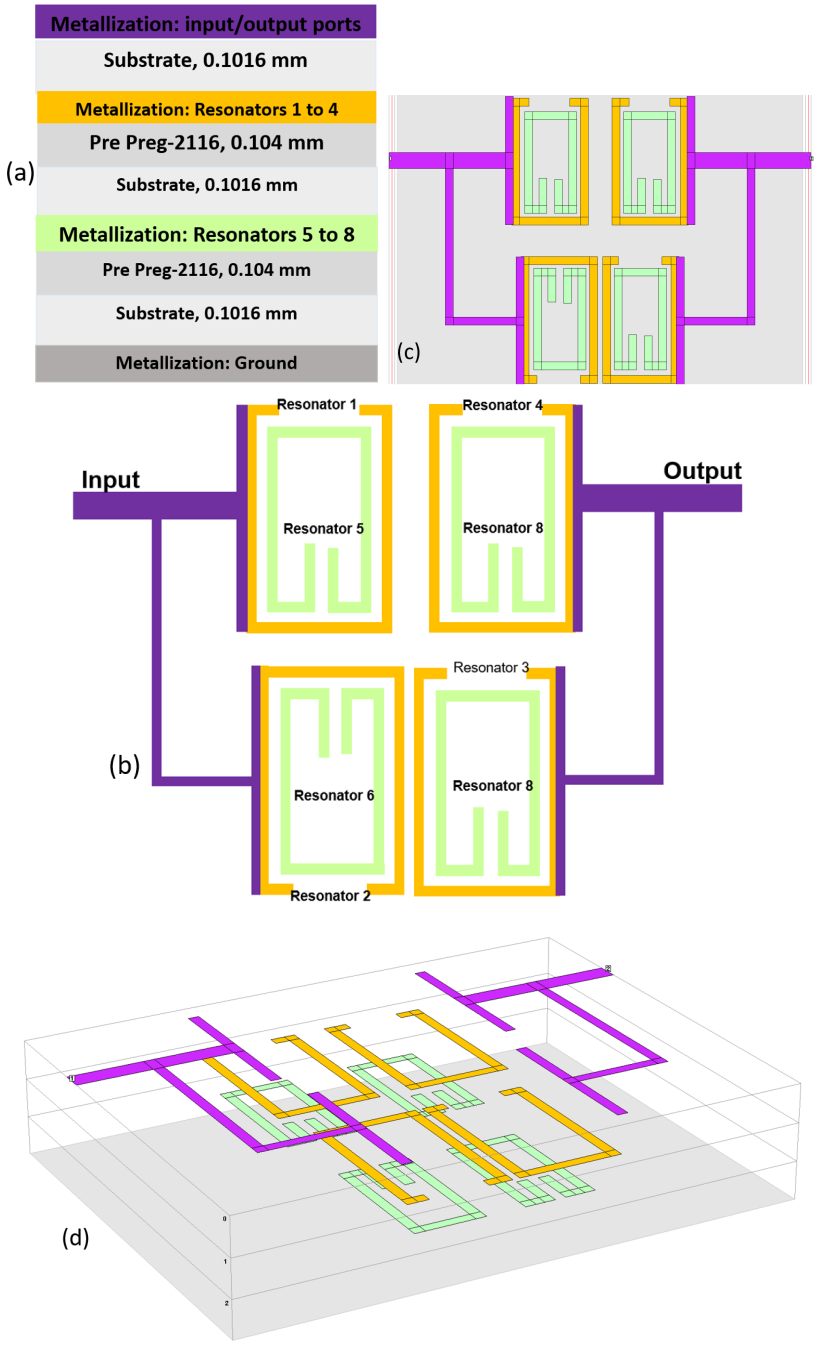

Fig. 4.26 The dual-path dual-band filter layout (a) layers stack up (indicated by different colors) of the topology corresponding to a dual-path dual-band Filter A (b) detailed microstrip open loop resonators layout (c) top view, and (d) 3-D view.

The appended resonators 7 to 12 lie on the next (third metallization from the top) layer (shaded light red) with substrate thickness of 0.1016 mm plus pre- preg of 0.0812 mm. As in the case of the dual path, inner resonators were folded inward to attain the required frequency. Coupling between single band basis resonators 1 to 6 and appended resonators 7 to 12 was realized in a nested coupling, in which resonators 7 to 12 were placed within single band basis resonators. The total substrate height of this filter added up to be 0.429 mm.

4.5.3 All poles quad band filters

An implementation of a quad-band, all-poles filter was detailed for two designs, namely the unchamfered (Filter C) and chamfered (Filter D) designs. The filters had an equal bandwidth of 150 MHz and equal separations between bands of 100 MHz. The complete filter on each design had a total number of 16 resonators, which was a challenge. The bands were closely separated, and the design required weaker input/output and inter-resonator couplings. The design above utilized a nested coupling approach, as nesting resulted in stronger couplings. For high frequency like the C band, the resonators' length were much shorter when compared to the S or L band. The nested design option was difficult to implement; hence, the all-poles, inter-resonator branch couplings employed a chain-link-like coupling (see Fig. 4.28). The chain link coupling option was more suitable to realize inter-resonator couplings; it was also flexible to alter the resonator length.

All poles quad-band unchamfered (Filter C)

The single-path, all-poles, quad-band filter was implemented as a micro-strip, planar structure on a Mercury wave, multi-layer substrate with four printed metallization layers as detailed in Fig. 4.29(a); (b) detailed the open loop resonators coupling arrangements; (c) shows the top view and (d) a 3-D view. On the top (first metallization) layer (shaded greenish) only the input/output ports lines were printed with a substrate thickness of 0.1016 mm. Both input and output ports were coupled to one resonator. The input/output ports and resonators couplings were realized by overlap between layers.

On the next (second metallization from the top) layer (shaded pinkish), resonators 1 to 4 and 9 to 12, lay on a substrate thickness of 0.1016 mm plus a pre-preg of 0.104 mm. The inter-resonator chain link couplings were realized by overlap between the resonators. Resonators 5 to 8 and 13 to16 lay on the next (third metallization from the top) layer (shaded purple), on the substrate thickness of 0.1016 mm plus a pre-preg of 0.104 mm. The total substrate height of this filter added up to be 0.508 mm.

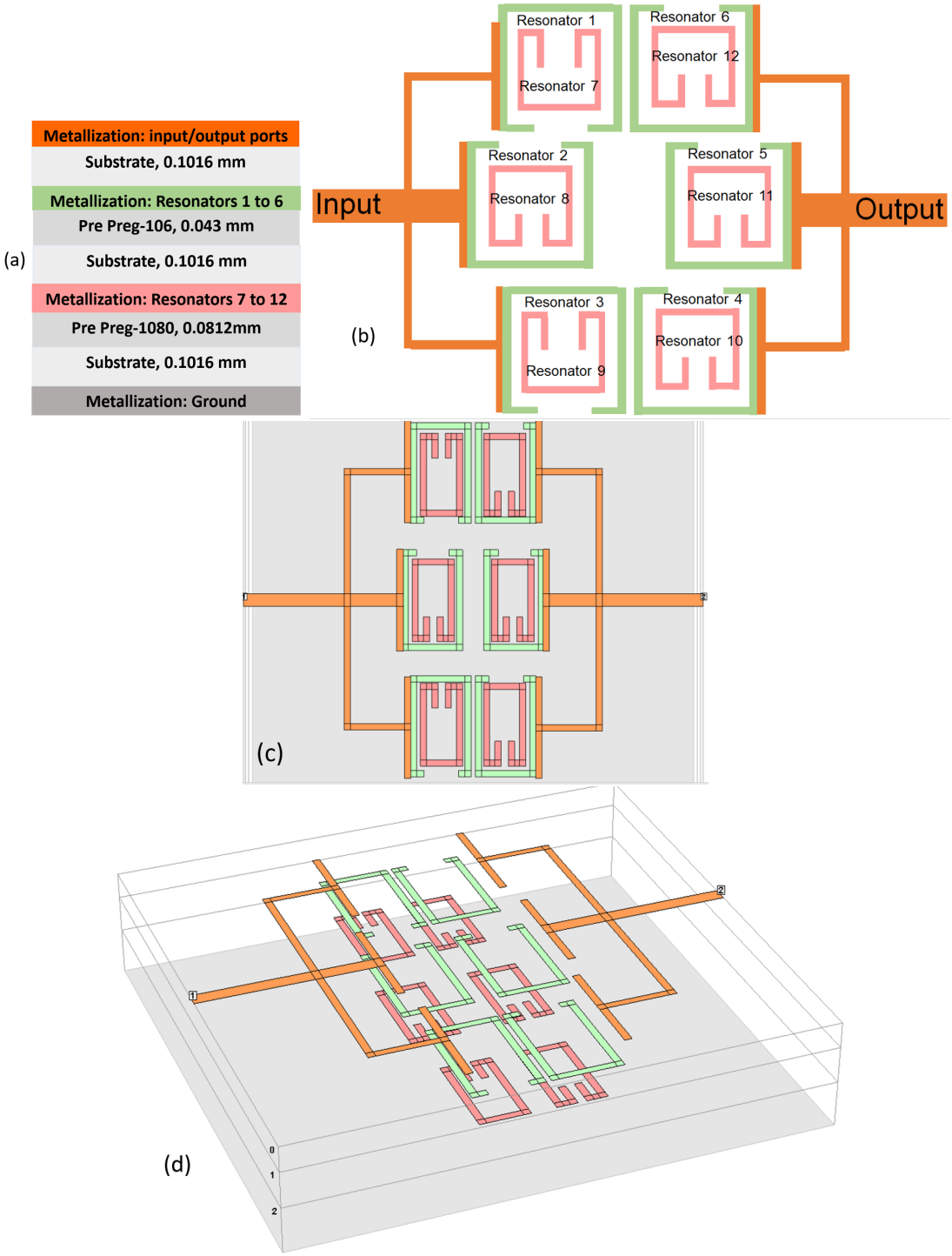

Fig. 4.27 The dual-path dual-band filter layout (a) layers stack up (indicated by different colors) of the topology corresponding to a dual-path dual-band Filter B (b) detailed microstrip open loop resonator layout (c) top view, and (d) 3-D view.

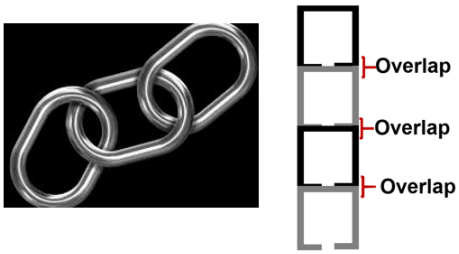

Fig. 4.28 A chain link, and a chain link like coupling realization.

All poles quad-band chamfered Filter D)

Figure 4.30(a), (b) details the open loop resonators coupling arrangement; (c) shows the top view and (d) the 3-D view. On the top (first metallization) layer (shaded reddish) only the input/output ports lines were printed with a substrate thickness of 0.211 mm. Both input and output ports were coupled to one resonator. The input/output ports and resonators couplings were realized by overlap between layers. On the next (second metallization from the top) layer (shaded turquoise) resonators 1 to 4 and 9 to 12, lay on substrate thickness of 0.211 mm plus a pre-preg of 0.0812 mm. Resonators 5 to 8 and 13 to16 lay on the next (third metallization from the top) layer (shaded dark blue) on a substrate thickness of 0.211 mm plus a pre- preg of 0.0812 mm. The total substrate height of this filter added up to be 0.7954 mm.

4.6 Construction and measured results

4.6.1 S-parameter measurements

All four coupled resonator filters (A, B, C, D) were constructed. The photographs of the constructed filters are shown in Fig 4.31. The size of Filter A including feed lines was 21.6 mm $\times$ 31.6 mm, Filter B was 33.7 mm $\times$ 43.4 mm, Filter C was 37.6 mm $\times$ 34.9 mm and Filter D had a size of 39.5 mm $\times$ 33.9 mm.

The constructed dual-band (Filter A) in Fig 4.31(a) had basis resonators of order 4. They are represented by a coupling topology in Fig 4.2 (b). The coupling matrix presenting the basis resonators in a dual band prototype has the form of equation 4.6

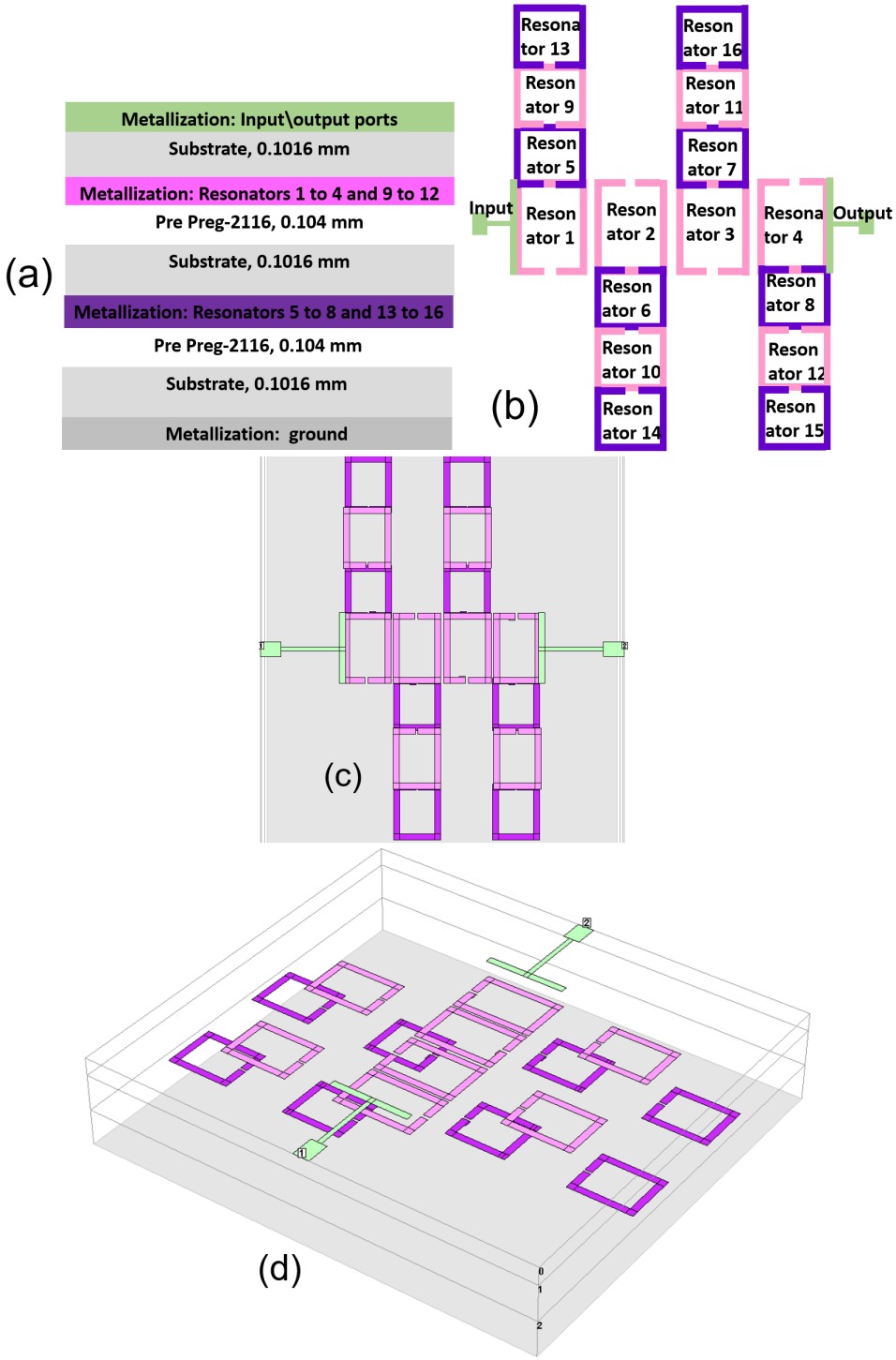

Fig. 4.29 The single-path quad- band filter layout (a) layers stack up (indicated by different colors) of the topology corresponding to a dual-path dual-band (Filter C) (b) detailed microstrip open loop resonator layout (c) top view, and (d) 3-D view.

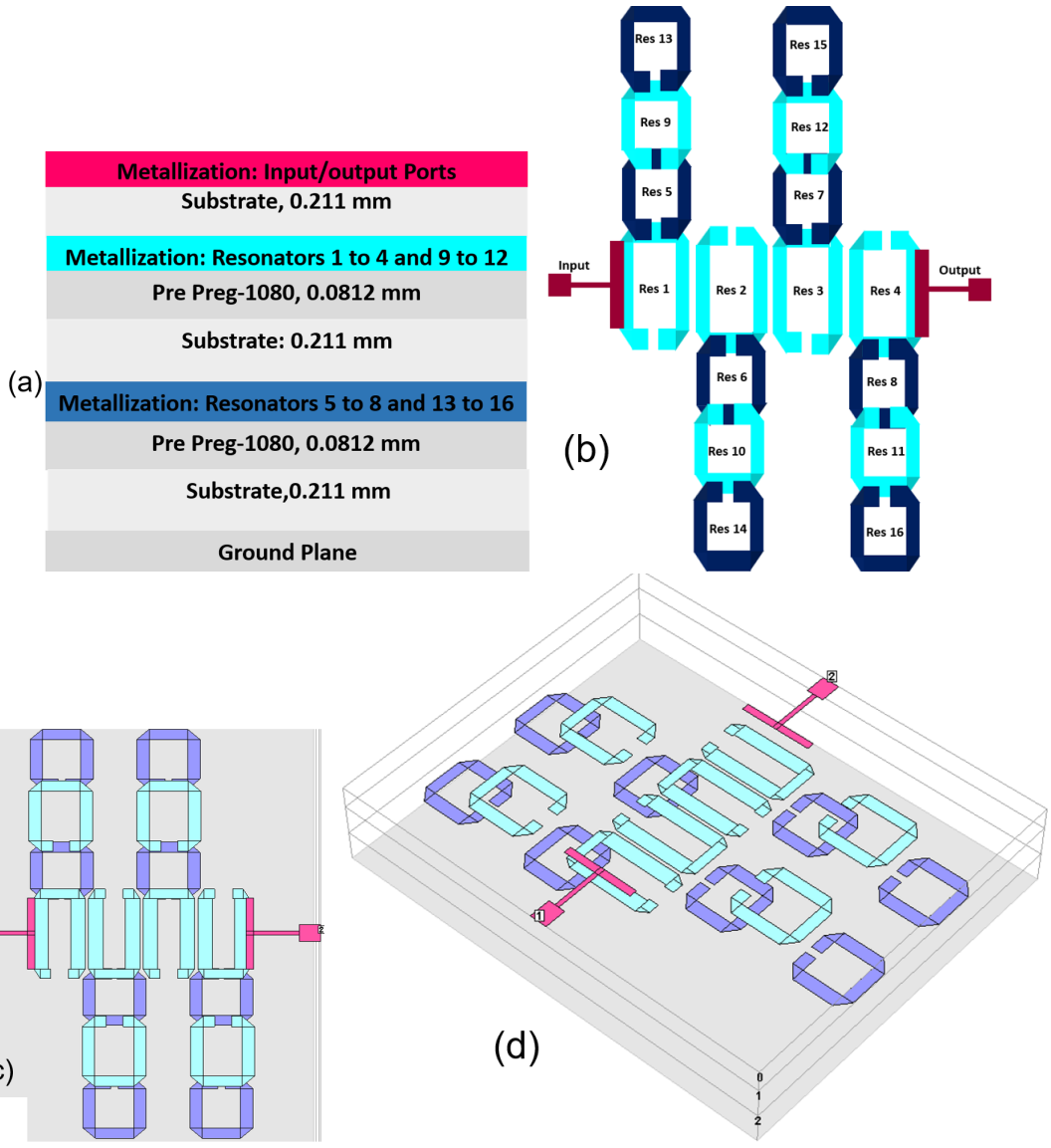

Fig. 4.30 The single-path quad-band filter layout (a) layers stack up (indicated by different colors) of the topology corresponding to a singlel-path quadl-band (Filter D) (b) detailed micro-strip open loop resonators layout (c) top view, and (d) 3-D view.

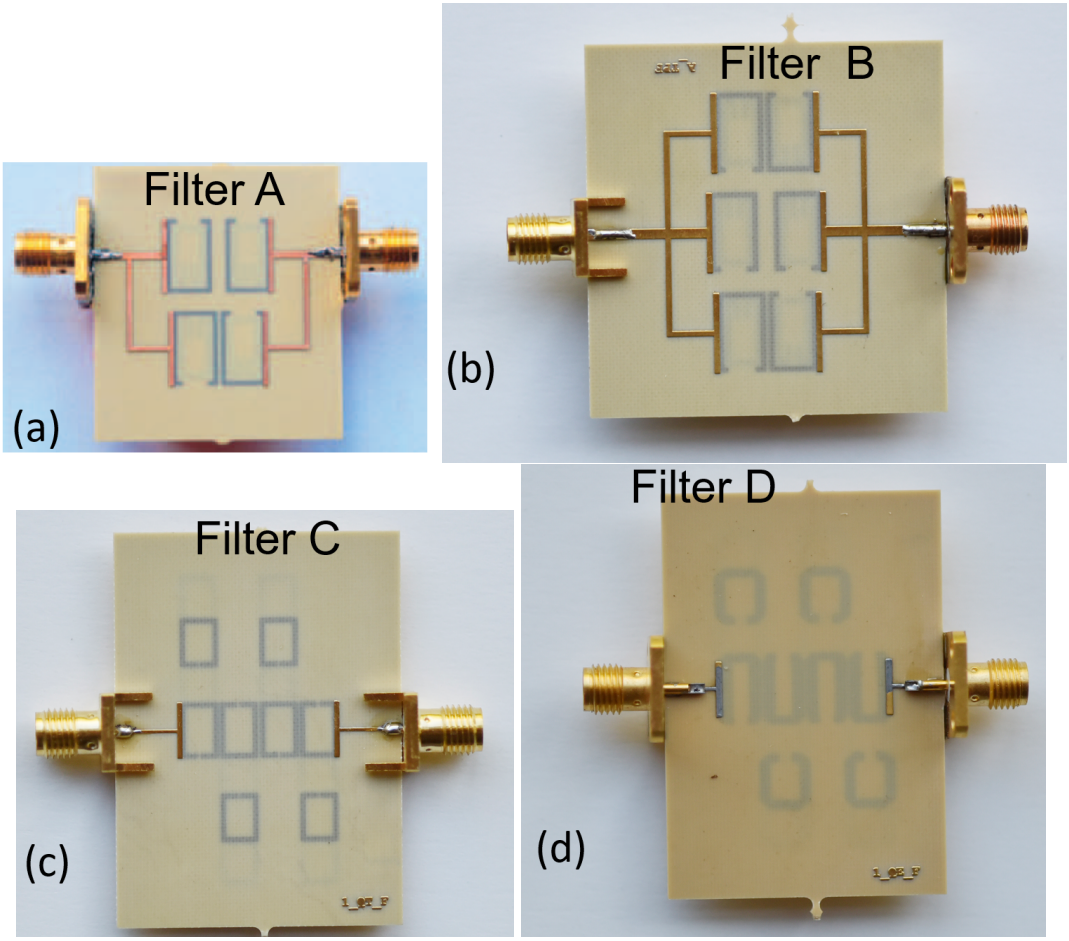

Fig. 4.31 Photographs of constructed filters: (a) Filter A: dual-path, dual-band filter; (b) Filter B: triple-path, dual-band filter; (c) Filter C: all-poles, quad-band, unchamfered filte; (d) all-poles, quad-band, chamfered filter.

$$M_{ADual} = \begin{bmatrix} 0 & M_{S1} & M_{S2} & 0 & 0 & 0 \\ M_{1S} & M_{11} & 0 & 0 & M_{14} & 0 \\ M_{2S} & 0 & M_{22} & M_{23} & 0 & 0 \\ 0 & 0 & M_{32} & M_{33} & 0 & M_{3L} \\ 0 & M_{41} & 0 & 0 & M_{44} & M_{4L} \\ 0 & 0 & 0 & M_{L3} & M_{L4} & 0 \end{bmatrix} \tag{4.6}$$

When we substituted the element values, equation 4.6 was equivalent to equation 4.7

$$M_{Adual} = \begin{bmatrix} 0 & 0.5355 & -0.8744 & 0 & 0 & 0 \\ 0.5355 & 0.0309 & 0 & 0 & 1.2939 & 0 \\ -0.8744 & 0 & 0.0309 & 0.6789 & 0 & 0 \\ 0 & 0 & 0.6789 & 0.0309 & 0 & 0.8744 \\ 0 & 1.239 & 0 & 0 & 0.0309 & 0.5355 \\ 0 & 0 & 0 & 0.8744 & 0.5355 & 0 \end{bmatrix} \tag{4.7}$$

While $M_{55} = M_{66} = M_{77} = M_{88} = -0.07241$ and $M_{15} = M_{26} = M_{37} = M_{48} = 0.6516$.

The constructed, dual-band (Filter B) in Fig 4.31(b) had basis resonators of order 6. It is represented by a coupling topology in Fig 4.2 (d). The coupling matrix presenting the basis resonators in a dual band prototype had the form of equation 4.8

$$M_{Bdual} = \begin{bmatrix} 0 & M_{S1} & M_{S2} & M_{S3} & 0 & 0 & 0 & 0 \\ M_{1S} & M_{11} & 0 & 0 & 0 & 0 & M_{16} & 0 \\ M_{2S} & 0 & M_{22} & 0 & 0 & M_{25} & 0 & 0 \\ M_{3S} & 0 & 0 & M_{33} & M_{34} & 0 & 0 & 0 \\ 0 & 0 & 0 & M_{43} & M_{44} & 0 & 0 & M_{4L} \\ 0 & 0 & M_{52} & 0 & 0 & M_{55} & 0 & M_{5L} \\ 0 & M_{61} & 0 & 0 & 0 & 0 & M_{66} & M_{6L} \\ 0 & 0 & 0 & 0 & M_{4L} & M_{5L} & M_{6L} & 0 \end{bmatrix} \tag{4.8}$$

When we substituted the element values, equation 4.8 was equivalent to equation 4.9

$$M_{Bdual} = \begin{bmatrix} 0 & -0.4304 & 0.6199 & -0.6548 & 0 & 0 & 0 & 0 \\ -0.4304 & 0.01548 & 0 & 0 & 0 & 0 & 1.1850 & 0 \\ 0.6199 & 0 & 0.01548 & 0 & 0 & 0.9927 & 0 & 0 \\ -06548 & 0 & 0 & 0.01548 & 0.3777 & 0 & 0 & 0 \\ 0 & 0 & 0 & 0.3777 & 0.01548 & 0 & 0 & 0.6548 \\ 0 & 0 & 0.9927 & 0 & 0 & 0.01548 & 0 & 0.6199 \\ 0 & 1.1850 & 0 & 0 & 0 & 0 & 0.01548 & 0.4303 \\ 0 & 0 & 0 & 0 & 0.6548 & 0.6199 & 0.4303 & 0 \end{bmatrix} \tag{4.9}$$

While $M_{77} = M_{88} = M_{99} = M_{1010} = M_{1111} = M_{1212} = -0.0465$ and $M_{17} = M_{28} = M_{39} = M_{410} = M_{511} = M_{612} = 0.5761$.

The constructed, dual-band (Filter C and D) in Fig 4.31(c) and (d) had basis resonators of order4. It is represented by a coupling topology in Fig 4.7(b). The coupling matrix presenting the basis resonators in a dual band prototype had the form of equation 4.10

$$M_{CDquad} = \begin{bmatrix} 0 & M_{S1} & 0 & 0 & 0 & 0 \\ M_{1S} & M_{11} & M_{12} & 0 & 0 & 0 \\ 0 & M_{21} & M_{22} & M_{23} & 0 & 0 \\ 0 & 0 & M_{32} & M_{33} & M_{34} & 0 \\ 0 & 0 & 0 & M_{43} & M_{44} & M_{4L} \\ 0 & 0 & 0 & 0 & M_{L4} & 0 \end{bmatrix} \tag{4.10}$$

When we substituted the element values, equation 4.6 was equivalent to equation 4.11

$$M_{CDquad} = \begin{bmatrix} 0 & 1.0352 & 0 & 0 & 0 & 0 \\ 1.052 & 0.009409 & 0.9106 & 0 & 0 & 0 \\ 0 & 0.9106 & 0.009409 & 0.6999 & 0 & 0 \\ 0 & 0 & 0.6999 & 0.009409 & 0.9106 & 0 \\ 0 & 0 & 0 & 0.9106 & 0.009409 & 1.0352 \\ 0 & 0 & 0 & 0 & 1.0352 & 0 \end{bmatrix} \tag{4.11}$$

While $M_{55} = M_{66} = M_{77} = M_{88} = -0.06509$, $M_{99} = M_{1010} = M_{1111} = M_{1212} = -0.03786$, $M_{1313} = M_{1414} = M_{1515} = M_{1616} = -0.08386$, $M_{15} = M_{26} = M_{37} = M_{48} = 0.4968$, $M_{59} = M_{610} = M_{711} = M_{812} = 0.4722$ and $M_{913} = M_{1014} = M_{1115} = M_{1216} = 0.3616$.

The results for Filter A are plotted in Fig 4.32 with the first graph showing the ideal lossless filter against the simulated lossy filter. The second graph compares simulation to measured results.

The results of Filter B are plotted in Fig 4.33, the first graph of Fig 4.33 shows the ideal lossless filter versus the simulated lossy response. The second graph compares simulation to measured results. The pass-bands both shifted to lower frequencies and the pass-band bandwidth increased.

Filter C data are plotted in Fig 4.34 showing the circuit theory versus simulation and Fig 4.35 shows measured results versus simulation. It was observed that there was an increase in the pass-band bandwidth of the outer bands, while the bandwidth of the inner bands appeared to be unchanged. All four pass-bands shifted to the lower frequencies.

Again for Filter D, data are plotted in Fig4.36 showing the circuit theory versus simulation. Figure 4.37 shows measured results versus simulation. The first three pass-bands shifted to the lower bands, suppression between pass-band 1 and 2 decreased, in pass-band 3 the bandwidth increased, the fourth pass-band agreed with the simulation and there was no change in the bandwidths.

It was observed that the measured pass bands shift to lower frequencies and pass band bandwidth increases as compared to the simulated ones. This shift is due to the reason that for a single a band filter, the modelled loss in simulation is only approximate to the actual substrate loss. This is not constant over frequency as modeled with software. The effect on a single band filter is that the bandwidth can change and the center frequency is affected somewhat. For multiband filter, which relies on a transformed single band filter, the bandwidth are indeed affected more dramatically. This was illustrated in [30]

4.6.2 Group delay measurements

Group-delay tuning was discussed in Chapter 3. Some of the tuning options for all-pole, quad-band, chamfered and unchamfered filters were constructed. To de-tune a resonator, their resonant frequency are altered in two ways; (1) inserting a cut, and (2) removing the appended resonators completely. There was a coincidence in the measured and simulation data, and the resonators, where a cut was inserted, provided similar results as those where some resonators were completely removed. Figures 4.38 to 4.42 show the coupling topology and group-delay response of Filter C. Figures 4.43 to 4.46 show the coupling topology and group delay response of Filter D. The solidly filled circles represent tuned resonators, while de-tuned resonators were represented by lined circles in which a cut was inserted to shift the resonant frequency. Similarly, like in the S parameters, there was a shift to the left on each group-delay responses.

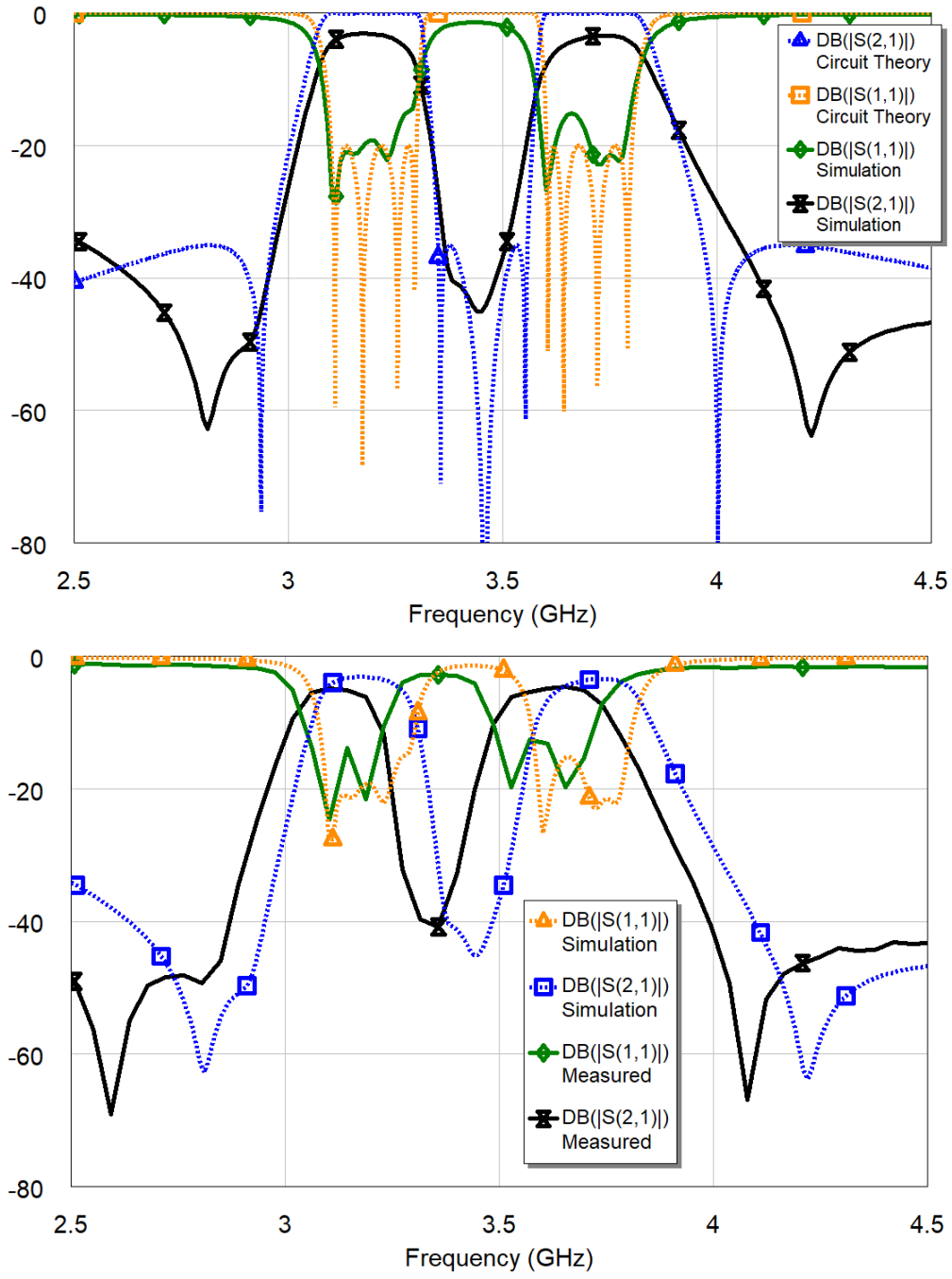

Fig. 4.32 The frequency response of the (a) ideal lossless dual-path dual-band filter versus a simulation of a lossy Filter A; (b) simulation versus measured data of Filter A.

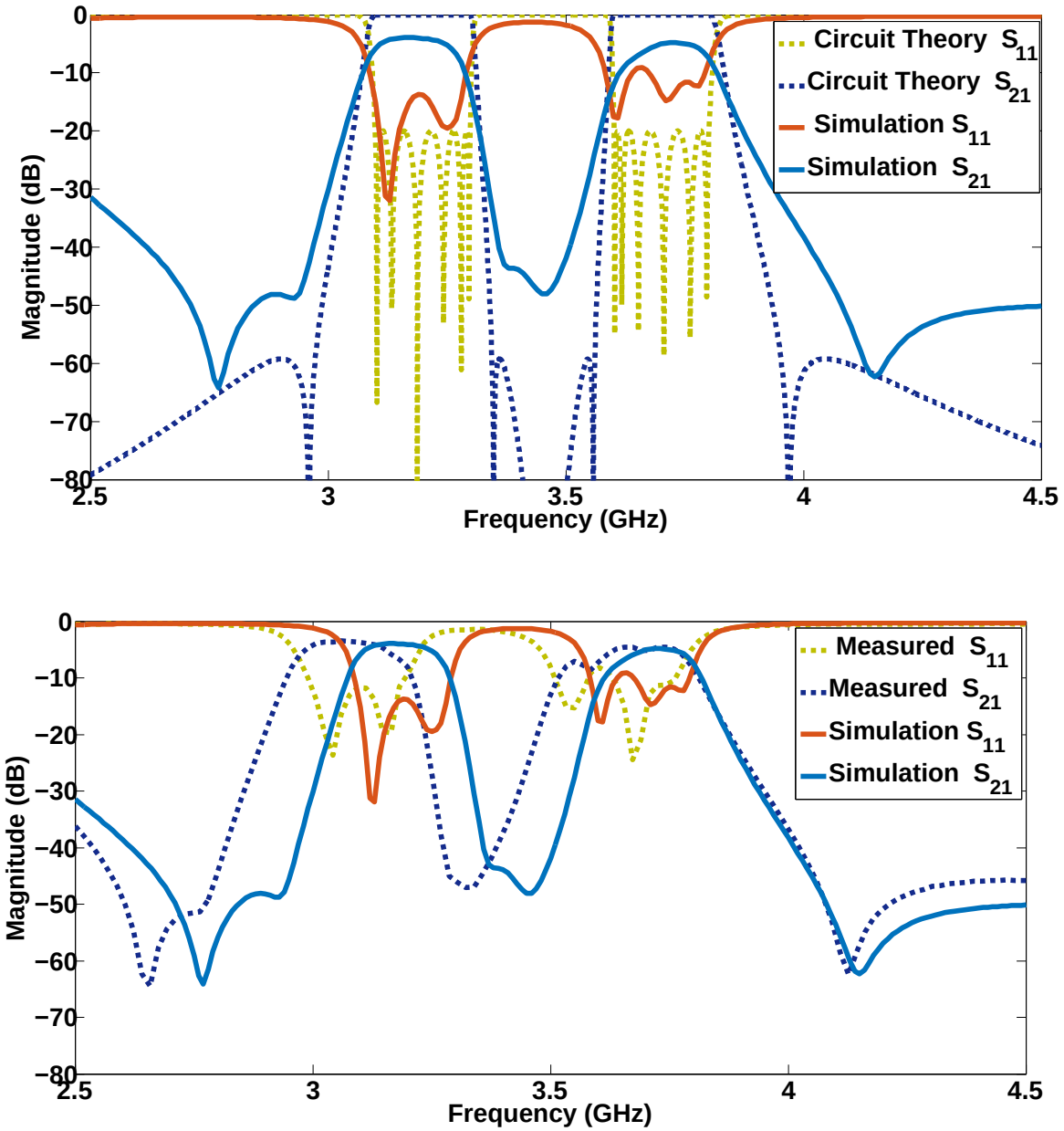

Fig. 4.33 The frequency response of the circuit theory and simulation for a dual-band, triple- path Filter B; the frequency response of the measured and simulation for a dual-band, triple-path Filter B.

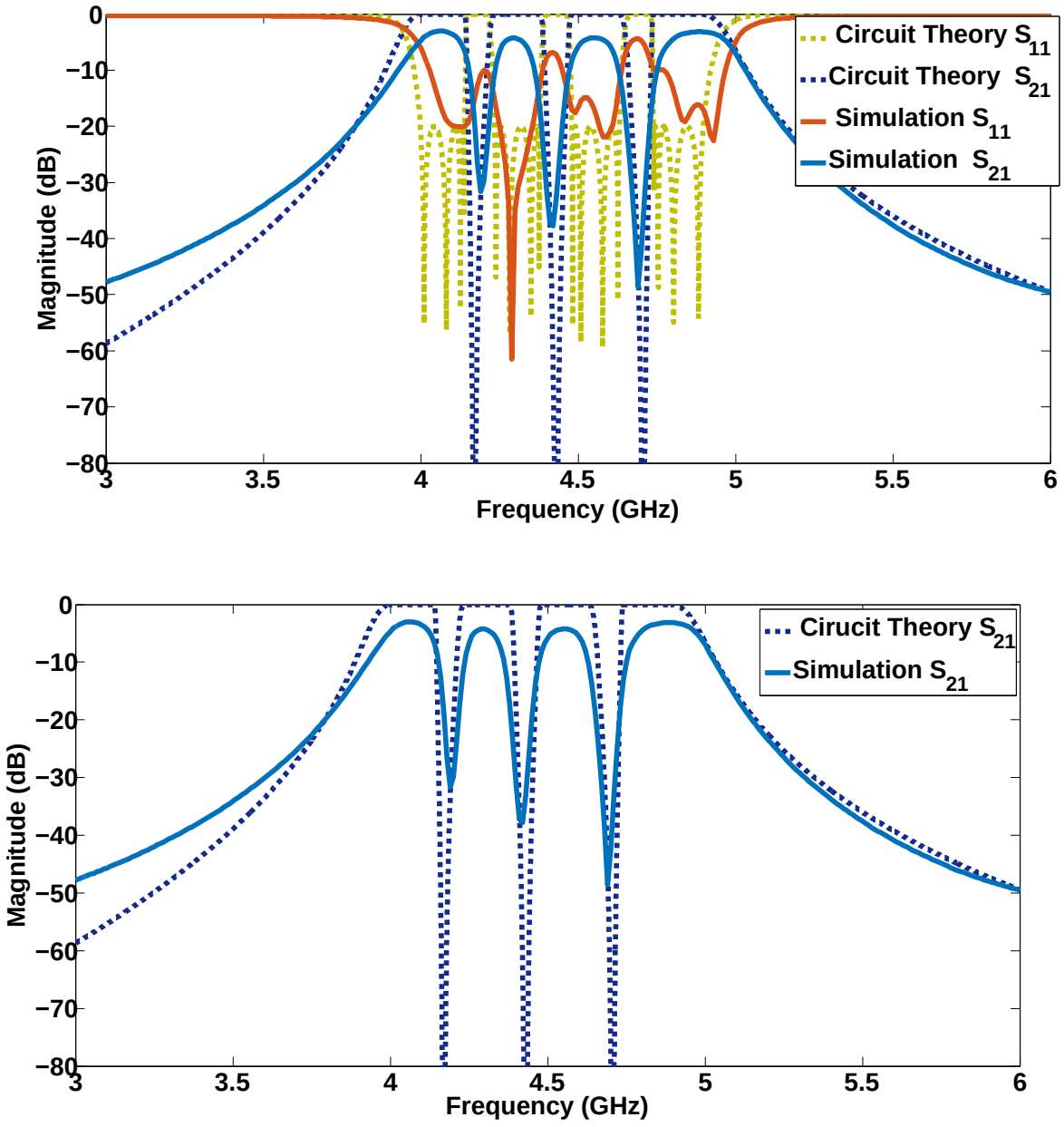

Fig. 4.34 S-parameters for Filter C lossless circuit response compared to the lossy simulation.

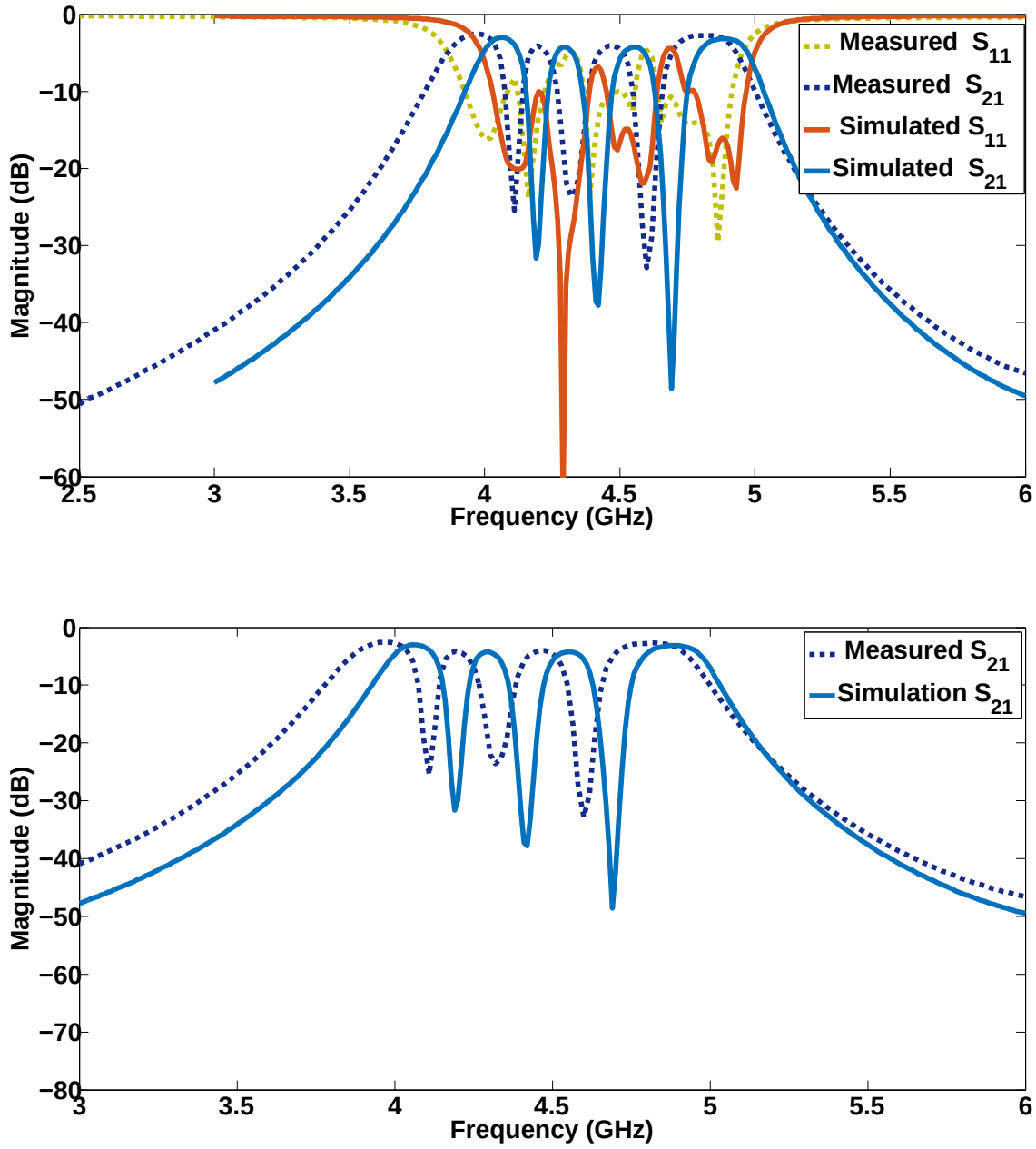

Fig. 4.35 S-parameters of the measured data for Filter C, compared to the lossy simulation

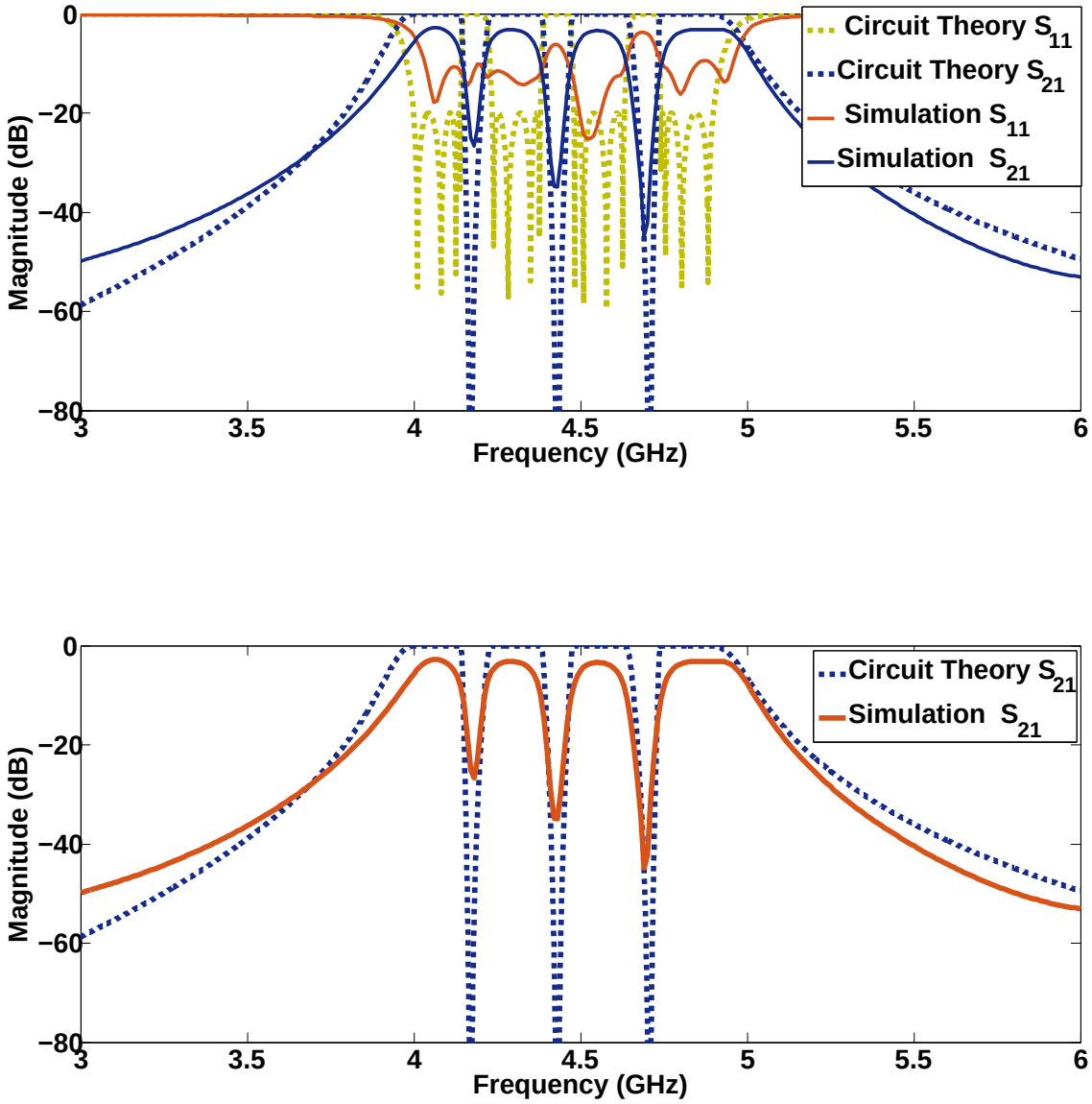

Fig. 4.36 S-parameters for Filter D lossless circuit response compared to the lossy simulation..

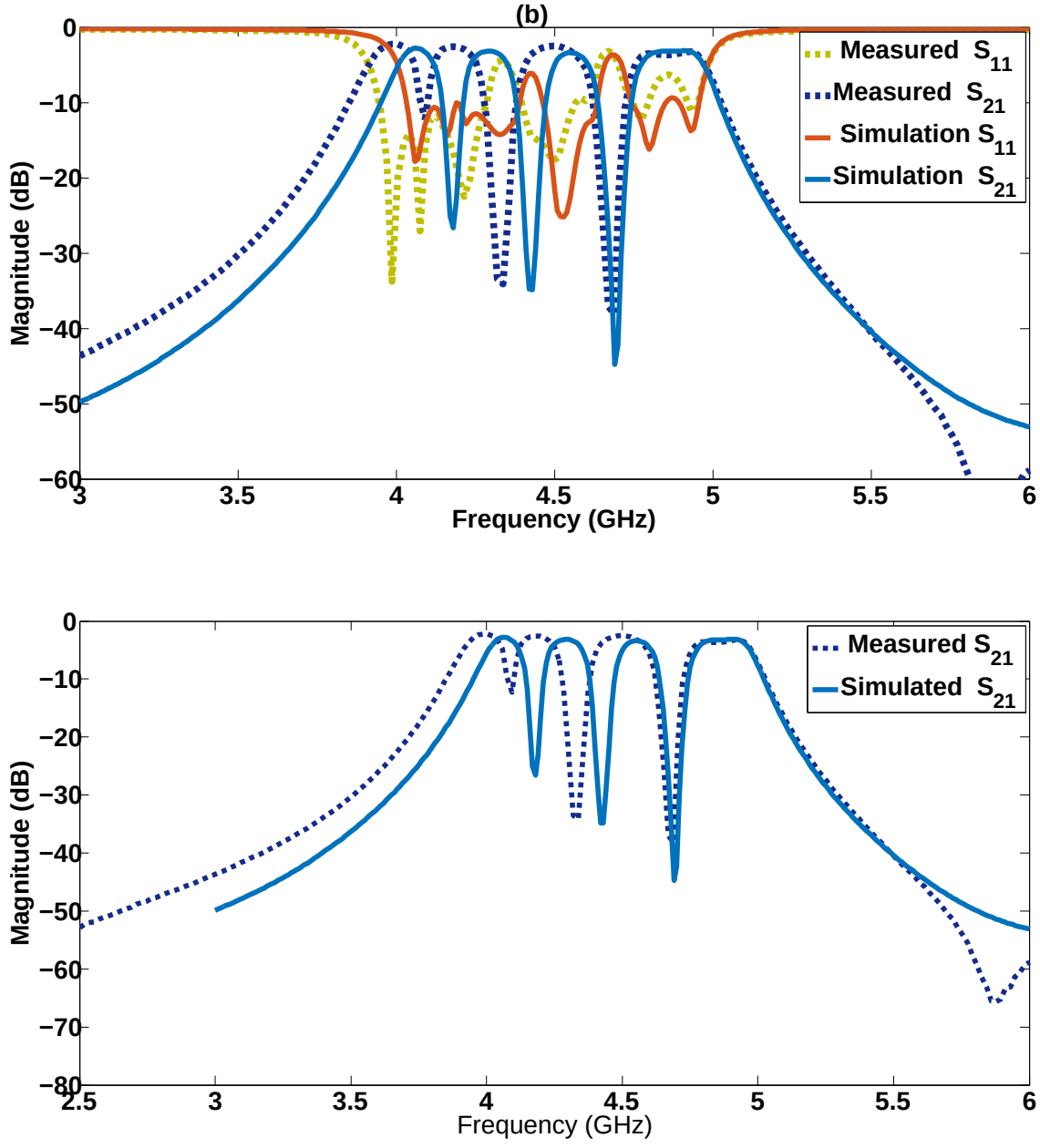

Fig. 4.37 S-parameters for Filter D measured data compared to the lossy simulation.

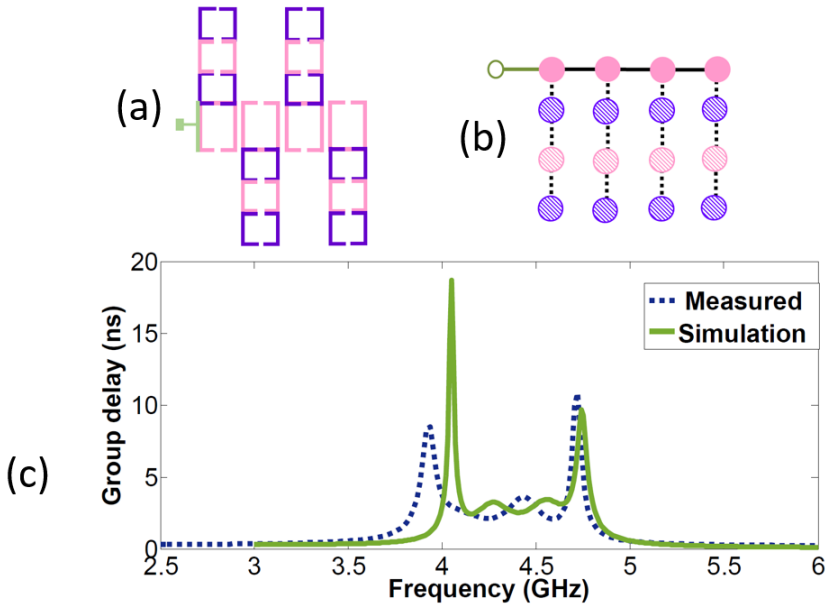

Fig. 4.38 Group delay for (a) quad-band filter with inserted cuts except for a single band, basis filter; (b) all-pole topology representing circuit in (a); (c) simulated data against measured data (Filter C).

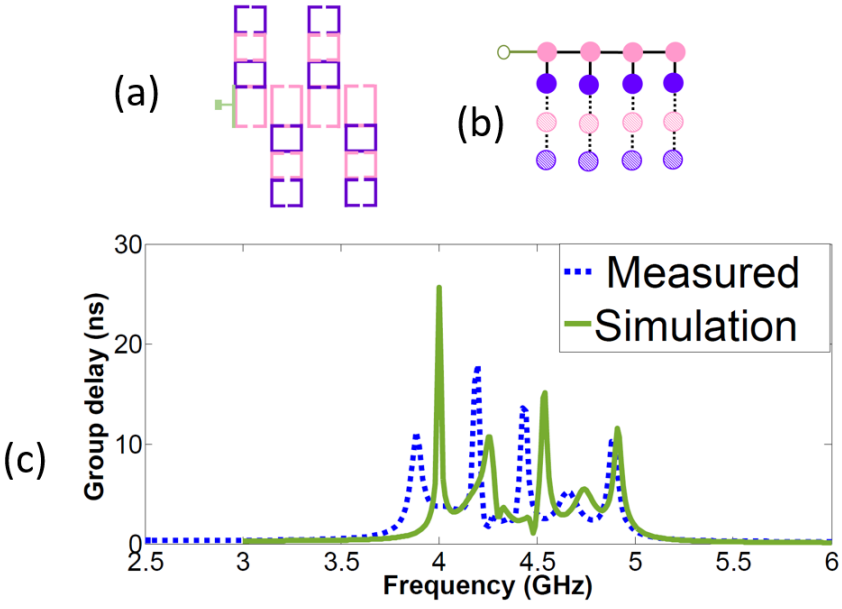

Fig. 4.39 Group delay for: (a) quad-band filter with inserted cuts except for single band, basis filter and the first line of the appended resonator in a horizontal plane; (b) all-pole topology representing the circuit in (a); (c) simulated data against measured data (Filter C).

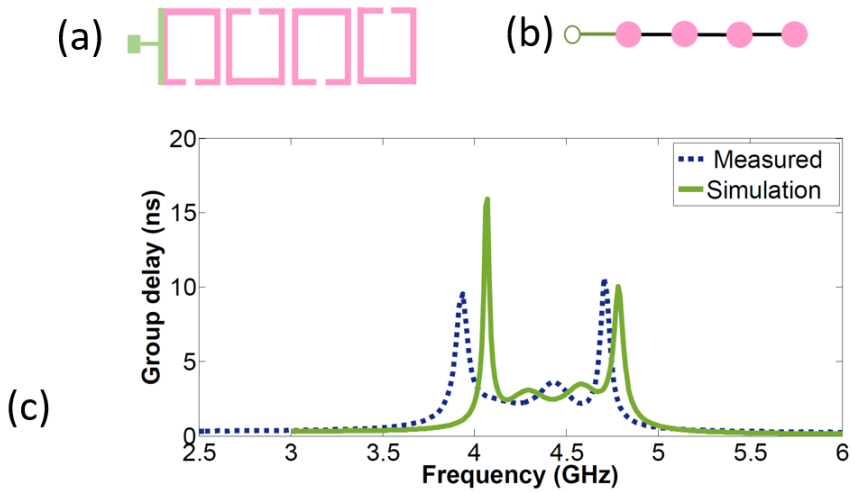

Fig. 4.40 Group delay for: (a) quad-band filter with the rest of the resonator removed except for the single band basis filter; (b) all-pole topology representing circuit in (a); (c) simulated data versus measured data (Filter C).

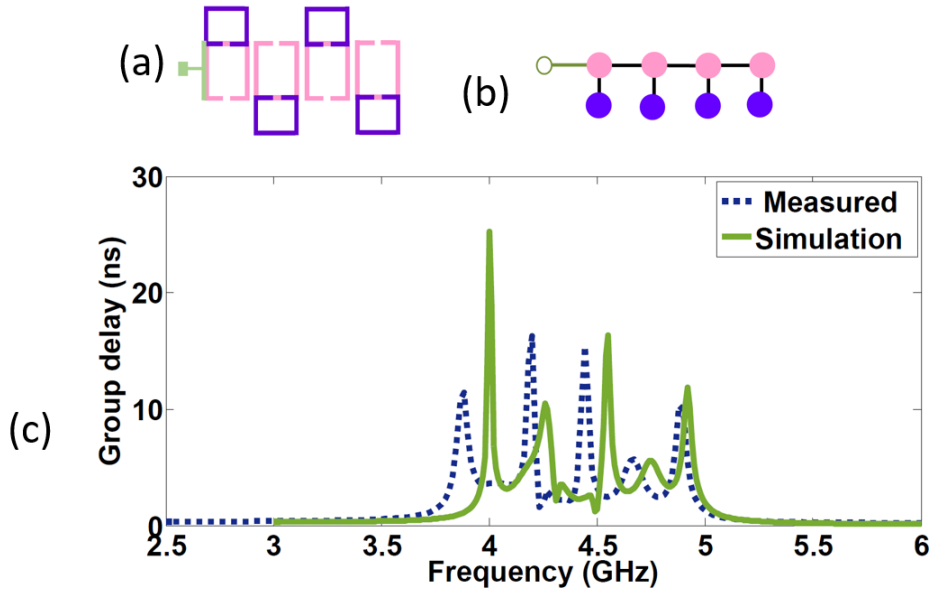

Fig. 4.41 Group delay for: (a) quad-band filter with the rest of the resonator removed except for the single band basis filter; (b) all-pole topology representing circuit in (a); (c) simulated data versus measured data (Filter C).

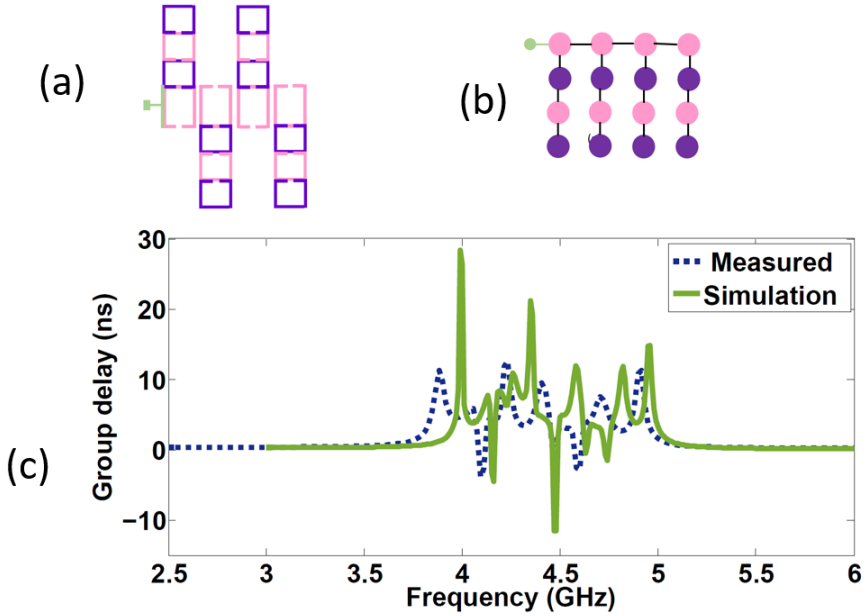

Fig. 4.42 Group delay for: (a) quad-band filter with the rest of the resonator removed except for the single band basis filter; (b) all-pole topology representing circuit in (a); (c) simulated data versus measured data (Filter C)

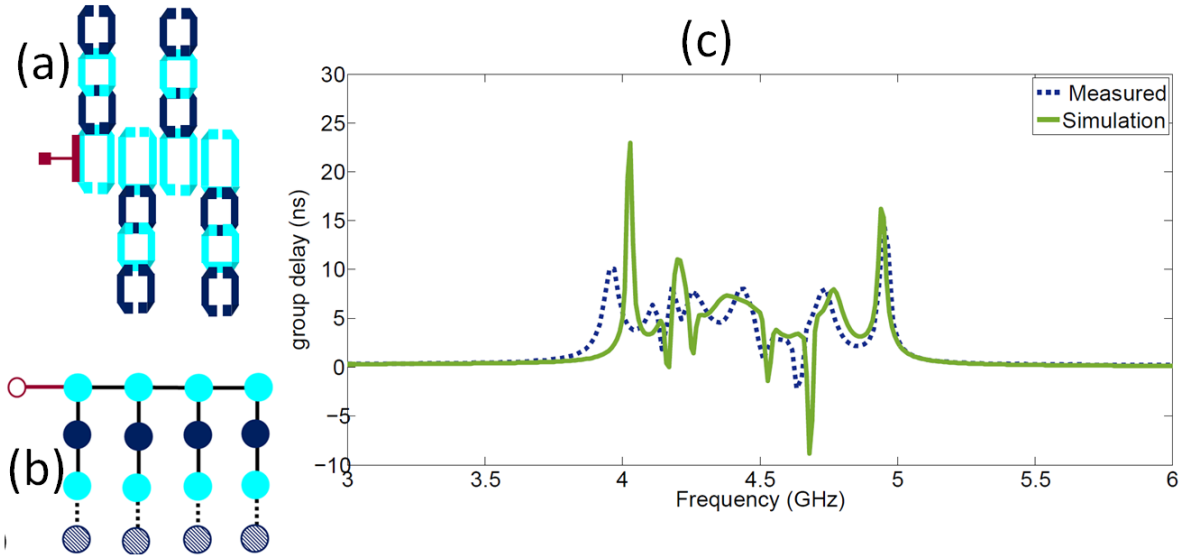

Fig. 4.43 Group delay for: (a) quad-band filter with inserted cuts except for single band basis filter and the first line of appended resonator in a horizontal plane; (b) all-pole topology representing circuit in (a); (c) simulated data against measured data (Filter D).

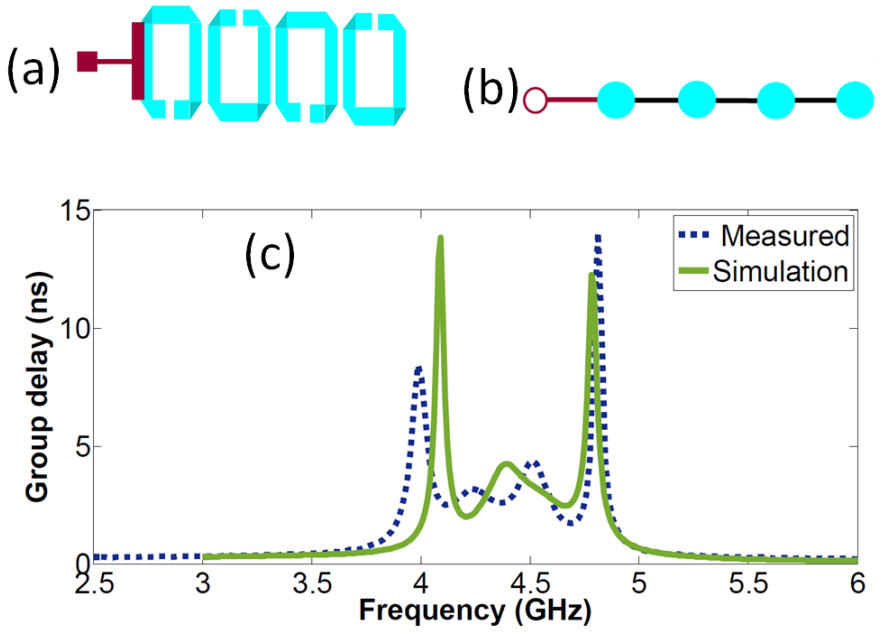

Fig. 4.44 Group delay for: (a) quad-band filter with inserted cuts except for single band basis filter and the first line of appended resonator in a horizontal plane; (b) all-pole topology representing circuit in (a); (c) simulated data against measured data (Filter D).

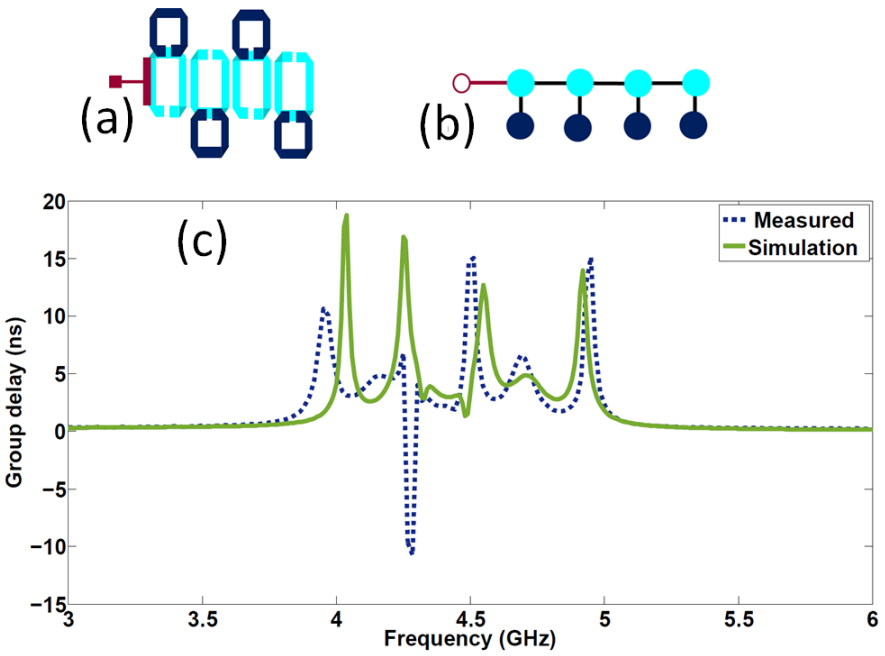

Fig. 4.45 Group delay for: (a) quad-band filter with inserted cuts except for single band basis filter and the first line of appended resonator in a horizontal plane; (b) all-pole topology representing circuit in (a); (c) simulated data against measured data (Filter D).

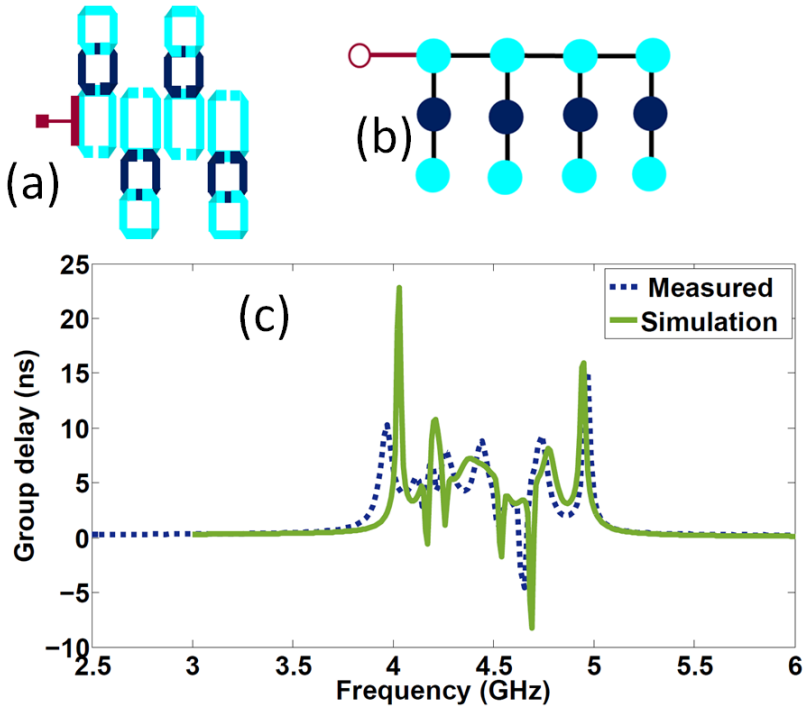

Fig. 4.46 Group delay for: (a) quad-band filter with inserted cuts except for single band basis filter and the first line of appended resonator in a horizontal plane; (b) all-pole topology representing circuit in (a); (c) simulated data against measured data (Filter D)).

4.7 Summary

This chapter dealt with the realization of four microstrip, multi-band filters. Two were transversal topologies with dual- and triple-path, main lines. In these kinds of topologies, resonators were connected to different main paths.

The chapter commenced with a discussion of the advantages of transversal topologies and their method of synthesis which was based on generalized, Chebyshev polynomials. The transversal topologies were achieved through the use of similarity transform. A mathematical technique simplified the coupling matrix to realized networks. The single band coupling matrix served as the basis of the multi-band prototypes which were synthesized, based on the reactance transform method, a fully analytical approach to design multi-band, coupled resonators. The implementation examples illustrate the coupling approaches of nested coupling required for strong coupling and chainlike coupling which provided the required weaker couplings. All the filters were designed on a multi-layer substrate with different substrate heights.

Chapter 5

Switchable Coupled Resonators Dual band Filters

5.1 Introduction

ALL microwave systems need filters to limit the received or transmitted spectrum to the required and legally allowed bands of operation. Multi-band operation of systems are becoming more relevant with the increase in operation over multiple bands. Electronic reconfigurability is an option for utilizing the same filter over more than one band. Over the years, the filter bank technique has been employed to provide multiple frequency responses. The filter bank technique is defined as utilizing several filters with different frequency characteristics, center frequency, as well as bandwidth, which can be switched on and off by employing multi-switches. Disadvantages of this method are that several filters take up a large printing size of the circuit board and too many switches cause losses due to parasitic in the tuning element that operates as switches. An example of the filter bank is presented in Fig. 5.1.

Reconfigurable/tunable filters are grouped as discretely or continuously tuned filters. In general, discrete tuning is possible by utilizing pin diodes or MEMS switches, while continuous tuning is achieved when utilizing varactor diodes, MEMS capacitors, ferro-electric or ferro-magnetic materials. In general, the parameters to reconfigure in a filter include center frequency, bandwidth or selectivity. The most common one is center frequency.

Selecting a switching element, generally, depends on the applications, and some requirements, such as power handling, linearity, loss, switching speed and whether the element suits the mass volume production, have to be considered.

It is preferred that the quality factor (Q factor) of resonators should be high, since it determines the insertion loss of the filter. Filters with high Q factors have excellent performance. Furthermore, ferro-electric varactor diodes have advantages because their quality factor, as well as tuning speed, is high in terms of the frequency range. Although ferro-electric diodes [70, 69]have this great advantage, the construction stage is very complicated because the elements have to be integrated within the substrate. The construction process, employs ferro-electric diodes, remains a challenge. Varactor diodes exhibit the characteristics of semiconductors. These operate as voltage-controlled, variable capacitors in their reversed biased state. In comparison with ferro-electric, varactor diodes have low quality factors. RF MEMS and pin diodes are mainly employed for discrete tuning. These elements switch on and off to activate or deactivate some part of the filter to obtain different frequency responses.

Reconfigurable characteristics in coupled resonator filters are presented in [36, 61] single-band cases. In [36]a varactor tuned, combline filter was designed for wide bandwidth tuning. The combline filter layout and its equivalent circuit consisted of multi-coupled resonators, coupled by series inductors, as shown in Fig. 5.2. In [61] several coupled resonators of orders two and three were tuned by utilizing RF MEMS technology.

In the case of dual-band, filters were designed to have switchable bands, one band at a time. This is demonstrated for multi-mode filters in [21]], based on odd and even mode filters; the layout and frequency response are shown in Fig. 5.3. Switchable filters were designed by combining two individual filters [25, 15] that demonstrated good isolation for prohibited bands, but [25] the size was very large, as two filters were combined to achieve dual bands. The circuit topology and layout for [25] and [15] are shown in Fig 5.5 and Fig 5.4 respectively .

This chapter proposes a switchable, dual-band, coupled resonator filter, with three related circuit models, which exhibits rejected band suppression differently. The proposed filters were analyzed theoretically and two of the three circuit models were constructed. The chapter is organized as follows: Section 5.2 presents a brief touch on the nature of the dual-band filter. Section 5.3 gives an introduction of a pre-selection circuit that served as the basis of the proposed switchable filter and its implementation. This is followed by Section5.4where the implementation and design of pre-selection circuits are discussed. The construction and measurement of the pre-selection, non-resonant circuit are detailed in Section5.5. Section 5.6 presents the three switchable filters (Filter A, Filter B, Filter C) and an analysis and demonstration of the operation of the filter, switching one band while leaving the other intact and vice-versa. Section 5.7 discusses the construction and measurement of switchable filters. Section 5.8 comprises a short summary of the chapter.

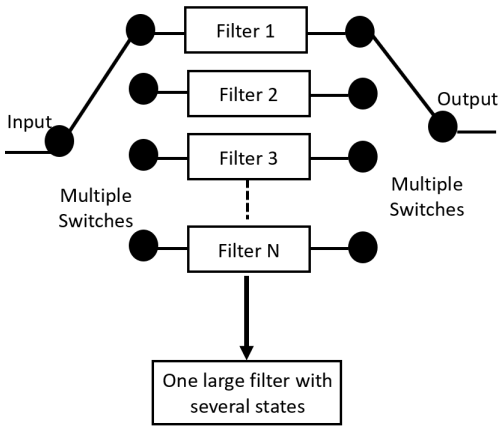

Fig. 5.1 Filter bank [47].

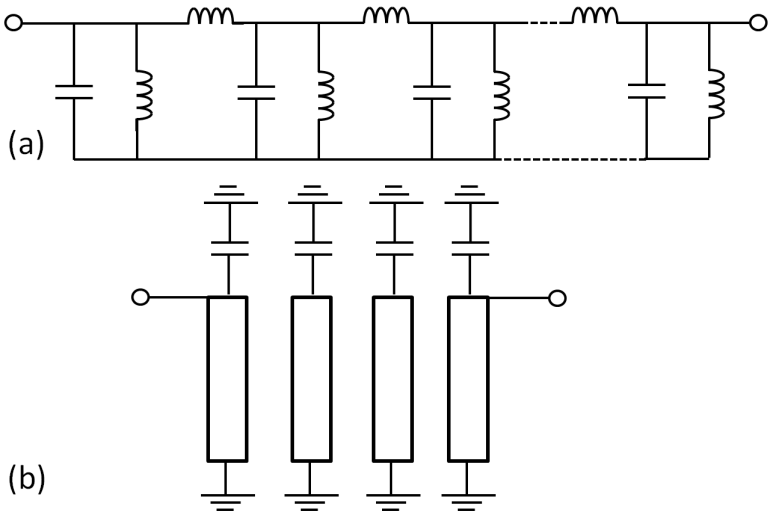

Fig. 5.2 Combline filter (a) equivalent circuit (b) layout [36].

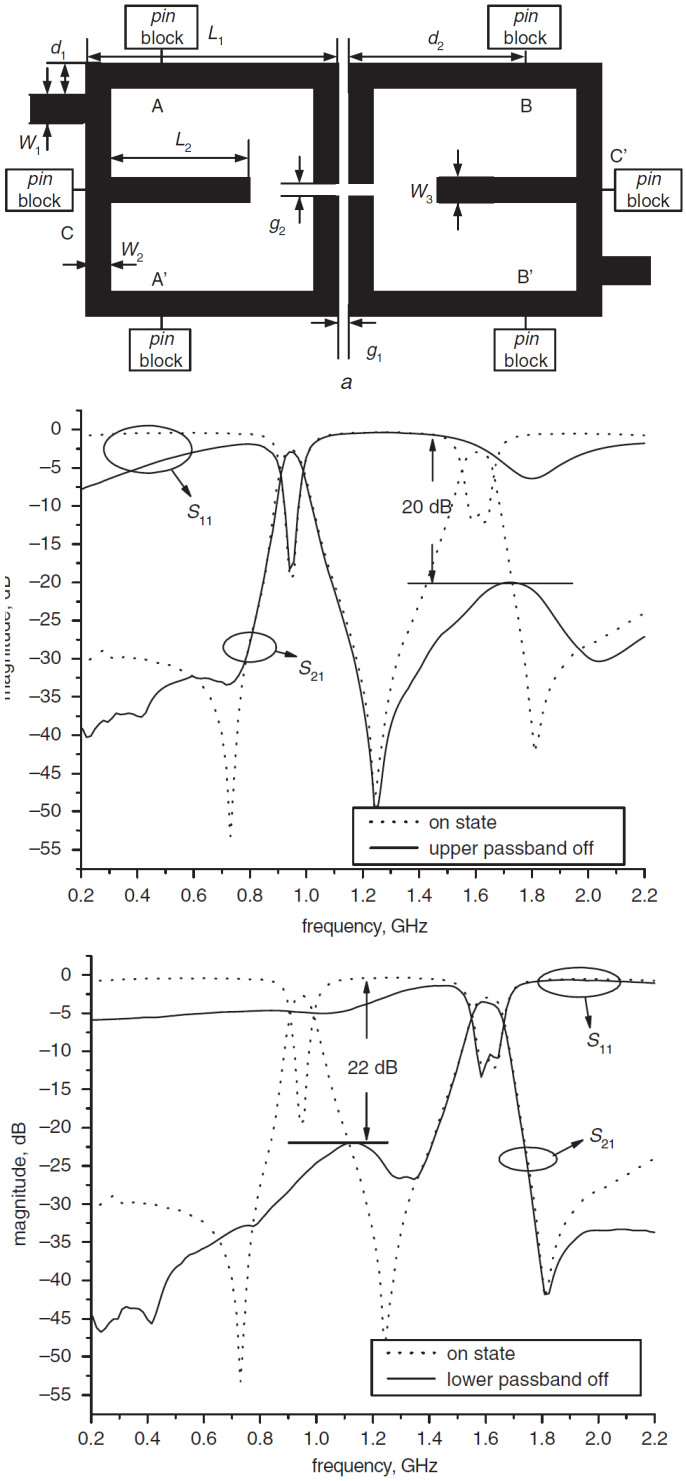

Fig. 5.3 Configuration of switchable filter and its frequency responses [21] .

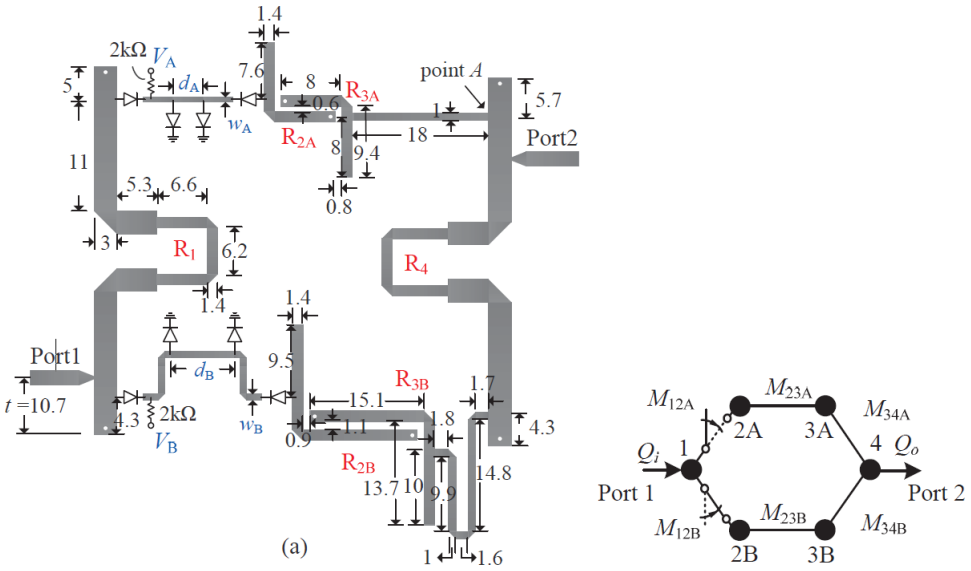

Fig. 5.4 Layout and circuit topology of switchable filter in [15] .

5.2 Coupled resonator dual-band filter

The proposed switchable filter is based on dual-band coupled-resonator filter synthesized based on a reactance transform method [7] as one filter structure. The filter was implemented on multiple layers for compact size as detailed in [30]. Figure 5.6 shows the filter topology employed for a parallel connected topology of order 4 (shaded in blue), with appended resonators added to define a total of 2 pass-bands.

For this topology, switching or tuning even one of these resonators affects the filter response in both bands. While it may be possible to switch and/or tune individual resonators separately to achieve changes in the pass-bands, it is clear from Fig 5.6 that the number of resonators involved (eight for our dual-band filter) would render this approach practically non-viable for all but the lowest order filters. Therefore, our proposed approach was to utilize a transmission line-based pre-selection filter of a very basic nature to select the desired pass-band out of the 2 pass-bands. This chapter details the utilization of a multi-band filter to produce a switchable filter with two different states. The approach was based on combining a pre-selection circuit to a dual band filter for switching the bands. The switchable filter operates between two pass-bands 3.1 GHz - 3.3 GHz and 3.6 GHz - 3.8 GHz. It selects one of the pass-bands at a time, as shown in the conceptual illustration graph in Fig 5.7(b) and (c).

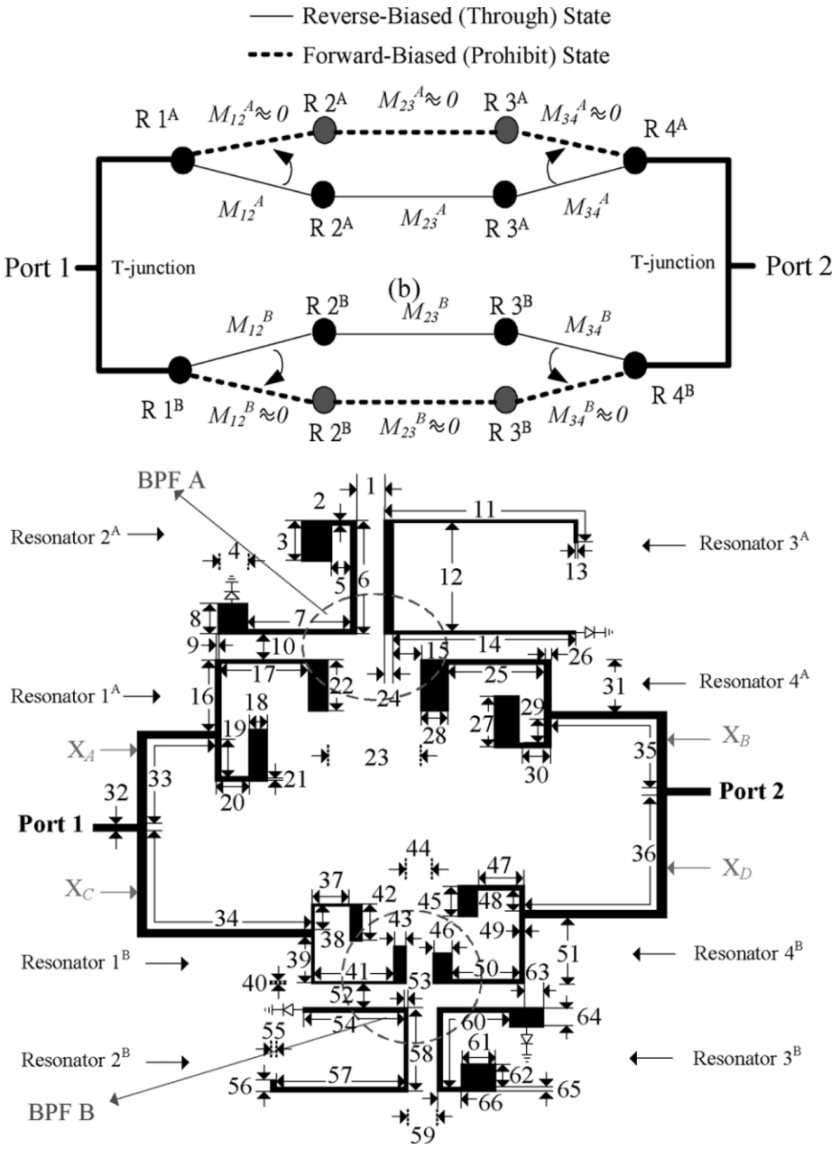

Fig. 5.5 Layout and circuit topology of switchable filter in [25].

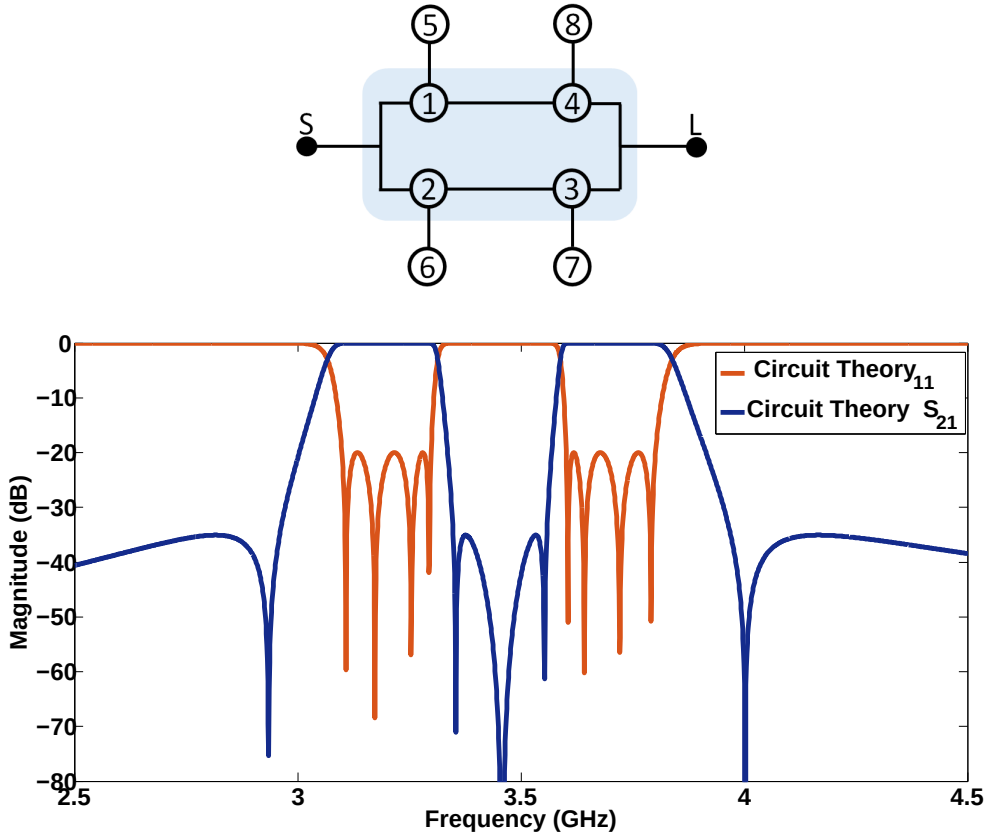

Fig. 5.6 Topology of a fourth order parallel connected single band prototype transformed to a dual band filter and its frequency response.

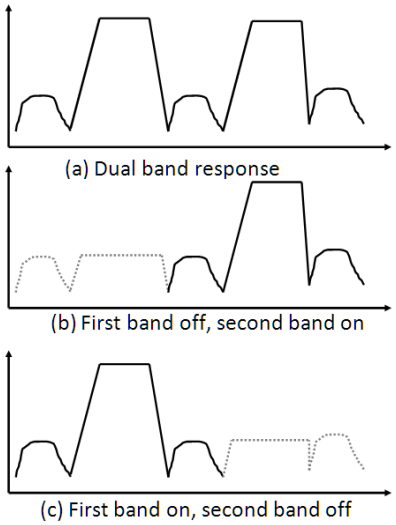

Fig. 5.7 (a) Conceptual illustration of the selected and prohibited bands.

5.3 Pre-selection non-resonant circuit theory

The reactance transform topology allows electronic reconfigurability but the system of coupled resonators is so interconnected that reconfiguring or switching one resonator affects all the pass bands. Since the coupled resonator multi-band filter relies on a network of coupled resonators, de-activating or de-tuning even one of the resonators would lead to the destruction of the entire filter response. To avoid this, a non-resonant method of electronic switching can be used instead. The non-resonant method has the following attractive features:

- It does not affect the order of the coupled resonator filter or any of the coupling elements.
- It has the ability to realize independent switching; thus, it is capable of switching off one band while keeping another standing.
- The transmission zeros produced by a dual-band filter remain static, and the non-resonant circuit does not interfere with the filter selectivity.
- The center frequency and the bandwidth of the desired pass band is preserved.
- It utilizes only two pin diodes; thus, the losses due to the lumped elements are minimal.

The concept relies on cascading the dual-band filter with an electronically switchable, pre-selection circuit, by employing PIN diodes as switches Fig. (see 5.9.)

The pre-selection filter is made of transmission line model. According to AWR software the transmission line is defined as a grounded shield (closed form) TLIN. The symbol of TLIN is presented in Fig 5.8. TLIN has the following parameters, (i) transmission line impedance (Z_0), (ii) electrical length (phase length) at F_0 (EL) and (iii) frequency employed to specify EL,(F_0). The parameters EL and F_0 determine the frequency dependence of the electrical length of the line, described as

$$\beta L = EL \cdot \frac{f}{F_0} \frac{\pi}{180} \tag{5.1}$$

where f is the evaluation frequency. TLIN simulates an ideal, lossless transmission line. The model requires that the line length be specified as electrical length (phase lag of mode propagating along the line) at user-specified frequency. The user must supply value the of characteristic impedance.

Fig. 5.8 Transmission line (TLIN) model

Table 5.1 Impedance and electrical values of the circuit in Fig 5.9 (a)

Impedance (Ω)		Electrical Length (degree)	
Z_0	57.1	θ_0	71.3
Z_1	16.1	θ_1	134
Z_2	23.65	θ_2	137
Z_3	131.4	θ_3	59.2
Z_4	69.8	θ_4	94
Z_5	40.55	θ_5	178
Z_6	72.2	θ_6	134
Z_7	37.1	θ_7	43.5

5.3.1 One stage pre-selection non-resonant circuit

Figure 5.9 shows the proposed pre-selection non-resonant circuit. The circuit is formed by the TLIN model, the two open ends are loaded with pin diodes; the other are entry to input and output port of the circuit. The pre-selection non-resonant circuit has characteristics impedance Z_1, Z_2, Z_3, Z_4, Z_5, Z_6, Z_7, and electrical length of θ_1, θ_2, θ_3, θ_4, θ_5, θ_6, θ_7. The values are provided in Table 5.1.

One of the contributions of this work is the manner in which a selected pass-band was activated or de-activated. When both diodes were switched on (forward biased), all transmission lines on the pre-selection filter were in full use (see Fig 5.9(b)). When both diodes were switched off (reversed biased), the transmission lines, Z_4, Z_6, with electrical length of θ_4, θ_6, were cut off from the rest of the model as depicted in (see Fig 5.9(c)). The ON and OFF state response produced by the circuit in Fig 5.9(a) is given in Fig 5.10.

5.3.2 Cascaded two stages pre-selection non-resonant circuit

The proposed non-resonant circuit in Fig 5.9 has the advantage of good selectivity as the transmission zeros are preserved. The suppression of the undesired band is below 20 dB. To increase the suppression, the approach is to cascade the non-resonant circuit to two stages, which further improves the suppression depth to almost 40 dB twice that of a single stage. Figure 5.11 presents the circuit which consists of two-stages, non-resonant sections and comprising cascaded connections, schematically. The frequency response of a lossless two

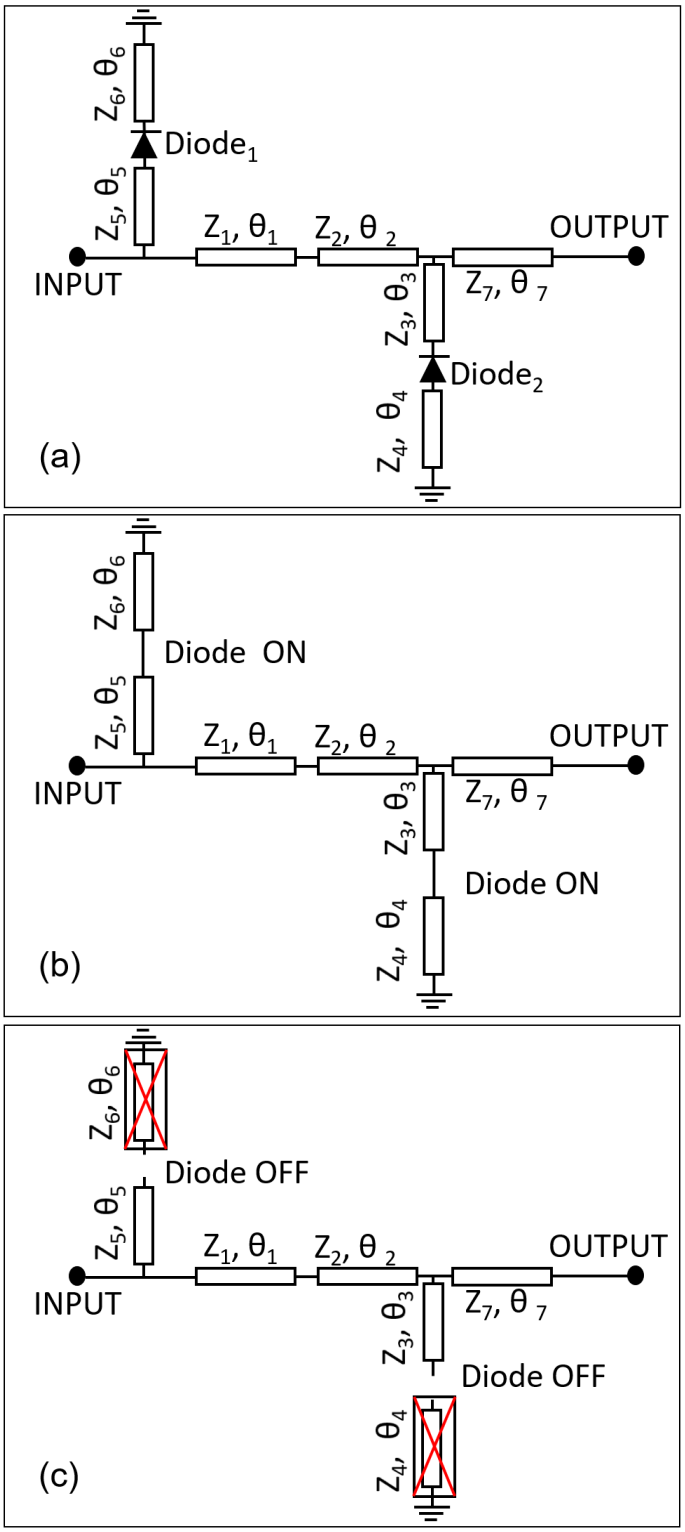

Fig. 5.9 Pre selection operation circuit (a) two pin diodes are inserted (b) On and (c) Off states

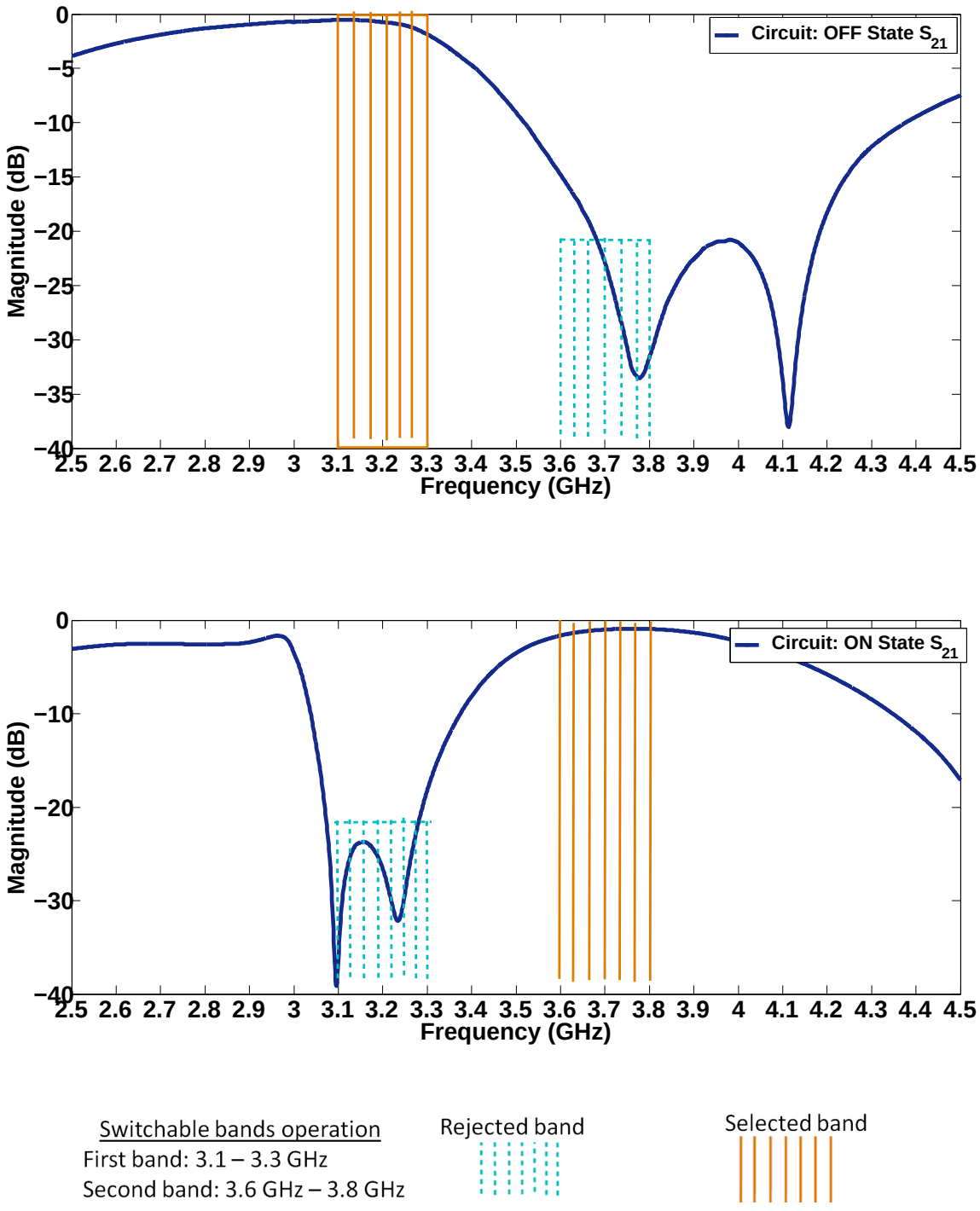

Fig. 5.10 Frequency responses of the pre selection non-resonant circuit operation OFF and ON states.

stages, pre-selection circuit is presented in Fig 5.12 . The non-resonant circuit is cascaded to two stages to increase the suppression of a prohibited band.

5.4 Design of a pre-selection non-resonant circuit

Figure 5.13 shows that the circuit structure consisted of unequal width transmission lines presenting different impedance and electrical lengths Z_3 and θ_3, Z_4 and θ_4, Z_5 and θ_5, Z_6 and θ_6 as well as Z_7 and θ_7 each had different width. The middle line Z_1 and θ_1, Z_2 and θ_2 as well as Z_7 and θ_7 were designed with stepped width. One important condition to note is that the pre-selection was designed on the same substrate as the dual-band filter. The pre-selection, non-resonant circuit was embedded on a Mercury wave substrate on the topmost layer. The single stage had two diodes while the two stages circuit consisted of four Skyworks PIN diodes (SMP1345-079LF) for switching, respectively. DC bias circuit elements and pin diodes were on the top layer, where capacitors blocked DC and inductors isolated the circuit from RF. The layout of the one-stage circuit is depicted in Fig. 5.13 and the two-stages is shown in Fig 5.15. Figure 5.14shows (a) a 3D view in (b), top view of the one-stage, pre-selected circuit. Thee two-stages are presented in Fig 5.16.

5.5 Construction and measurement of the pre-selection, non-resonant circuit

The proposed, pre-selection, non-resonant circuits discussed above were constructed and photographs of the single and two stages circuit with biasing scheme are presented in Fig 5.18. The measured results versus simulation are plotted in Fig 5.18 (a) for OFF and (b) ON states of the one-stage circuit. Figure 5.19 shows the response of the two stages circuit.

5.6 Switchable filter designs

The pre-selection, non-resonant circuit and a dual-band filter were combined to create a new network comprising a switchable dual-band filter. The following steps detail the design procedures of the switchable, dual-band, coupled resonator filter:

- Synthesize and design a dual-band filter as detailed in [7] and [30] respectively .
- Design the pre-selection non-resonant circuit discussed in Sections 5.3 to 5.4. Include the PIN diodes (SMP1345-079) model. The pin diodes data files were available

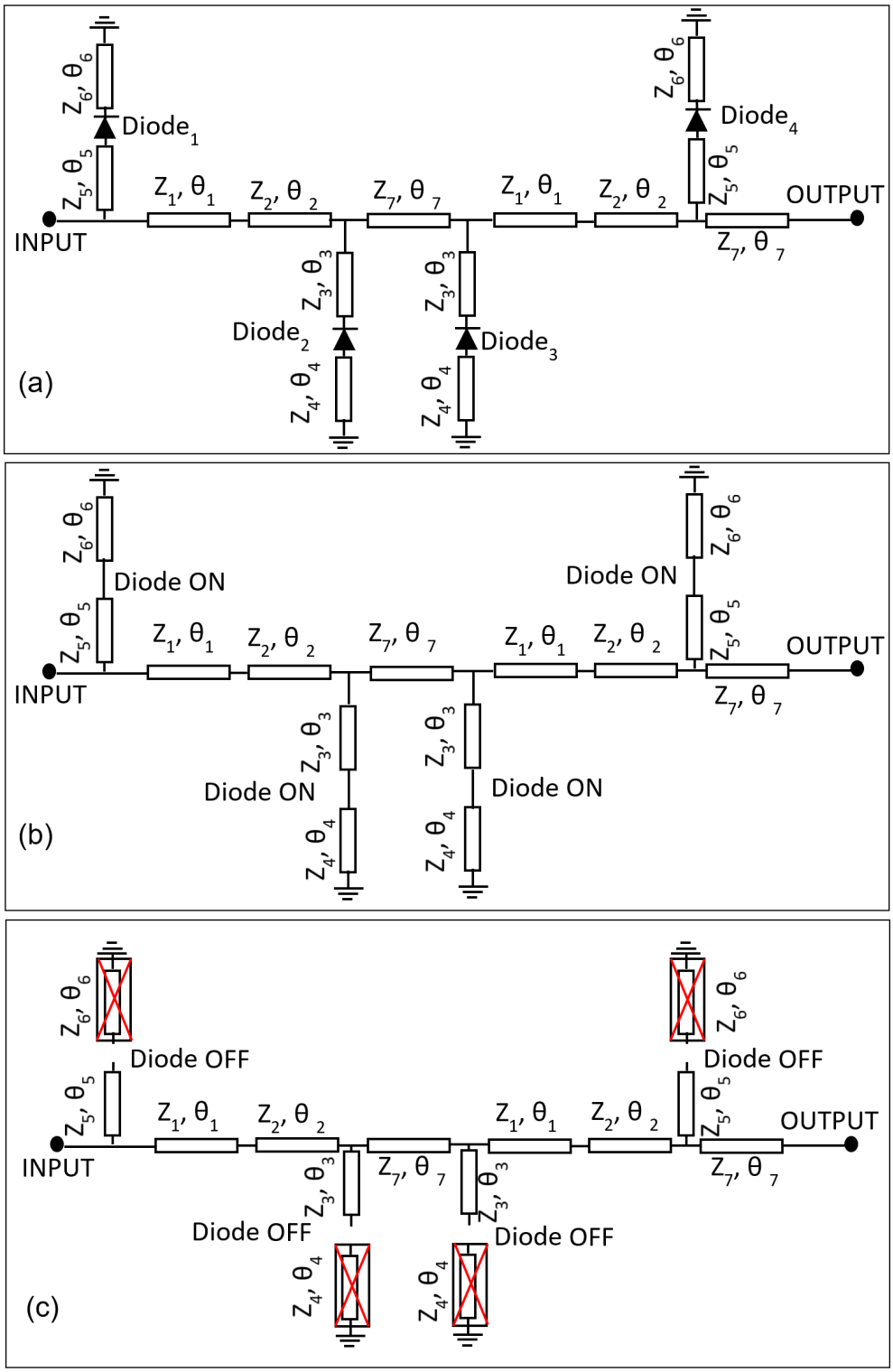

Fig. 5.11 (a) Two stage pre-selection non-resonant circuit topology (b) On and (c) Off states

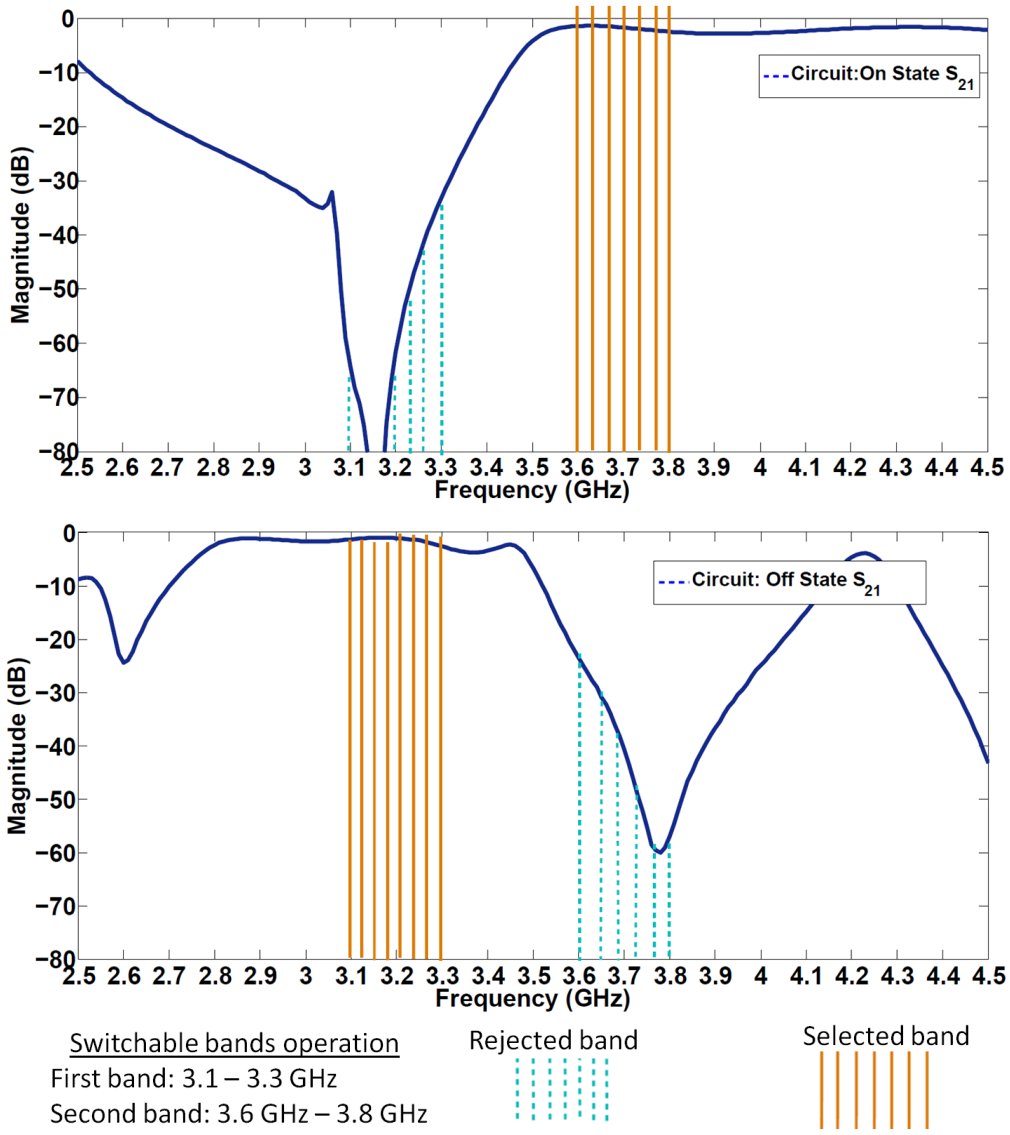

Fig. 5.12 Frequency responses of the two stages pre-selection non-resonant circuit topology.

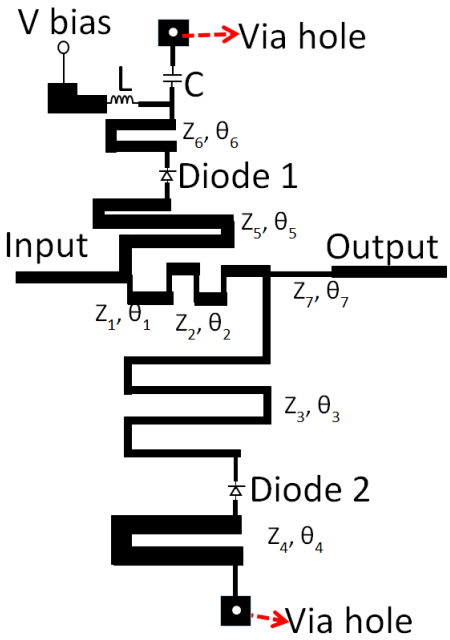

Fig. 5.13 One-stage pre-selection circuit layout.

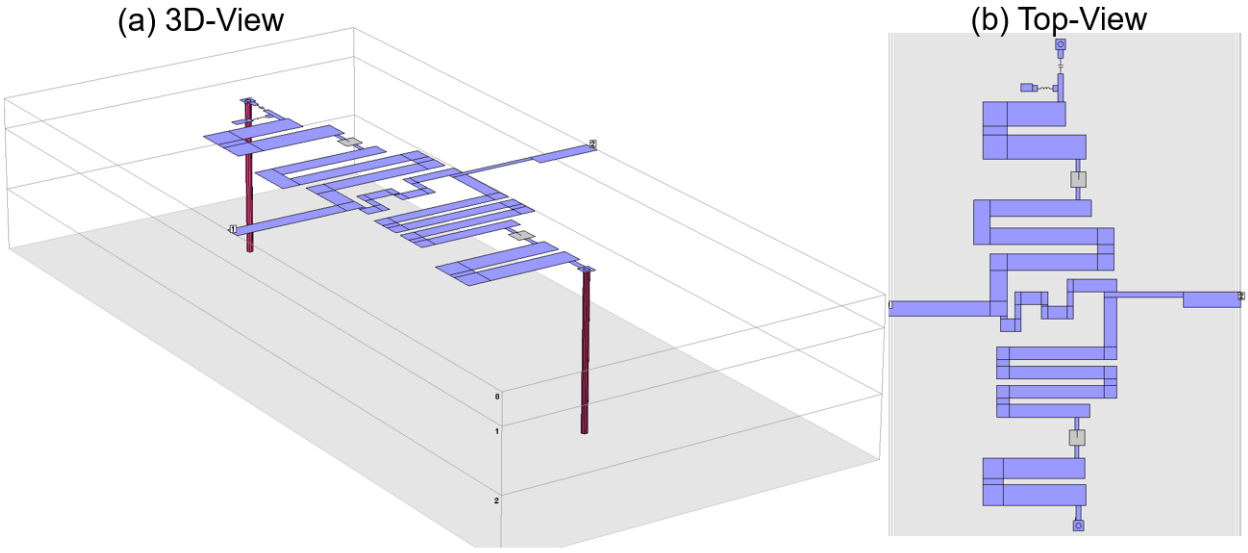

Fig. 5.14 The design of the pre-selection non-resonant circuit (a) 3 D view, (b) Top View.

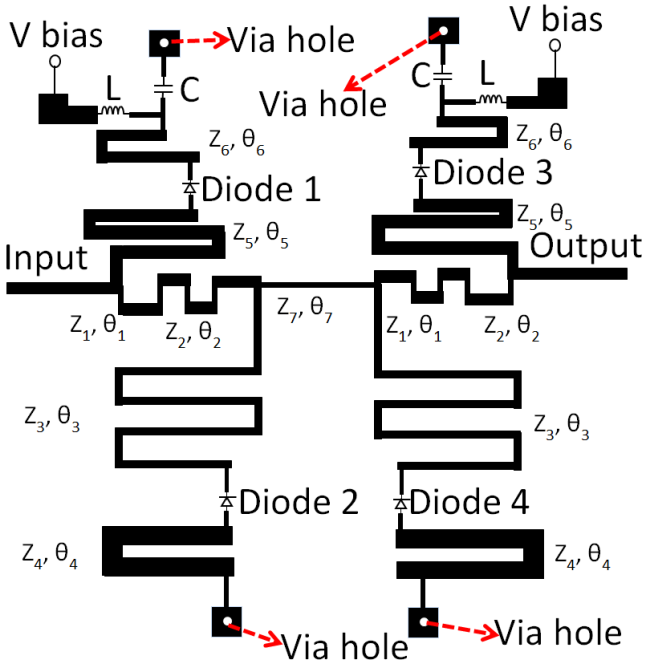

Fig. 5.15 Two-stages pre-selection non-resonant circuit layout.

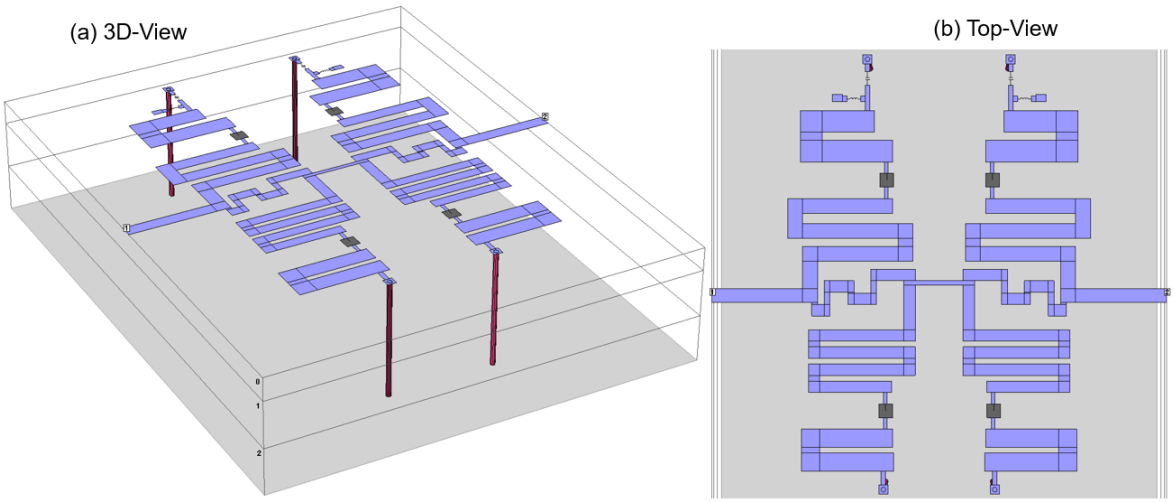

Fig. 5.16 The design of the two-stages pre selection non-resonant circuit (a) 3 D view, (b) Top View.

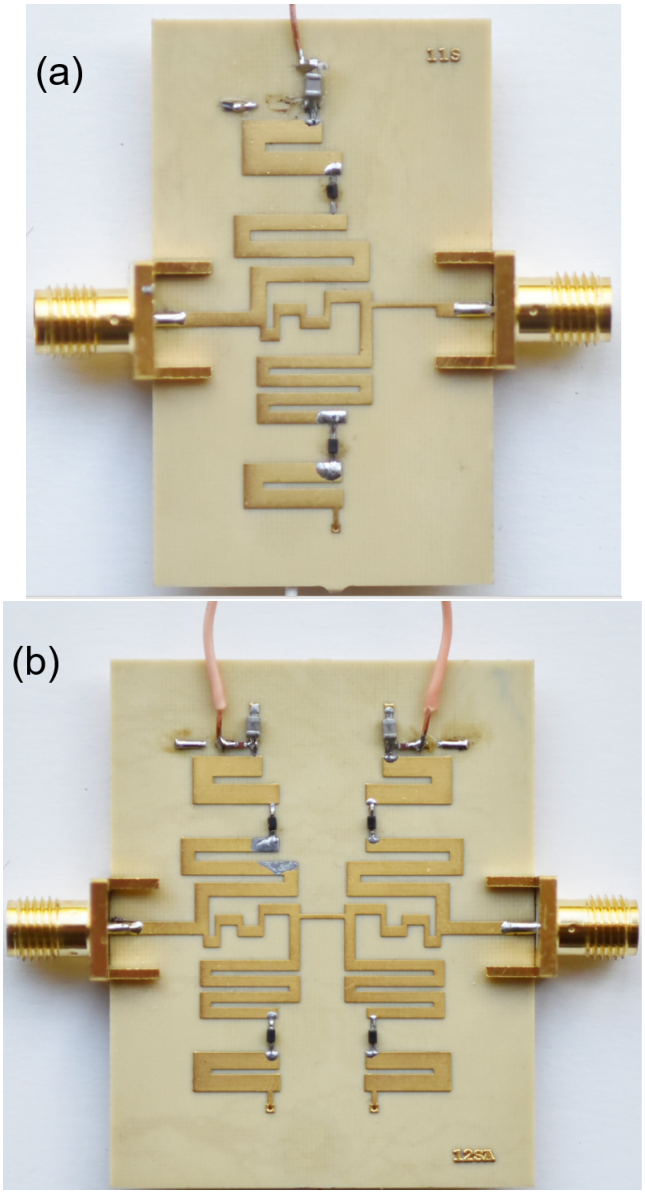

Fig. 5.17 The photographs of the fabricated pre-select non-resonant circuit (a) one stage (b) two stages.

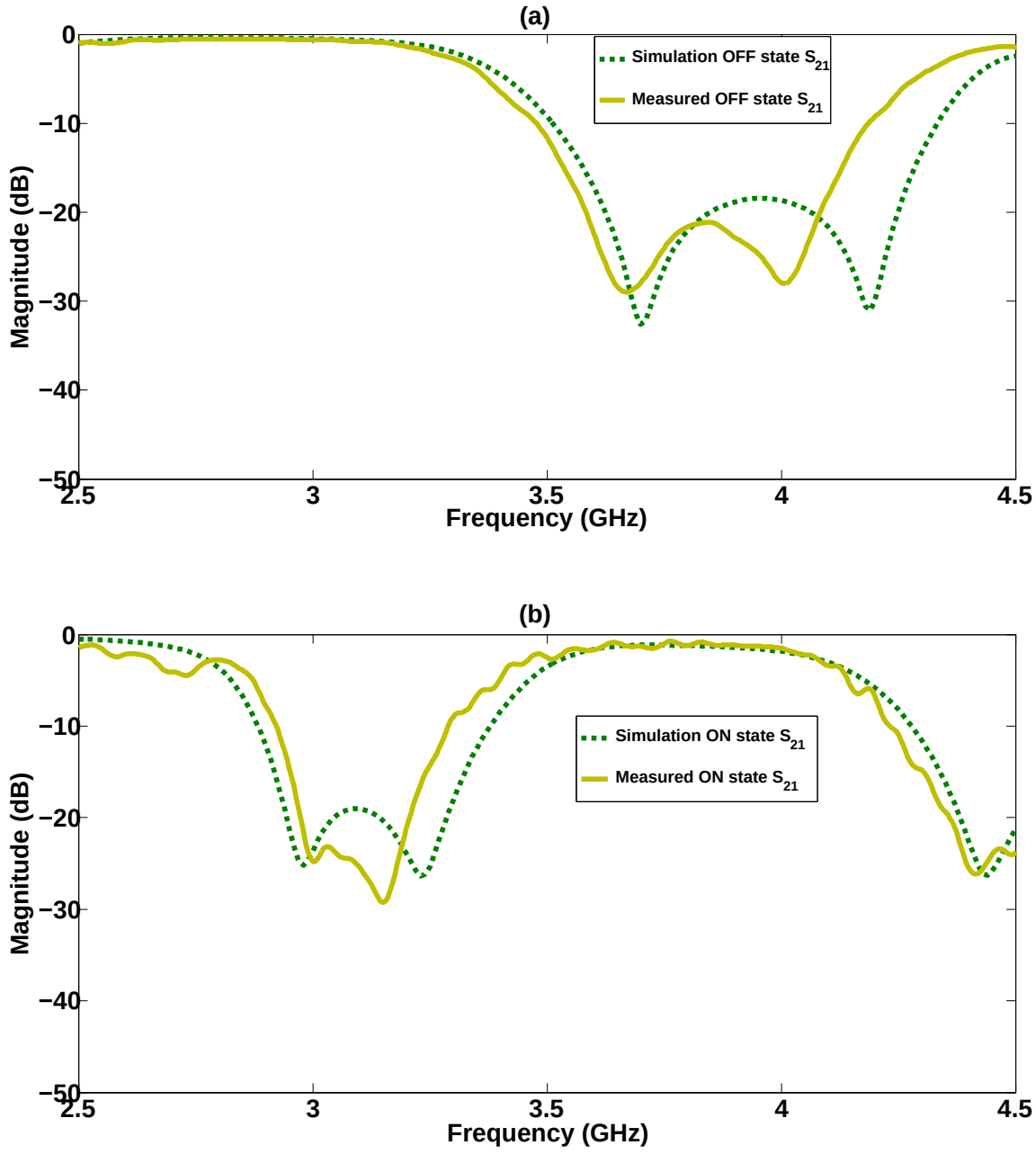

Fig. 5.18 The simulation versus measured plot of one stage pre-select non-resonant circuit (a) OFF state (b) ON state.

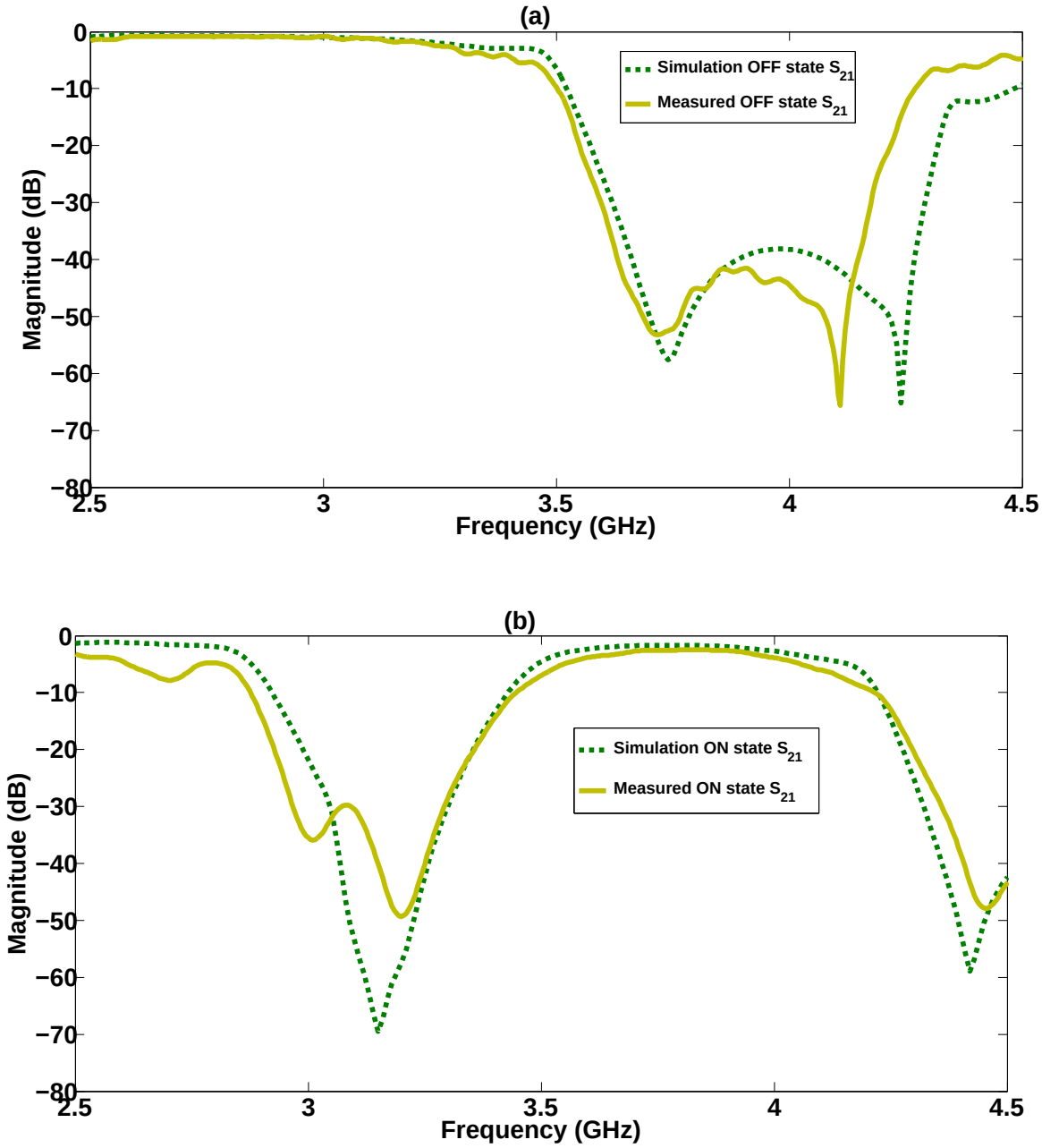

Fig. 5.19 The simulation versus measured plot of two stages pre-select non-resonant circuit (a) OFF state (b) ON state.

at the Skyworks websites. By the reversed- and forward-biasing of the diodes, the pre-selection, non-resonant circuit suppressed one band and selected another.

- Cascade/combine the dual-band network to the pre-select non-resonant circuit to create a switchable filter.

5.6.1 5.6.1 The implementation and analysis of the switchable dual-band filter

The lumped-element schematic circuit in Fig 4.3(b) represents a dual-band circuit topology in Fig 5.6. The coupling matrix of this topology is provided in Section 4.2 as $M_{FilterA}$. The pre-selection non-resonant circuit discussed in 5.3 to 5.4 was cascaded to a dual-band filter. The core subject of this section regards the physical implementation of a switchable dual-band microwave filter, which was realized on a Mercury wave, multi-layer substrate with a dielectric constant of 3.5 and total thickness of $h = 0.5126$ mm simulated by employing sonnet software.

Physical structure of a switchable dual-band filter

The physical structure of a dual-band filter is presented in 3 related implementations of Filters A, B and C. The circuit model of Filter A is shown in Fig. 5.21, representing the layouts in Fig.5.22. Figure 5.24 presents the Filter B circuit model, and its layout is shown in Fig. 5.25 . The Filter C circuit model and its layout are presented in Fig.5.27 and 5.28. Filter A consists of a one-stage, pre-selection, non-resonant circuit with only two pin diodes. Filters B and C consist of a two-stages, non-resonant circuit, each loaded with four pin diodes. The diodes are responsible for switching the bands, the capacitance (C's) serves as the dc block; inductance (L's) is an RF choke in all three filters. To understand the layouts and the associated circuit models, the corresponding circuit model parameters are indicated on the layout of each filter (A, B, C). All filters were designed on the same substrate height, with four metallic layers, as detailed in Fig. 5.20.

5.6.2 Performance analysis

Ideal switchable dual-band filter

Switching is experimented on an ideal lossless circuit in Fig (see 5.21, 5.24 and 5.27) to predict switching in a physical layout in (see Fig 5.22 , 5.25 and 5.28) respectively. Although the pin diodes were included for switching, from the observation the response obtained was

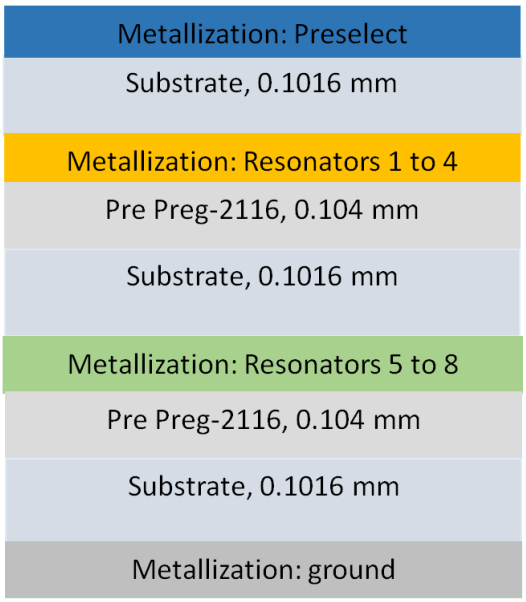

Fig. 5.20 Layer stack up of switchable filters A, B, and C.

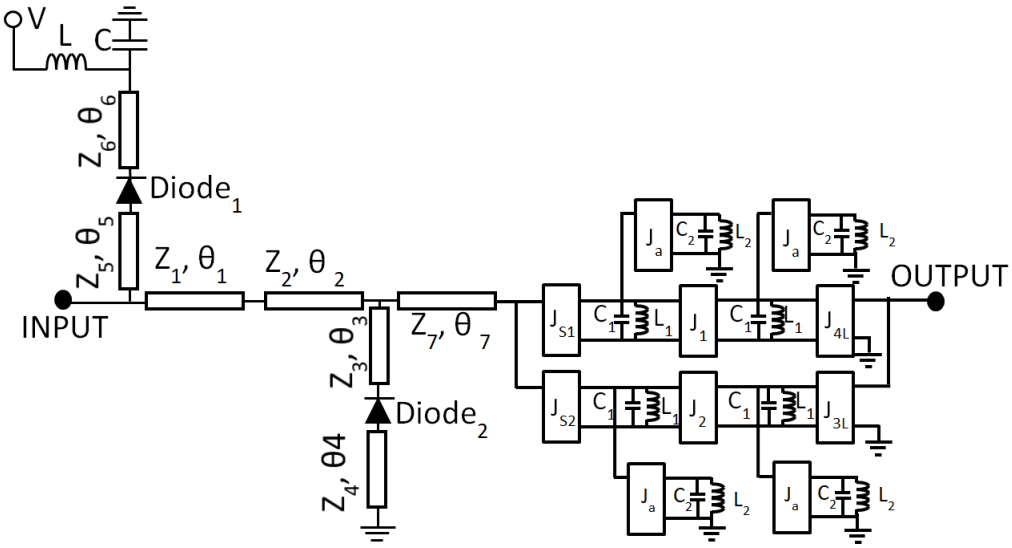

Fig. 5.21 Proposed switchable dual-band filter topology (Filter A).

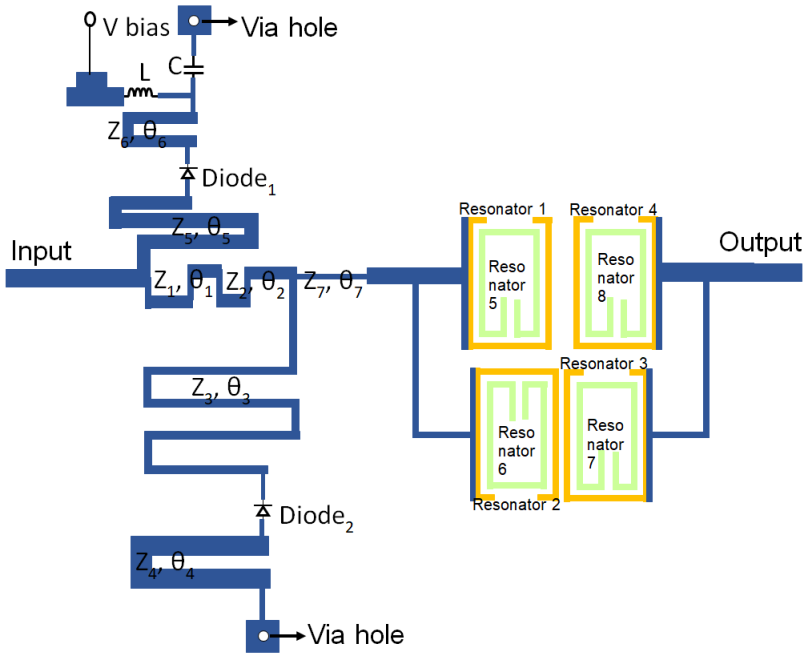

Fig. 5.22 The proposed pin-diode-based switchable dual-band filter layout (Filter A).

that little effect of the losses was due to the pin diodes. The frequency responses of the lossless ideal circuit of Filter A is shown in Fig 5.30. The ideal frequency response for Filter B is shown in Fig 5.32 and that for Filter C in Fig 5.34. Regarding Filter A, suppression of the undesired band was about 20 dB in both cases ON and OFF. The rejection of the prohibited band could be increased by cascading the pre-selection circuits to two stages and the suppression range from 30 to 40 dB. The two stages were implemented in a symmetric (Filter B) where dual-band filter was sandwiched between two pre-select circuit stages. For thr asymmetric Filter A and C the pre-select circuit is next to the dual-band filter.

Frequency selectivity of the switchable filter

From the ideal responses, all Filters A, B and C, exhibited good selectivity of the selected band. The non-resonant, pre-select circuit did not interfere with the original transmission zeros appearing in a dual-band filter. The two transmission zeros on each side of the selected band remained static. This was confirmed by the plotting of each filter (A, B, C) of lossless, switchable filters versus the fixed, dual-band filter circuit model in Fig. 5.30 for Filter A, Fig.5.32 for Filter B and Fig. 5.34 for Filter C. The graph for the lossless, switchable filter simulation versus the lossless circuit model ON and OFF state are presented in Fig. 5.31 for filter A, Fig. 5.33 for filter B and Fig. 5.35 for filter C.

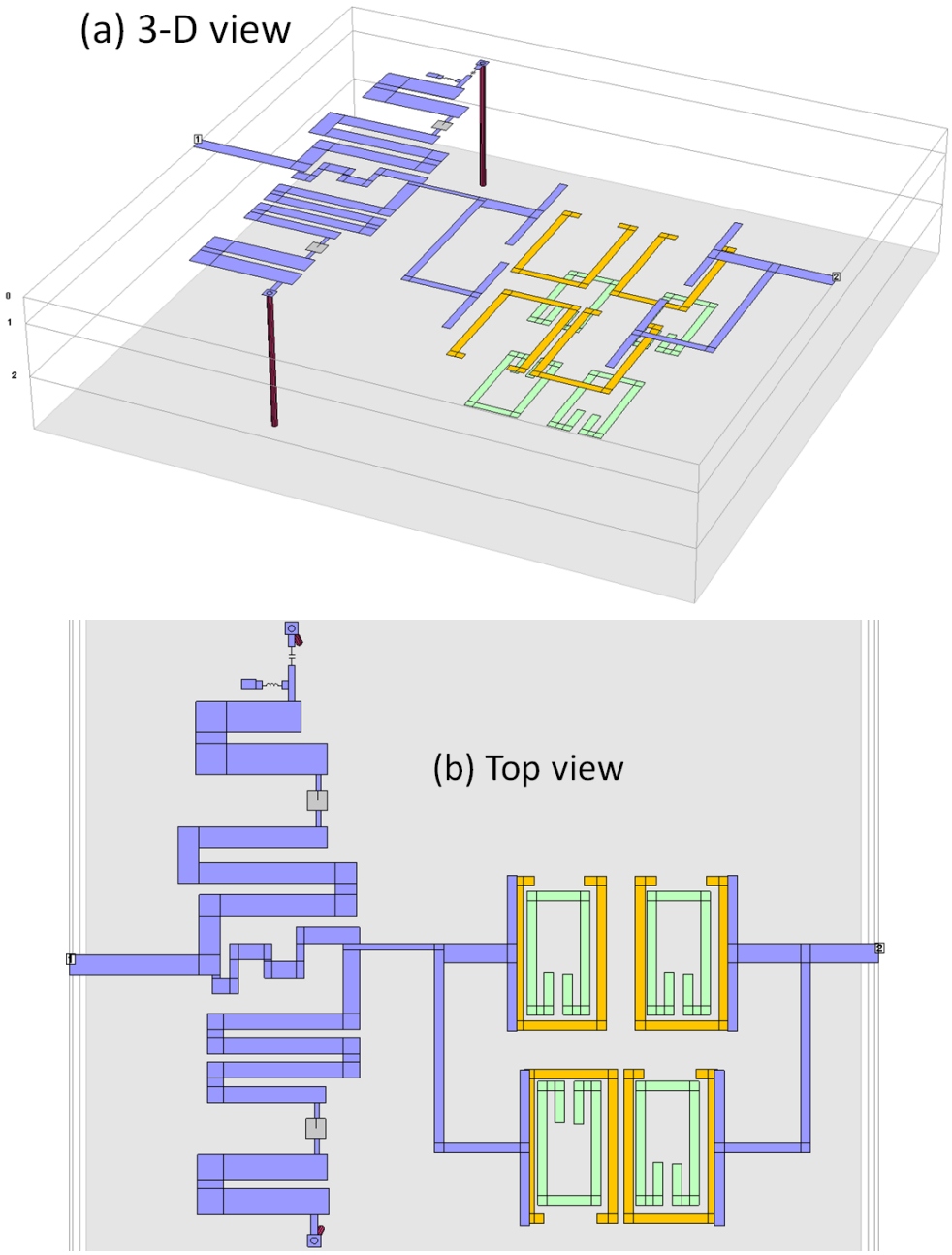

Fig. 5.23 Switchable filter (a) 3 D view, and (b) Top View of Filter A

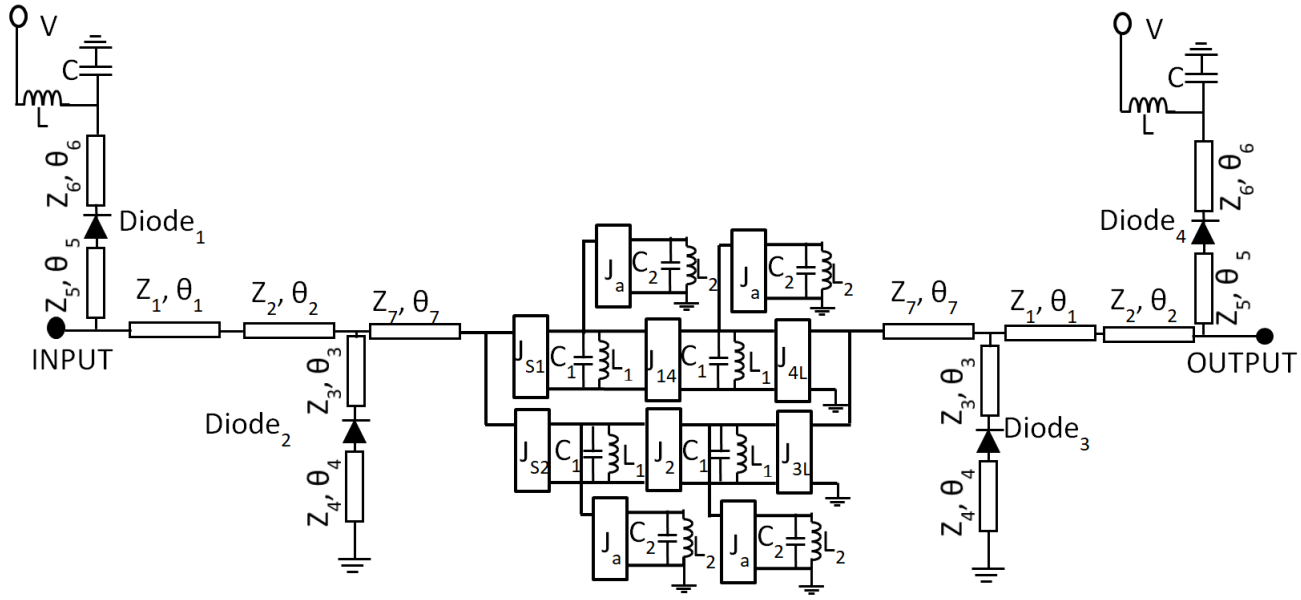

Fig. 5.24 Proposed switchable dual-band filter topology (Filter B) with two stages pre-select non-resonant circuit (Symmetric arrangement).

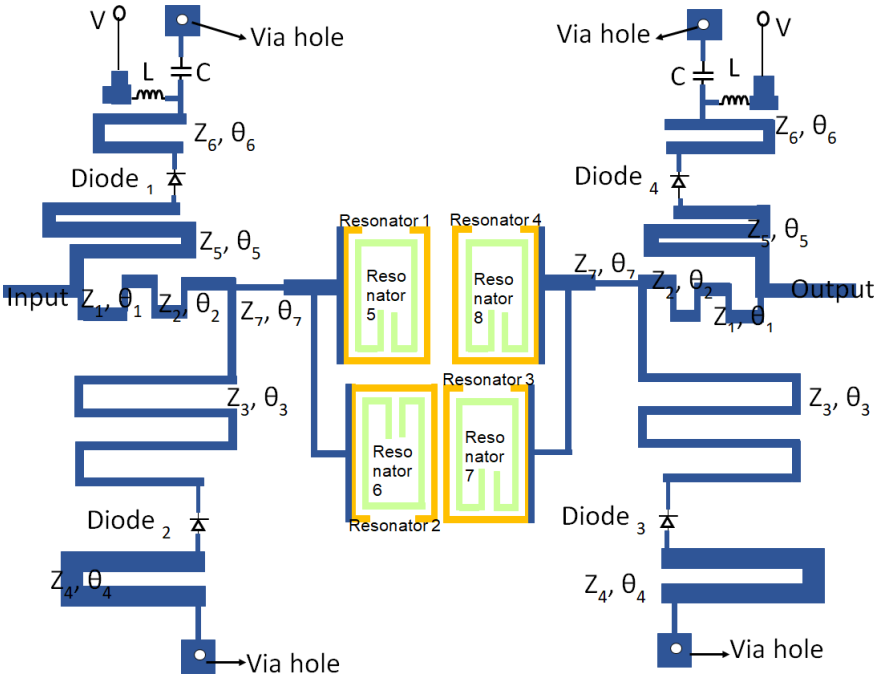

Fig. 5.25 The proposed pin-diode-based switchable dual-band filter layout (Filter B) with two stages pre-select non-resonant circuit (Symmetric arrangement).

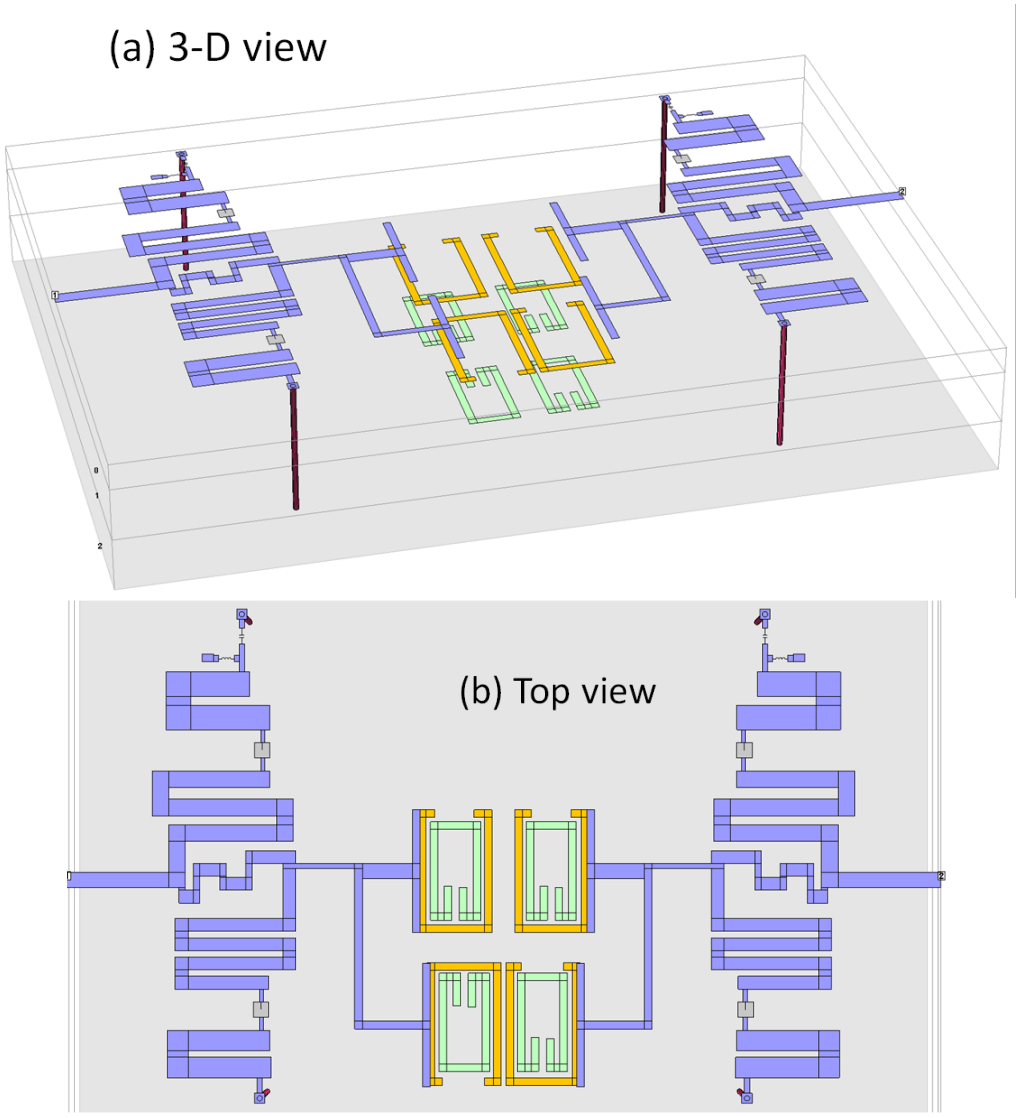

Fig. 5.26 Switchable filter (a) 3 D view, and (b) Top View of Filter B

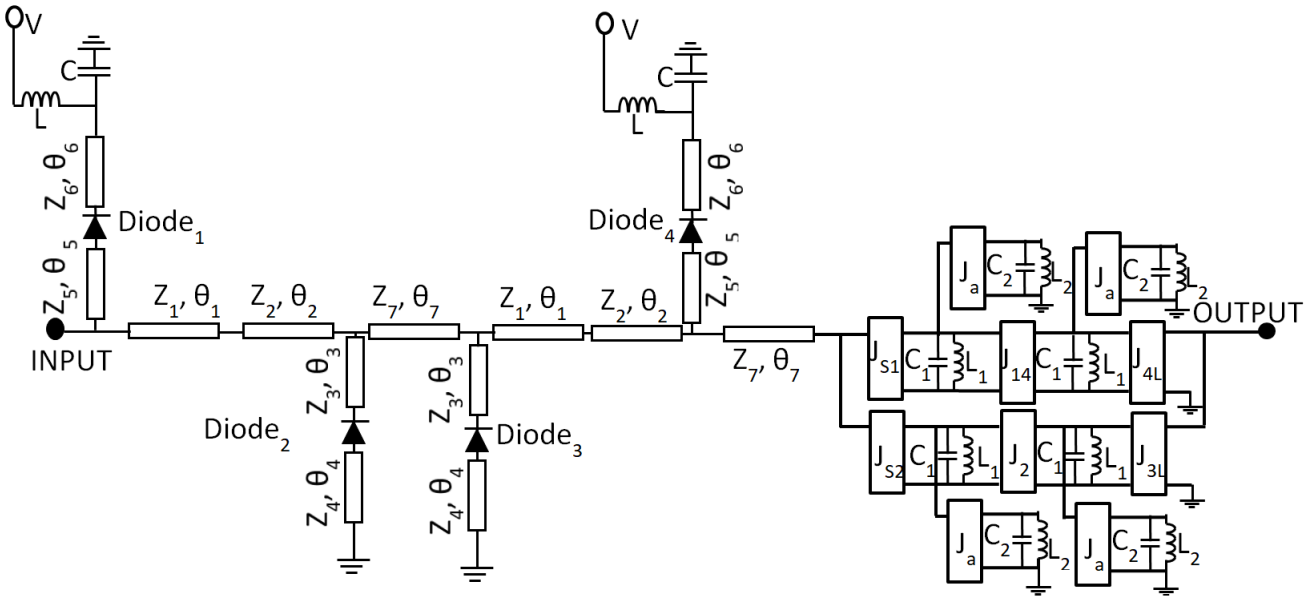

Fig. 5.27 Proposed switchable dual-band filter topology (Filter C) with two stages pre-select non-resonant circuit.

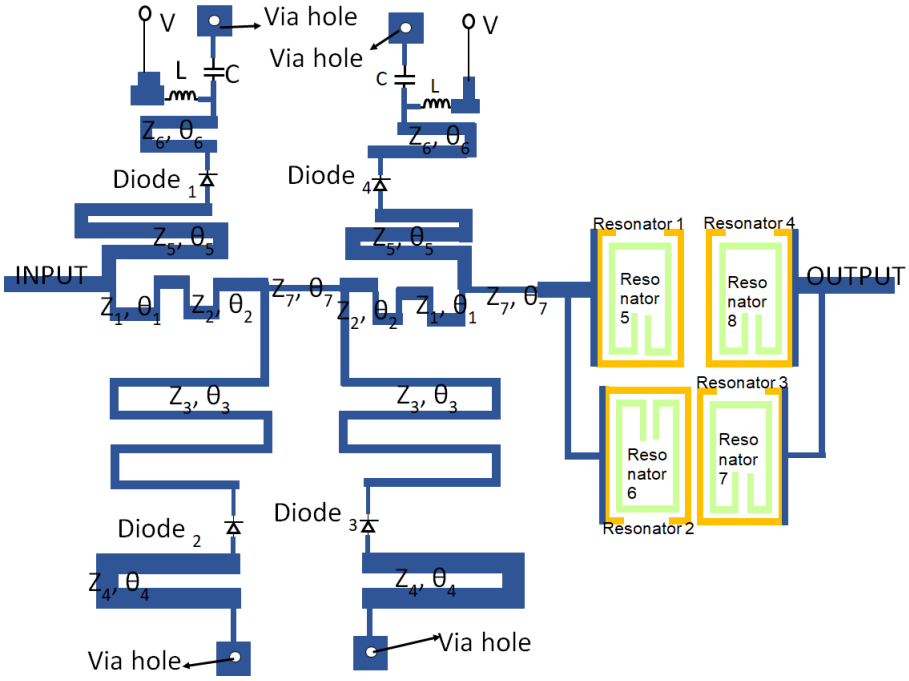

Fig. 5.28 The proposed pin-diode-based switchable dual-band filter layout (Filter C) with two stages pre-select non-resonant circuit.

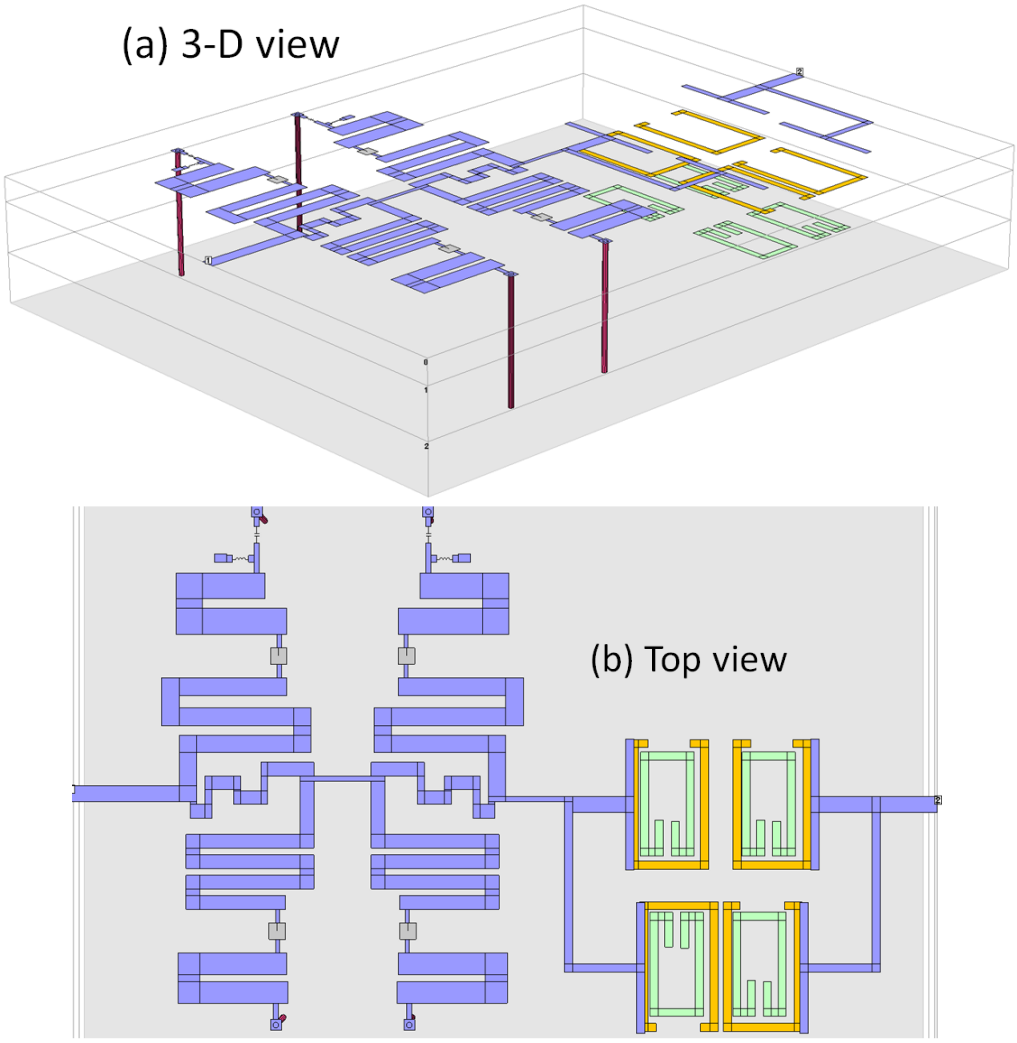

Fig. 5.29 Switchable filter (a) 3 D view, and (b) Top View of Filter C

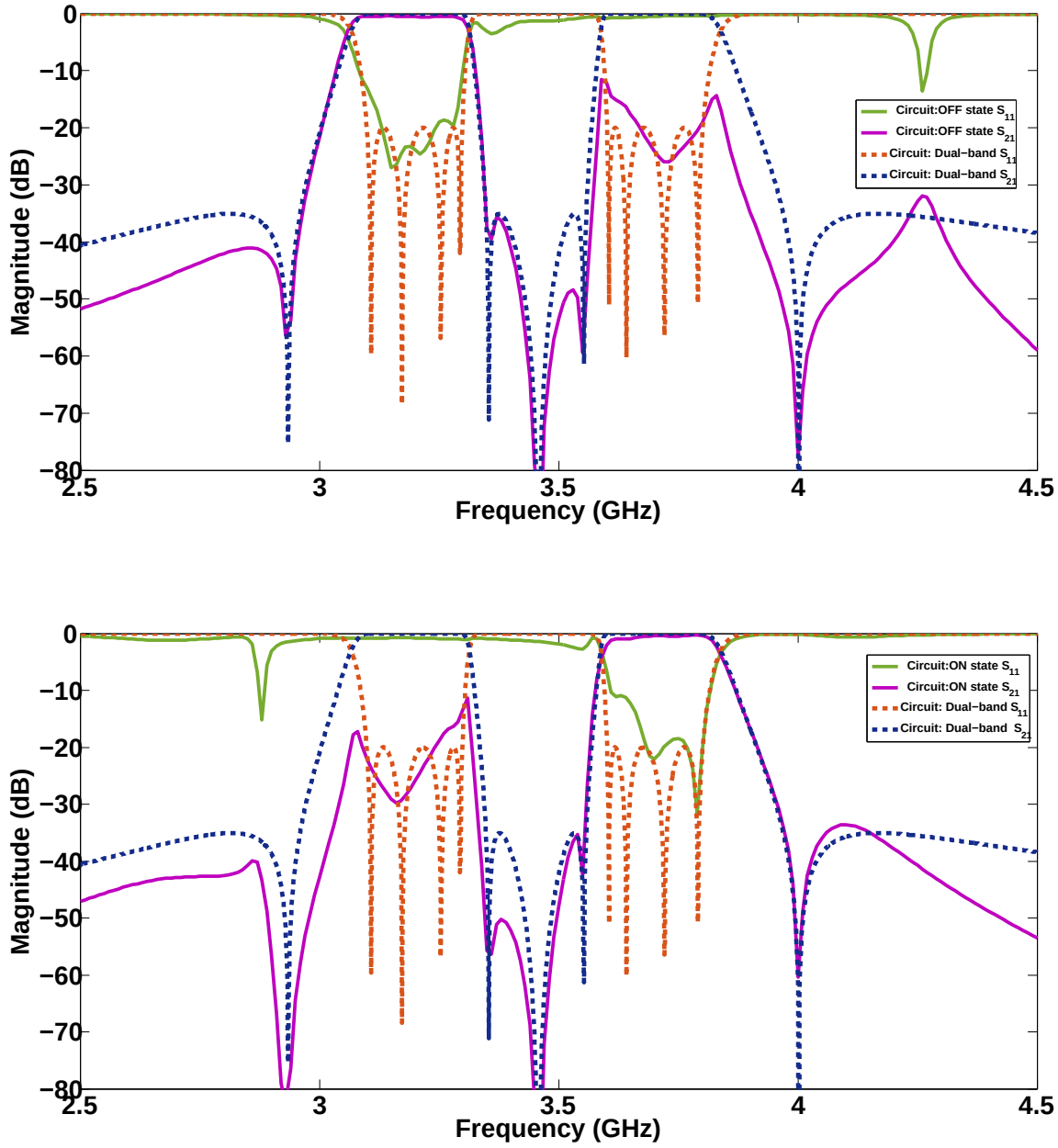

Fig. 5.30 Lossless frequency response of ON and OFF state of Filter A versus fixed dual-band (These are circuit models).

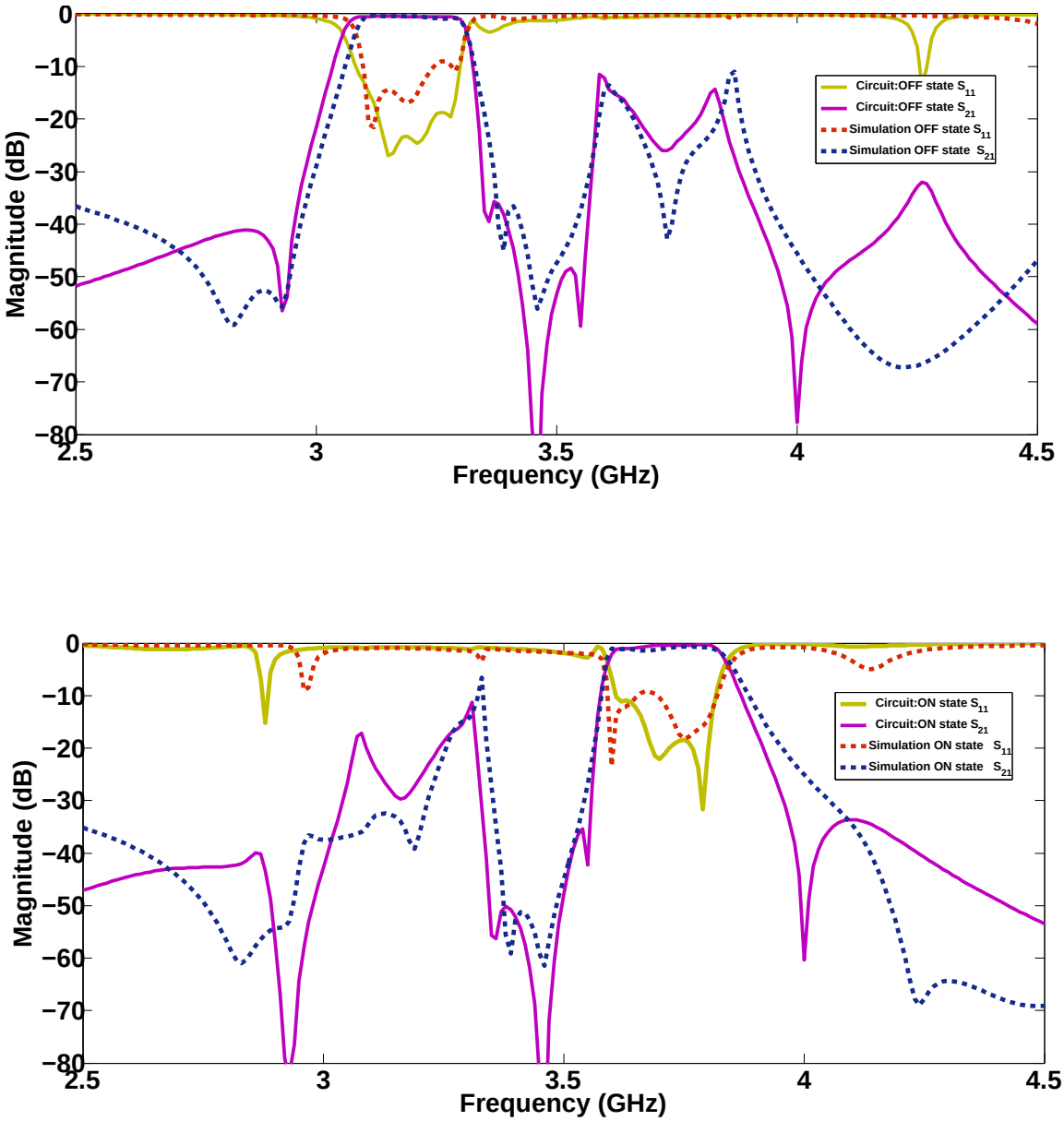

Fig. 5.31 Lossless frequency response of ON and OFF state of Filter A circuit model versus simulation .

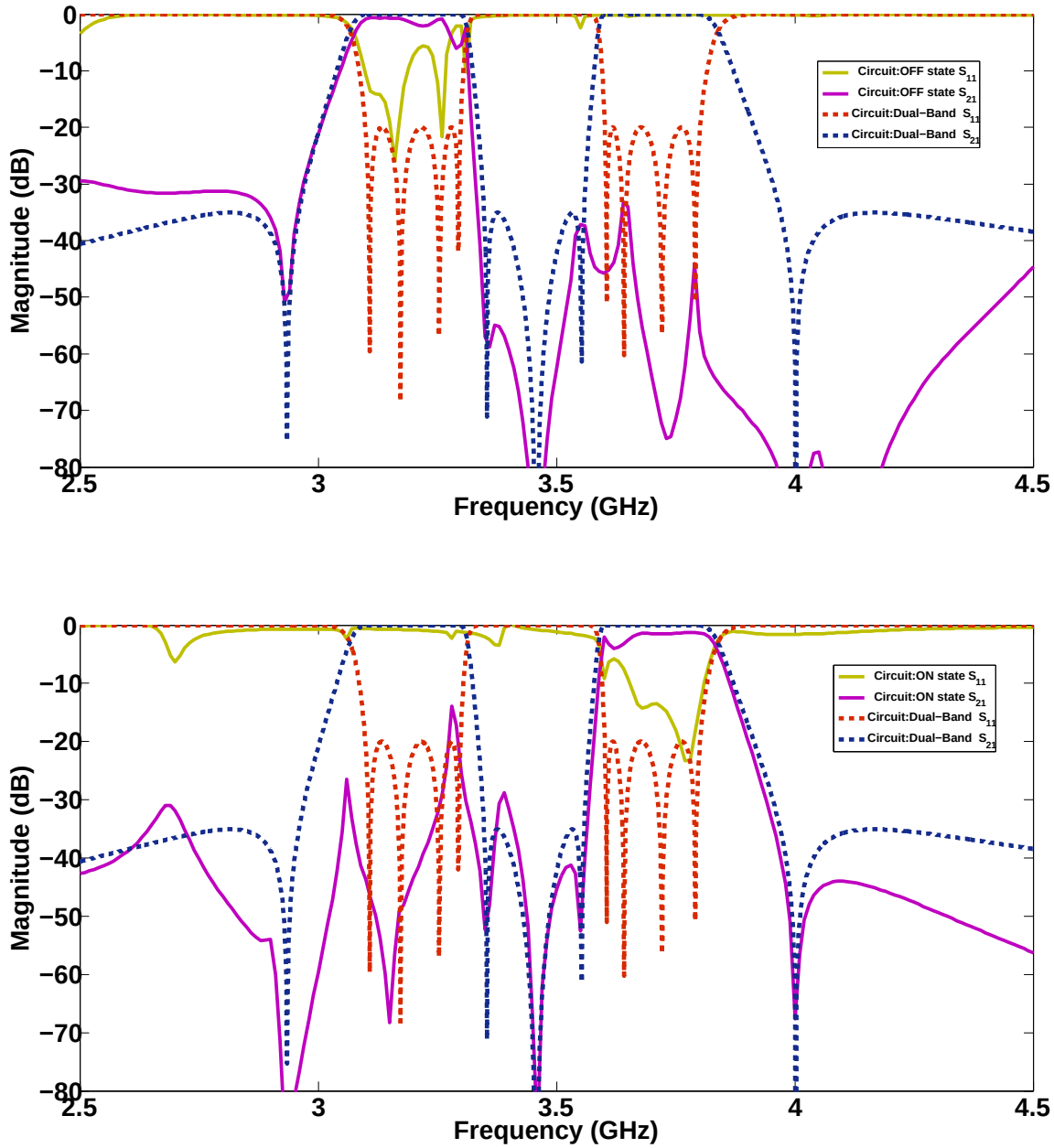

Fig. 5.32 Lossless frequency response of ON and OFF state of Filter B versus fixed dual-band (These are circuit models.)

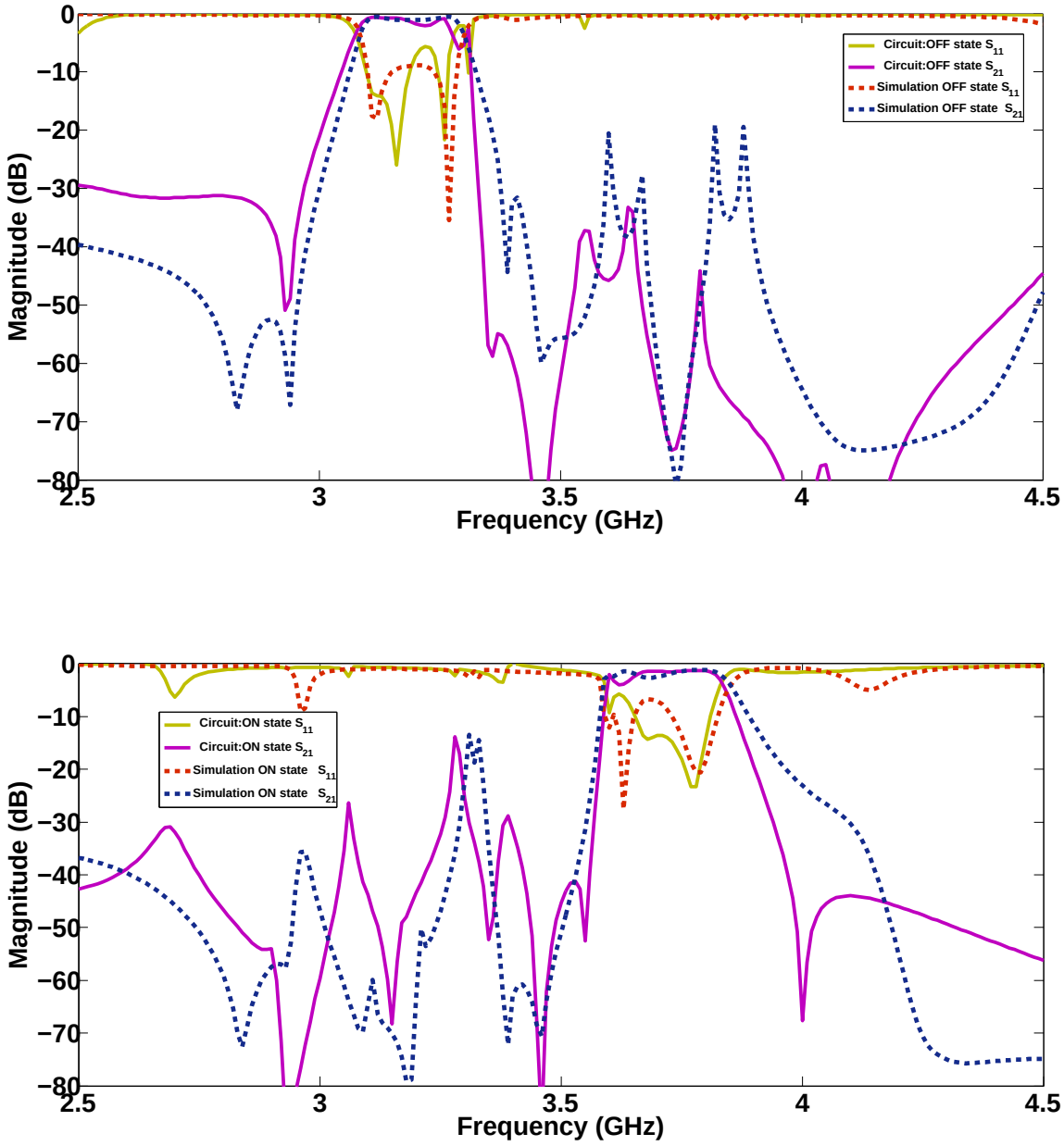

Fig. 5.33 Lossless frequency response of ON and OFF state of Filter B circuit model versus simulation.

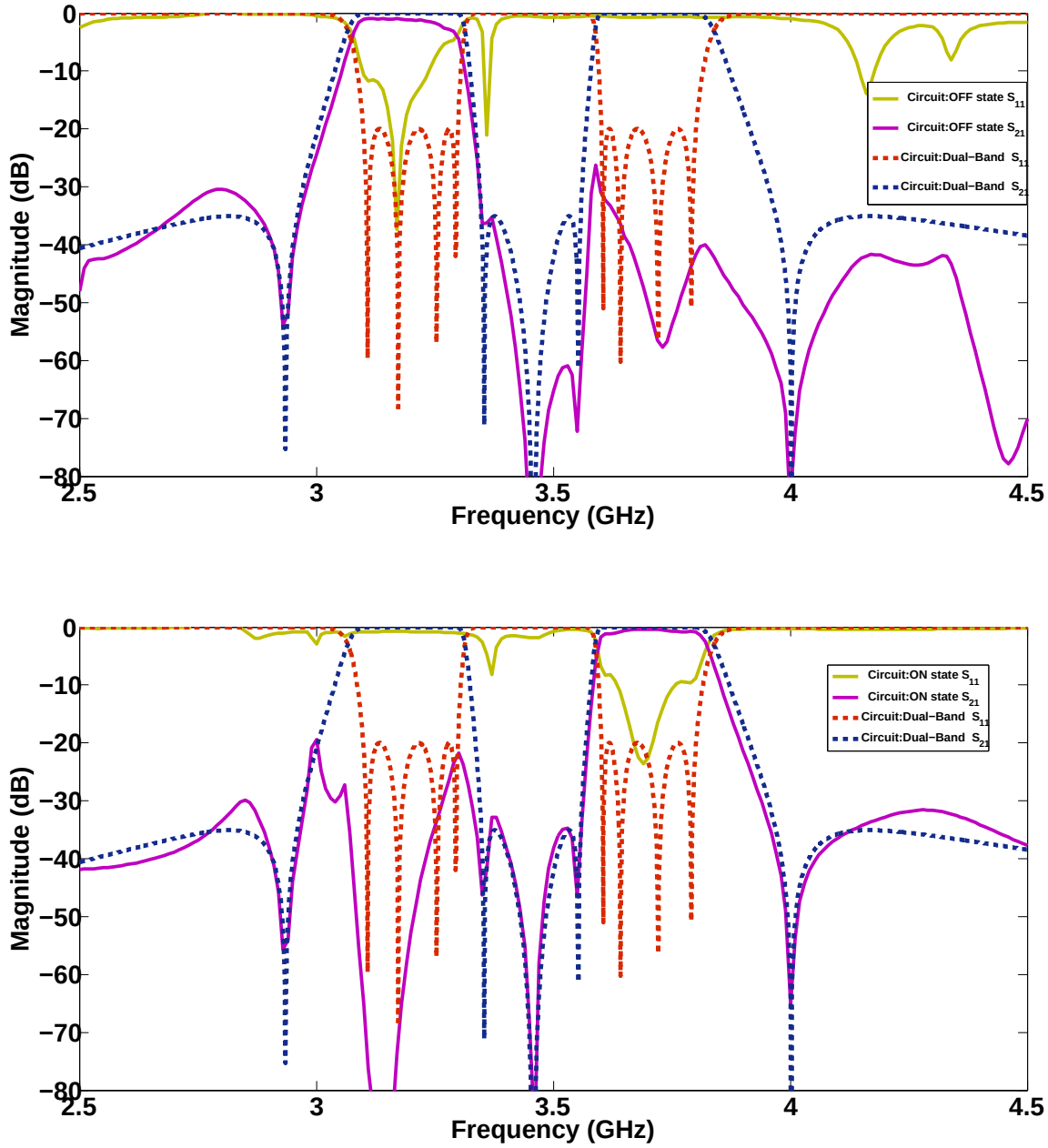

Fig. 5.34 Lossless frequency response of ON and OFF state of Filter C versus fixed dual-band. (These are circuit models)

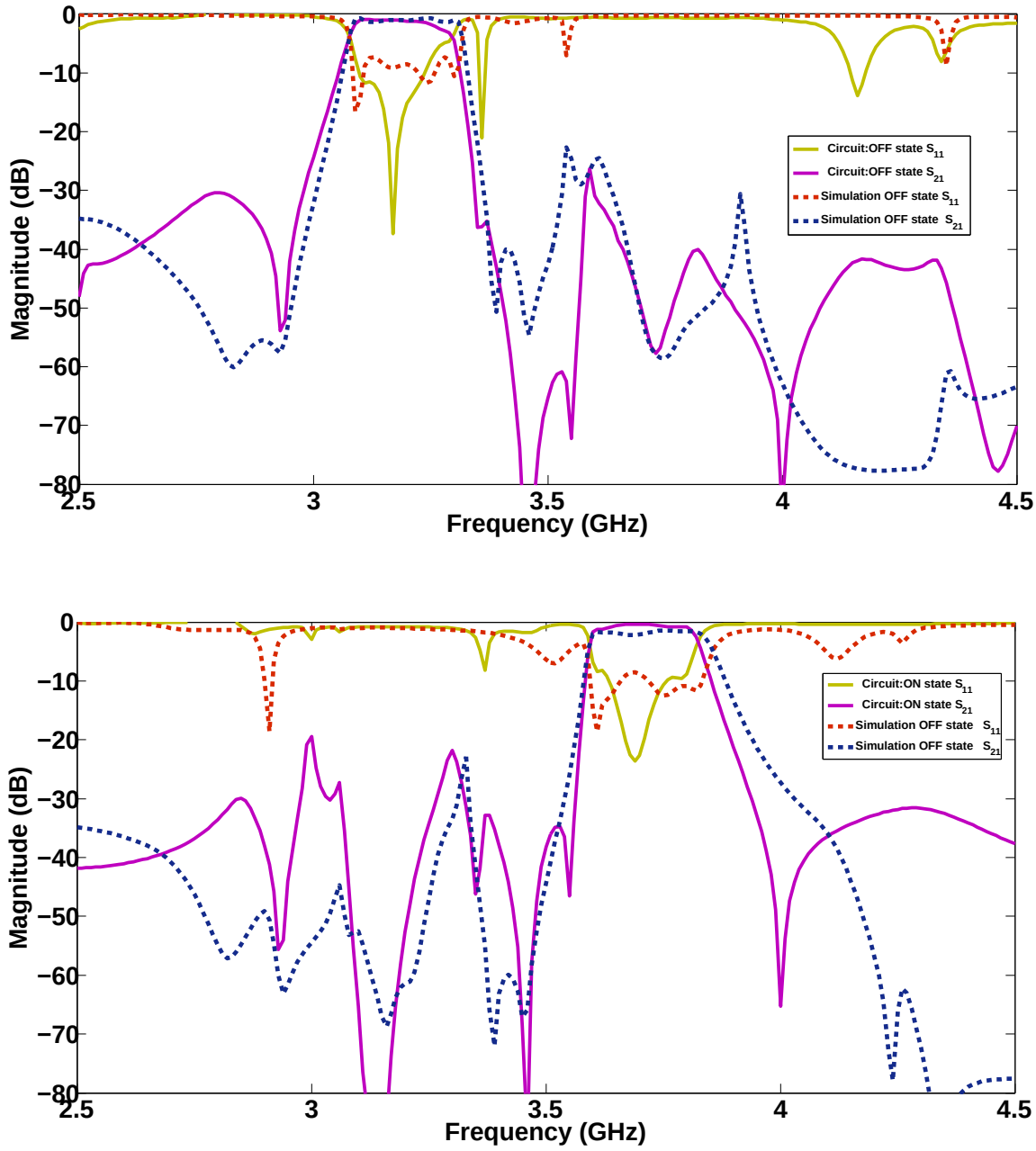

Fig. 5.35 Lossless frequency response of ON and OFF state of Filter C circuit model versus simulation.

Losses

The Q-factor of the lossy, fixed, dual-band filter (simulated) was calculated to be equal to 99. When one takes this Q factor in a circuit model with lossy resonators into consideration, losses of the switchable filters are predicted. The graphs in Fig. 5.36 to Fig. 5.38 are plotted for a lossy, fixed, dual-band circuit model and lossy, switchable filters against lossy, EM, simulated, switchable filters, as presented in Fig. 5.36 to Fig. 5.38 for Filter A, B and C. From the response's inspection, it was clear that the insertion loss of the filters was reasonable; there was a little difference in the losses of a fixed, dual-band filter with the Q of 99. The drawback was the return losses: the deeper the suppression depth of the prohibited band, the poorer the return losses in the selected band. For Filter A, the return losses were better than for the two-stages filters, but the two-stages had better suppression; it was thus a tradeoff. The ON and OFF state suppression depth of the three filters are depicted in Fig. 5.39 to 5.41.

5.7 Construction and measurements of the filter

The proposed switchable Filters A and B were constructed on Mercury wave substrate with a total thickness of 0.5128 mm and a loss tangent of 0.004. A detailed photograph of the filters with the biasing scheme is shown in Fig 5.42 for Filter A and Fig 5.43 shows Filter B. Including the feed lines and bias circuits, the size of Filter A was 38.5 mm $\times$ 49.9 mm while the size of filter B was 38.5 mm $\times$ 68.2 mm. The measured versus simulated results are plotted in Fig 5.44 for Filter A and in Fig 5.45 for Filter B (a) OFF state; (b) ON state.

5.8 Summary

A new switchable filter, comprising a dual-band filter, that cascades to pre-select, non-resonant, transmission lines, which select the desired band and switch OFF the other, has been demonstrated. A dual-band filter was designed based on the reactance transform method. The pre-selection did not interfere with the characteristics of the dual-band filter, such as transmission zeros, center frequency and bandwidth; instead it switched one of the bands ON and OFF. The related filters were analyzed, and two of them were designed. Although the response of the filter shifted to the left, switching is performed as expected.

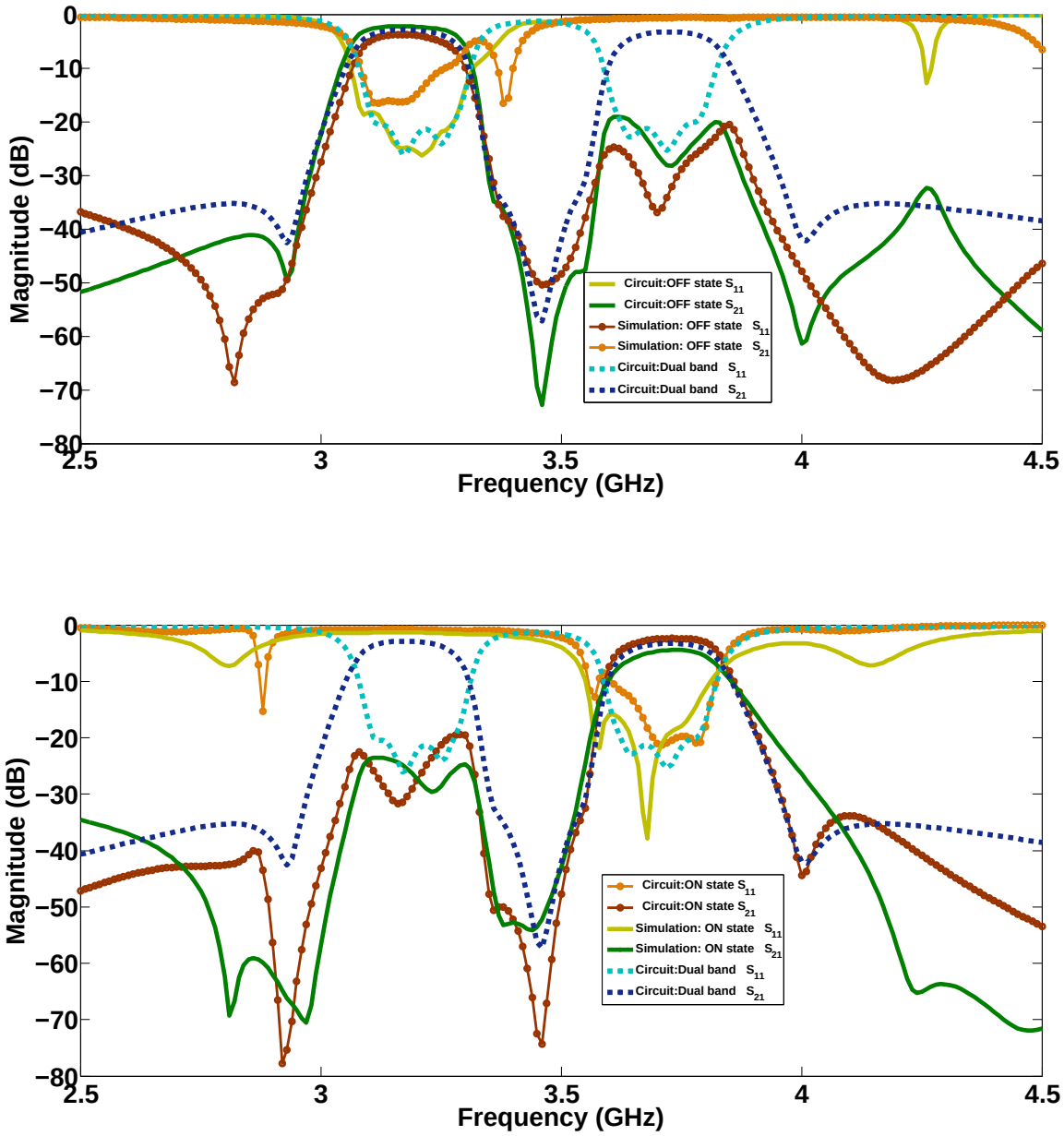

Fig. 5.36 Lossy frequency response of a switchable Filter A circuit model versus Filter A simulation versus fixed dual-band circuit model.

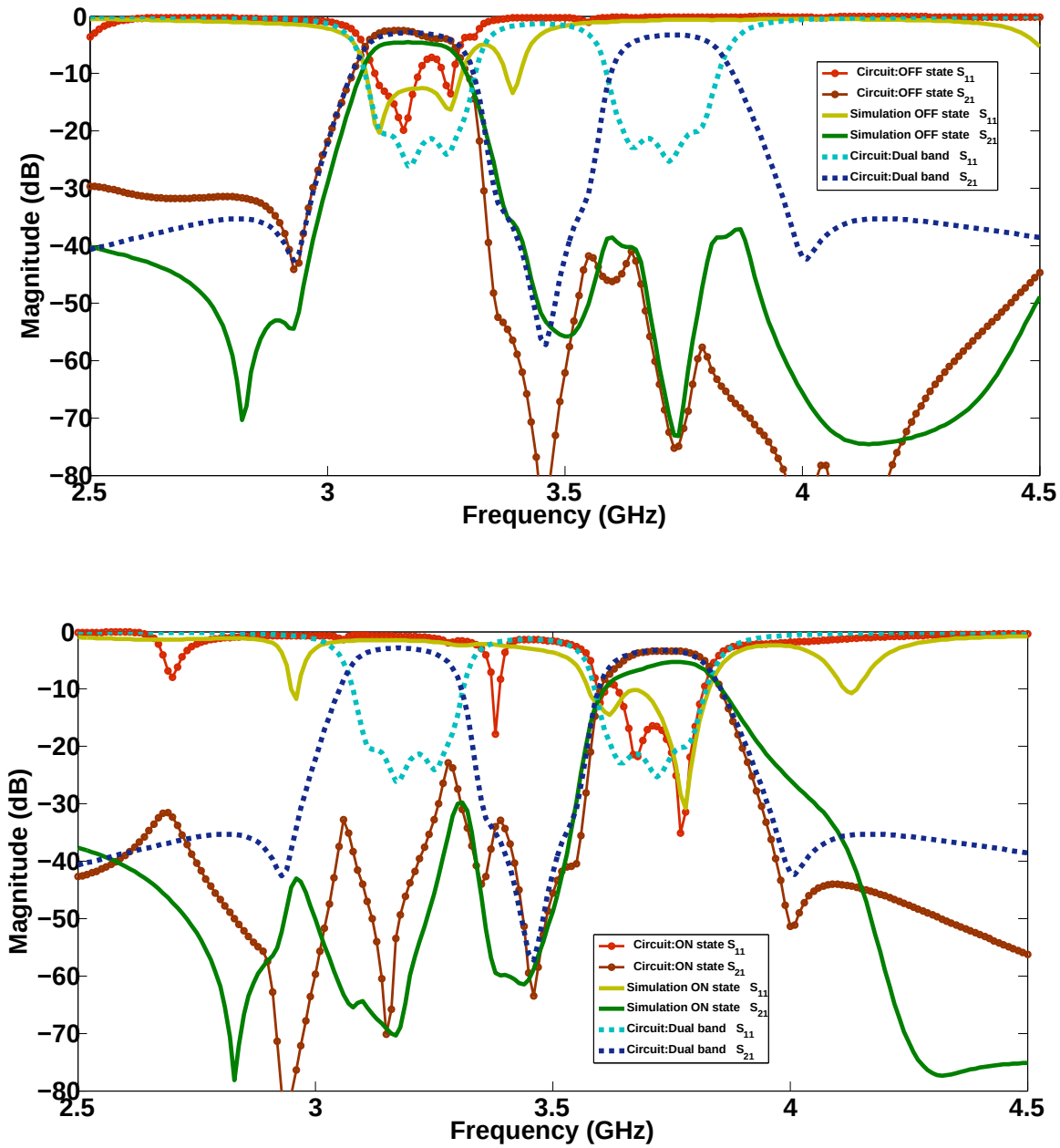

Fig. 5.37 Lossy frequency response of a switchable Filter B circuit model versus Filter B simulation versus fixed dual-band circuit model.

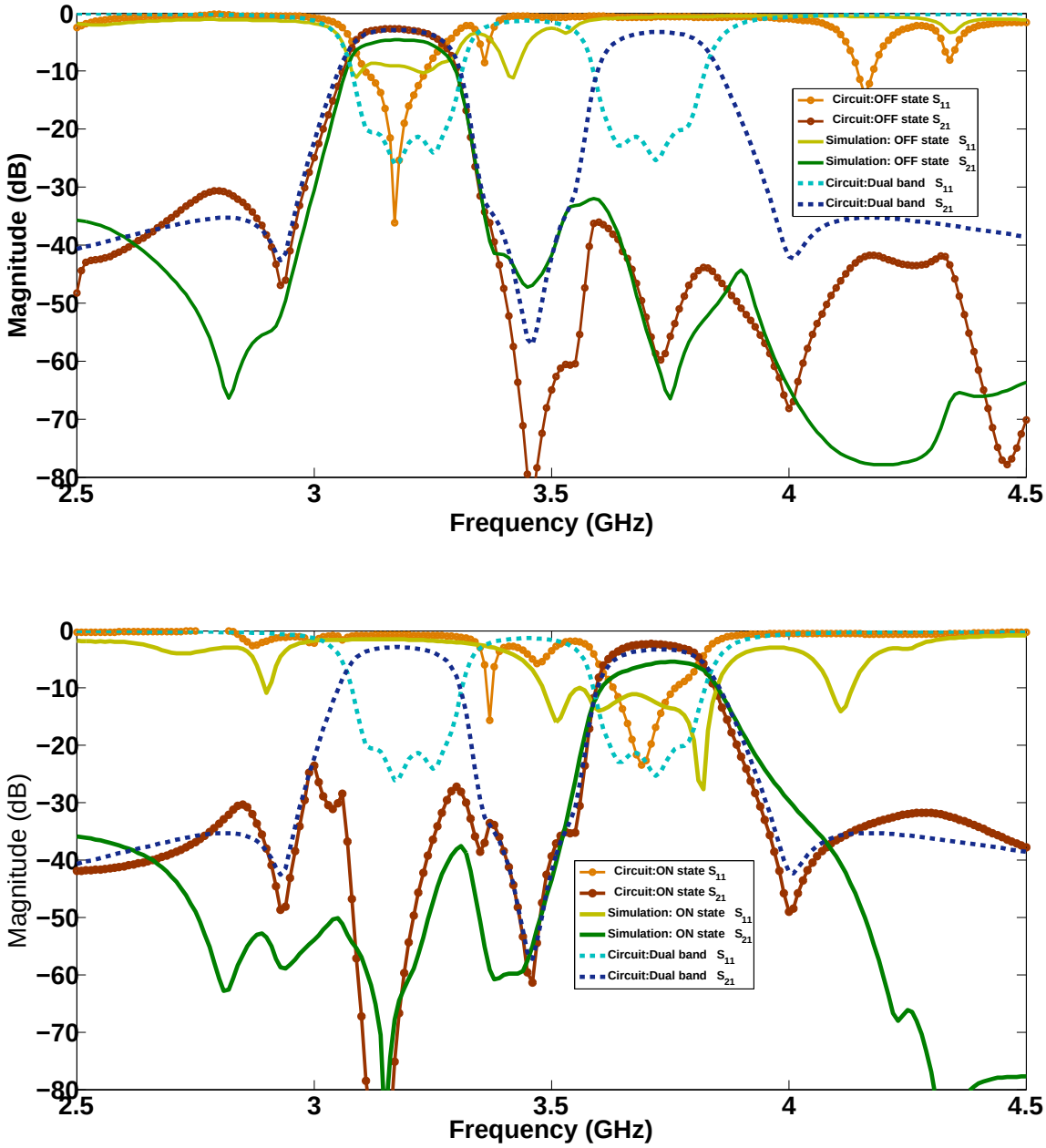

Fig. 5.38 Lossy frequency response of a switchable Filter C circuit model versus Filter C simulation versus fixed dual-band circuit model.

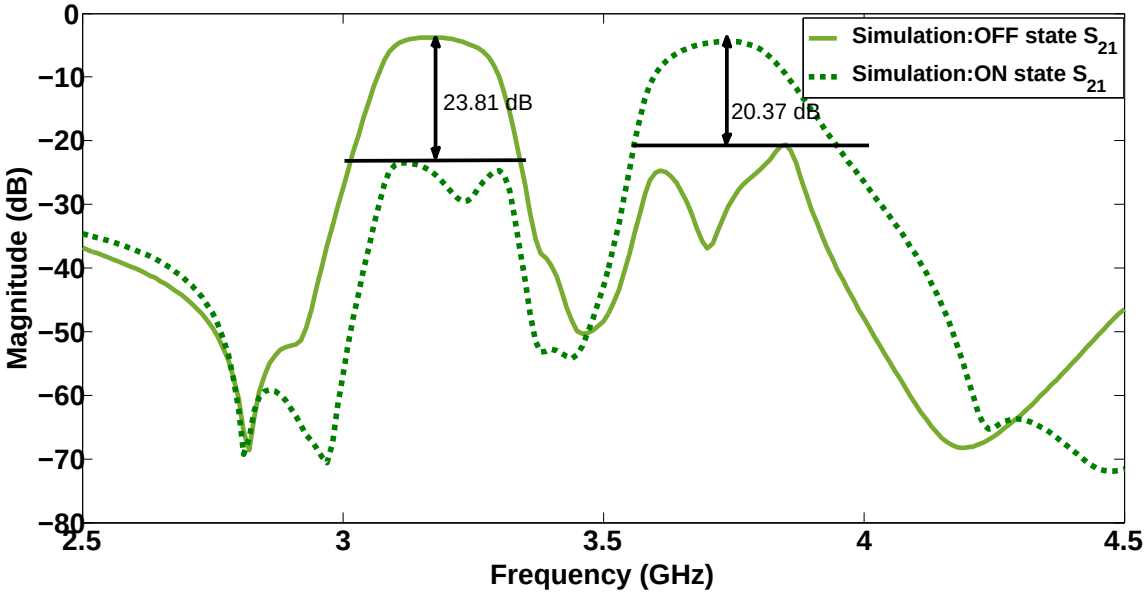

Fig. 5.39 Frequency response of the switchable Filter A.

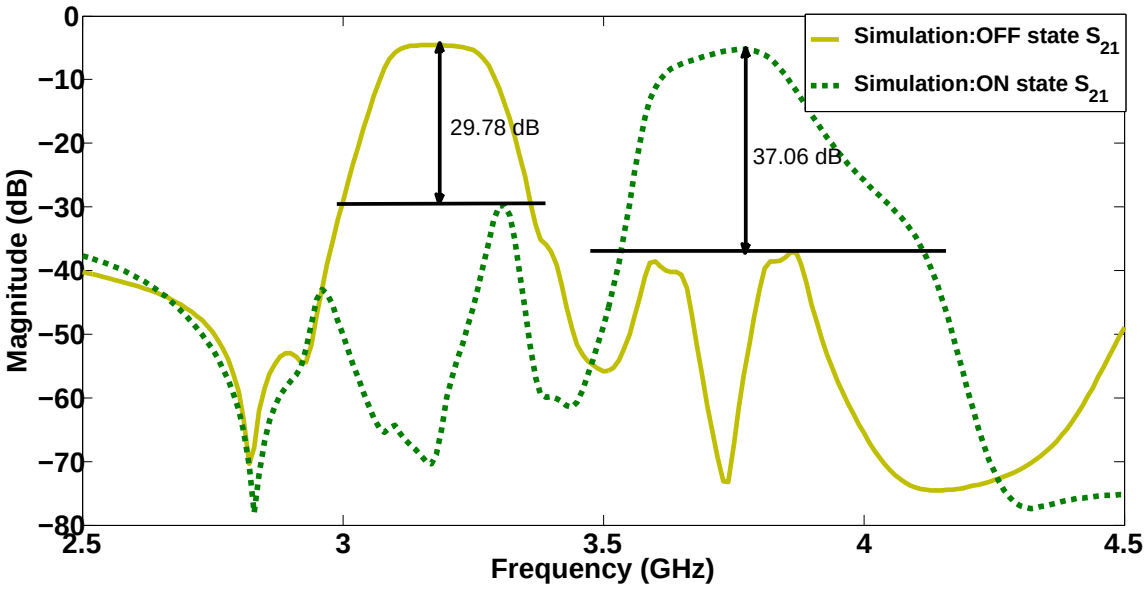

Fig. 5.40 Frequency response of the switchable Filter B.

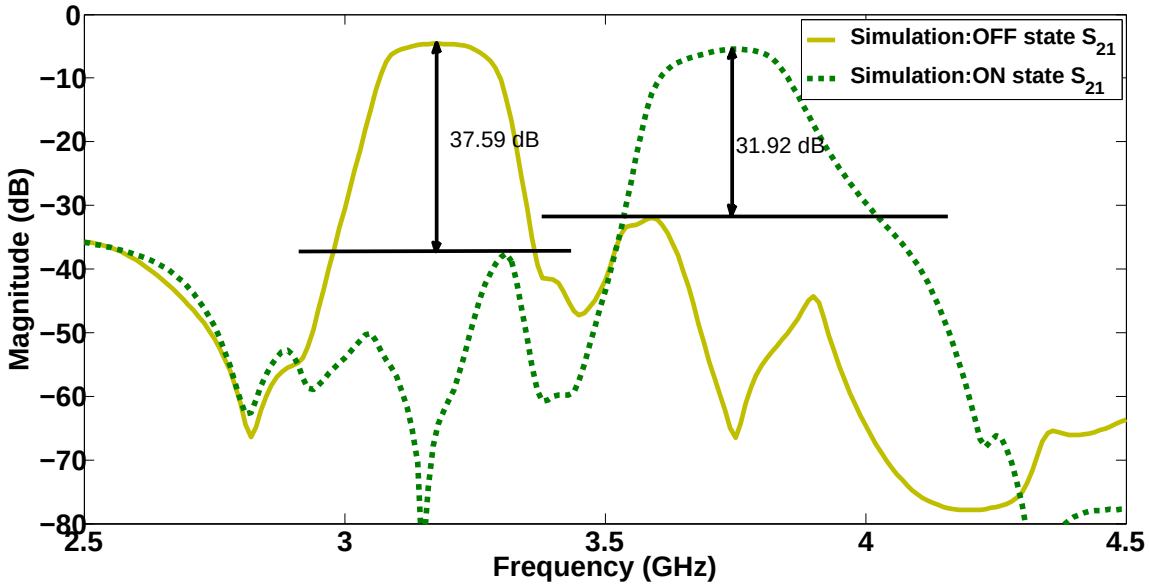

Fig. 5.41 Frequency response of the switchable Filter C.

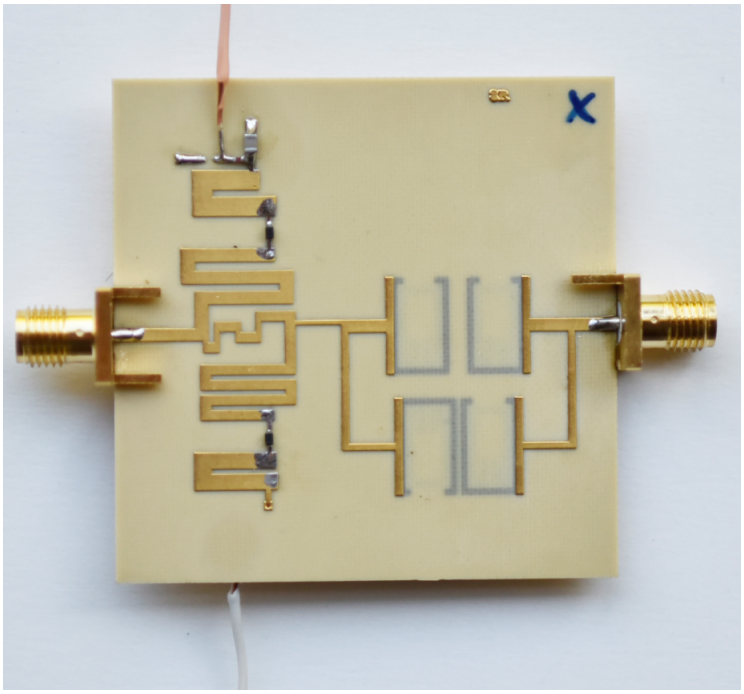

Fig. 5.42 Photograph of the fabricated Filter A switchable filter.

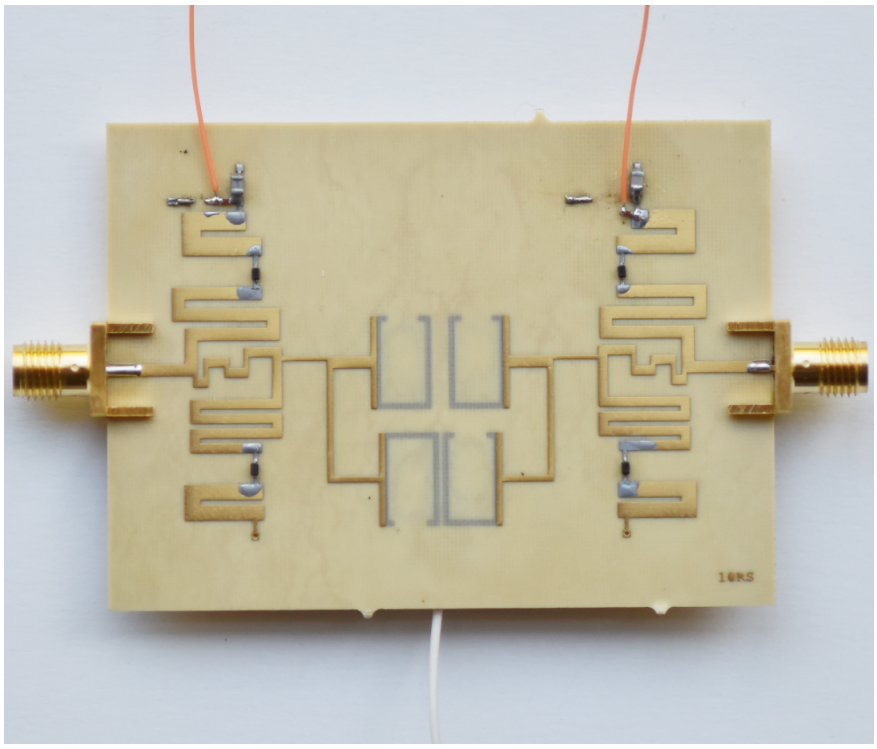

Fig. 5.43 Photograph of the fabricated Filter B switchable filter.

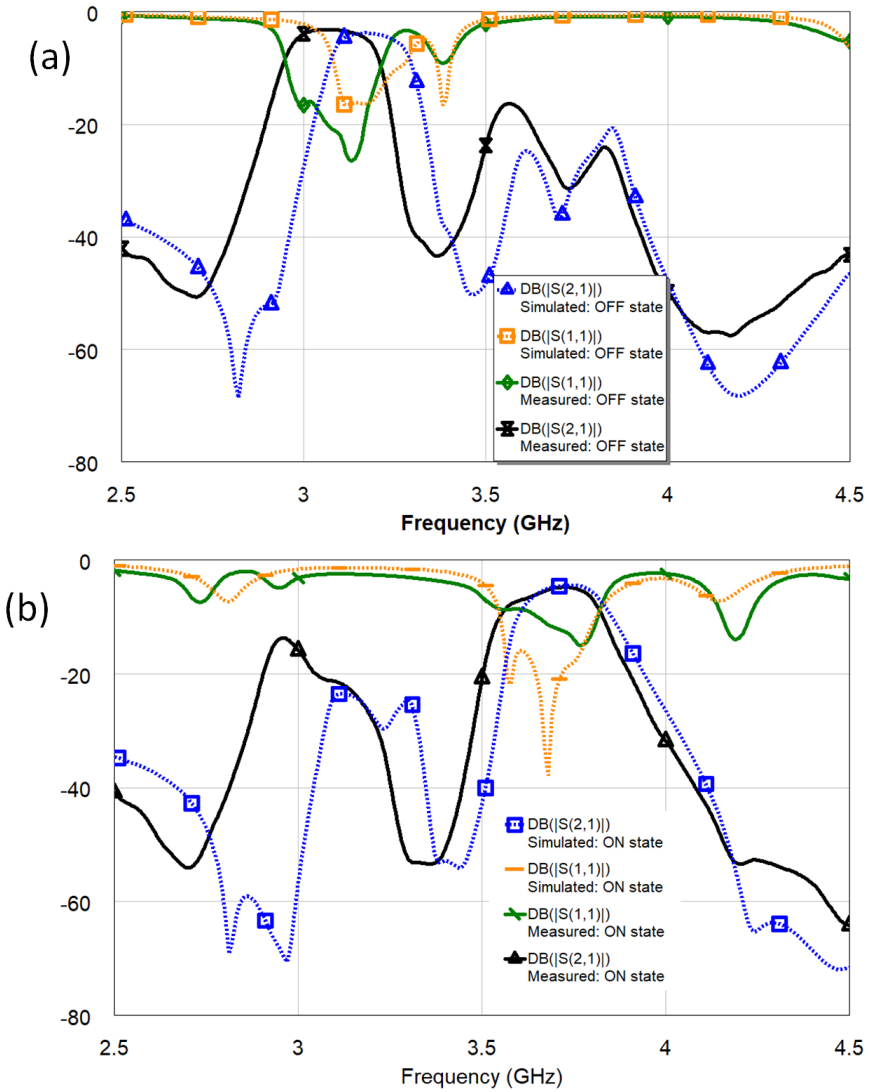

Fig. 5.44 Measured (solid line) and simulated (dash line) S-parameters of the proposed switchable filter A, (a) is the OFF state where lower band is selected and the upper band is prohibted, (b) is the ON state, the upper band is selected and the lower band is prohibited.

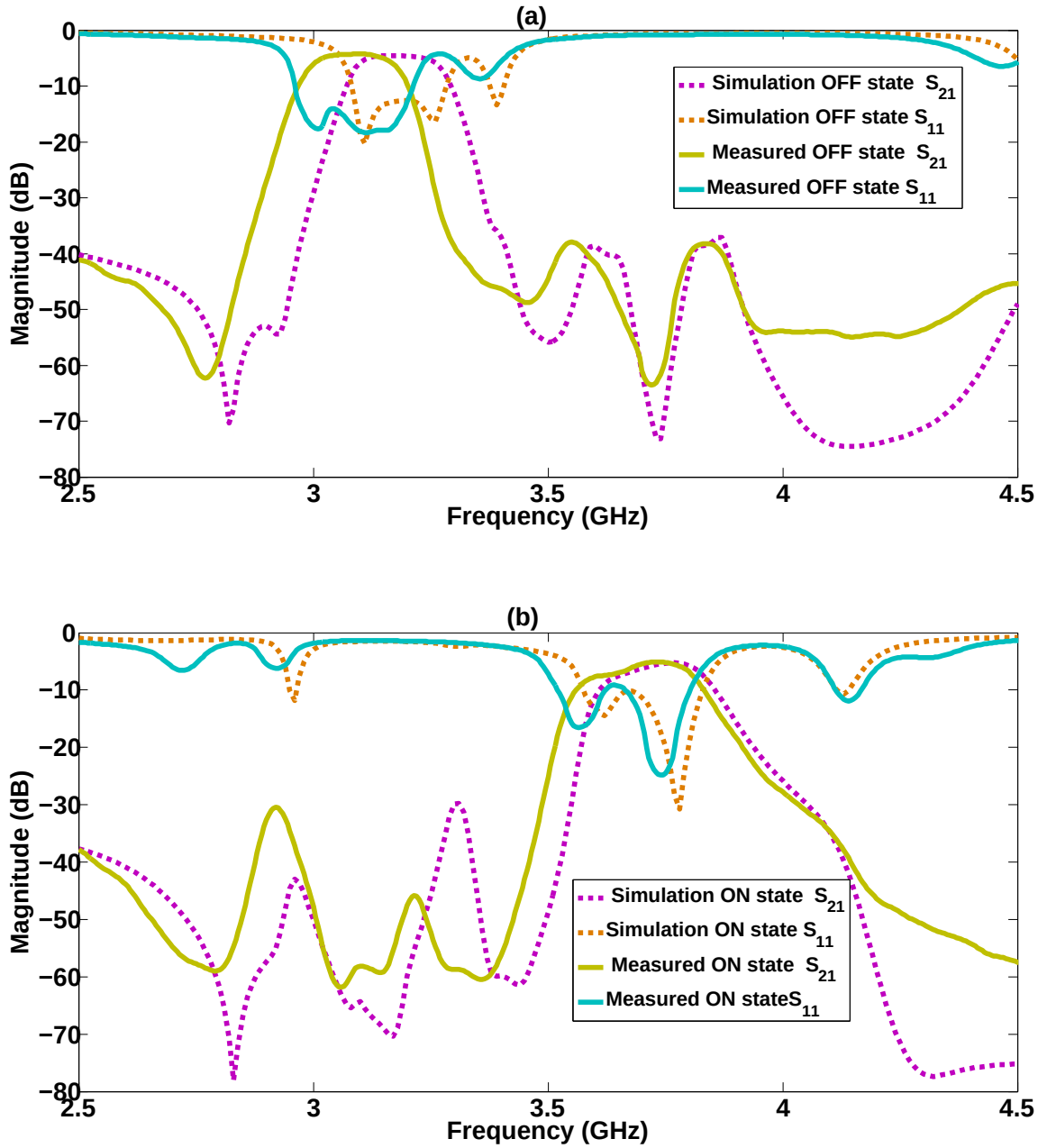

Fig. 5.45 Measured (solid line) and simulated (dash line) S-parameters of the proposed switchable filter B, (a) is the OFF state where lower band is selected and the upper band is prohibted, (b) is the ON state, the upper band is selected and the lower band is prohibited.

Chapter 6

Tunable quasi-lumped element dual band Filters

6.1 Introduction

In general, lumped elements (LE) are described as passive components which are related to the wavelength of operation. The sizes and dimension of a lumped element are considerably smaller in comparison with the wavelength of operation. It is reasonable to have a maximum dimension of less than $\lambda/20$, [2], where λ is the guide wavelength.The dimensions and sizes of lumped elements create a huge difference between their distributed elements counterparts. Lumped elements do not have a substantial phase shift between input and output terminals whereas in distributed elements a phase shift may be noticeable. Lumped elements can be regarded as the basis of microwave circuits, with three basics elements, namely capacitors, inductors and resistors.

The use of a lumped-element in microwave circuits or microwave-integrated circuits (MIC), as they are known (see [14, 22, 23]) was practiced, with the major aim to resolve and decrease the size of the MIC at the lower end of the microwave frequency bands. At high frequencies, the MIC can be implemented as distributed circuits, such as strip-lines, with the disadvantage of occupying a large printing area on a circuit board. The quality factors of inductors and capacitors were measured in [23] with the result that high Q capacitors and single turn inductors were confirmed as truly lumped up to 10 Ghz. The report also shows that multiple turn inductors had higher inductances than single turn inductors, with the drawback of showing distributed effects. For these reasons, only single turn inductors in the range of 3-6 nH can be used above 6 GHz. In [23] it was further concluded that, in the range of 2- 6 GHz, distributed circuits demonstrate slightly higher performance advantages

over low loss, lumped elements, but in the S-band zone the performance of lumped-element circuits is equivalent to that of distributed circuits.

Apart from circuit size reductions, lumped-element circuits have other advantages over distributed circuits. These include wide bandwidth, little coupling effects and smaller amplitude and phase variations. Wide bandwidth is achieved because of frequency dependent reactance. Little coupling effects are due to the smaller size, even if lumped-elements are positioned close together coupling effects are smaller in comparison to distributed circuits, Smaller phase delays have little phase and amplitude variations.

Since the early years of the development of lumped-element circuits (1960's to 1970's), there has been a dramatic change in the synthesis and implementation of lumped-element circuits. The circuits are often implemented on multi-layer technologies, such as LTCC (low temperature co-fired ceramic) and LCP (liquid crystal polymer) or on CMOS (complementary metal oxide semi-conductor). While the size advantage of quasi-lumped elements over distributed elements are pronounced at frequencies below 2 GHz, it is not limited to the lower GHz frequencies. LE is also employed at frequencies up to 100 GHz. An example of a filter based on LE in CMOS technology is found in [27] and, [71], where single-layer capacitors are preferred to multi-layer capacitors to reduce loss. Inductors at mm-wave frequencies need special care in design [40] Another example of a millimeter wave design on SiGe technology at 77 GHz is presented in [24].

For microwave filters, lumped elements were employed to design and realize [35], Chebyshev-like filters, based on a commonly known ladder network low-pass equivalent circuits where all transmission zeros were placed at infinity or quasi-lumped elliptic (QLE) low-pass circuits based on elliptic functions where transmission zeros could be placed at finite positions.

This chapter presents a dual-band filter based on a synthesis method without bandwidth limitation. A single-band wide-band filter design on LCP, based on the cascade of a low-pass and high-pass filter, with a similar fractional bandwidth and frequency range as the filters presented in this chapter, is described in [57]. While this is a single-band filter, it provides comparative data on element Q-factors for quasi-lumped elements on LCP in a similar frequency range as the filters in this chapter.

A single band Chebychev filter on LCP in [3] was the basis for two pass-bands. This was achieved by a transformation that replaced a second order LC resonator filter with a fourth order network. The realized filter is compact and easy to implement. Its downside is that the circuit topology provides limited suppression between pass-bands.

Dual-band filters in [34], [53], were designed on LTCC, while the suppression between bands was achieved. The prototype circuits include inverters that, in return, limit the bandwidth of the filter; hence, the downside of these filters is a bandwidth limitation.

The filter in [38] has a feedback capacitor C_f that is connected in parallel to the main structure. Both bands were first designed without C_f, after which C_f was chosen for transmission zero placements. The limitation of this technique was that the upper band selectivity was not steep as C_f does not provide the transmission zero on the right side of the upper band, C_f was limited to produce three transmission zeros.

Recently, a synthesis method to produce exact, lumped element models for multi-band filters was developed [7]. The wide-band version of this method for multi-band, lumped, element filters [6] is based on rational functions, such as frequency mapping functions. It transforms each single band, lumped element into a one-port, cascaded circuit of inductors and capacitors according to the required number of pass-bands. The two filter prototypes, described in this chapter, were derived from this procedure. The prototypes were further extended to include tunability in the design. Tunable filters are related to shifting the filter's center frequencies and bandwidths, which requires a tuning element, a varactor diode in this case.

The chapter is arranged as follows: Section 6.2 presents a synthesis based on a wide-band reactance transform. Section 6.3 presents a circuit analysis of filter topologies. Section 6.4 mainly presents the implementation of a microstrip, dual-band, wide-band, quasi-lumped element (QLE) filter on multi-layer substrates. In Section 6.5, the constructed filte measurements and experimental results are provided. Moreover, spurious effects of non-idealities were tested and described in section 6.6. Tunability features are discussed in Section 6.7. Finally the chapter is summarized in Section 6.8.f

6.2 Synthesis based on a wide-band Reactance Transform

Wide-band filters were synthesized by utilizing rational mapping functions [7] of the form 2.16 to obtain driving point functions of a foster form 2.18 and a mixed Cauer I and II form 2.21 required for frequency transformation sub-circuits. The rational mapping function for the dual band filters was computed as:

$$\Omega' = \frac{11.1615\Omega^4 - 8.5167\Omega^2 + 1}{-5.9251\Omega^3 + 2.2804\Omega} \tag{6.1}$$

The wide-band, rational mapping functions provide filter symmetry around zero frequency as detailed in Fig 6.1.

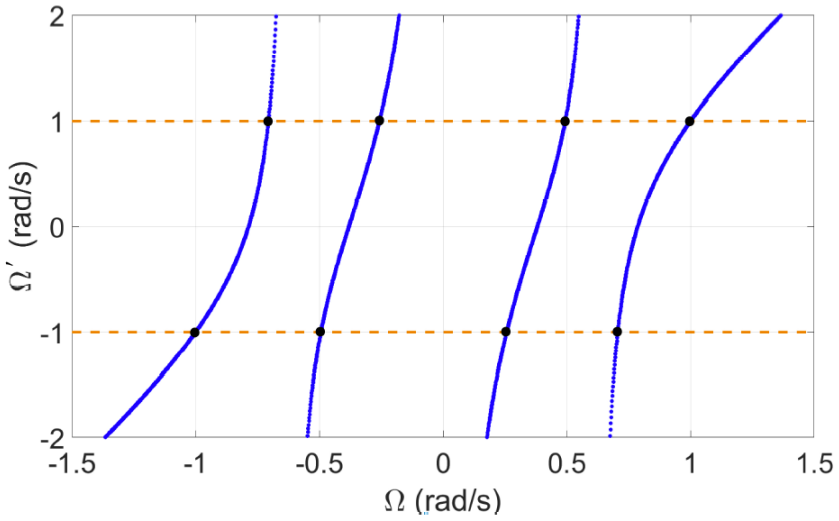

Fig. 6.1 Symmetry of the wide-band dual-band filter.

The general driving point function for Foster dual-band expansion is:

$$H(s) = \frac{0.4385}{S} + \frac{0.1369}{S - j\omega_1} + \frac{0.1369_1}{S + j\omega_1} + 1.8837S \tag{6.2}$$

and the mixed Cauer type I and II expansion is:

$$H(s) = 1.8837S + \frac{0.4385}{S} + \frac{1}{3.6513 + 1.4053S} \tag{6.3}$$

A quasi-lumped element (QLE) third order low-pass prototype shown in Fig 6.2 served as a basis frequency transformation circuit, the g-values are provided in Table 6.1. The shunt branch with the series resonant L-C circuit realized a finite frequency transmission zero above the pass-band. The low-pass prototype in Fig 6.2 was transformed to a dual-band network as shown in Fig 6.3.

The two dual-band filters represented by circuits in Fig 6.3 have the same L's and C's values. The two circuits are similar, except for the fact that the sequence of the elements are different. The computed L's and C's values following the sequence of Foster expansion, are provided in Table 6.2. The transformation replaced each inductor and capacitor in the low-pass circuit by a one-port network. The colour blocks (see Fig. 6.2) were transformed to equivalent circuits for a specified dual-band filter in (see Fig. 6.3). Since the reactance transformation directly transformed a low-pass filter prototype into a dual-band filter, the implication is that the low-pass response is repeated for each pass-band.In practice, this means that, in the case of a dual-band, each series inductor (see Fig. 6.2) is transformed into

Table 6.1 The g-values found from the Table in [35] of the circuit in Fig 6.2

g-values	
g_0	1.0
g_1	0.9471
g_2	0.1205
g_2'	1.0173
g_3	0.9471
g_{n+1}	1.0

a series L and C and a parallel L-C combination, as indicated by the matching colour-coded shading in Fig 6.3. The low-pass and dual-band responses are shown in Fig 6.4 .

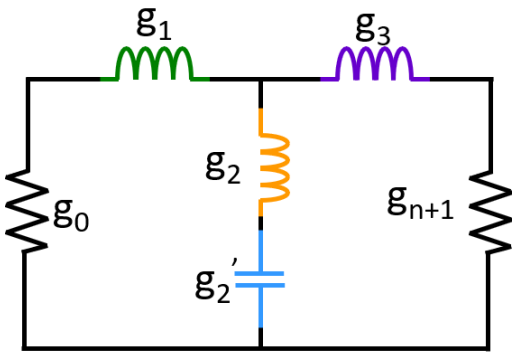

Fig. 6.2 A third order quasi-elliptic lowpass prototype is the basis for two dual-band filter implementations. This filter's cutoff frequency is 1 rad/s and it has one finite transmission zero at 2.5 rad/s.

6.3 Circuit analysis of filter topologies

The prototype circuits consist of sixteen (16) lumped element components, eight (8) capacitors and eight (8) inductors. The reactive element values in Table 6.2 show that $L_{1a} = L_{3a}$, $L_{1b} = L_{3b}$, and $C_{1a} = C_{3a}$, $C_{1b} = C_{3b}$, the number of unique reactive elements were reduced to twelve (12). The reactive element values of a dual-band prototype filter in Fig. 6.3 were compared to a single-band filter with the same overall bandwidth of the same quasi-elliptic filter to see how the values spread over overall bandwidth. The maximum to minimum ratio of the inductances/capacitance values of a dual band prototype was 42.05, a factor 2.4 higher than a (single) wide-band filter with the same overall bandwidth. This is confirmation that a dual-band filter with the same overall bandwidth as a wide-band filter is more challenging to design, owing to an increased number of lumped elements and to the increased range of

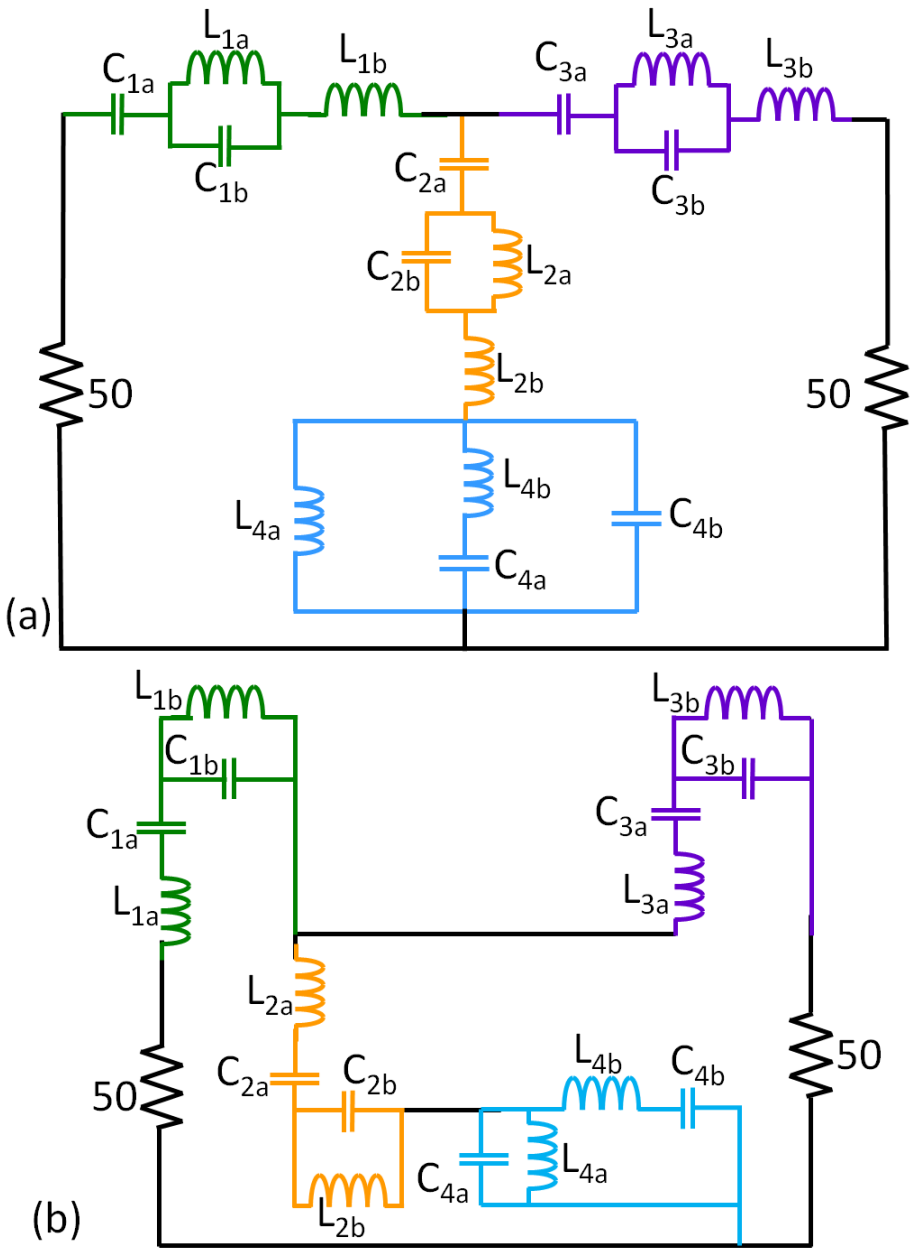

Fig. 6.3 A dual-band filter results after a transformation from the basis low-pass filter in 6.2. This prototype is created from the (a) Foster expansion and (b) mixed Cauer I and II expansions of the driving point function in the form of a partial fraction expansion. Each inductor and capacitor in the lowpass filter is transformed into its corresponding equivalent reactance for a dual-band filter. This is indicated by the same colour blocks. All capacitors are in units of pF and inductors in nH.

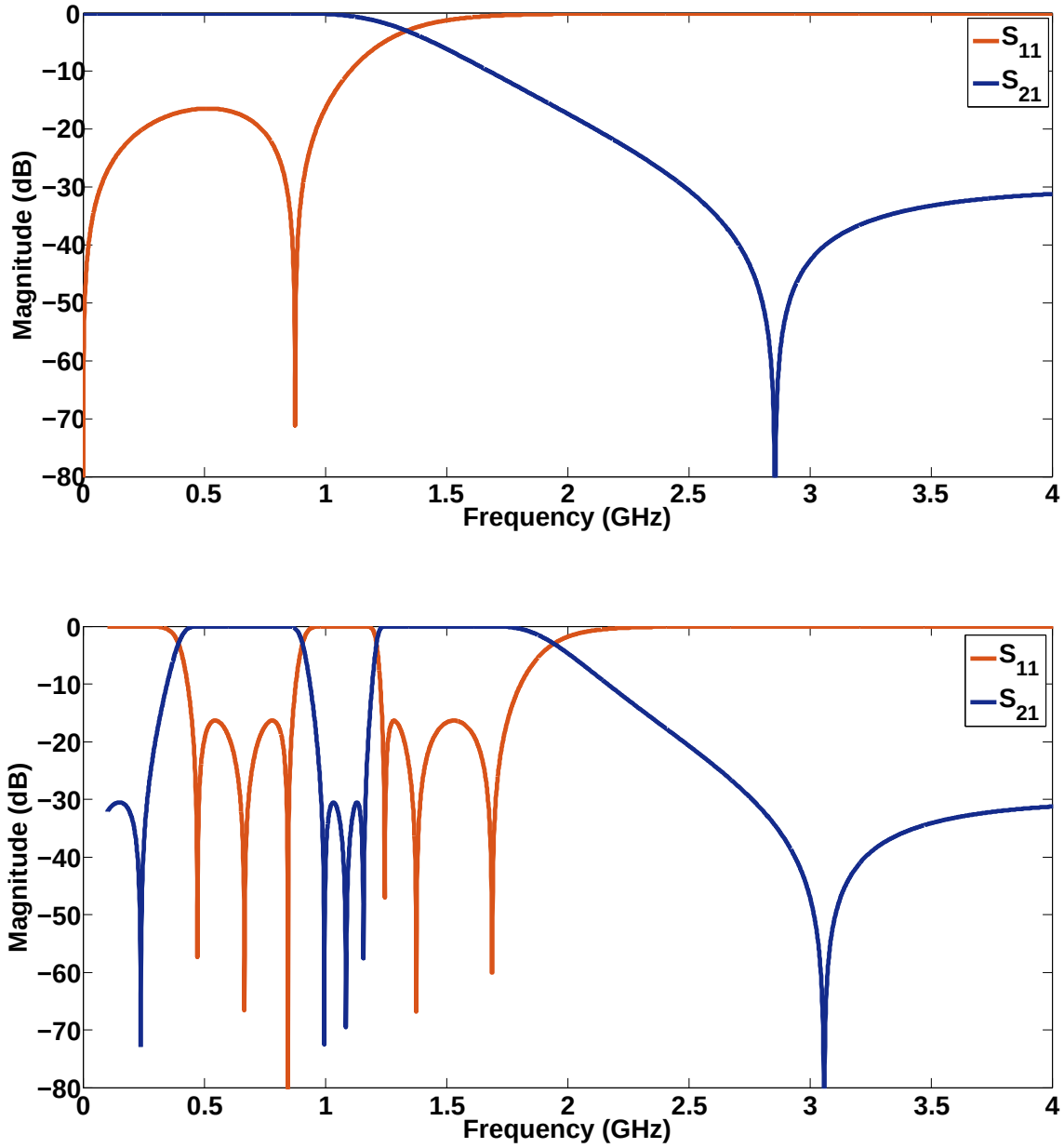

Fig. 6.4 The responses of the lowpass in Fig 6.2 and dual-band filter in Fig 6.3. The dual band filter has finite transmission zeros at zero, 0.238, 0.996,1.085,1.157 and 3.059 GHz.

Table 6.2 The calculation of the lumped-element values calculation based on [6] of the circuit in Fig 6.3

Capacitance (pF)		Inductance (nH)	
C_{1a}	4.38	L_{1a}	3.064
C_{1b}	7.014	L_{1b}	8.113
C_{2a}	34.42	L_{2a}	0.3898
C_{2b}	55.13	L_{2b}	1.032
C_{3a}	4.38	L_{3a}	3.064
C_{3b}	7.014	L_{3b}	8.113
C_{4a}	1.311	L_{4a}	10.24
C_{4b}	3.471	L_{4b}	16.39

Table 6.3 Comparison of element value ranges for a wide-band and dual-band filter with the same overall bandwidth. This factor is a measure of the challenge level to design a dual-band filter as compared to a single band filter with the same bandwidth. Units of inductors are in (nH) and capacitors in (pF).

Filter type	bands	Bands (GHz)	L_{max}	L_{min}	C_{max}	C_{min}	L_{max}/ L_{min}	C_{max}/C_{min}
Dual band	2	band 1: 0.45-0.91						
		band 2: 1.24-1.75	16.39	0.39	55.13	1.311	42.05	42.05
Wideband	1	0.45 to 1.75	0.26	0.015	0.28	0.12	17.51	2.23

element values. The comparison is detailed in Table 6.3, and maximum to minimum ratio of capacitance and inductance are presented in Fig.6.5.

6.4 Practical design and implementation

6.4.1 Capacitor and inductor models

Generally, inductors are realized in one of the three types [2], a strip-line, a single turn/ single loop and/or spiral. A strip-line is adequate to design a low inductance values typically less than 2 nH, the drawback is the increasing size(length) of the line. The solution to this is to meander a line to a single turn/loop. Spiral inductors consist of multi-turns and are known to have high inductance values.

For the dual-band filter, inductors are realized in a single turn and spiral models. The layout of these inductors are presented in Fig 6.6 showing the required parameters for the design namely width (W), length (L) and spacing (S) between the turns in a multi-turn model. For multi-layer designs, a 3 D illustration of the one turn and spiral model are presented in Fig 6.7. They are interconnected from one layer to another layer by employing a metallic

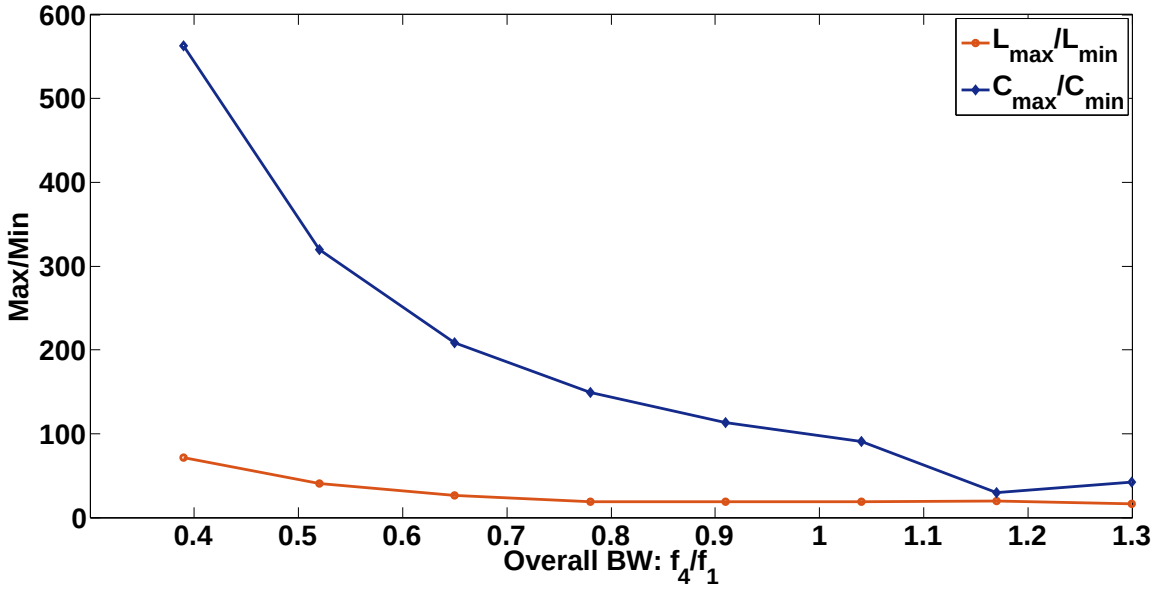

Fig. 6.5 The ratio of maximum to minimum element value ranges for a wide-band (single) and dual-band Filter with the same overall bandwidth

via. Metallic vias have an effect on circuit performance, as these add resistance and parasitic inductance. In order to minimize these effects, the interconnections should be very compact. For multilayer implementations, multi-plate capacitors (rectangular shape) are suitable for realizations. The general multi-plate configuration is depicted in Fig 6.8, where coupling is realized on the broad side of the plate of length L and breath b; d is the substrate thickness between the plates. The coupling plates can be coupled up to *n*, where*n* is the number of the desired plates. When *n* is large, the design and construction become more challenging. For the dual-band filter, broadside coupling plates were connected from two different layers by metallic vias used. The 3-D view of the capacitor is shown in Fig 6.9.

6.4.2 Via holes

The designs on multi-layers require the use of via holes to interconnect different layers. There are two types of via holes [2]. The one used for interconnections of metal layers is also known as a blind via, and the backside via hole ground is known as a through via. The two vias connection is illustrated in Fig. 6.10. In general, the blind via area is described as holes punched in a sheet. The holes are filled with metallic paste which interconnects each layer. On the other hand, through vias are described as opening in a dielectric made either by dry or wet etching or punching technology or by employing laser drills depending

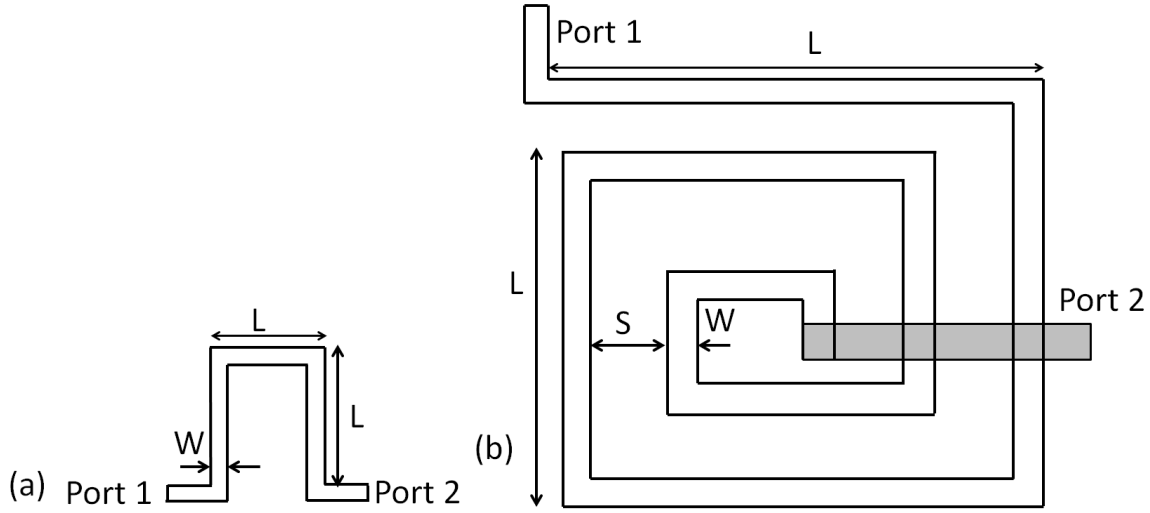

Fig. 6.6 Layout of inductor models (a) a single turn and (b) spiral inductor.

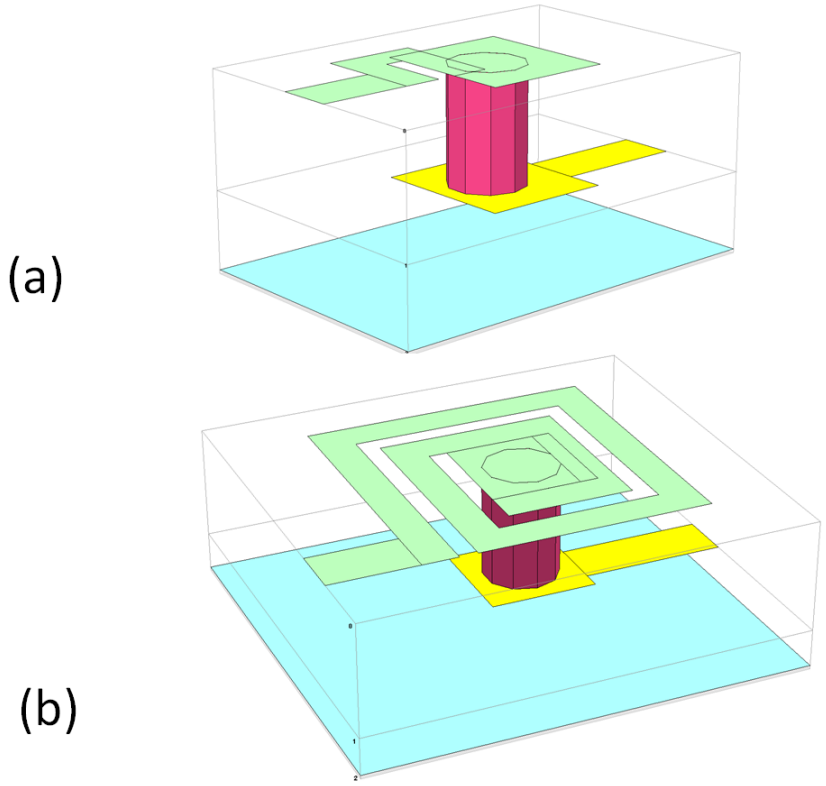

Fig. 6.7 3-D view of of inductor models (a) a single turn and (b) spiral inductor.

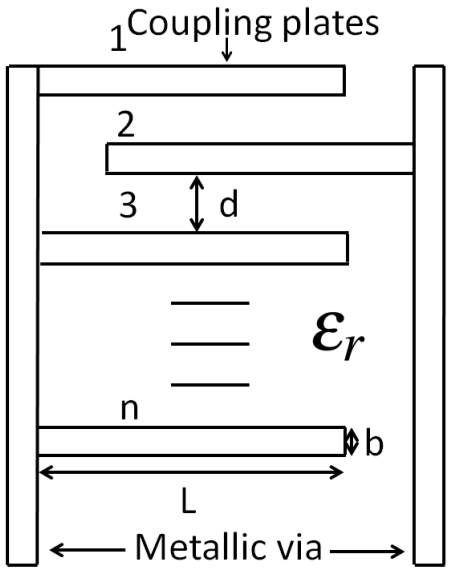

Fig. 6.8 Layout of multi-plate capacitor comprising n plates [2].

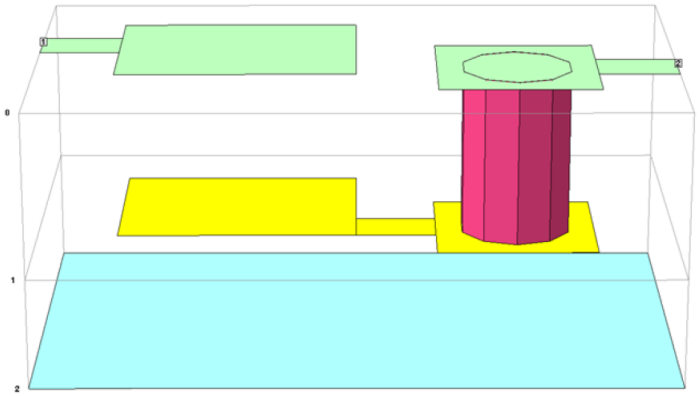

Fig. 6.9 3-D view of of the capacitor

on the nature of the substrates. Through via holes are metallized to connect the top and the bottom side. The via holes can be either rectangular or circular [4, 48]. The typical discontinuity problem is discussed in [4] and the equivalent circuit model of the via with frequency independent reactance's was obtained. The side view of the rectangular and circular via is connecting different layers and their equivalent circuit is shown in Fig 6.11. The advantages of employing via holes are listed and explained in [2], the list includes (1) Low-inductance grounds, (2) Excellent thermal paths, (3) Compatible with MIC technology. For the quasi-lumped, dual-band filters, a circular shaped via hole of 0.4 mm in diameter was employed for both blind and through vias.

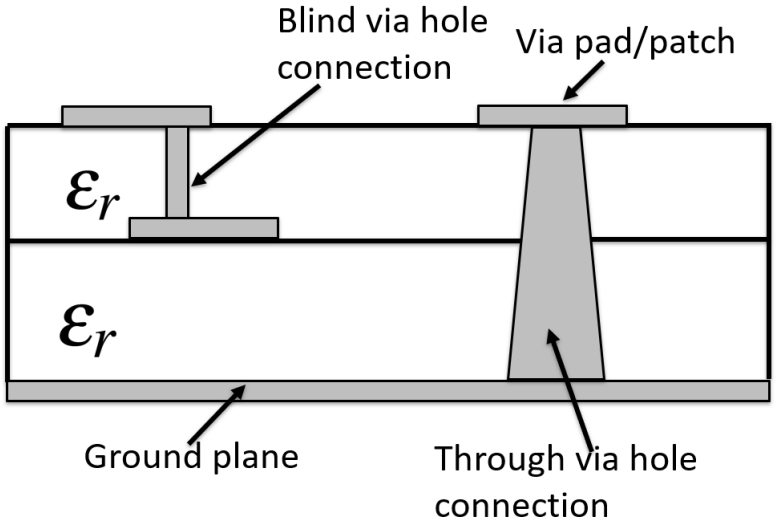

Fig. 6.10 Blind via hole connecting two layers and a through via hole (top to ground) [2].

6.4.3 Design of a dual-band filter

The lumped elements circuit, shown in Fig. 6.3(a) and (b), serves as equivalent to the practical microwave filter structure. The next step was to convert the lumped element circuit into a physical microwave filter. This section discusses the implementation of a quasi-dual-band filter for two topologies (Foster), referred to as Design A and (mixed Cauer I and II) as Design B. The layout of the circuit model (Foster topology: Design A) (see Fig. 6.12) was presented in Fig. 6.3(a), while the layout in Fig. 6.13 represents the circuit model (mixed Cauer I and II: Design B), presented in Fig. 6.3 (b).

Each filter has eight (8) capacitors (broadside coupling plates) and eight (8) inductors (spirals and one-turn models) on each design. There is a total of 12 vias, of which one is the through via and the rest are blind vias. Considering, connecting lines, via patches and via

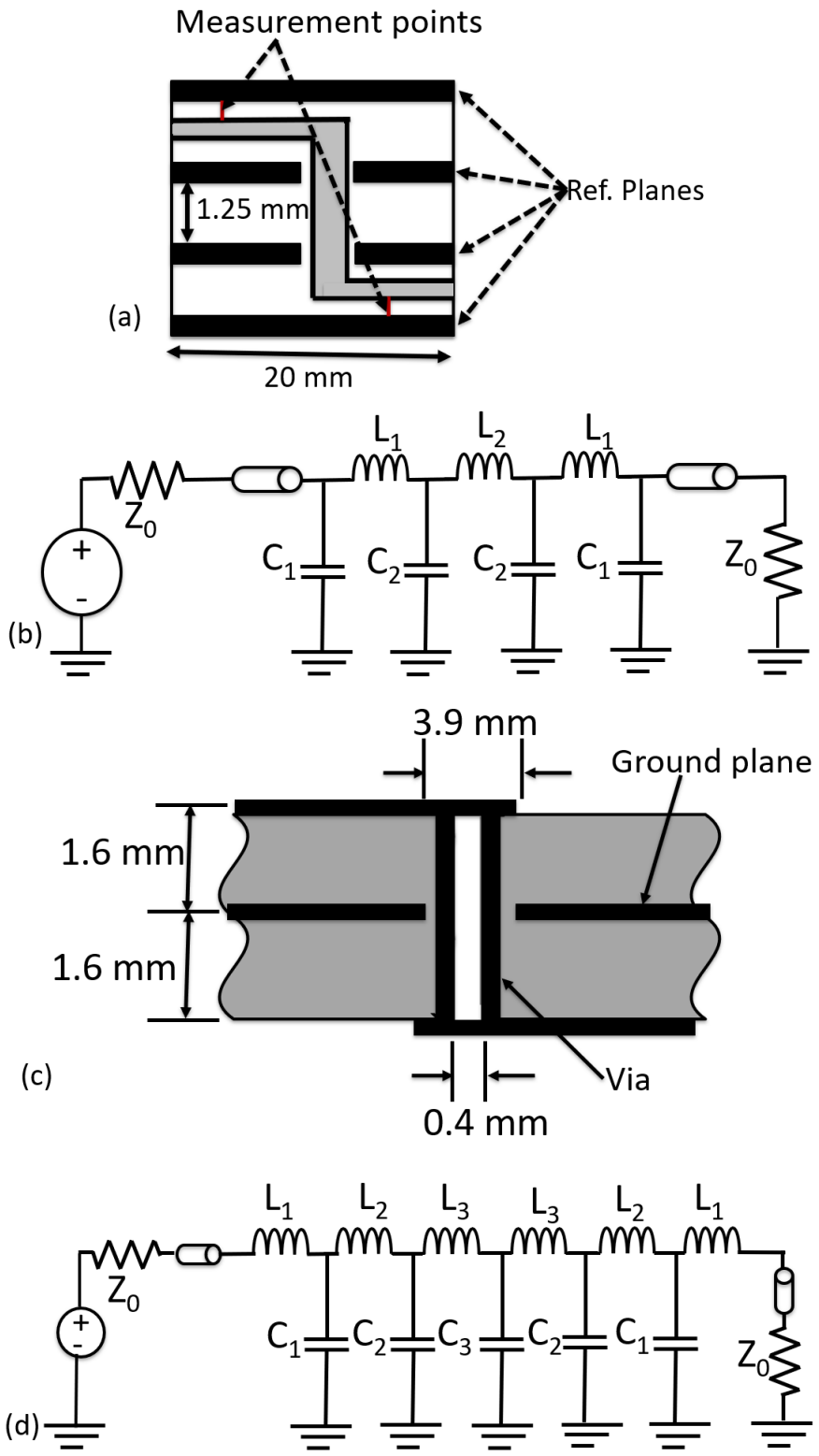

Fig. 6.11 (a) A side view of a rectangular via connecting two strip-lines on different levels in a multi-layer circuit board con- figuration. The strip-lines are 0.25 mm by 1.25 mm, the via is 0.5 by 0.75 mm, and the reference planes are separated from the via by 0.25 mm. (b) The equivalent circuit chosen to represent the rectangular via discontinuity. The transmission lines represent the strip-line portions and the inductors and capacitors represent various parts of the via. (c) The geometry of the cylindrical via discontinuity. (d) An equivalent circuit of the cylindrical via discontinuity [4].

holes, the final structure of design A have $L_{1a} = L_{1b}$, $L_{3a} = L_{3b}$, $L_{2a} = L_{2b}$, $L_{4a} = L_{4b}$, while $L_{1a} = L_{3a}$, $L_{1b} = L_{3b}$, $L_{2a} = L_{2b}$, $L_{4a} = L_{4b}$ for design B. In the final physical structure, there are four unique inductors for both designs, which are label as L_{1a}, L_{1b}, L_{1a} and L_{4a} shown in Fig. 6.15.

The sizes of capacitors patches are different from each other. The layouts show connecting lines, vias, capacitors patches and inductors placements. The two implementations were designed on the same substrate with a layer stack up and substrate height detailed in Fig 6.14. The 3-D view layout of implementation A and B are shown in Fig 6.16 and Fig 6.17 respectively.

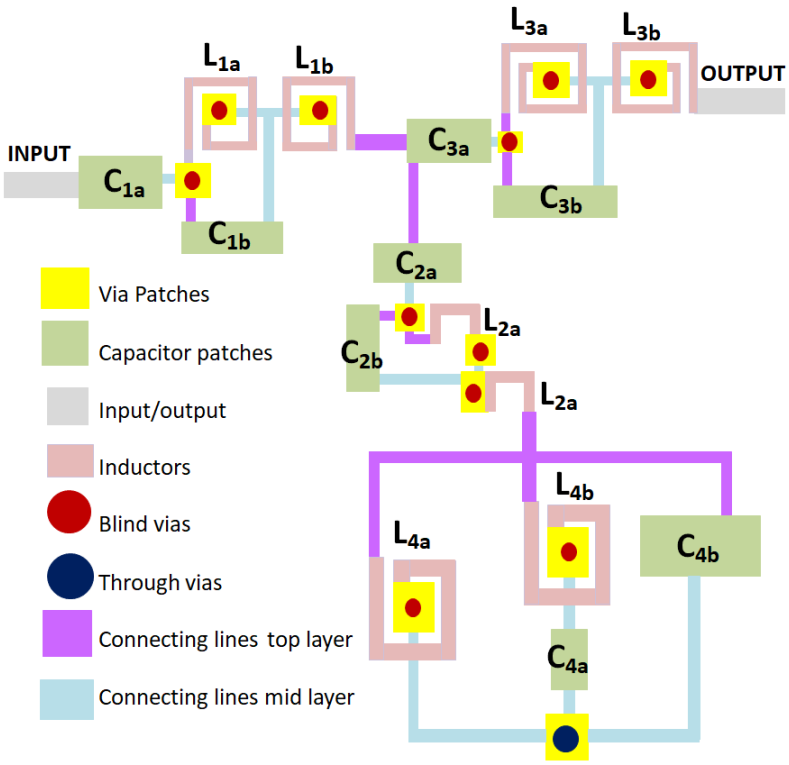

Fig. 6.12 The layout of Design A (Foster) implementation

6.5 Construction and measurements

The quasi-lumped, dual-band filters of Designs A and B were designed, constructed and measured. The first passband reached from 0.45 to 0.86 GHz and the second from 1.24 to 1.75GHz. The frequency responses of the simulated and measured results are shown in Fig. 6.20. Fig. 6.20 (a) shows the simulated implementation of A versus the lumped element model, (b) shows the implementation of the A simulation against measurement, (c) shows the

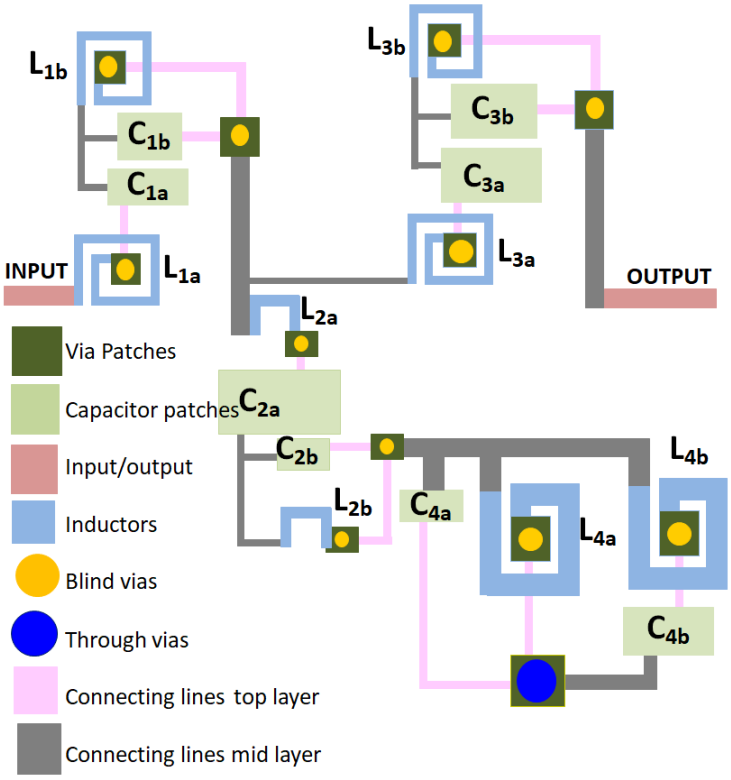

Fig. 6.13 The layout of Design B (mixed Cauer I and II) implementation

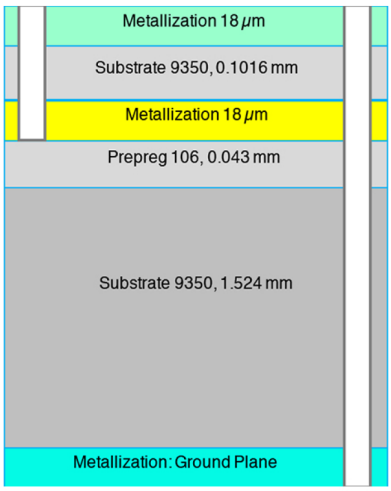

Fig. 6.14 Layer stack-up based on Park Electrocomp's Mercurywave 9350 and 106 prepreg layers.

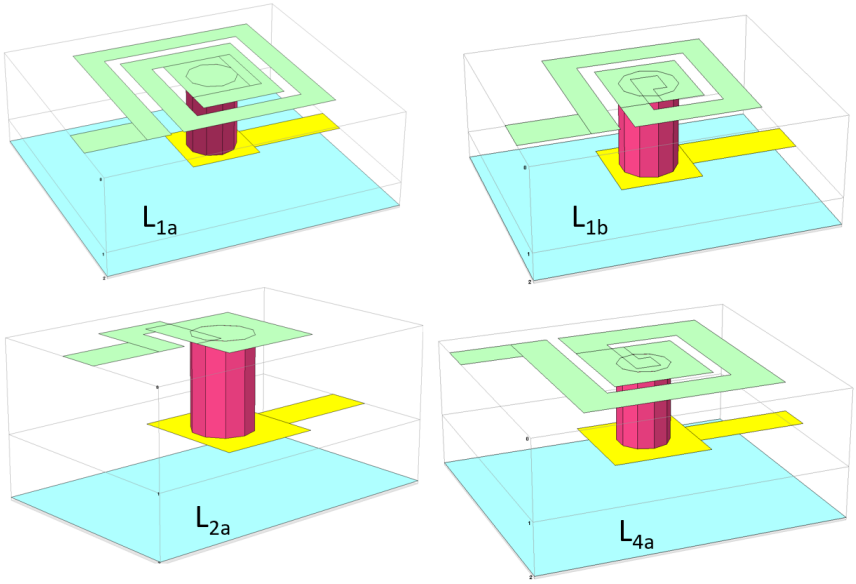

Fig. 6.15 Inductor implementation for the filter of Fig 6.3.

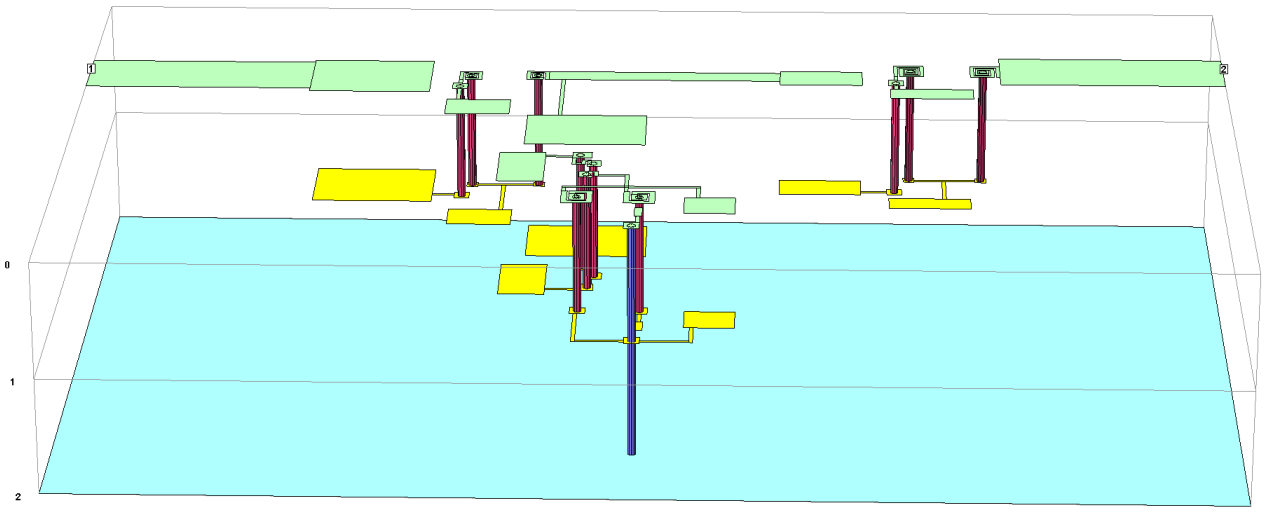

Fig. 6.16 The 3-D view of Design A of the Foster expansion corresponding to the circuit diagram of Fig. 6.2 (a)

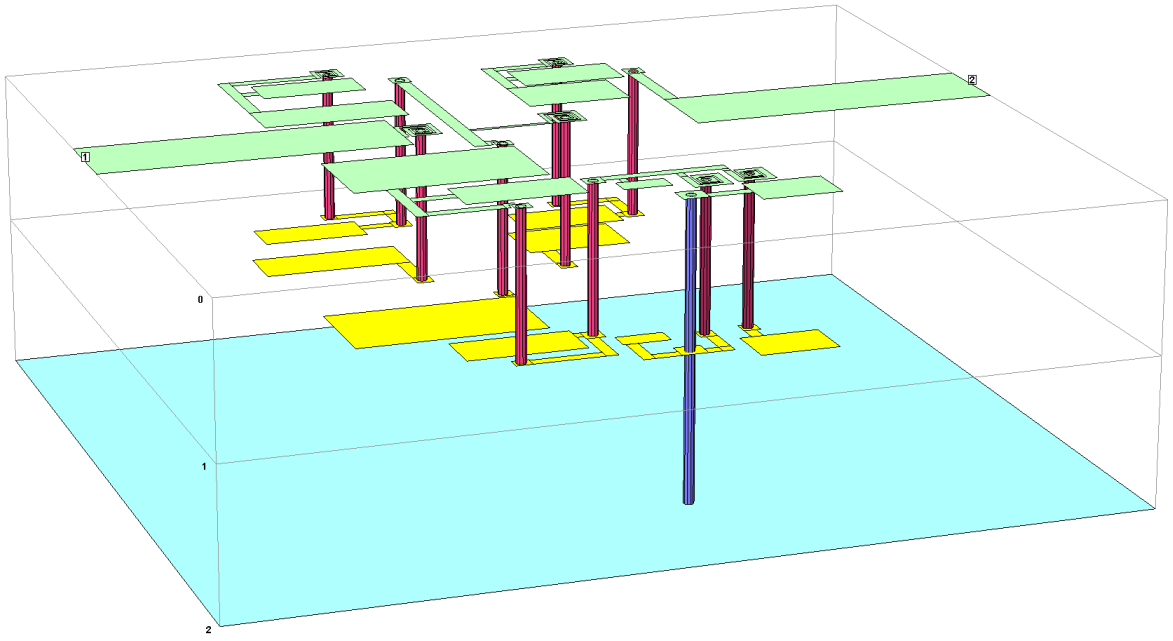

Fig. 6.17 The 3-D view of Design B of mixed Cauer I and II corresponding to the circuit diagram of Fig. 6.2 (b)

simulated implementation of B against measurements and (d) shows A versus B measurement results. The average, pass-band, insertion loss was 0.64 dB for filter A and 0.9 dB for filter B. There was good agreement for the implementation of A and B. This demonstrates that two different designs produced very similar results, indicating that the design method was sound and repeatable. The top view and photographs of the constructed filters are shown in Fig. 6.18 and Fig. 6.19 respectively.

6.5.1 Effect of Q on Filter response

As quasi-lumped element inductors have lower Q-factors than capacitors, as was also shown in [57], we investigated the Q-factors for inductors in the design using Sonnet. Fig 6.21 demonstrates that inductors based on more turns have lower Q-factors (for example inductorL_{4b}), while the highest Q-factor is for inductor L_{2a}, realized by half a turn and a via only. Given that Sonnet simulations for a dual-band filter insertion loss agree very well with the measurements as detailed in Fig 6.20, these Q-factors are considered a reasonable approximation of the actual values and their variation of the frequency band of interest.

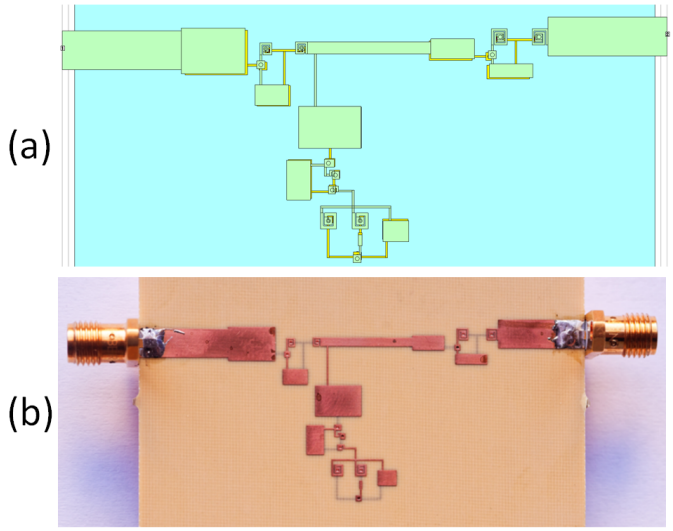

Fig. 6.18 Top view; (b) Photographs of the constructed filter design A of the Foster expansion corresponding to the circuit diagram of Fig. 6.2 (a).

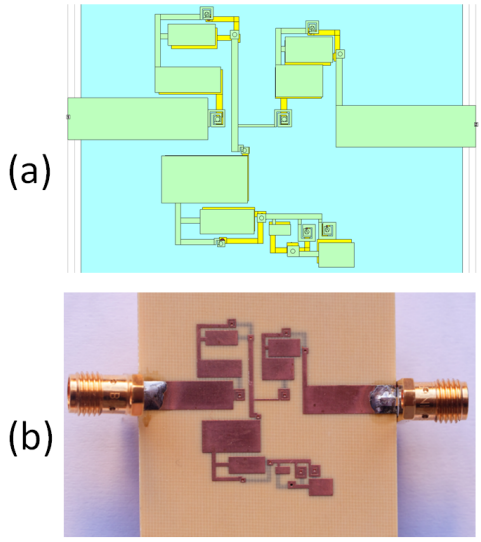

Fig. 6.19 Top view; (b) Photographs of constructed filters of Design B of mixed Cauer I and II corresponding to the circuit diagram of 6.2 (b).

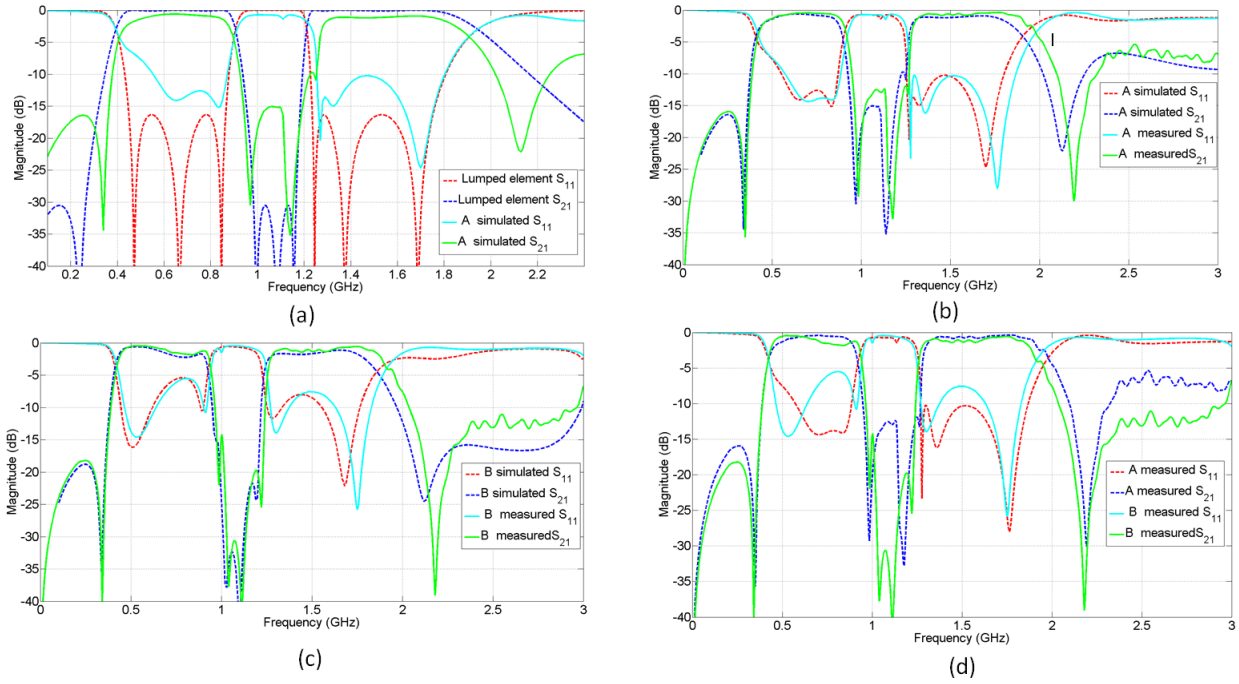

Fig. 6.20 S-parameters for (a) Ideal lumped element filter compared to Design A simulated data, (b) Design A simulated against measured data, (c) Design B simulated against measured data and (d) A comparison of design A and design B measured data.

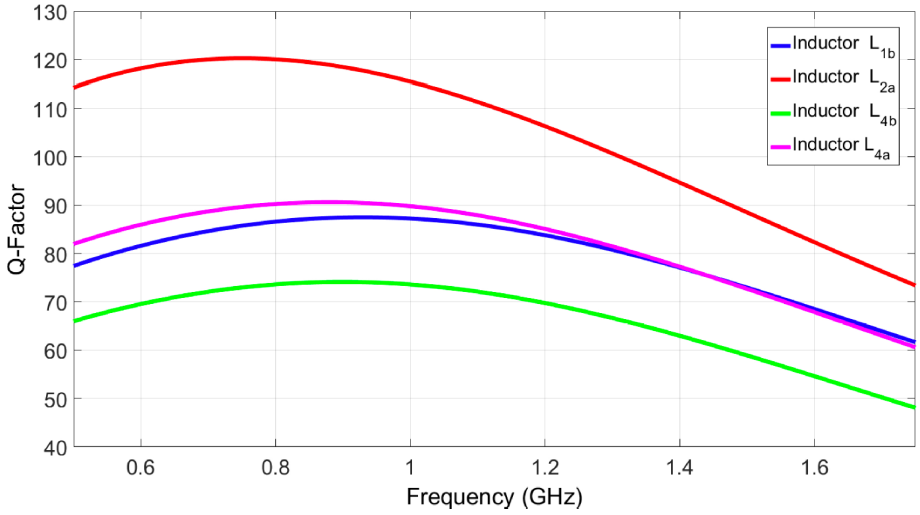

Fig. 6.21 Q-factors estimated by Sonnet for selected inductors as labelled in Fig. 4.2.

6.6 The Influence of non-idealities on the realisation of filters

Parasitic elements exist inside the electrical component and generally has unfavorable consequences, causing poor performance of the circuit. A quasi-lumped element was implemented by employing inductors and capacitors, and parasitic of inductors has powerful influence and noticeably affected the circuits more than the capacitor parasitic. An investigation of a dual-band, quasi-lumped element illustrating how inductor implementation influences filter features, especially bandwidth selectivity and harmonics, is presented.

First each unique inductor employed in the design was simulated individually to generate an equivalent circuit in sonnet software. The EM simulation took into consideration all the effects from the substrate properties, layer thickness, effects from vias and their parasitic, as well as dispersion of the material properties. The EM generated equivalent circuit is shown in Fig 6.22 where C_s is the fringing capacitance between the inductor turns, R_s the series resistance of the inductor metal, Ls the total inductance, R_k the series resistance of the inductor metal,L_k series inductance of the inductor metal, C_{ox1} and C_{ox2} the shunt capacitances of the oxide layer, C_{sub1}, C_{sub2} total shunt capacitance of the dielectric layers and R_{sub1} , R_{sub2} shunt resistance due to substrate losses. The values of all these elements are provided in Table 6.4as extracted from sonnet.

To analyse the parasitic effects on the ideal dual-band circuit of Fig. 6.3, the EM generated inductor of each inductor in Fig. 6.22 was inserted in a dual-band model replacing the ideal inductors one by one to observe the impact on the frequency. The values of all parasitic elements generated from the four unique inductor designs are detailed in Table. 1 with inductors in nH, capacitors in pF and resistance in. Several examples are indicated in Fig 6.23 to Fig 6.31 .

Figure 6.23 focuses on L_{1a}, where the generated spurious elements are included in the model of Fig 6.23 (a) as shown in Fig 6.23 (b). The dominant spurious effects from the inductor L_{1a} was the influence on the bandwidth on band two, as is evident from the first graph of Fig 6.32, while band one was not affected significantly. In practice inductor L_{1a} had a large physical dimension. The next was inductor L_{1b} replaced by a parasitic equivalent circuit 6.24 (b). The impact on the frequency response is indicated on the second graph of Fig 6.32. InductorL_{1b} affected the bandwidth of the second band and the suppression between the bands was affected. Inductor L_{3a} and L_{3b} were replaced by the parasitic equivalent circuit in Fig 6.25 and 6.26 respectively.

Again the second band bandwidth was affected as indicated in Fig. 6.33. Noticeably, inductor L_{3b} affected the response in a similar manner as L_{1b}. To model the spurious effects

of L_{1b} andL_{3b}, as indicated in Fig 6.27 (a) were replaced by the full circuit models including parasitic elements as detailed in Fig 6.27 (b). The main influence here was the suppression between the pass-bands of Fig 6.34, which if these effects were not included in the design, would have destroyed suppression between the two bands. In the design process these effects were taken into consideration to meet the filter specifications. Inductors L_{2a} and L_{2b}, were replaced in the circuits of Fig 6.28 and 6.29 respectively. The effects on frequency responses are indicated in Fig 6.35. The first graph in Fig 6.35 shows harmonic effects arising from the second band; its bandwidth was almost halved. The last two inductors are the L_{4a} and L_{4b} circuit shown in Fig 6.30 and 6.30. Their spurious effects are indicated in Fig 6.36. In general, parasitic elements affect the bandwidths and the suppression between bands.

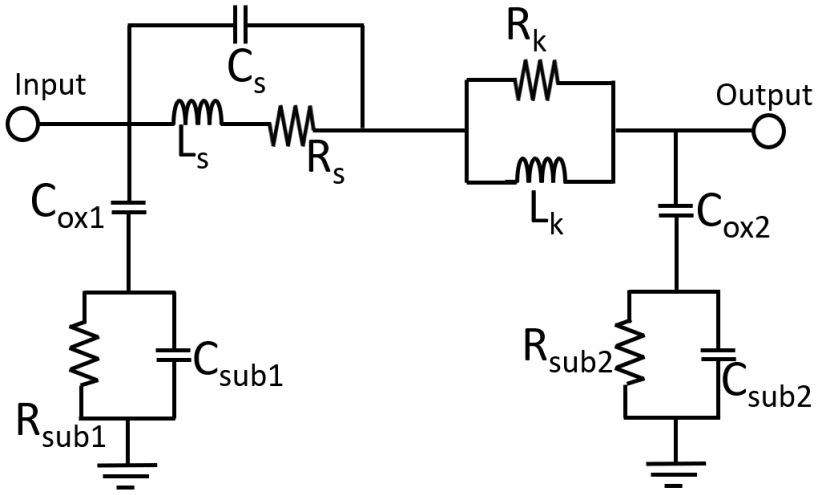

Fig. 6.22 Equivalent circuit with the parasitic elements for an inductor of the filter of Fig. 6.3. L_s is the desired inductance and the other elements are spurious elements.

6.7 Tunable Dual- band filters

Electronically tunable filters are popular in the communication industry as the filter has multiple frequency operations. Tuning a planar filter, typically requires a tuning device, a varactor diode.

A simple second order tunable bandpass filter is reported in [37]. Tunability was achieved with the use of varactor diodes. The position and the number of varactors was important for this design as they provided the required capacitance for the filter in parallel arrangement. The varactor tuned, dual-band filter in [33] achieved frequency variation in the second band while the first band was fixed. The similar tunability characteristics are presented in [75]

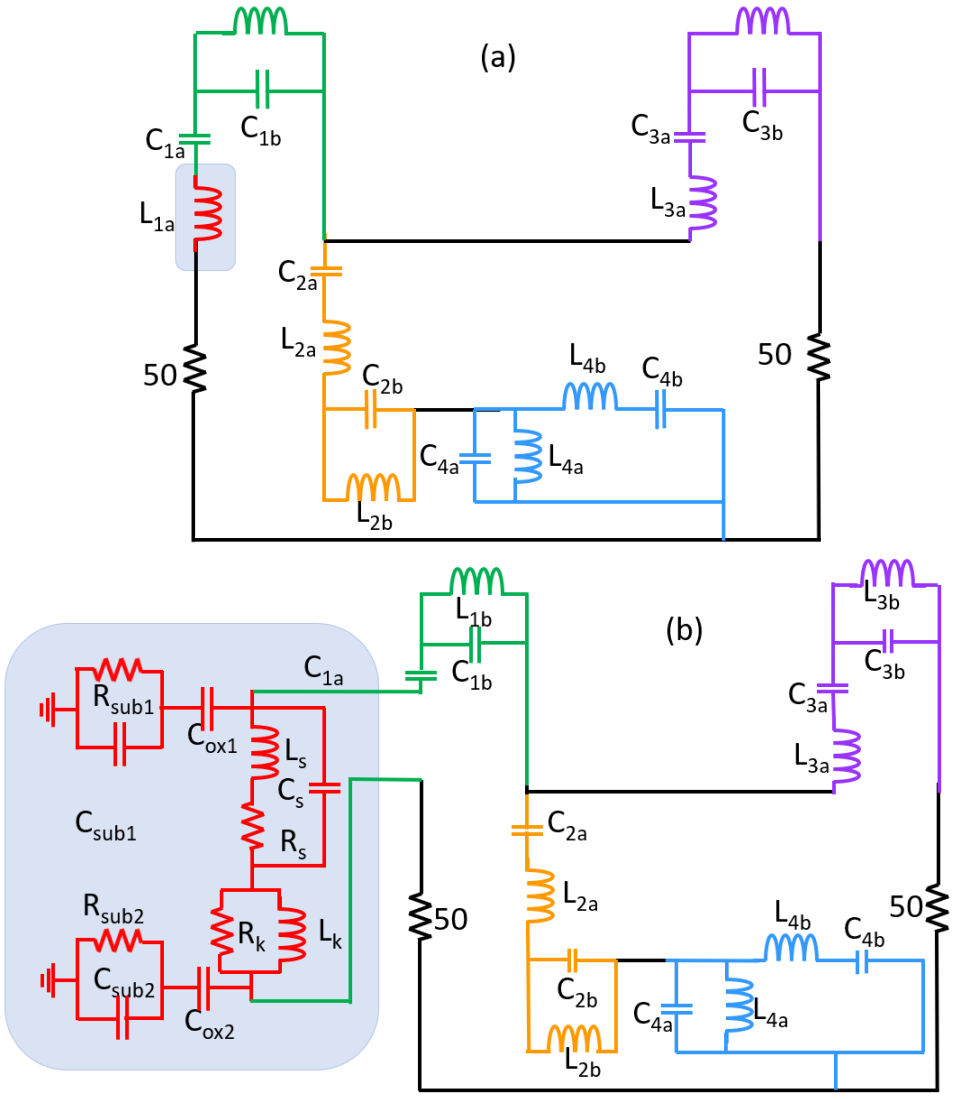

Fig. 6.23 The ideal circuit model in which the highlighted inductor L_{1a} is replaced by the corresponding circuit in (b) with parasitic elements (refer to Fig. 6.22).

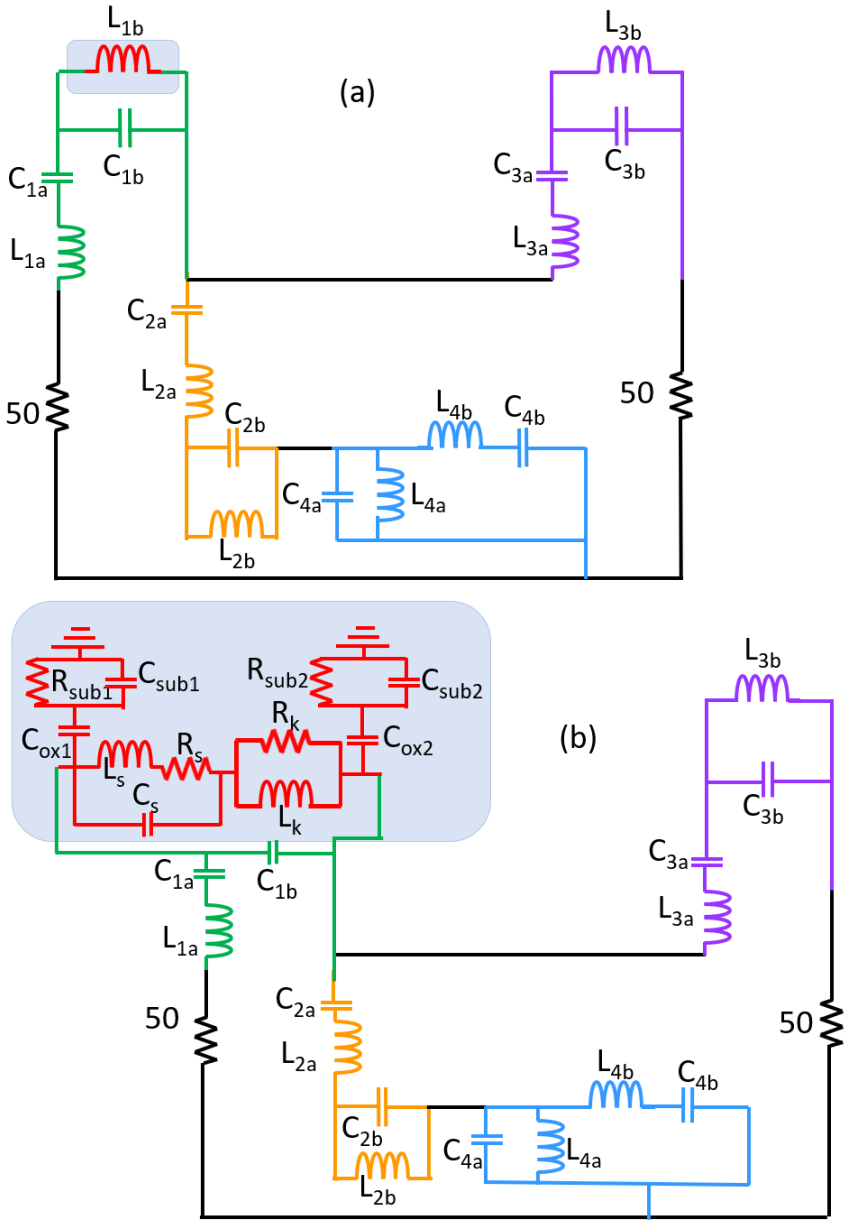

Fig. 6.24 The ideal circuit model in which the highlighted inductor L_{1b} is replaced by the corresponding circuit in (b) with parasitic elements (refer to Fig. 6.22).

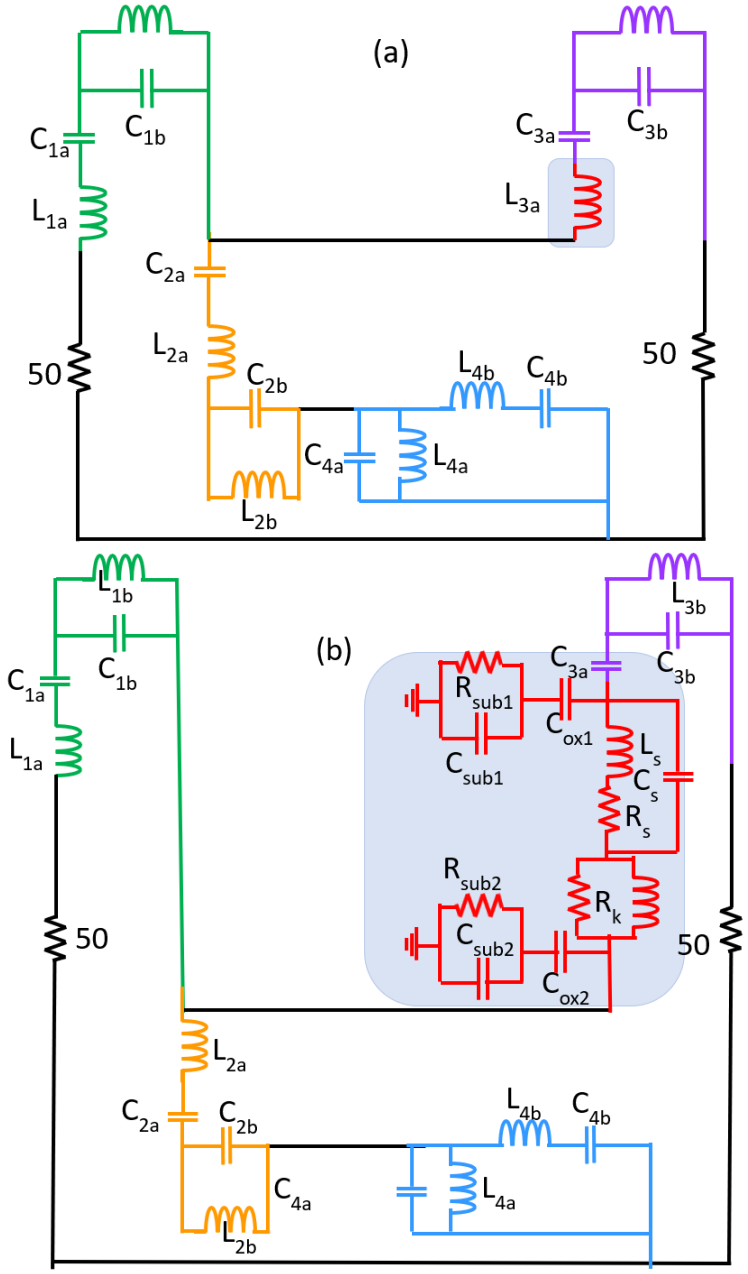

Fig. 6.25 The ideal circuit model in which the highlighted inductor L_{3a} is replaced by the corresponding circuit in (b) with parasitic elements (refer to Fig. 6.22).

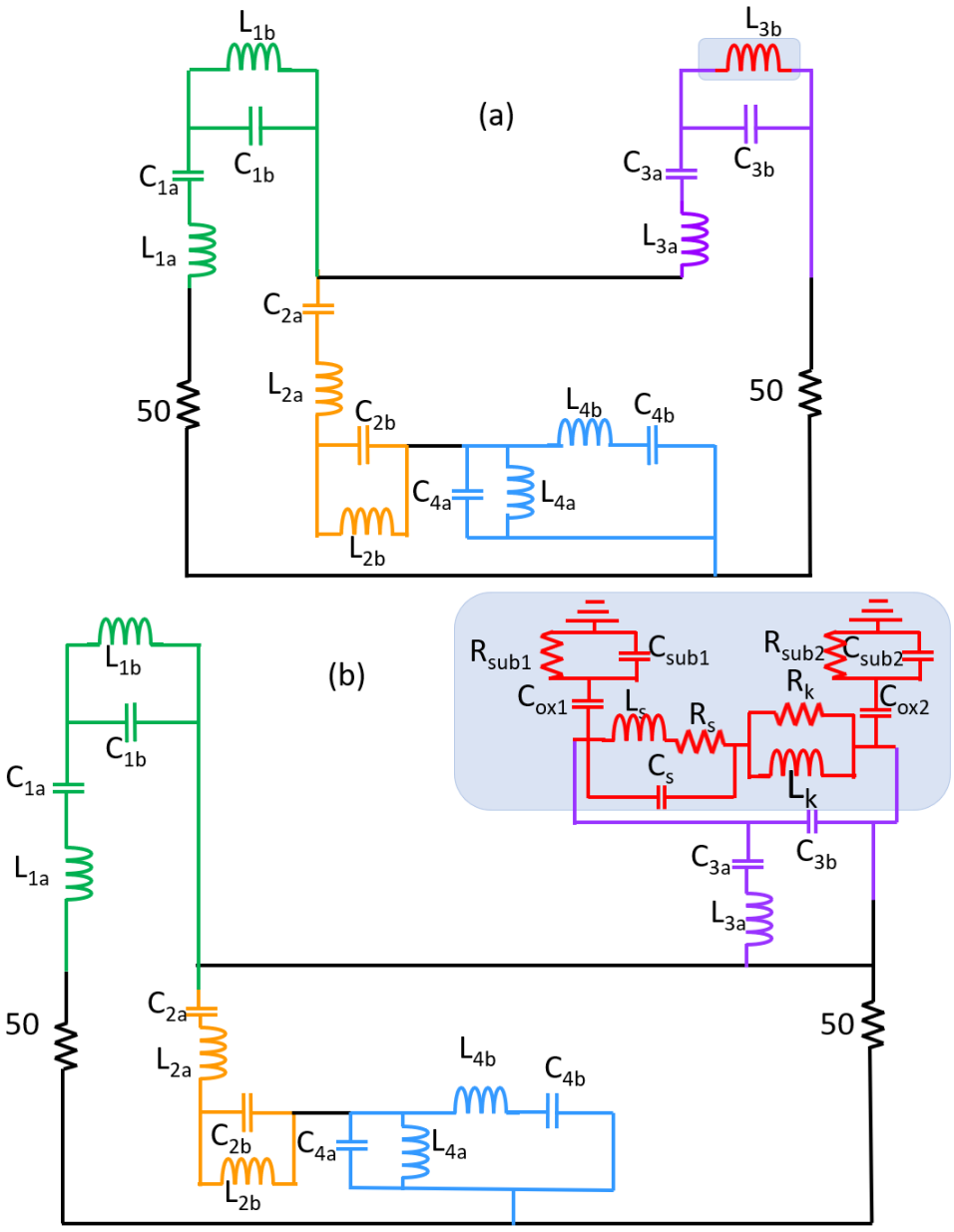

Fig. 6.26 The ideal circuit model in which the highlighted inductor L_{3b} is replaced by the corresponding circuit in (b) with parasitic elements (refer to Fig. 6.22).

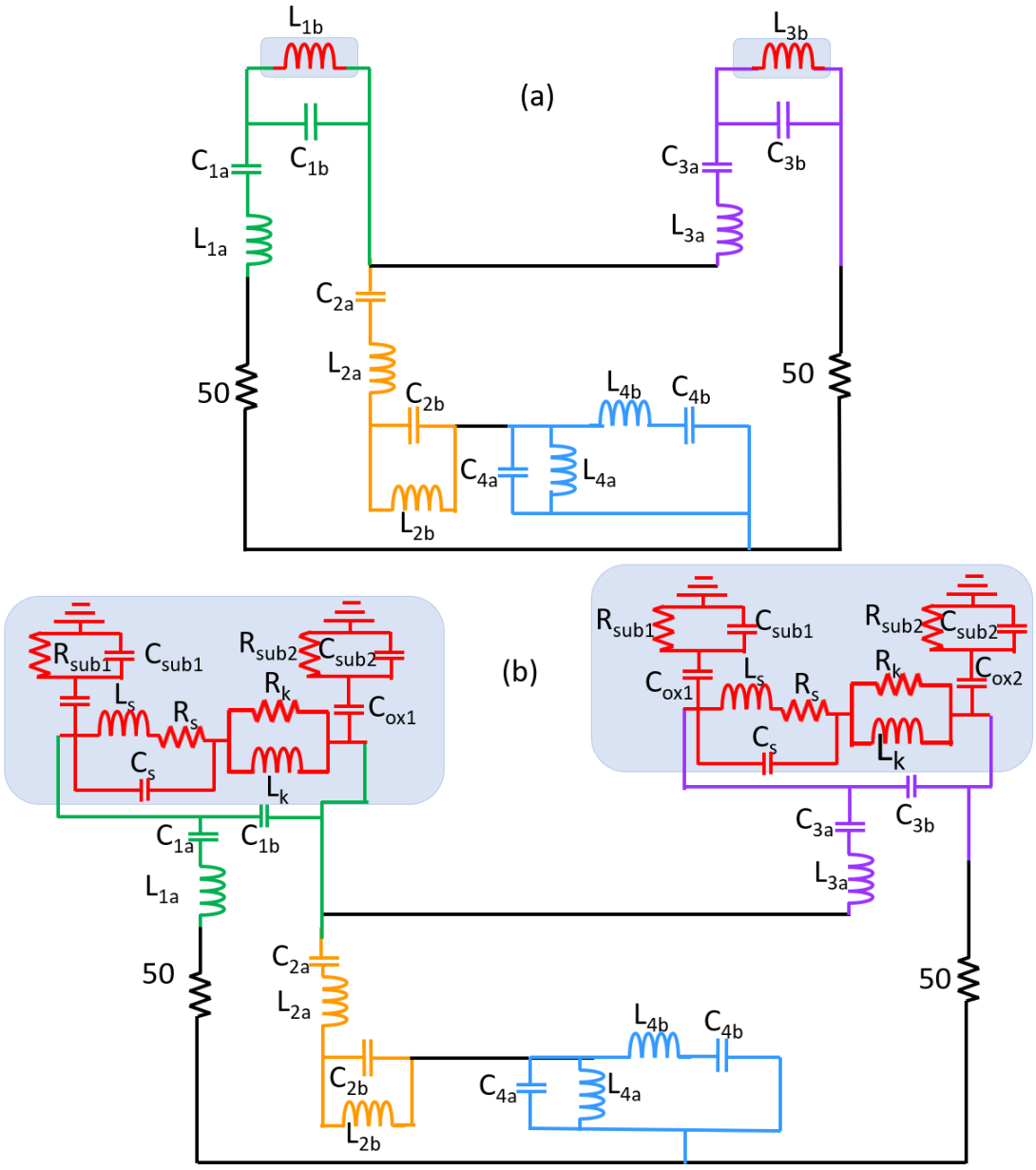

Fig. 6.27 The ideal circuit model in which the highlighted inductor L_{1b} and L_{3b} is replaced by the corresponding circuit in (b) with parasitic elements (refer to Fig. 6.22).

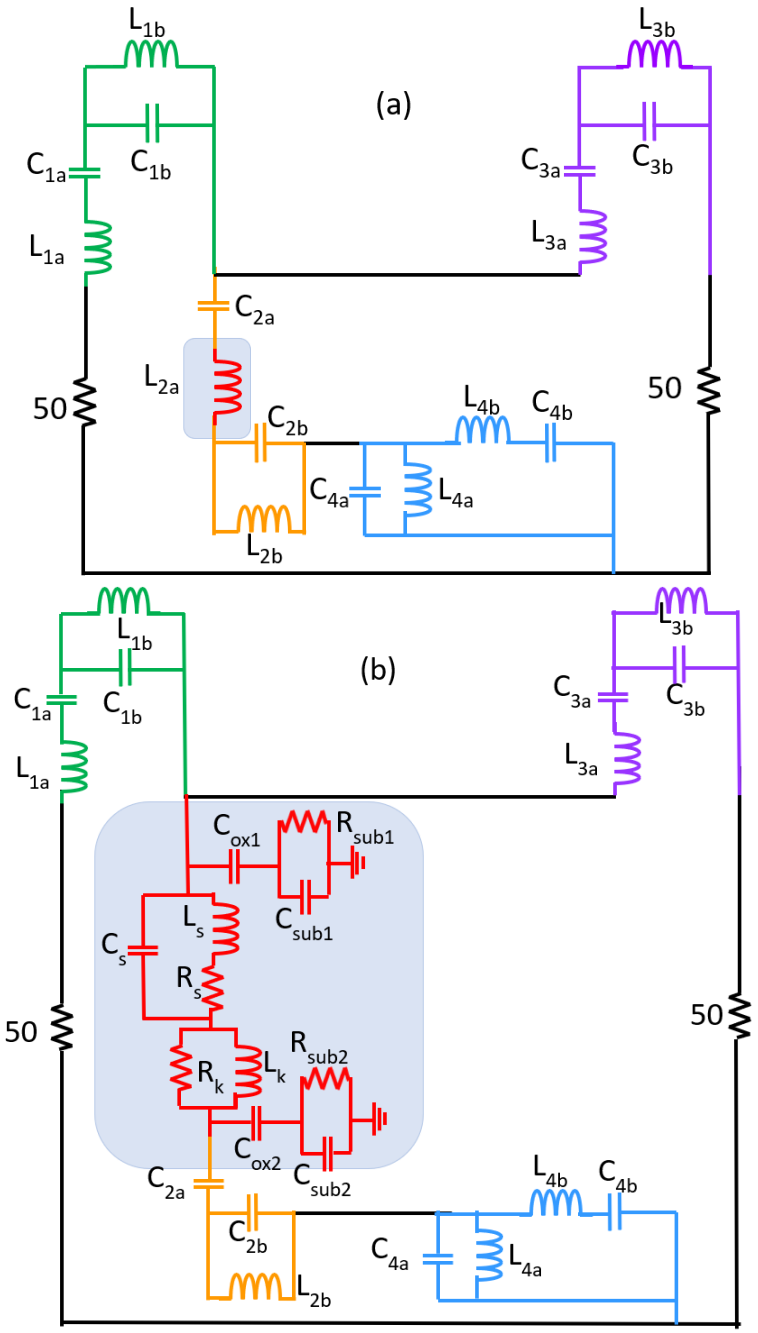

Fig. 6.28 The ideal circuit model in which the highlighted inductor L_{2a} is replaced by the corresponding circuit in (b) with parasitic elements (refer to Fig. 6.22).

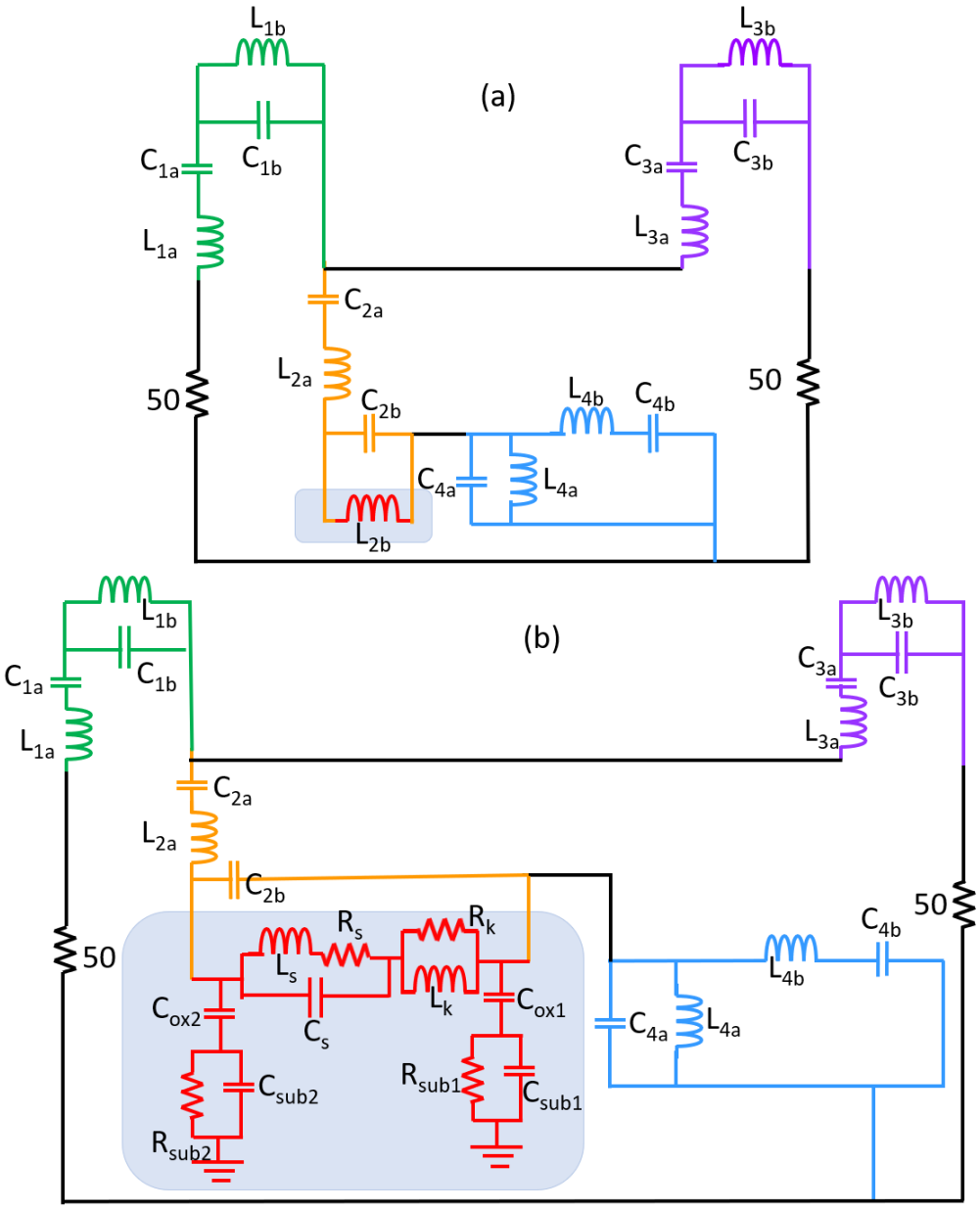

Fig. 6.29 The ideal circuit model in which the highlighted inductor L_{2b} is replaced by the corresponding circuit in (b) with parasitic elements (refer to Fig. 6.22).

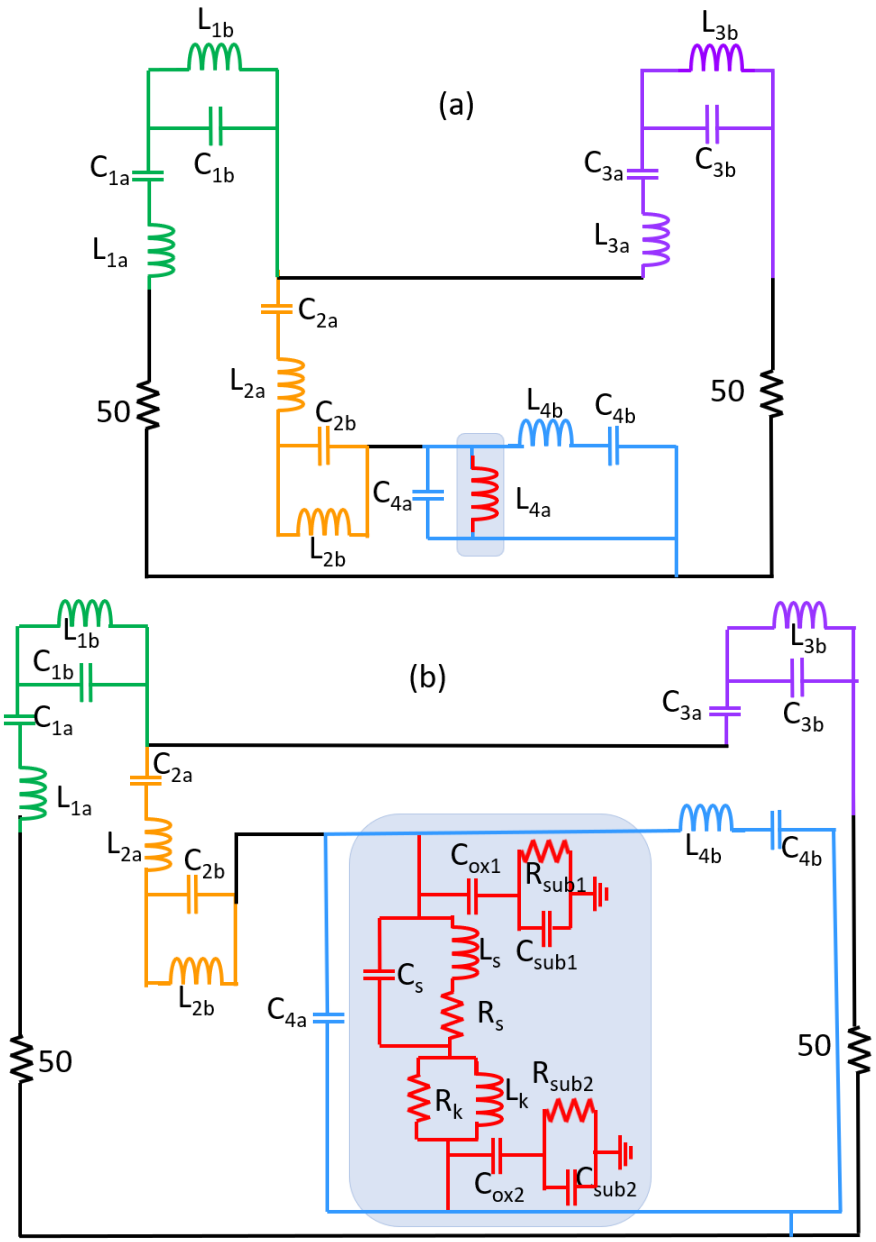

Fig. 6.30 The ideal circuit model in which the highlighted inductor L_{4a} is replaced by the corresponding circuit in (b) with parasitic elements (refer to Fig. 6.22).

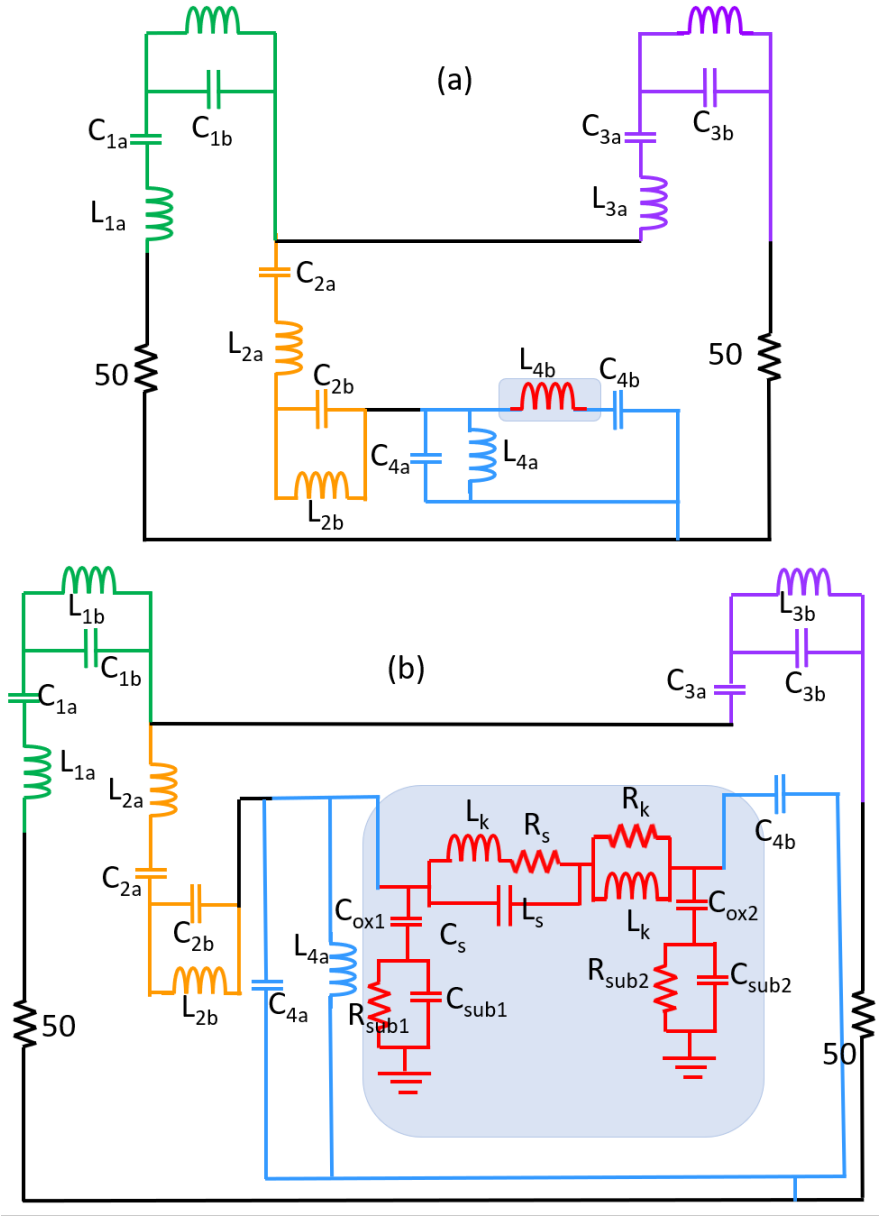

Fig. 6.31 The ideal circuit model in which the highlighted inductor L_{4b} is replaced by the corresponding circuit in (b) with parasitic elements (referto Fig. 6.22).

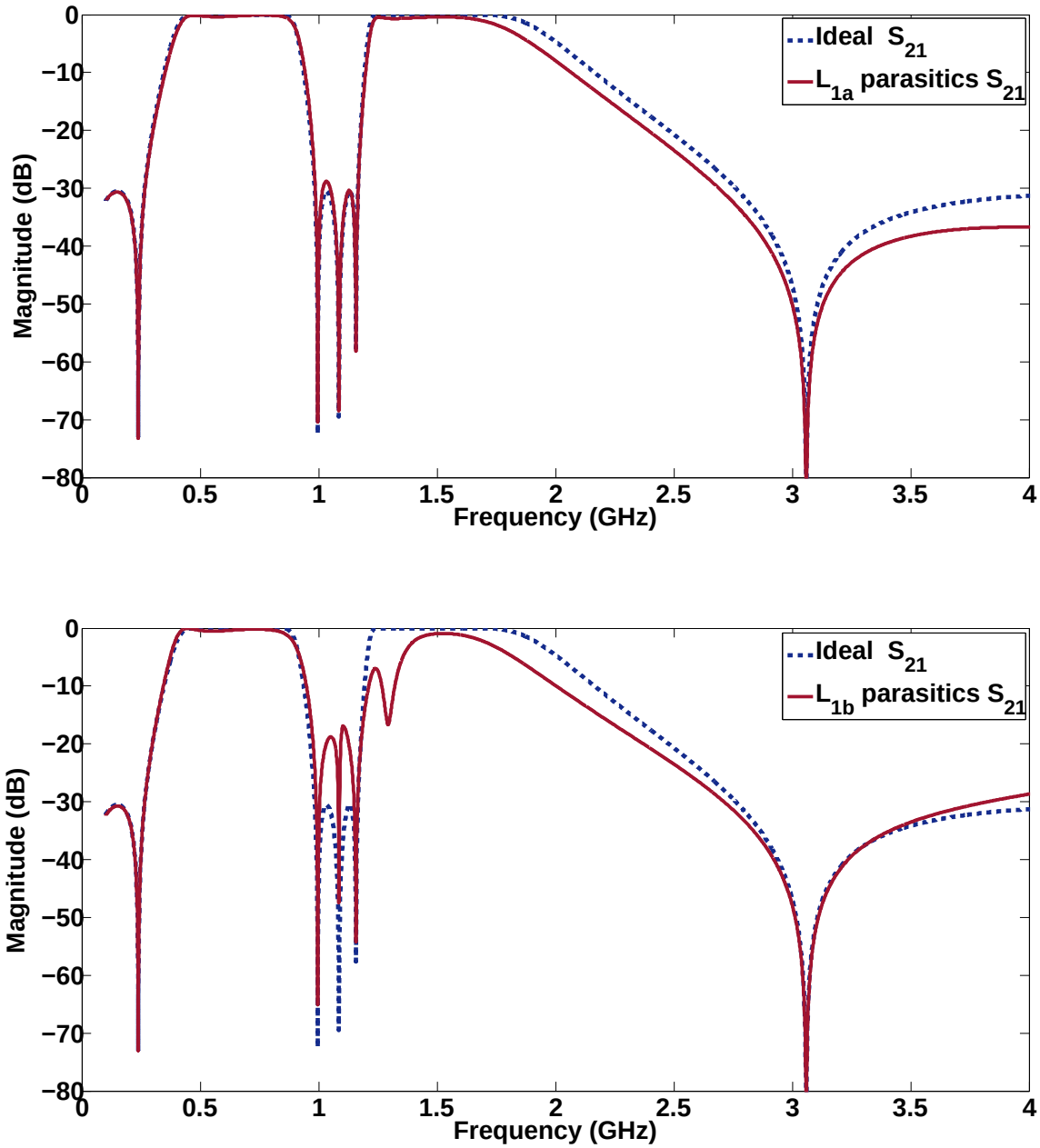

Fig. 6.32 The effect of the spurious components of the inductor L_{1a} and L_{1b}, detailed in Fig. 6.23 and Fig. 6.24 on the ideal lumped-element filter response. The bandwidth of band two is affected most dramatically

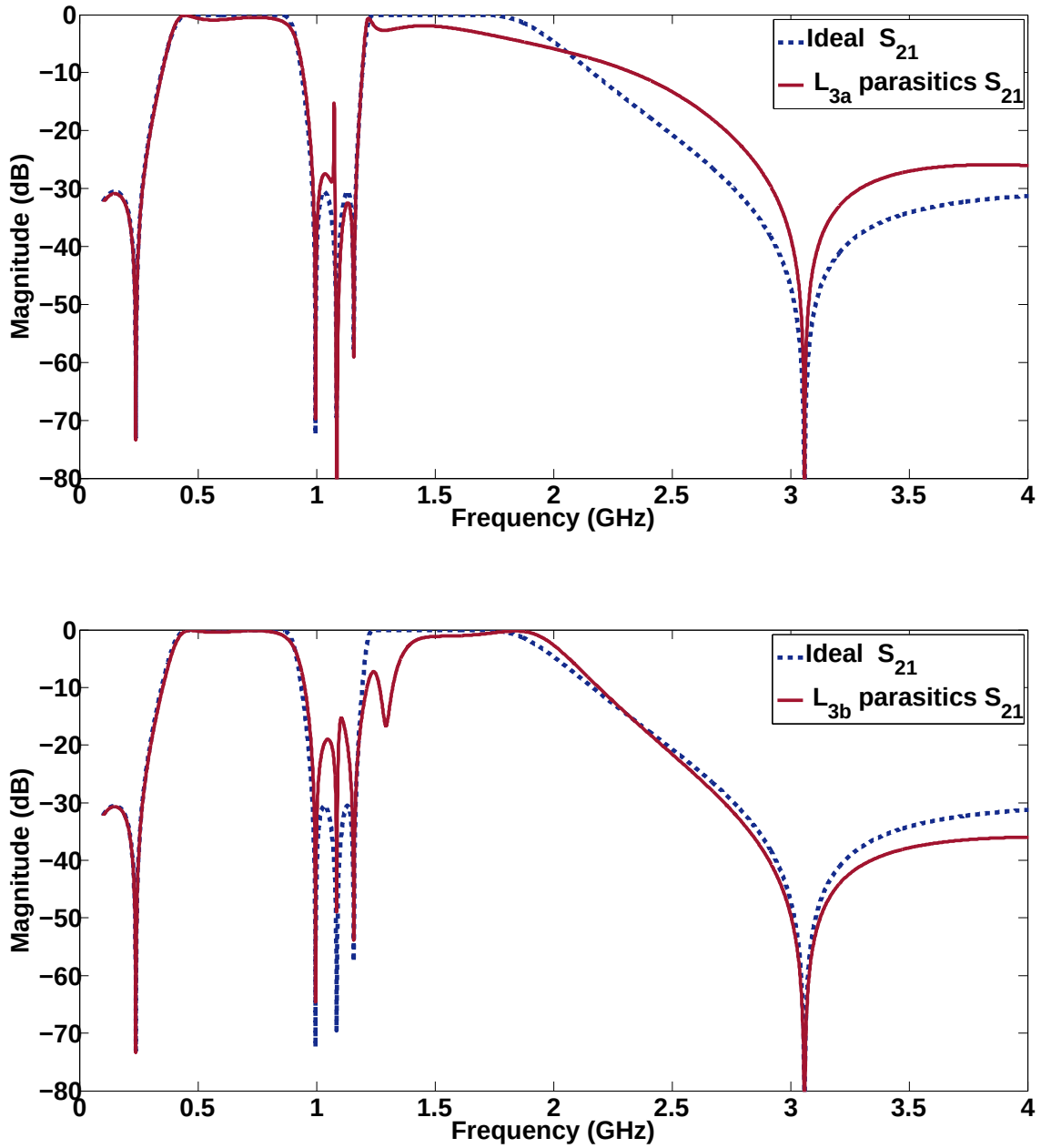

Fig. 6.33 The effect of the spurious components of the inductor L_{3a} and L_{3b}, detailed in Fig. 6.25 and Fig. 6.26 on the ideal lumped-element filter response. The bandwidth of band two is affected most dramatically

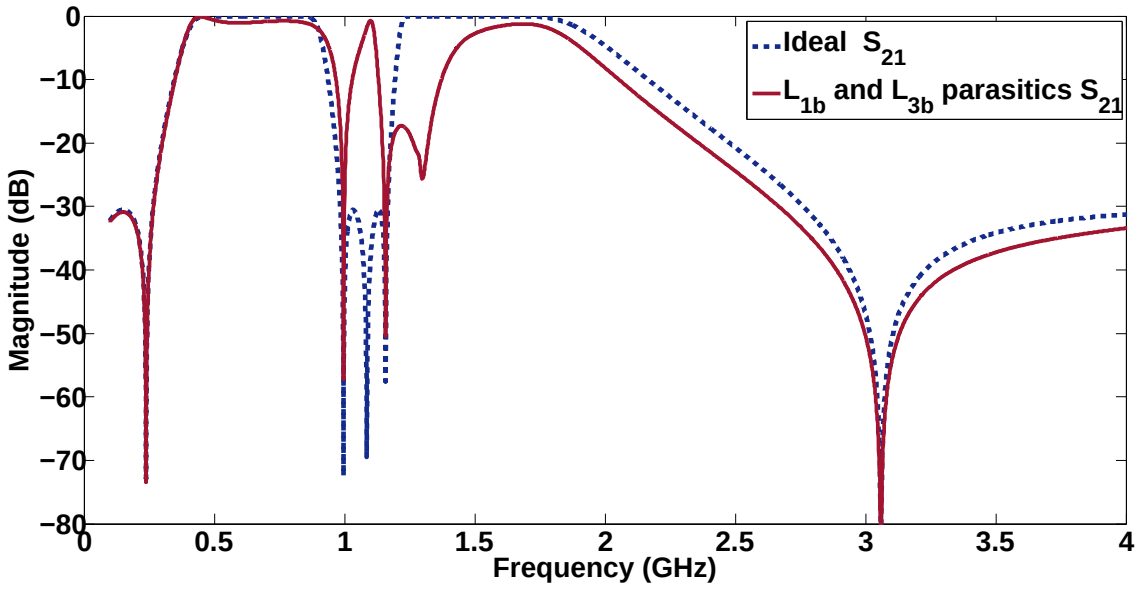

Fig. 6.34 The effect of the spurious components of the inductor L_{1b}, L_{3b}, detailed in Fig. 6.27 on the ideal lumped-element filter response. The bandwidth of band two is affected most dramatically

Parasitic elements	L_{1a}	L_{1b}	L_{2a}	L_{4a}
C_s	0.104	1.78	0.673	1.52
L_s	6.78	1.36	2.44	1.64
R_s	0.0727	0.0323	0.0225	0.0382
R_k	0.478	51.5	5.01	47.2
L_k	0.161	0.545	0.218	0.543
C_{ox1}	0.654	0.633	0.639	0.647
C_{ox2}	0.672	0.641	0.641	0.654
R_{sub1}	7.68	8.75	10.4	8.51
R_{sub2}	8.08	8.11	8.58	7.89
C_{sub1}	17.1	16.7	16.9	17.0
C_{sub2}	17.7	16.4	17.0	16.6

Table 6.4 Extracted element Values of Fig. 6.22 for each inductor. The units of the extracted elements: inductors in nH, capacitors in pF, and resistors in Ω

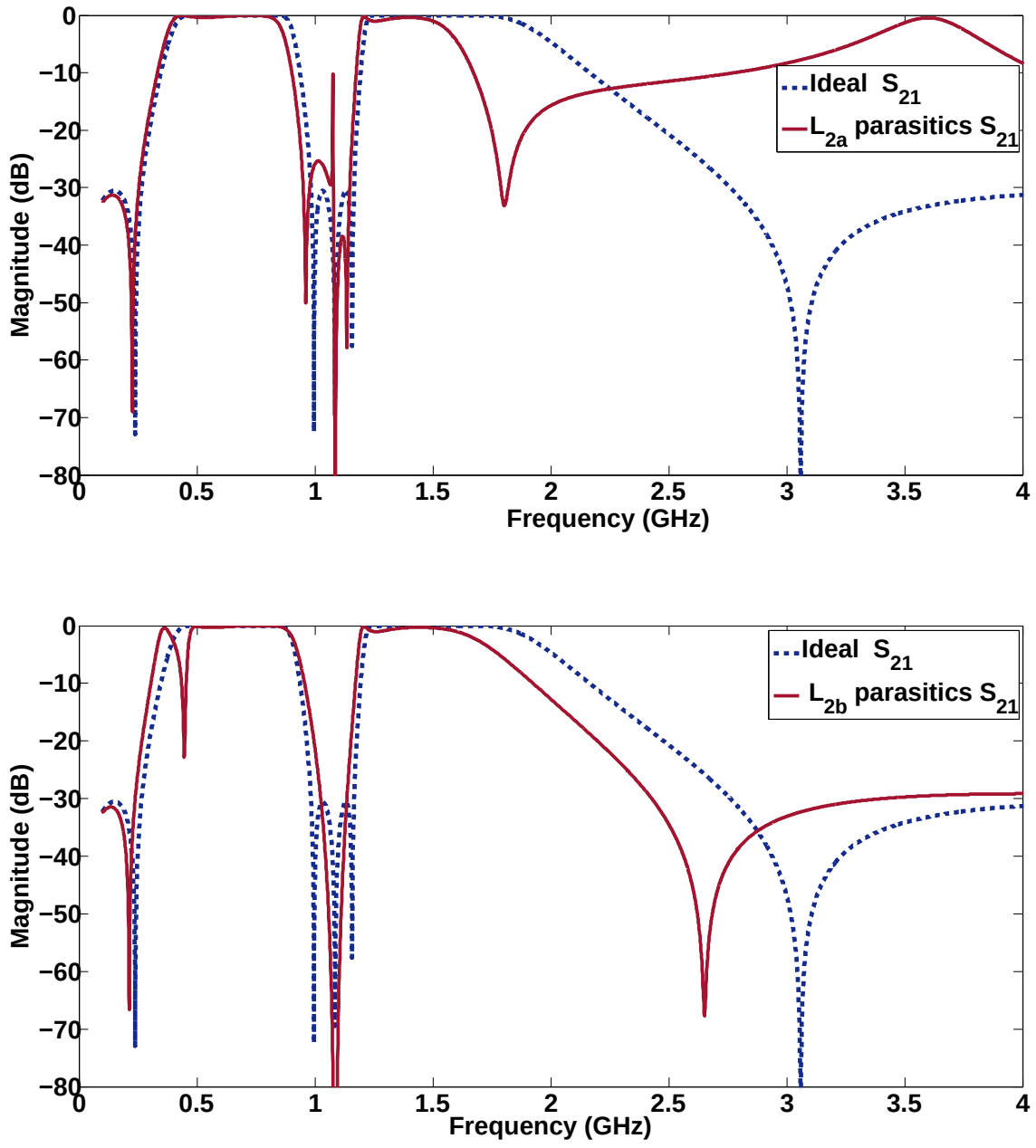

Fig. 6.35 The effect of the spurious components of the inductor L_{2a} and L_{2b}, detailed in Fig. 6.28 and Fig. 6.29 on the ideal lumped-element filter response. The bandwidth of band two is affected most dramatically

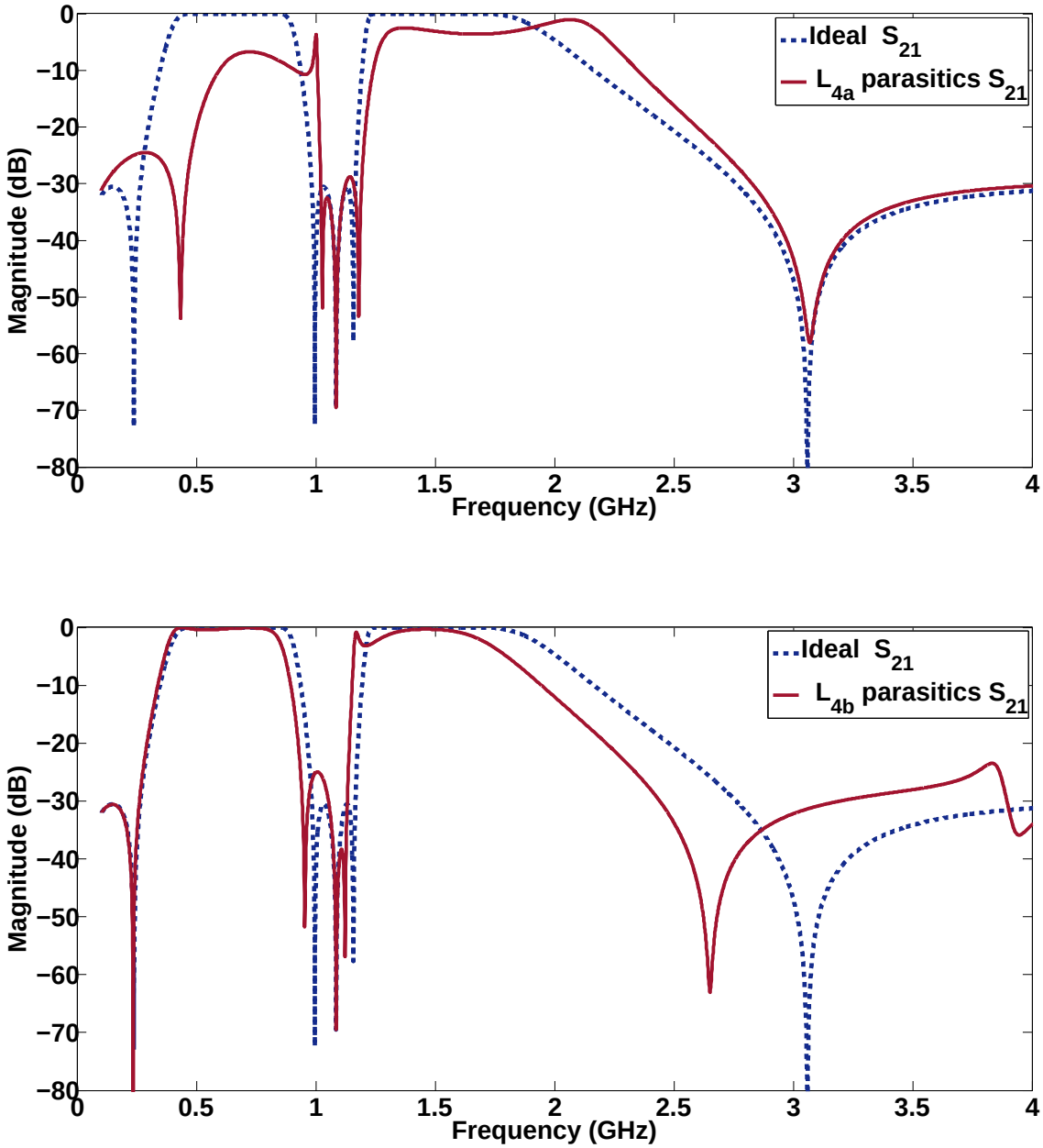

Fig. 6.36 The effect of the spurious components of the inductor L_{4a} and L_{4b}, detailed in Fig. 6.30 and Fig. 6.31 on the ideal lumped-element filter response. The bandwidth of band two is affected most dramatically

for a lumped element filter operating at the similar frequency range as filters in this chapter. In general, frequency variations are achieved by tuning a capacitor only, an inductor only or both. A resonant circuit in [46] shown in Fig 6.37 approximates frequency variations by tuning a series capacitor only. In this case an additional parallel resonant circuit added a pole of reactance at frequency w_∞. As the resonator was tuned to high frequency the slope parameter increased more rapidly than it would if the pole reactance were not there. The resonant circuit in [46] is similar to the dual-band quasi-lumped element resonators discussed in this chapter. It is possible to design a tunable circuit by adding a varactor diode without changing the lumped-element values that provide dual band response.

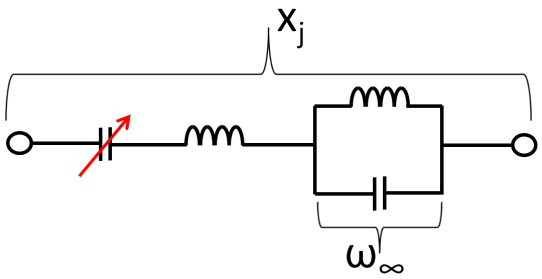

Fig. 6.37 Resonator Circuit [46]

6.7.1 Implementation and analysis of the tunable dual-band filter

The fixed, dual-band, quasi-lumped element filter was designed, analyzed and implemented in the previous sections. This section discusses the possibility of including tunable characteristics and the implementation of the proposed tunable, dual-band filter of design B. The filter employed the same Mercury wave substrates and had the same thickness as the fixed design.

Structure of the proposed tunable filter

The circuit model which includes varactor diodes (SMV1405-040LF) model (see Fig. 6.38 (a) for Design B) represents the physical structure of the tunable, microstrip quasi-lumped element filter in Fig. 6.38 (b) with varactor diodes attached to the series capacitor. C1 is a bypass capacitor and L is an RF choke. The tuning capability of the physical structure is illustrated in the circuit model in Fig. 6.38, that provides a response that takes into consideration the loss and parasitic of the varactor utilized. Fig. 6.39 plots four, simulated, quasi-lumped element responses versus the circuit model. The filter had a fixed lower band and a tunable upper band. The tunable upper band had good selectivity on the edge of the

upper band. It is of importance to note that the suppression between the bands remained the same and was comparable to the fixed response.

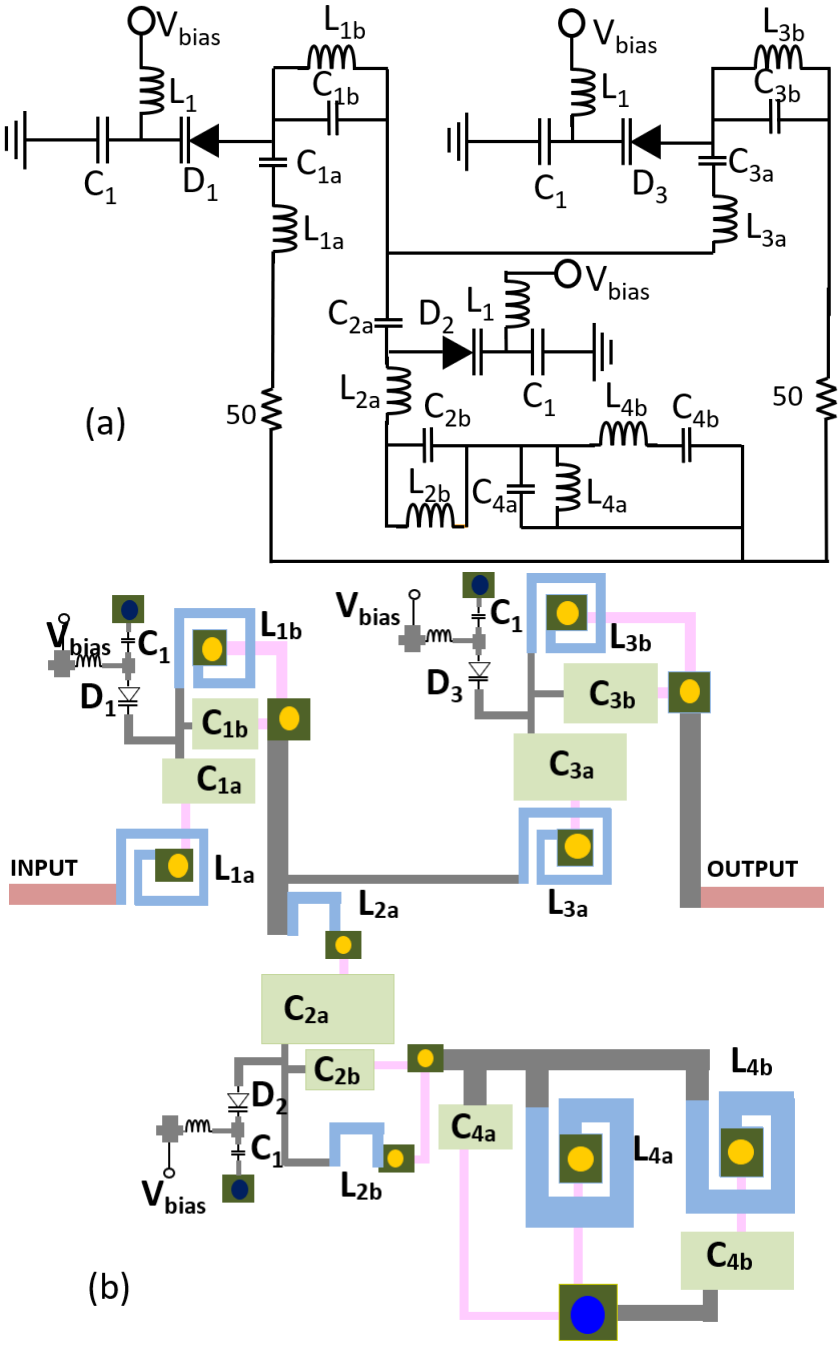

Fig. 6.38 Tunable mixed Cauer I and II dua- band prototype filters (a) mixed Cauer I and II circuit model, and its (b) its physical layout.

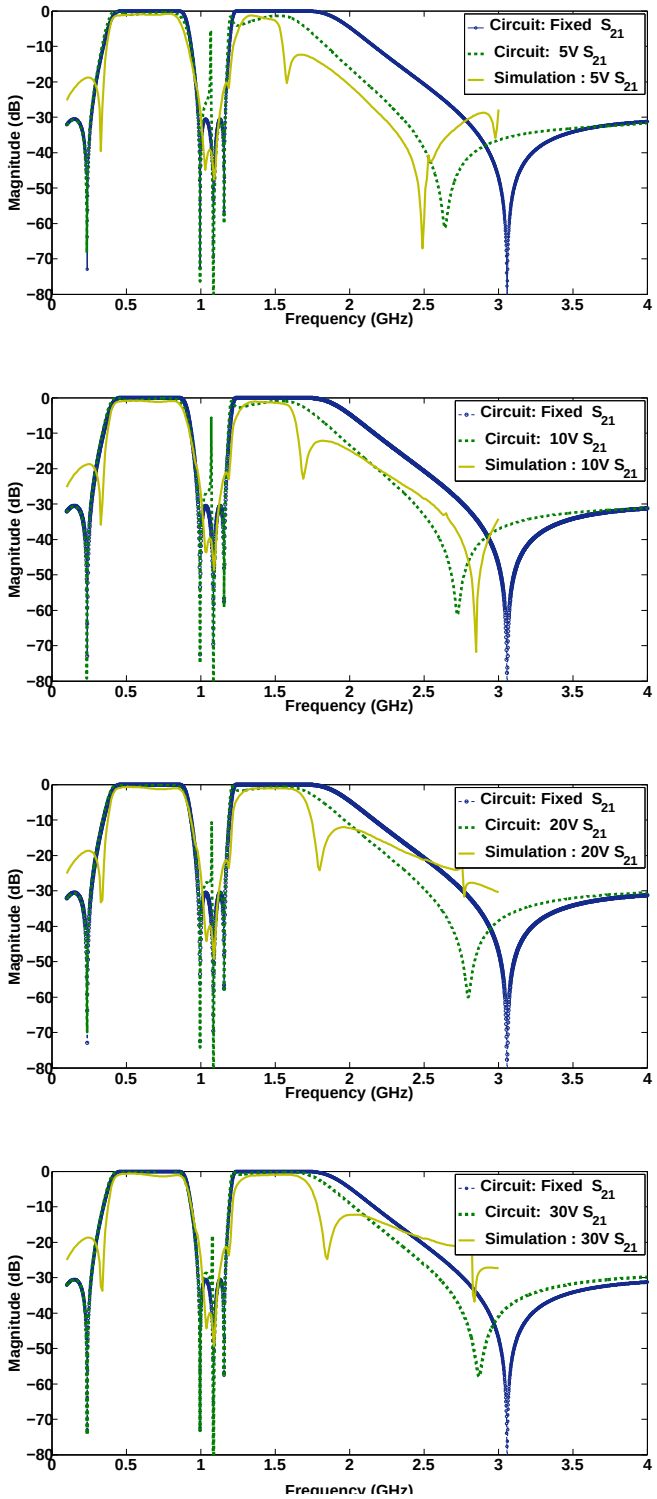

Fig. 6.39 Fixed ideal response of the circuit in Fig. 6.3 versus tunable response of the circuit and simulated prototypes of Fig 6.38 .

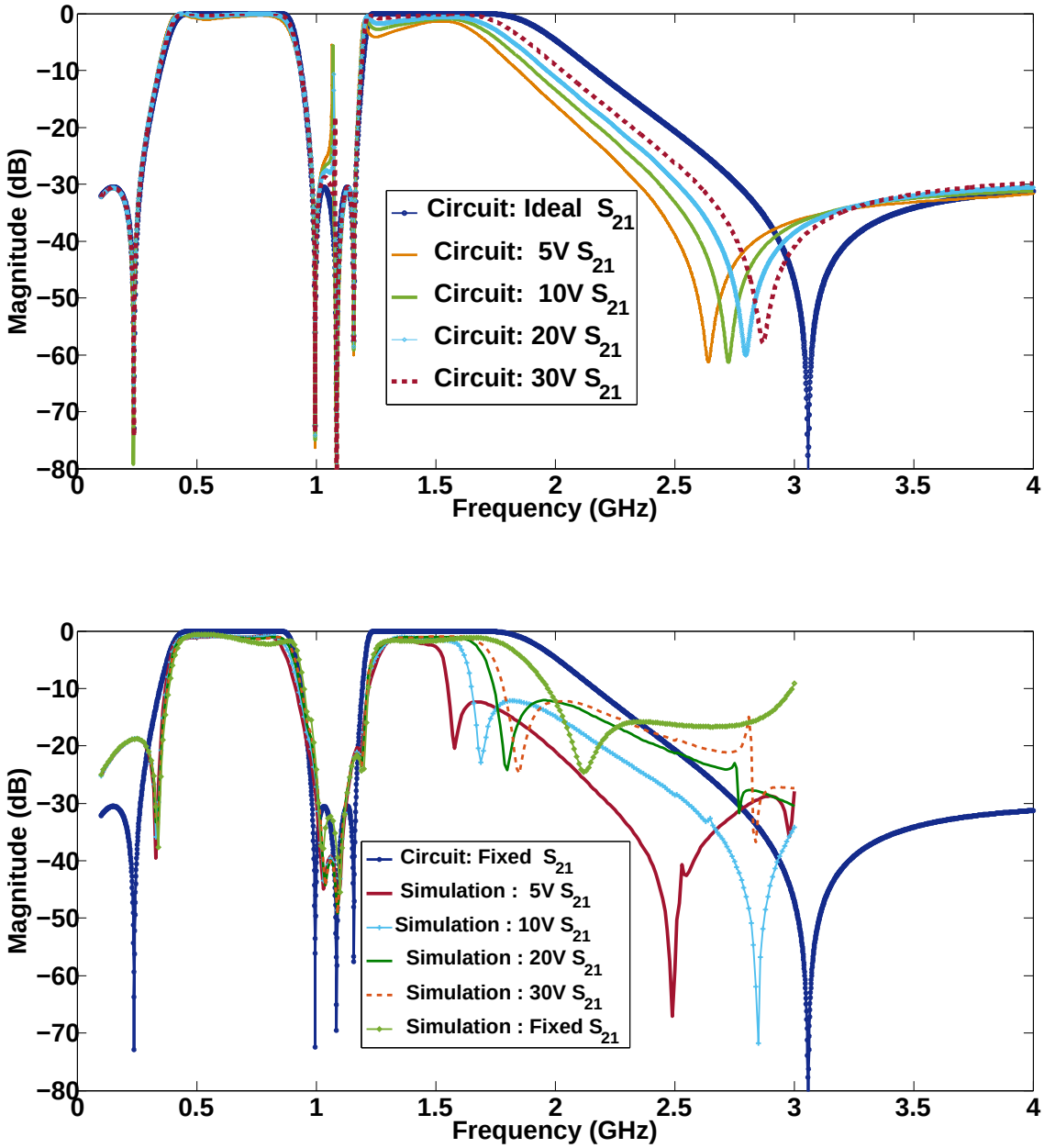

Fig. 6.40 Fixed ideal response of the circuit in Fig. 6.3 versus tunable response of the circuit and simulated prototypes of Fig 6.38 .

6.8 Summary

This chapter demonstrated the use of a reactance transform method to design quasi-lumped element dual-band filters. The filter is a wide with a centre frequency ratio of 2.3 between passband centre frequencies. The individual fractional bandwidths are 68 % (band 1) and 34 % (band 2). Two filters were implemented for practical demonstration and provided similar results, which provides the assurance that the design procedure could be implemented to meet any similar dual-band filter specifications. The effect of parasitic, especially in inductors, were detailed. Finally, an attempt to introduce tuning features in reactance transform was made in the last section. With the use of PIN diodes, it is possible to tune an upper band while keeping the lower band at a fixed position. The center frequency and bandwidths of the upper band are tunable.

Chapter 7

Conclusion and Future Works

7.0.1 Conclusion

The multi-band filters were designed, based on the reactance, transform method for narrow band, coupled, resonator, as well as wideband, lumped element, representations. The practical aspects related to the physical implementation of the multi-layer substrate, such as selectivity, losses and group-delay tuning, were investigated. Selectivity was influenced by the order of the single band basis filter, the total number of resonators and bands, as well as the relative bandwidth of the filter.

The numerical tuning of reactance transformed, coupled resonator filters has a remarkable feature in which group-delays of the sub-sections had the S_{11} phase at some frequencies, changing slope, which resulted in a negative group delay at some points. These effects were unforeseeable and associated with the increasing number of bands and the result of the number of resonators. Regarding loss analysis, as the resonator loss increased, the bandwidths of the inner bands differed from that of the outer bands. For the same resonator loss or Q factor, the passband levels appeared different from one another and increasingly different when the number of bands increased.

A reactance, transformed, coupled resonator with switchable dual bands was proposed. Due to the nature of resonator couplings, the fixed dual-band filter was interconnected; tuning even one of the resonators degraded the filter's performance. The non-resonant, pre-selection network was employed to enable switching, with Pin diodes embedded in the network. The pre-selection network did not obstruct or interfere with the specifications of the dual-band filter. The center frequency, bandwidth and transmission zeros of the selected band were not affected by the pre-selection network.

The design of the quasi-lumped element, wide-band, dual-band, bandpass filters were realized in a multi-layer. The developed circuit showed high performance and there was a co-

occurrence between the electromagnetic simulation and the measured data of the constructed filter. Parasitic elements that were present in the lumped element components affected the circuit performance. The effects of parasitic were more dominant in inductors than in capacitors. These effects were analyzed by generating an equivalent circuit of individual inductors from electro-magnetic simulations and replacing them in an ideal, equivalent circuit of the dual-band filter in a circuit analysis tool, to observe the impact on the frequency response. From the frequency response, it was noticeable that parasitic affected bandwidth, suppression between bands or caused harmonics near the passband. It is of importance to note that if these effects were not included in the design, it would have destroyed or degraded the performance of the circuit.

A reactance, transformed, quasi-lumped element, dual-band filter accommodates tunable features based on varactor diodes. By utilizing the same circuit element parameter (L and C values) and adding varactor diodes, it was found that the filter exhibited tunable features; the first band was fixed and the lower band bandwidth and center frequency were tuned.

7.0.2 Future work

Cross coupling

Cross coupling for multi-band may occur during the design. The cross coupling may be very strong, it become challenging to establish a reasonable tuning order. Other tuning techniques based on optimization may be explored.

Q factor

An attempt to improve the Q factor of a multi-band filter is to position the resonators on stepped layers/levels, while keeping the Q-factor equal. A technique to improve loss compensation must be developed by introducing uneven Q-factors, positioning the resonators on stepped or different layers in order to improve filter losses due to the number of resonators and bands.

Switchable filter

At this stage a pre-selection proposed for a coupled resonator, switchable filter, based on reactance transform, is limited to switching between dual bands. A simple pre-selection network, able to select a band a time for a filter of more than two bands, could form the basis for future research.

References

[1] Atia, A., Williams, A., and Newcomb, R. (1974). Narrow-band multiple-coupled cavity synthesis. *IEEE Transactions on circuits and systems*, 21(5):649–655.

[2] Bahl, I. J. (2003). *Lumped elements for RF and microwave circuits*. Artech house.

[3] Bavisi, A., Swaminathan, M., and Mina, E. (2007). Liquid crystal polymer-based planar lumped component dual-band filters for dual-band wlan systems. In *Radio and Wireless Symposium, 2007 IEEE*, pages 539–542. IEEE.

[4] Becker, W., Harms, P., and Mittra, R. (1992). Time domain electromagnetic analysis of a via in a multilayer computer chip package. In *Microwave Symposium Digest, 1992., IEEE MTT-S International*, pages 1229–1232. IEEE.

[5] Bell, H. C. (2001). Zolotarev bandpass filters. *IEEE transactions on microwave theory and techniques*, 49(12):2357–2362.

[6] Brand, T. G. (2014). *Synthesis methods for multi-band coupled resonator filters*. PhD thesis, Stellenbosch: Stellenbosch University.

[7] Brand, T. G., Meyer, P., and Geschke, R. H. (2015). Designing multiband coupled-resonator filters using reactance transformations. *International Journal of RF and Microwave Computer-Aided Engineering*, 25(1):81–92.

[8] Cameron, R. J. (1999). General coupling matrix synthesis methods for chebyshev filtering functions. *IEEE Transactions on Microwave Theory and Techniques*, 47(4):433–442.

[9] Cameron, R. J. (2003). Advanced coupling matrix synthesis techniques for microwave filters. *IEEE Transactions on Microwave Theory and Techniques*, 51(1):1–10.

[10] Cameron, R. J., Kudsia, C. M., and Mansour, R. (2015). *Microwave filters for communication systems*. John Wiley & Sons.

[11] Cañete Rebenaque, D., Martínez-Mendoza, M., Gómez-Tornero, J. L., Pascual-García, J., and Álvarez-Melcón, A. (2008). Analysis and implementation of different topologies of transversal filters in planar technology. *Radio Science*, 43(4).

[12] Canete-Rebenaque, D., Martinez-Mendoza, M., Pascual-Garcia, J., Diaz, J. S. G., and Alvarez-Melcon, A. (2011). Novel implementations for microstrip resonator filters in transversal and alternative topologies. *IEEE Transactions on Microwave Theory and Techniques*, 59(2):242–249.

[13] Carbonell, J., Lheurette, E., and Lippens, D. (2011). From rejection to transmission with stacked arrays of split ring resonators. *Progress In Electromagnetics Research*, 112:215–224.

[14] Caulton, M. (1971). Film technology in microwave integrated circuits. *Proceedings of the IEEE*, 59(10):1481–1489.

[15] Chao, S.-F., Kuo, C.-Y., Lin, W.-C., Li, W.-R., and Deng, P.-H. (2014). A dual-band switchable bandpass filter using connected-coupling mechanisms. In *Microwave Conference (EuMC), 2014 44th European*, pages 941–944. IEEE.

[16] Chaubey, M. K. and Bhadauria, A. (2018). Rf mems based tunable bandpass filter for x-band applications. In *IOP Conference Series: Materials Science and Engineering*, volume 331, page 012030. IOP Publishing.

[17] Cheab, S., Peng Wen, W., and Soeung, S. (2018). Design of multi-band filters using parallel connected topology. *RADIOENGINEERING*, 27(1):187.

[18] Chen, C.-F. (2012). Design of a compact microstrip quint-band filter based on the tri-mode stub-loaded stepped-impedance resonators. *IEEE Microwave and Wireless Components Letters*, 22(7):357–359.

[19] Chen, C.-F., Huang, T.-Y., Chen, C.-C., Shen, T.-M., and Wu, R.-B. (2011). Design of compact microstrip triple-passband quasi-elliptic filters with multi-order spurious mode suppression. In *Microwave Conference Proceedings (APMC), 2011 Asia-Pacific*, pages 1090–1093. IEEE.

[20] Cohn, S. B. (1957). Direct-coupled-resonator filters. *Proceedings of the IRE*, 45(2):187–196.

[21] Dai, G. and Xia, M. (2009). Design of compact dual-band switchable bandpass filter. *Electronics letters*, 45(10):506–507.

[22] Daly, D. A., Knight, S. P., Caulton, M., and Ekholdt, R. (1967). Lumped elements in microwave integrated circuits. *IEEE Transactions on Microwave Theory and Techniques*, 15(12):713–721.

[23] DeBrecht, R. and Caulton, M. (1970). Lumped-elements in microwave integrated circuits in the 1-12 ghz range. In *Microwave Symposium, G-MTT 1970 International*, pages 14–18. IEEE.

[24] Dehlink, B., Engl, M., Aufinger, K., and Knapp, H. (2007). Integrated bandpass filter at 77 ghz in sige technology. *IEEE Microwave and Wireless Components Letters*, 17(5):346–348.

[25] Deng, P.-H. and Jheng, J.-H. (2011). A switched reconfigurable high-isolation dual-band bandpass filter. *IEEE Microwave and Wireless Components Letters*, 21(2):71–73.

[26] Devlin, L., Pearson, G., Pittock, J., and Hunt, B. (2001). Rf and microwave component development in ltcc. In *IMAPS Nordic 38th Annu. Conf*, pages 96–110.

[27] Dickson, T. O., LaCroix, M.-A., Boret, S., Gloria, D., Beerkens, R., and Voinigescu, S. P. (2005). 30-100-ghz inductors and transformers for millimeter-wave (bi) cmos integrated circuits. *IEEE transactions on microwave theory and techniques*, 53(1):123–133.

[28] Farhat, M., Munisami, J., Abdul-Niby, M., and Nahas, M. (2017). A compact quint-band bandpass filter based on stub-loaded resonators. *Engineering, Technology & Applied Science Research*, 7(3):1694–1698.

[29] Garcia-Lamperez, A. and Salazar-Palma, M. (2011). Single-band to multiband frequency transformation for multiband filters. *IEEE Transactions on Microwave Theory and Techniques*, 59(12):3048–3058.

[30] Geschke, R. and Nepaya, L. (2016). Practical realisation of multiband planar filters based on a reactance transform method. In *Microwave Conference (EuMC), 2016 46th European*, pages 134–137. IEEE.

[31] Geschke, R. H. and Nepaya, L. (2017). Lossy multiband filters and ghost passbands. In *European Microwave Conference (EuMC), 2017 47th*, pages 648–651. IEEE.

[32] Gilmore, R. and Besser, L. (2003). *Practical RF Circuit Design for Modern Wireless Systems: Passive Circuits and Systems, Volume 1*, volume 1. Artech House.

[33] Girbau, D., Lázaro, A., Martínez, E., Masone, D., and Pradell, L. (2009). Tunable dual-band bandpass filter for wlan applications. *Microwave and Optical Technology Letters*, 51(9):2025–2028.

[34] Guo, Y.-X., Ong, L., Chia, M., and Luo, B. (2005). Dual-band bandpass filter in ltcc. In *Microwave Symposium Digest, 2005 IEEE MTT-S International*, pages 4–pp. IEEE.

[35] Hong, J.-S. G. and Lancaster, M. J. (2004). *Microstrip filters for RF/microwave applications*, volume 167. John Wiley & Sons.

[36] Hunter, I. and Rhodes, J. D. (1982). Electronically tunable microwave bandpass filters. *IEEE Transactions on Microwave Theory and Techniques*, 30(9):1354–1360.

[37] Jeganathan, K. (2000). Design of a simple tunable/switchable bandpass filter. *Applied Microwave and Wireless*, 12(3):32–41.

[38] Joshi, H. and Chappell, W. J. (2006). Dual-band lumped-element bandpass filter. *IEEE transactions on microwave theory and techniques*, 54(12):4169–4177.

[39] Kingsley, N. (2008). Liquid crystal polymer: enabling next-generation conformal and multilayer electronics. *Microwave journal*, 51(5):188.

[40] Kraemer, M., Dragomirescu, D., and Plana, R. (2010). Accurate electromagnetic simulation and measurement of millimeter-wave inductors in bulk cmos technology. In *Silicon Monolithic Integrated Circuits in RF Systems (SiRF), 2010 Topical Meeting on*, pages 61–64. IEEE.

[41] Lamperez, A. G. (2007). Analytical synthesis algorithm of dual-band filters with asymmetric pass bands and generalized topology. In *Microwave Symposium, 2007. IEEE/MTT-S International*, pages 909–912. IEEE.

[42] Levy, R. (1970). Generalized rational function approximation in finite intervals using zolotarev functions. *IEEE Transactions on Microwave Theory and Techniques*, 18(12):1052–1064.

[43] Lin, S.-C. (2011). Microstrip dual/quad-band filters with coupled lines and quasi-lumped impedance inverters based on parallel-path transmission. *IEEE Transactions on Microwave Theory and Techniques*, 59(8):1937–1946.

[44] Liu, H., Wang, X., Wang, Y., Li, S., Zhao, Y., and Guan, X. (2014). Quad-band bandpass filter using quad-mode stub-loaded resonators. *ETRI journal*, 36(4):690–693.

[45] Martínez Mendoza, M., Gómez Díaz, J. S., Cañete Rebenaque, D., Álvarez Melcón, A., et al. (2008). Design of dual-bandpass hybrid waveguide–microstrip microwave filters.

[46] Matthaei, G., Young, L., and Jones, E. (1980). Microwave filters, impedance-matching networks, and coupling structures (artech microwave library). *Artech House, February*.

[47] Miller, A. et al. (2012). *Electronically reconfigurable wideband microwave filters*. PhD thesis, Citeseer.

[48] Mittra, R. (1992). Electromagnetic modeling and simulation of electronic packages. In *Computer Design: VLSI in Computers and Processors, 1992. ICCD'92. Proceedings, IEEE 1992 International Conference on*, pages 214–217. IEEE.

[49] Mokhtaari, M., Bornemann, J., Rambabu, K., and Amari, S. (2006). Coupling-matrix design of dual and triple passband filters. *IEEE Transactions on Microwave Theory and Techniques*, 54(11):3940–3946.

[50] Ness, J. B. (1998a). Alignment of cross-coupled resonator filters using the group delay technique. *Microwave and Optical Technology Letters*, 18(3):174–179.

[51] Ness, J. B. (1998b). A unified approach to the design, measurement, and tuning of coupled-resonator filters. *IEEE Transactions on Microwave Theory and Techniques*, 46(4):343–351.

[52] Nicholson, G. and Lancaster, M. (2009). Coupling matrix synthesis of cross-coupled microwave filters using a hybrid optimisation algorithm. *IET microwaves, antennas & propagation*, 3(6):950–958.

[53] Park, J.-H., Cheon, S.-J., and Park, J.-Y. (2013). A compact ltcc dual-band wlan filter using two notch resonators. *Journal of Electrical Engineering and Technology*, 8(1):168–175.

[54] Pham, A.-V. (2011). Packaging with liquid crystal polymer. *IEEE Microwave Magazine*, 12(5):83–91.

[55] Pommier, V., Cros, D., Guillon, P., Carlier, A., and Rogeaux, E. (2000). Transversal filter using whispering gallery quarter cut resonators. In *Microwave Symposium Digest. 2000 IEEE MTT-S International*, volume 3, pages 1779–1782. IEEE.

[56] Pozar, D. M. (2005). Microwave engineering.

[57] Qian, S. and Hong, J. (2012). Miniature quasi-lumped-element wideband bandpass filter at 0.5–2-ghz band using multilayer liquid crystal polymer technology. *IEEE Transactions on Microwave Theory and Techniques*, 60(9):2799–2807.

[58] Rautio, J. C. (2008a). Perfectly calibrated internal ports in em analysis of planar circuits. In *Microwave Symposium Digest, 2008 IEEE MTT-S International*, pages 1373–1376. IEEE.

[59] Rautio, J. C. (2008b). Shortening the design cycle. *IEEE Microwave Magazine*, 9(6).

[60] Rautio, J. C. (2010). Microwave filter optimization using perfectly calibrated ports. In *Applied Computational Electromagnetics Symposium (ACES 2010)*, pages 896–901.

[61] Rebeiz, G. M., Entesari, K., Reines, I. C., Park, S.-J., El-Tanani, M. A., Grichener, A., and Brown, A. R. (2009). Tuning in to rf mems. *IEEE microwave magazine*, 10(6).

[62] Rebenaque, D., García, J., Pereira, F., Tornero, J., and Melcon, A. (2010). Novel implementation of transversal filters in multilayered microstrip technology. *Journal of Electromagnetic Waves and Applications*, 24(8-9):1241–1253.

[63] Ren, L.-Y. (2010). Quad-band bandpass filter based on dual-plane microstrip/dgs slot structure. *Electronics Letters*, 46(10):691–692.

[64] Rosenberg, U. and Amari, S. (2002). Novel coupling schemes for microwave resonator filters. *IEEE Transactions on Microwave Theory and Techniques*, 50(12):2896–2902.

[65] Shaman, H. N. (2012). New s-band bandpass filter (bpf) with wideband passband for wireless communication systems. *IEEE Microwave and Wireless Components Letters*, 22(5):242–244.

[66] Shang, X., Wang, Y., Nicholson, G., and Lancaster, M. (2012). Design of multiple-passband filters using coupling matrix optimisation. *IET microwaves, antennas & propagation*, 6(1):24–30.

[67] Shen, W., Yin, W.-Y., and Sun, X.-W. (2010). Compact substrate integrated waveguide transversal filter with microstrip dual-mode resonator. *Journal of Electromagnetic Waves and Applications*, 24(14-15):1887–1896.

[68] Suarez, M., Villegas, M., and Baudoin, G. (2010). Rf and microwave band-pass passive filters for mobile transceivers with a focus on baw technology. In *Advanced Microwave and Millimeter Wave Technologies Semiconductor Devices Circuits and Systems*. InTech.

[69] Subramanyam, G., Ahamed, F., and Biggers, R. (2005a). A si mmic compatible ferroelectric varactor shunt switch for microwave applications. *IEEE Microwave and wireless components Letters*, 15(11):739–741.

[70] Subramanyam, G., Ahamed, F., Biggers, R., Campbell, A., Neidhard, R., Nykiel, E., Cortez, R., Stamper, K., and Calcatera, M. (2005b). A new ferroelectric varactor shunt switch for microwave and millimeterwave reconfigurable circuits. *Frequenz*, 59(1-2):37–48.

[71] Vanukuru, V. N. R., Godavarthi, N., and Chakravorty, A. (2014). Miniaturized millimeter-wave narrow bandpass filter in 0.18 μm cmos technology using spiral inductors and inter digital capacitors. In *Signal Processing and Communications (SPCOM), 2014 International Conference on*, pages 1–4. IEEE.

[72] Varshney, S., Kumar, M., Kumar, A., and Pandey, U. (2013). Miniaturized microstrip low insertion loss band-pass filter for l-band receiver. In *9th International Radar Symposium India*.

[73] White, J. F. (2004). *High Frequency Techniques: An Introduction to RF and Microwave Design and Computer Simulation*. John Wiley & Sons.

[74] Wu, J.-Y. and Tu, W.-H. (2011). Design of quad-band bandpass filter with multiple transmission zeros. *Electronics letters*, 47(8):502–503.

[75] Xu, J., Wu, W., and Wei, G. (2016). Novel dual-band bandpass filter and reconfigurable filters using lumped-element dual-resonance resonators. *IEEE Transactions on Microwave Theory and Techniques*, 64(5):1496–1507.

[76] Zhu, L., Sun, S., and Li, R. (2011). *Microwave bandpass filters for wideband communications*, volume 232. John Wiley & Sons.

Appendix A

Dimensions of the Coupled resonators filters

The dimensions of the filters A, B , C, D designed in Chapter 4 are provided here. All filters are design on multilayers. The dimensions includes the lengths, width, spacing, gaps and overlaps in mm.

The dimensions of the filter A

The dimensions of the filter B

The dimensions of the filter C

The dimensions of the filter D

Table A.1 Length of Filter A for Fig A.1, Fig A.2 and Fig A.3

L	mm	L	mm	L	mm
L_1	8.7	L_{11}	9.6	L_{21}	9.6
L_2	4.2	L_{12}	1.3	L_{22}	4.0
L_3	3.9	L_{13}	5.8	L_{23}	7.8
L_4	4.2	L_{14}	9.6	L_{24}	1.7
L_5	9.6	L_{15}	1.4	L_{25}	2.7
L_6	4.2	L_{16}	5.8	L_{26}	2.6
L_7	11.7	L_{17}	9.6	L_{27}	1.7
L_8	5.3	L_{18}	1.2	L_{28}	7.8
L_9	4.5	L_{19}	1.3		
L_{10}	14.5	L_{20}	9.6		

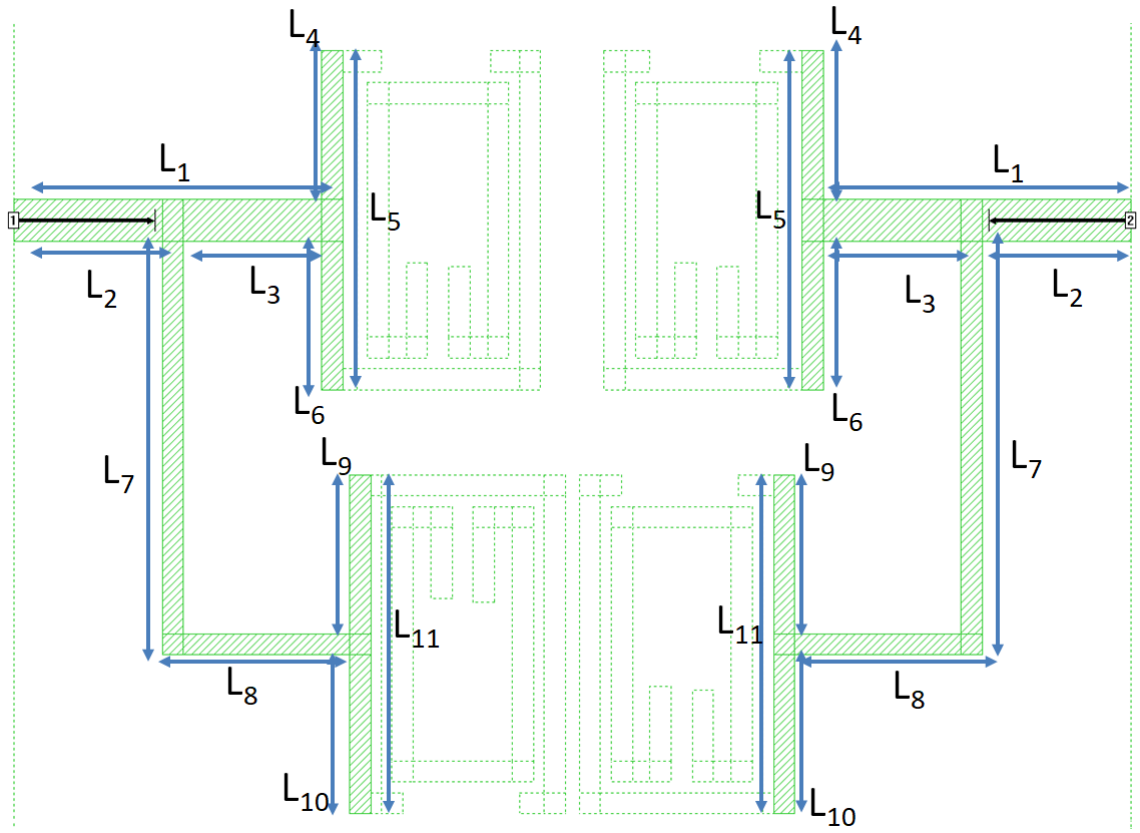

Fig. A.1 Length of the Feeds on the top layer: filter A

Table A.2 Layer overlapping of Filter A shown in Fig A.4

O	mm
O_1	0.2
O_2	0.3

Table A.3 Spacing and gaps of Filter A shown in Fig A.5 and Fig A.6

G & S	mm
G_1	3.1
G_2	3.3
G_3	0.3
S_1	1.8
S_2	2.4
S_3	2.4
S_4	0.4
S_5	0.3

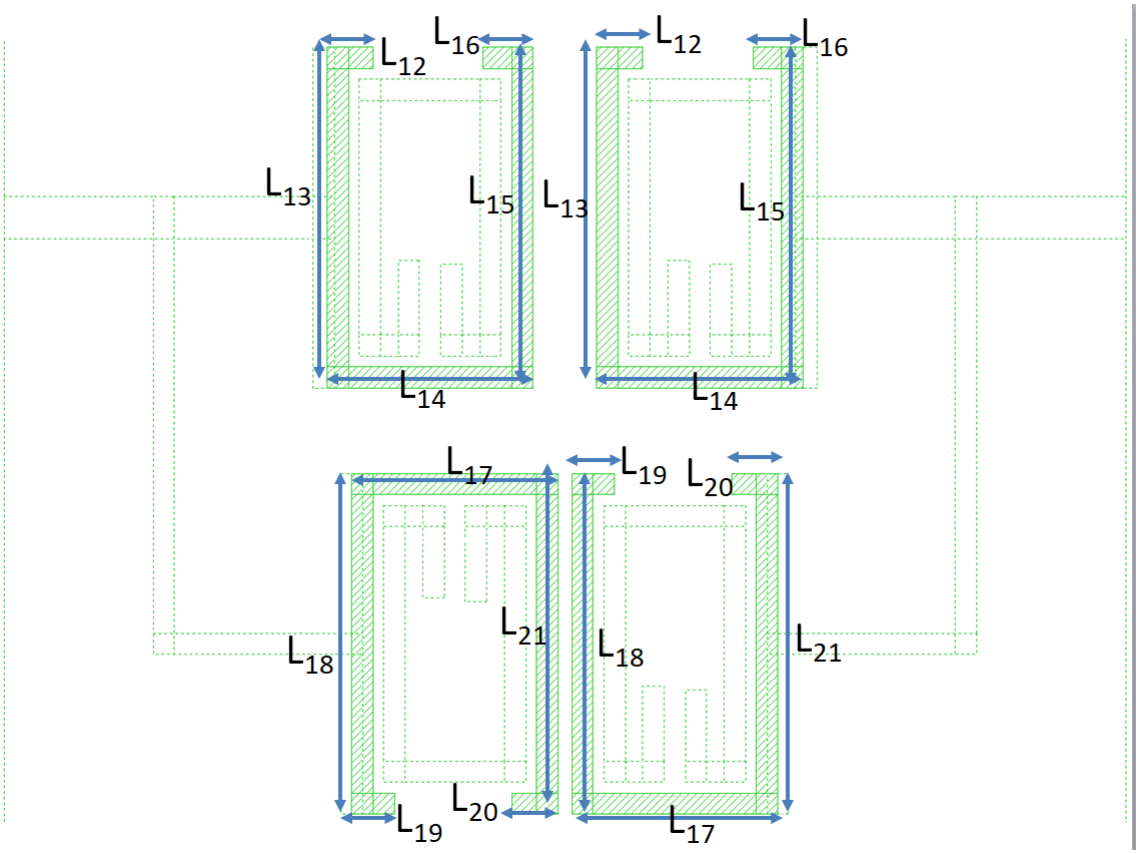

Fig. A.2 Length of resonator 1 to 4: filter A

Table A.4 Length of Filter B for Fig A.7, Fig A.8 and Fig A.9

L	mm	L	mm
L_1	15.1	L_{11}	1.4
L_2	11.8	L_{12}	1.3
L_3	11.6	L_{13}	9.6
L_4	6.3	L_{14}	5.8
L_5	4.5	L_{15}	1.3
L_6	4.2	L_{16}	1.2
L_7	4.5	L_{17}	1.7
L_8	9.6	L_{18}	2.4
L_9	9.5	L_{19}	8.0
L_{10}	4.4	L_{20}	4.1

Table A.5 Layer overlapping of Filter B shown in Fig A.10

O	mm
O_1	0.1
O_2	0.2
O_3	0.1

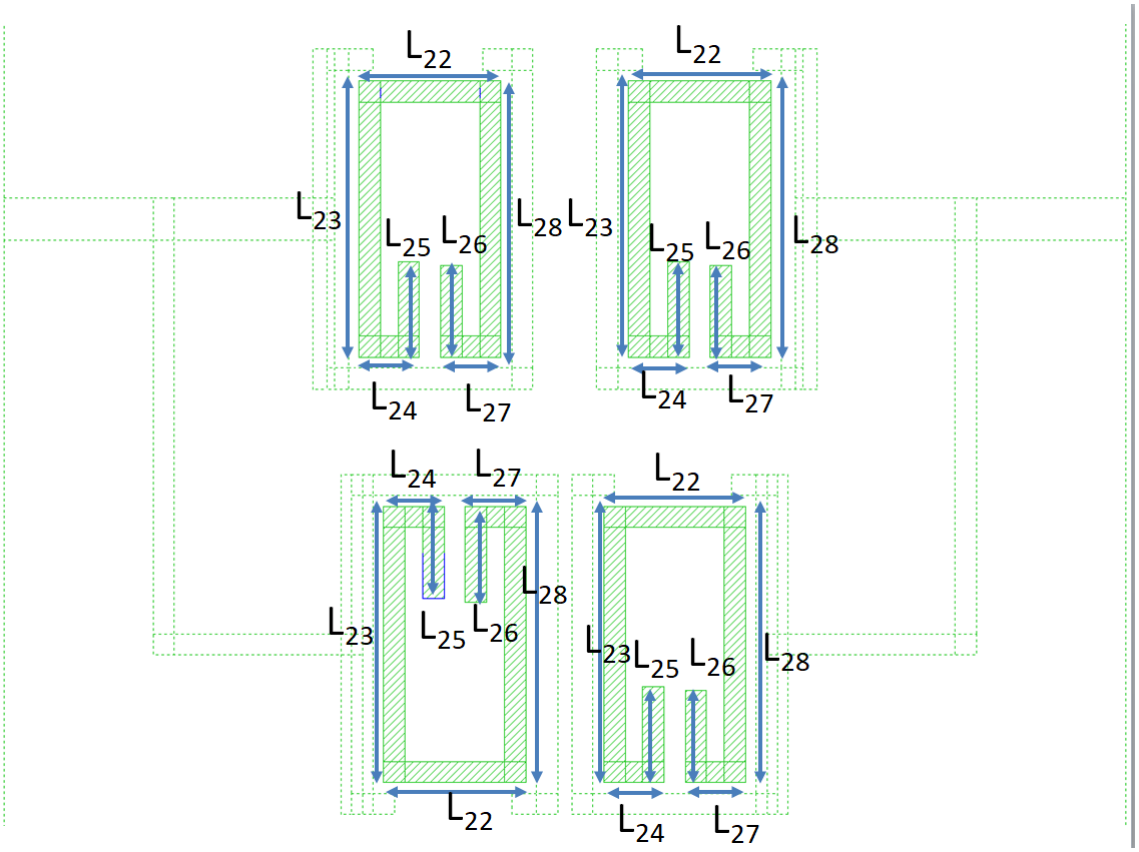

Fig. A.3 Length of the resonators 5 to 8: filter A

Table A.6 Spacing and gaps of Filter B shown in Fig A.12 and Fig A.12

G & S	mm
G_1	3.3
G_2	3.1
G_3	0.7
S_1	0.4
S_2	2.0
S_3	2.5
S_4	2.4
S_5	0.2
S_6	0.3

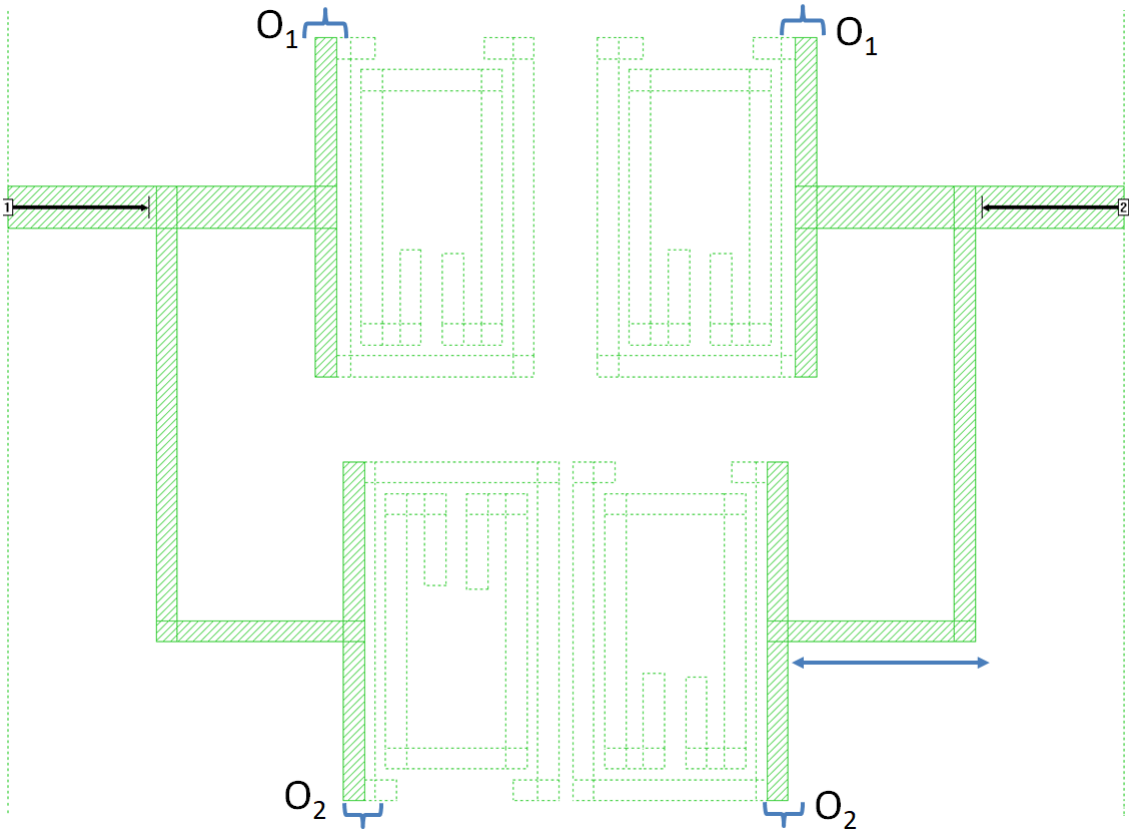

Fig. A.4 Overlaps between feeds and resonator 1 to 4: filter A

Table A.7 Length of Filter C for Fig A.13, Fig A.14 and Fig A.15

L	mm	L	mm
L_1	2.0	L_{11}	2.2
L_2	0.5	L_{12}	5.9
L_3	1.4	L_{13}	4.6
L_4	6.2	L_{14}	5.2
L_5	3.2	L_{15}	2.2
L_6	6.8	L_{16}	4.6
L_7	2.1	L_{17}	2.2
L_8	2.2	L_{18}	5.5
L_9	6.8	L_{19}	4.6
L_{10}	4.6		

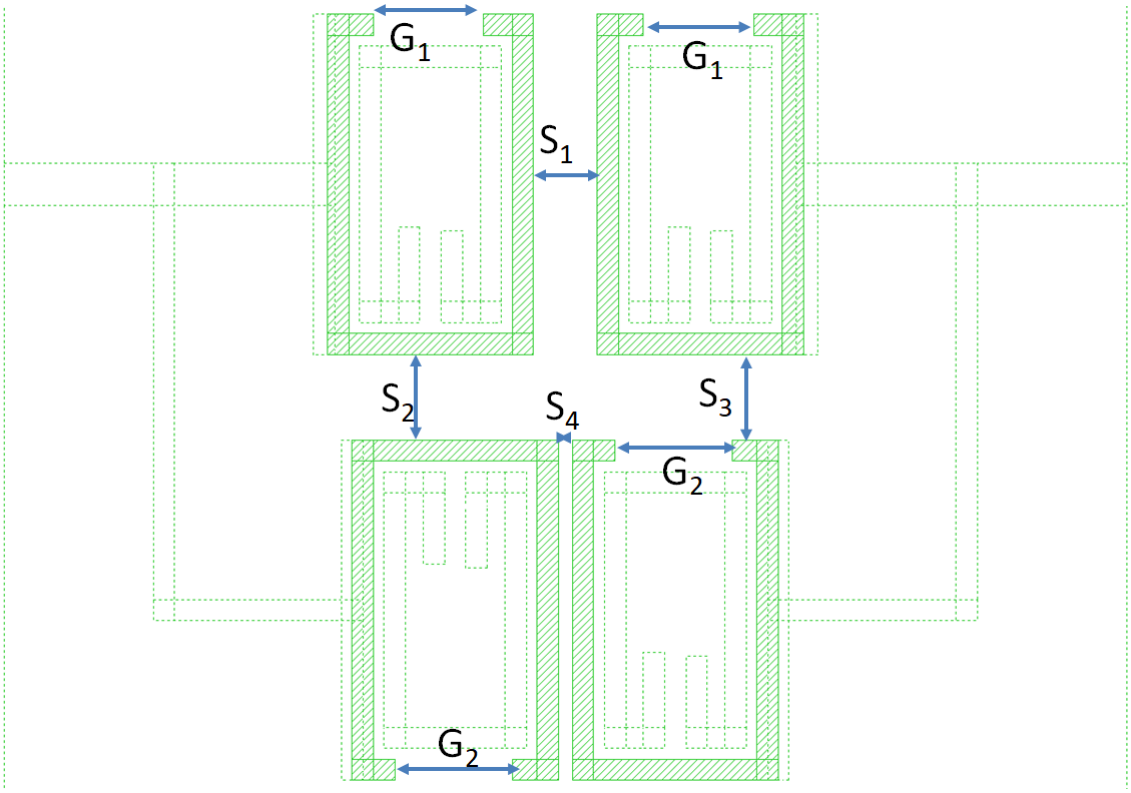

Fig. A.5 Spacing and gaps of resonators 1 to 4: filter A

Table A.8 Width of Filter C shown in Fig A.16

W	mm
W_1	1.4
W_2	2.0
W_3	0.4
W_4	0.6

Table A.9 Gaps, spacing and overlaps of Filter C shown in Fig A.17 and Fig A.18

G, S &O	mm
G_1	0.3
G_2	0.2
G_3	0.3
S_1	0.2
S_2	0.3
O_1	0.3
O_2	0.5
O_3	0.4
O_4	0.3

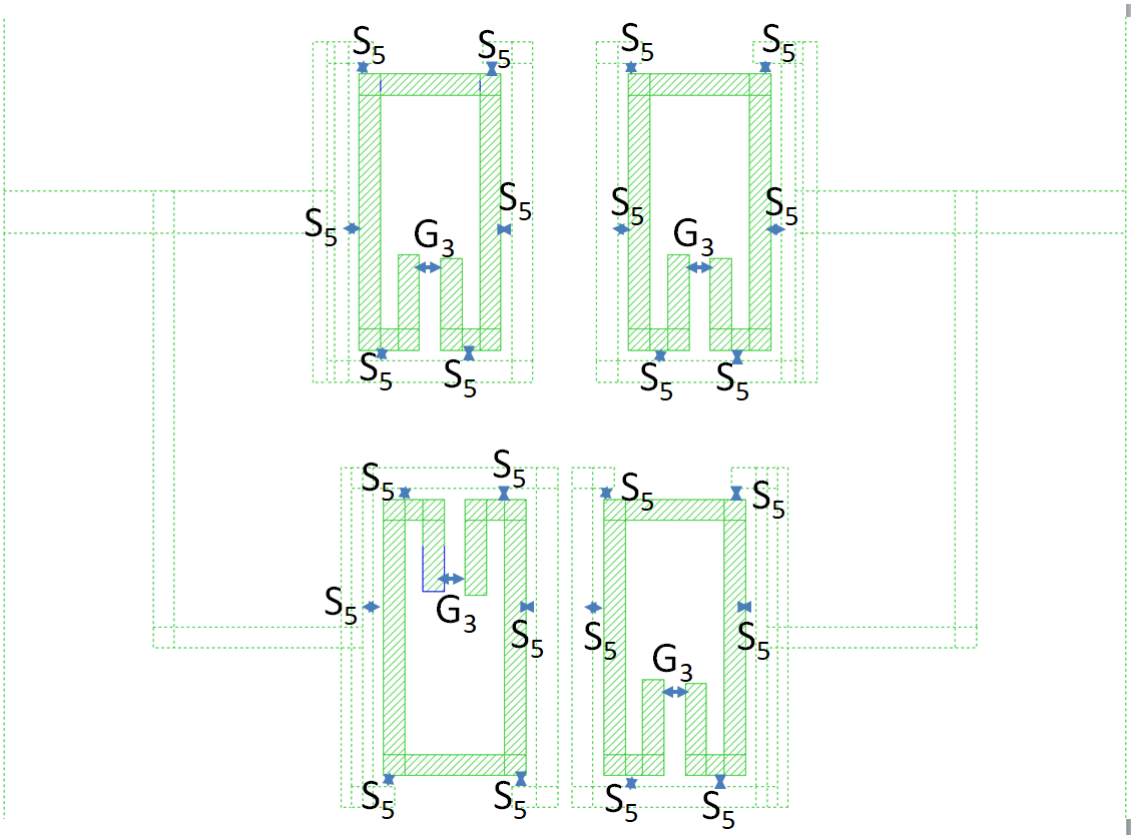

Fig. A.6 Gaps and spacing between Resonators 1 to 4 and the appended resonators 5 to 8: filter A

Table A.10 Length of Filter D for Fig A.19, Fig A.20 and Fig A.21

L	mm	L	mm
L_1	1.6	L_{11}	2.3
L_2	2.0	L_{12}	2.2
L_3	0.6	L_{13}	6.7
L_4	5.0	L_{14}	6.1
L_5	2.5	L_{15}	2.8
L_6	2.6	L_{16}	5.5
L_7	6.7	L_{17}	6.1
L_8	1.6	L_{18}	2.7
L_9	8.5	L_{19}	5.8
L_{10}	4.9	L_{20}	6.1

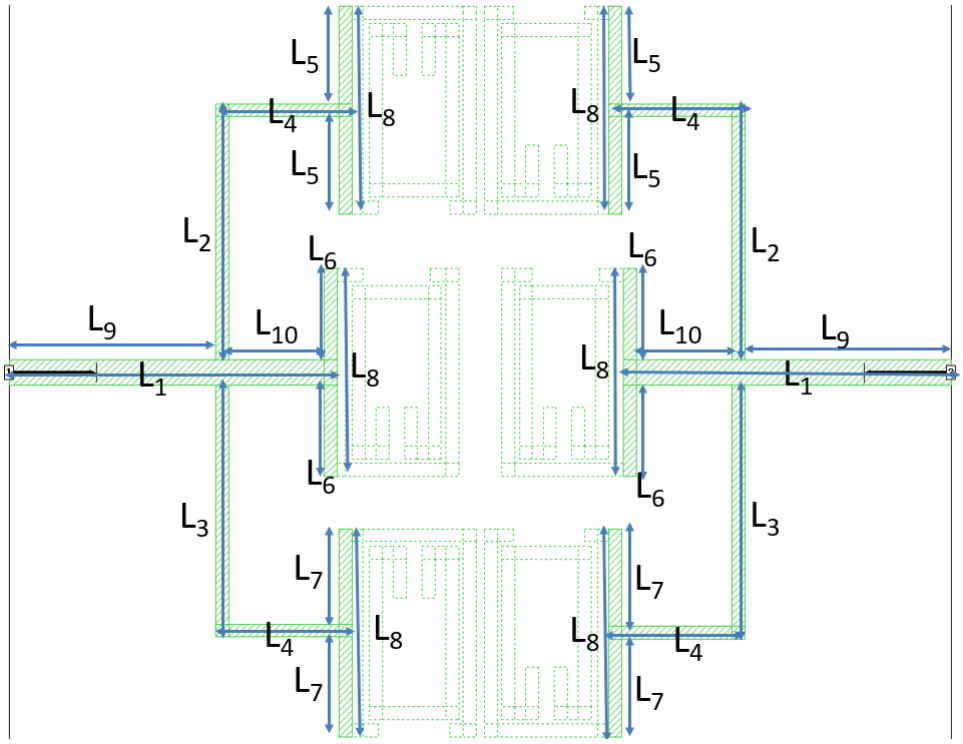

Fig. A.7 Length of the Feeds on the top layer: filter B

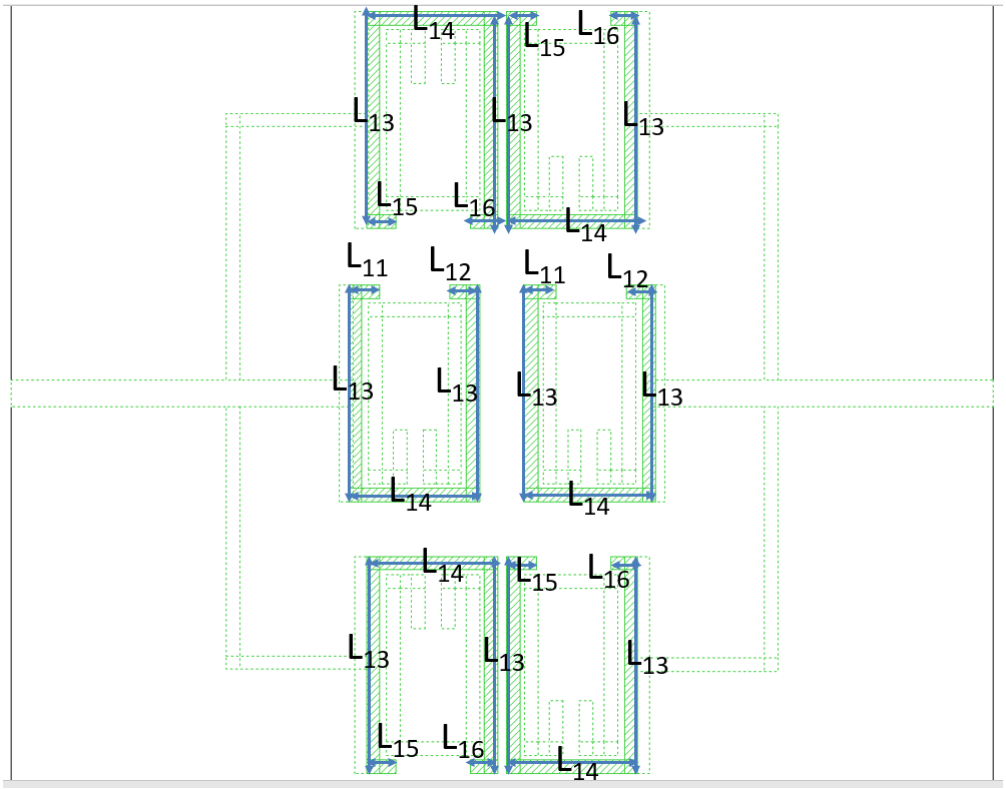

Fig. A.8 Length of resonator 1 to 6: filter B

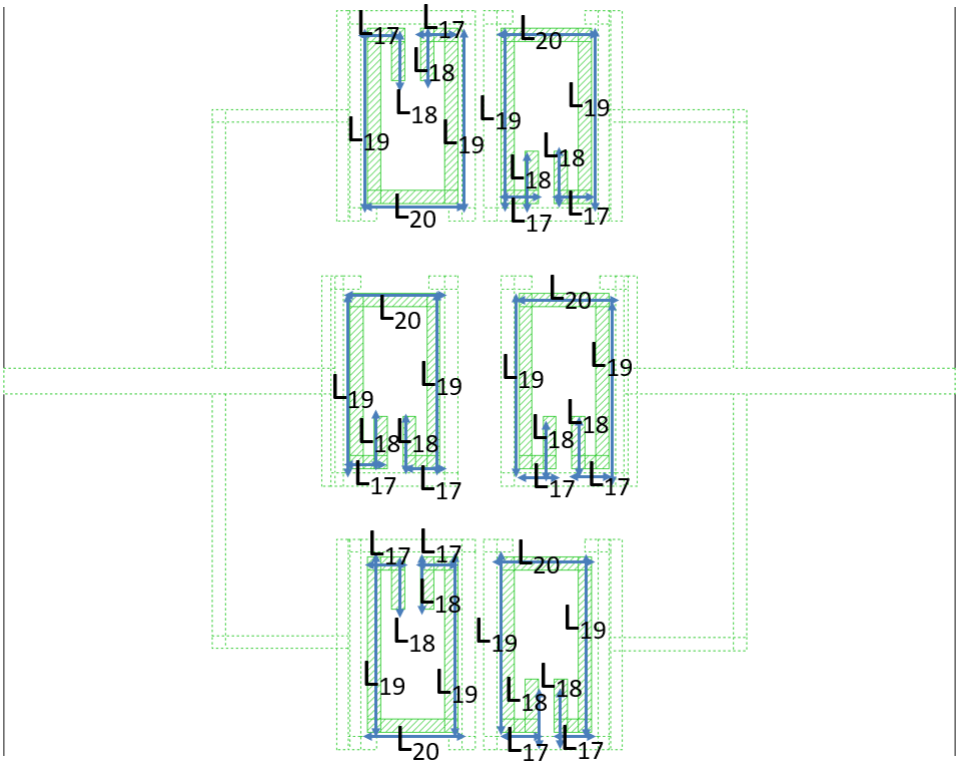

Fig. A.9 Length of the resonators 7 to 12: filter B

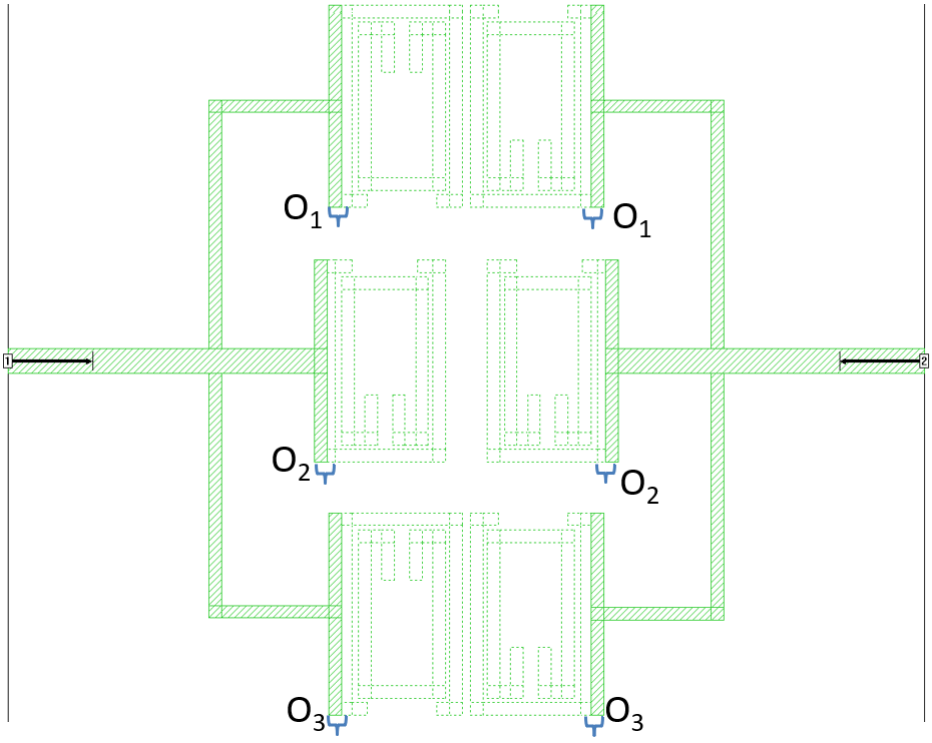

Fig. A.10 Overlaps between feeds and resonator 1 to 6: filter B

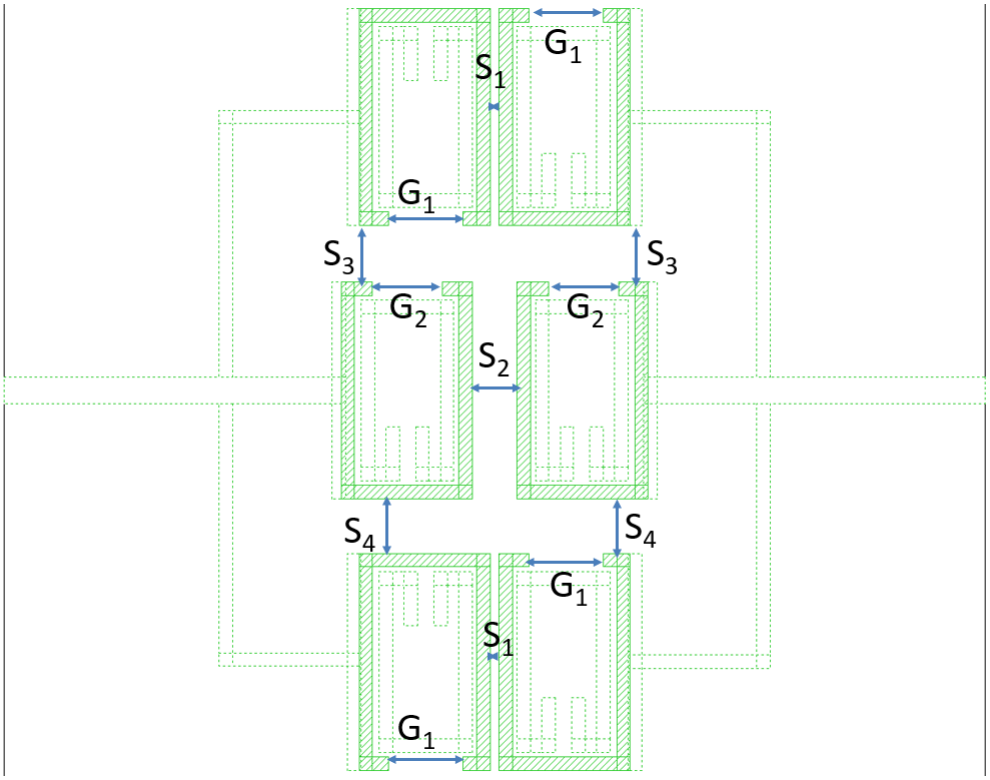

Fig. A.11 Spacing and gaps of resonators 1 to 6: filter B

Table A.11 Width of Filter D shown in Fig A.22, Fig A.23, Fig A.24

W	mm
W_1	1.6
W_2	0.4
W_3	0.7
W_4	1.6
W_5	0.9
W_6	0.9
W_7	1.0
W_8	1.2
W_9	1.0
W_{10}	1.2
W_{11}	1.0

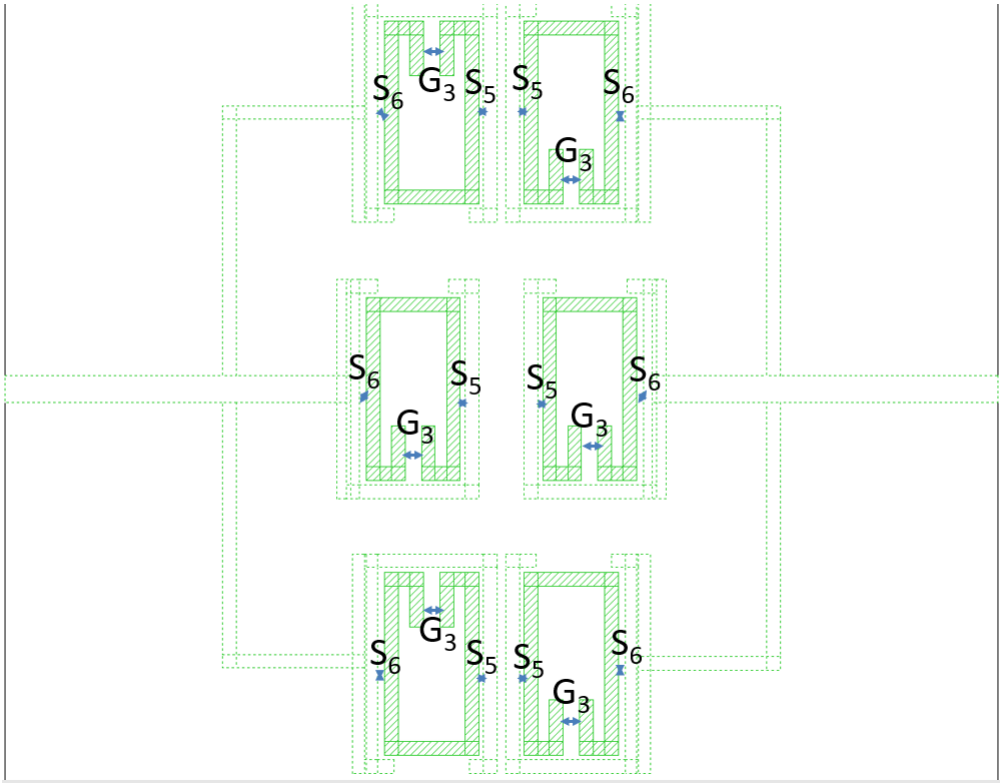

Fig. A.12 Gaps and spacing between Resonators 1 to 6 and the appended resonators 7 to 12: filter B

Table A.12 Gaps, spacing and overlaps of Filter D shown in Fig A.25 and Fig A.26

G, S &O	mm
G_1	1.7
G_2	1.6
G_3	0.5
G_4	0.7
S_1	0.3
O_1	0.3
O_2	0.9
O_3	1.0
O_4	0.6

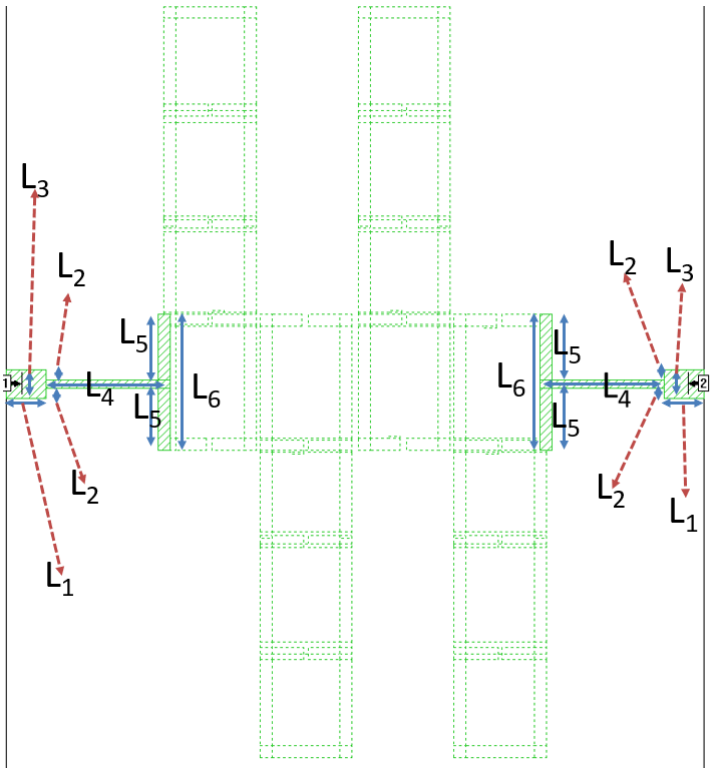

Fig. A.13 Length of the Feeds on the top layer: filter C

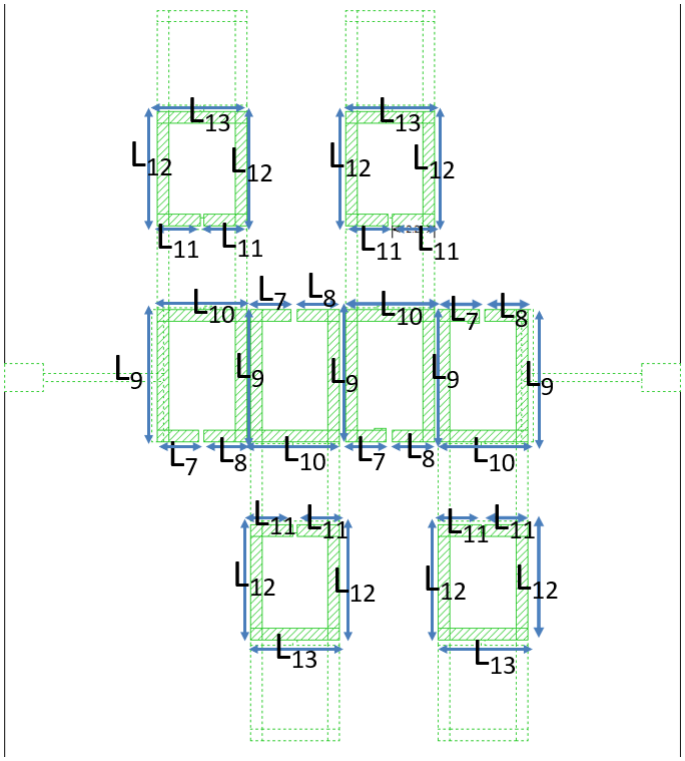

Fig. A.14 Length of resonator 1 to 4 and resonators 9 to 12: filter C

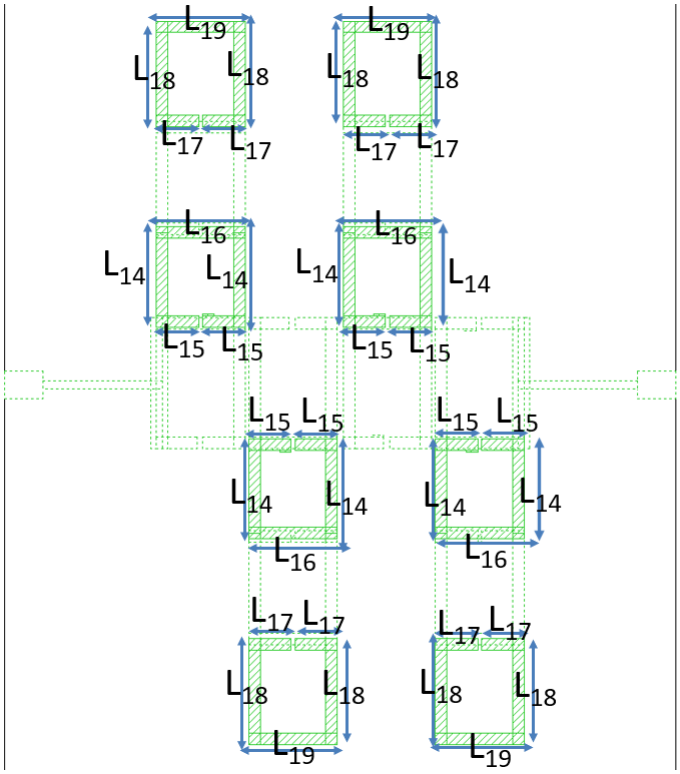

Fig. A.15 Length of the resonators 5 to 8 and resonators 13 to 16 : filter C

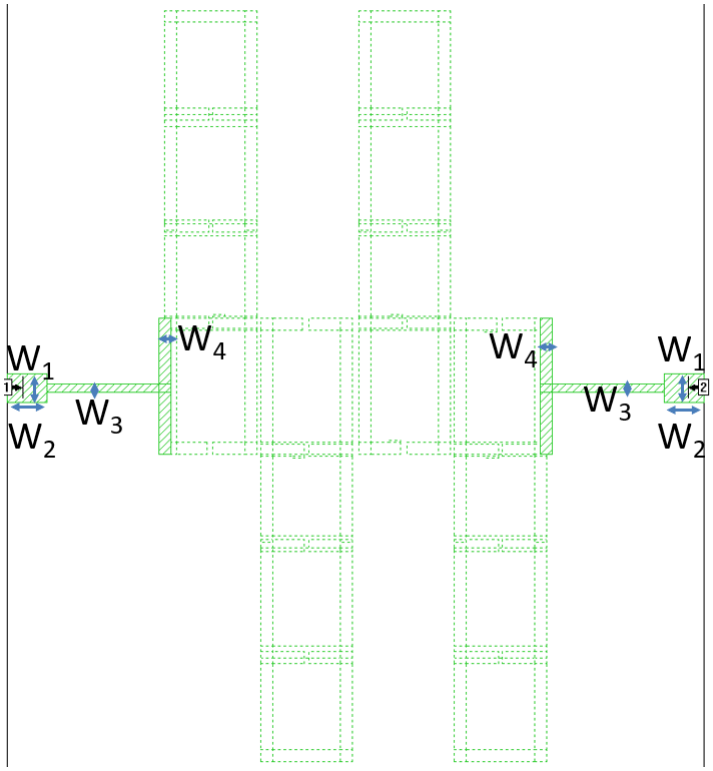

Fig. A.16 Width of the feeds: filter C

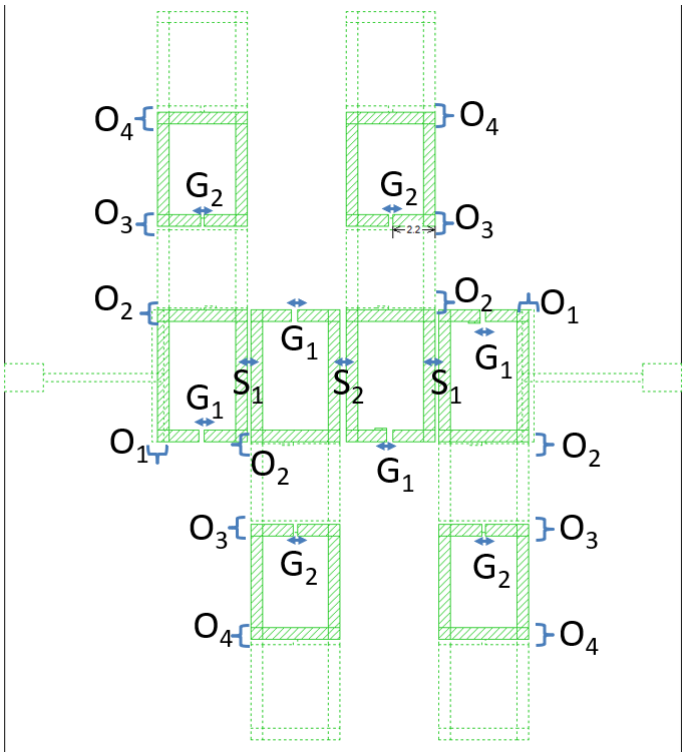

Fig. A.17 Gaps and spacing and overlaps : filter C

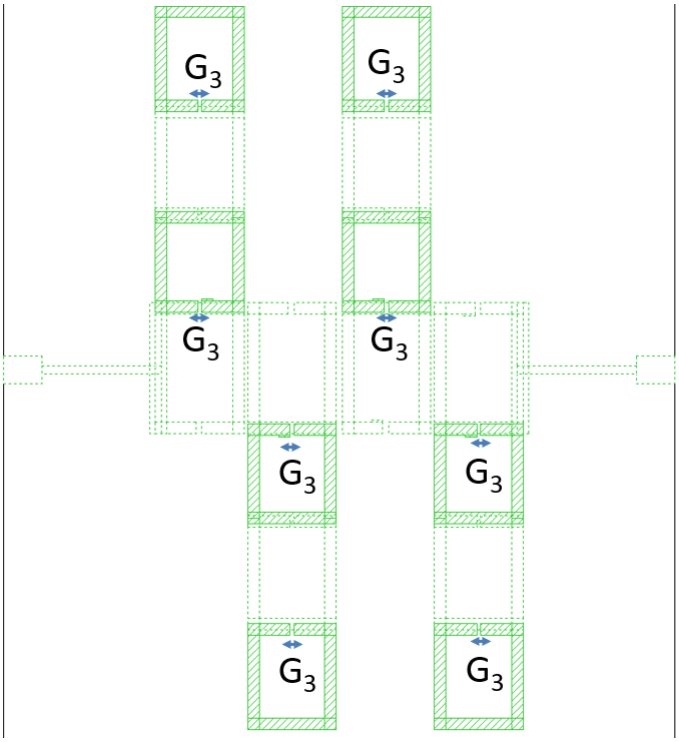

Fig. A.18 Gaps of resonators 5 to 8 and resonators 13 to 16: filter C

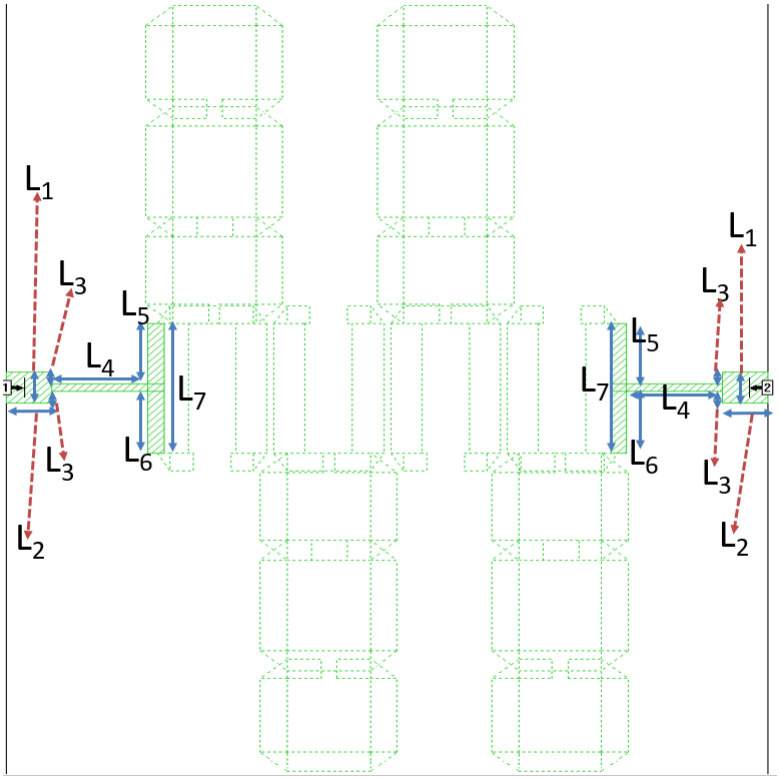

Fig. A.19 Length of the Feeds on the top layer: filter D

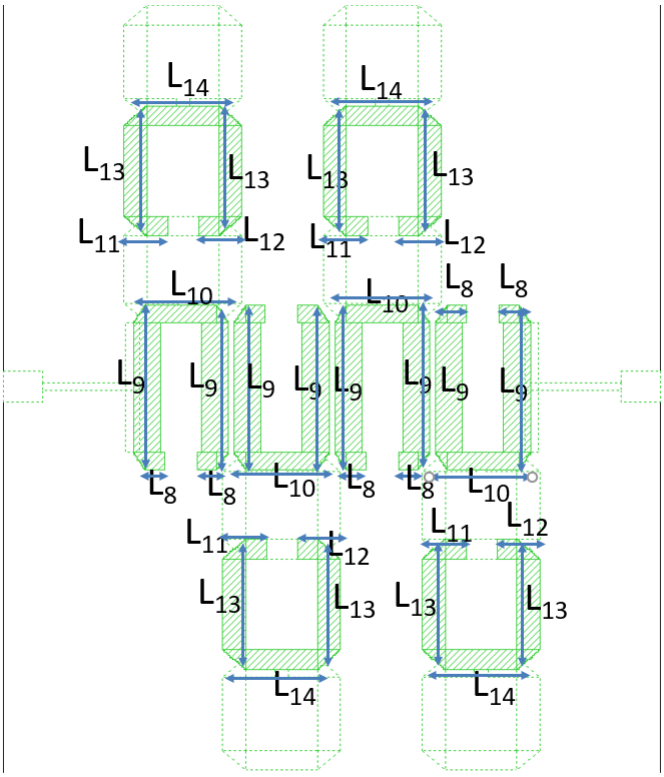

Fig. A.20 Length of resonator 1 to 4 and resonators 9 to 12: filter D

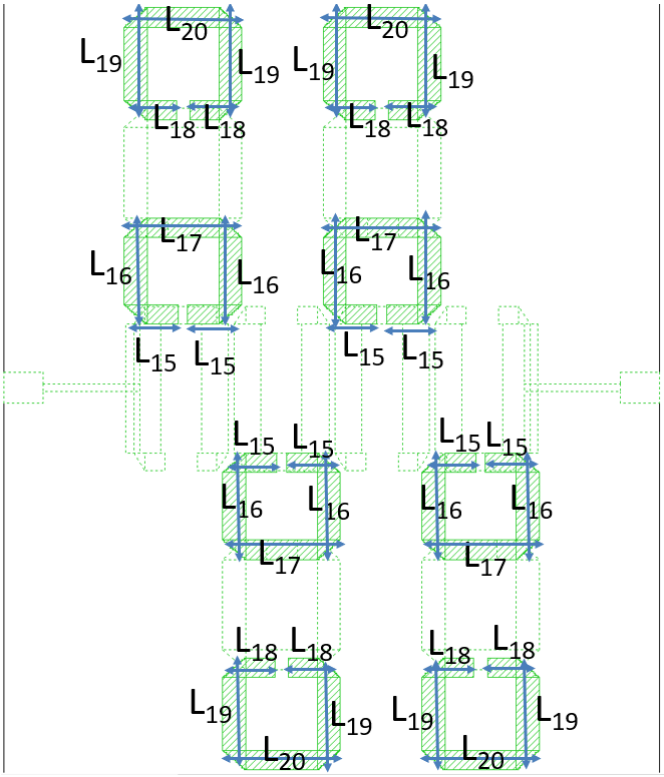

Fig. A.21 Length of the resonators 5 to 8 and resonators 13 to 16 : filter D

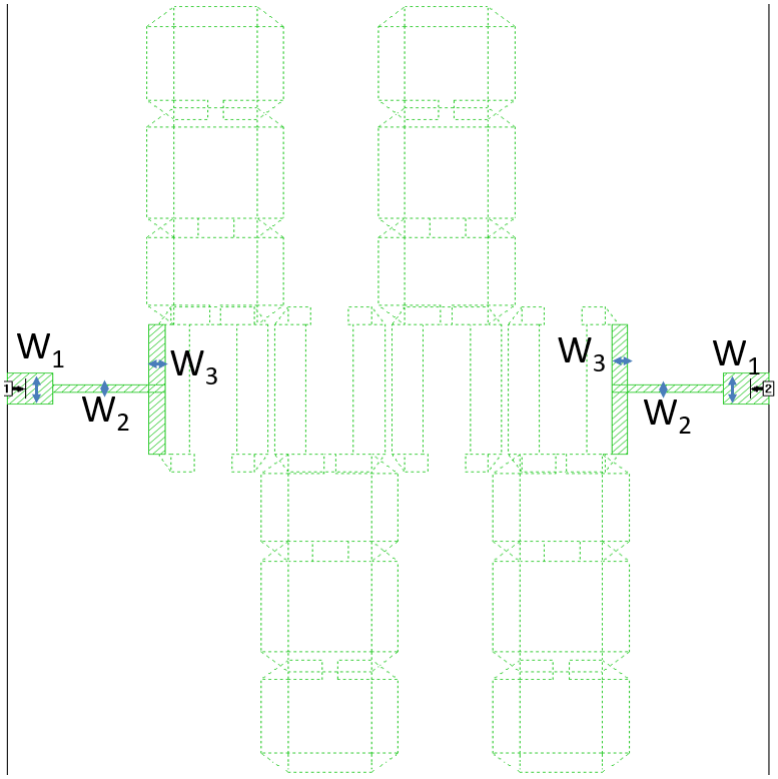

Fig. A.22 Width of the feeds: filter D

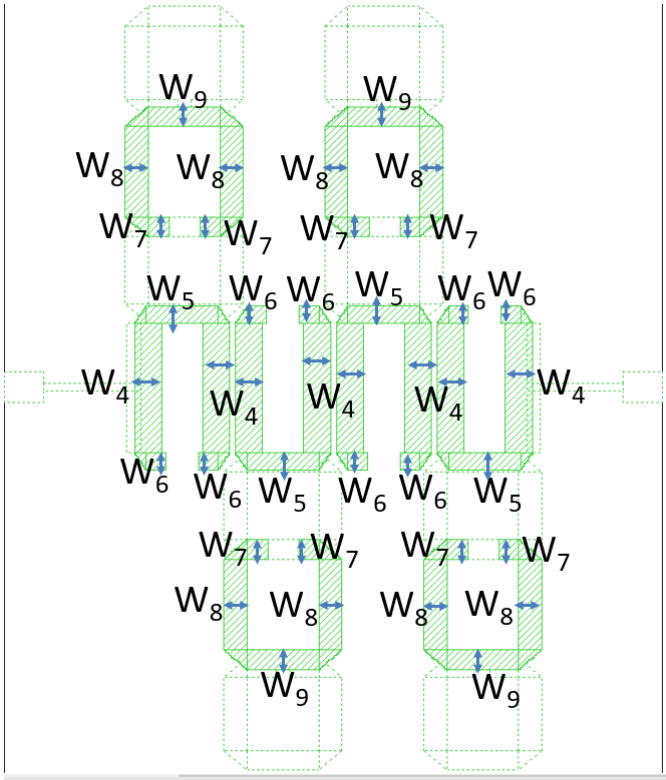

Fig. A.23 Widths of resonators 1 to 4 and resonators 9 to 12: filter D

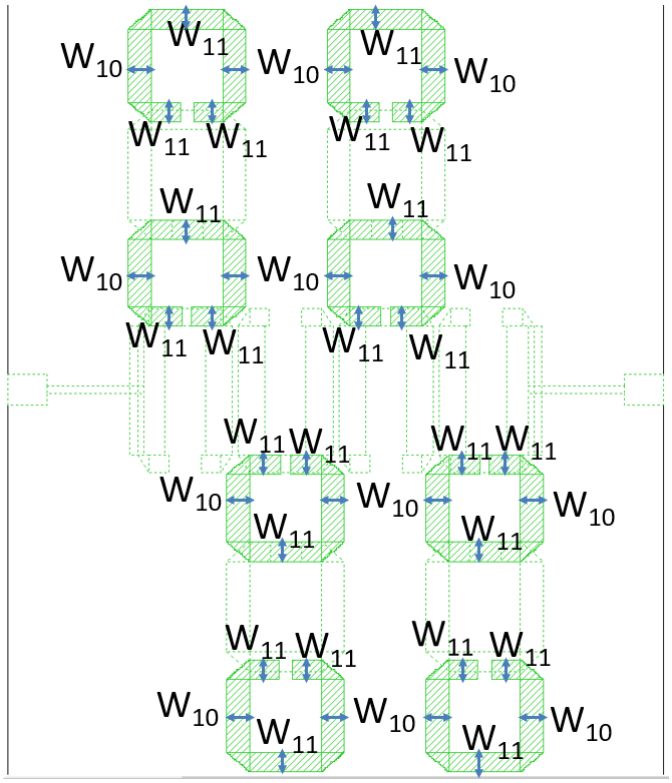

Fig. A.24 Widths of resonators 5 to 8 and resonators 13 to 16: filter D

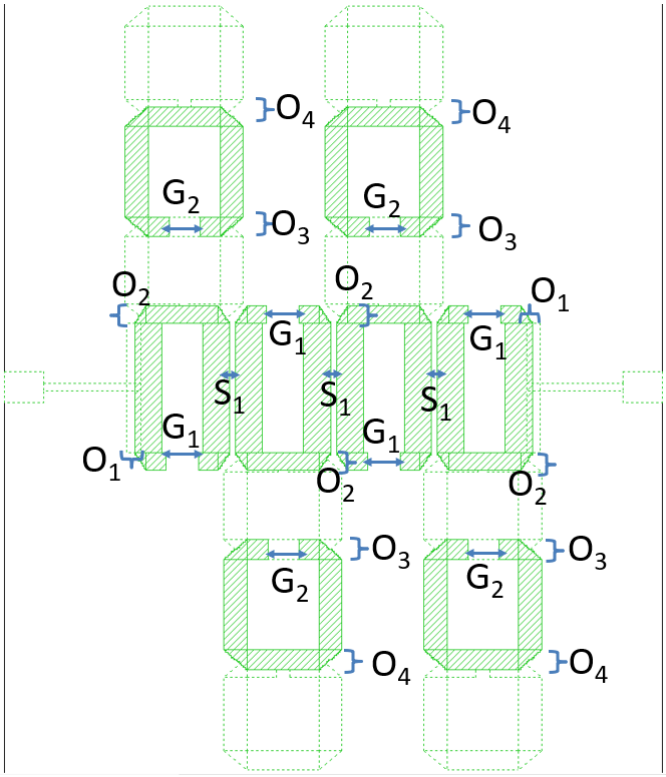

Fig. A.25 Gaps for resonators 1 to 4 and resonators 9 to 12 , spacing and overlaps : filter D

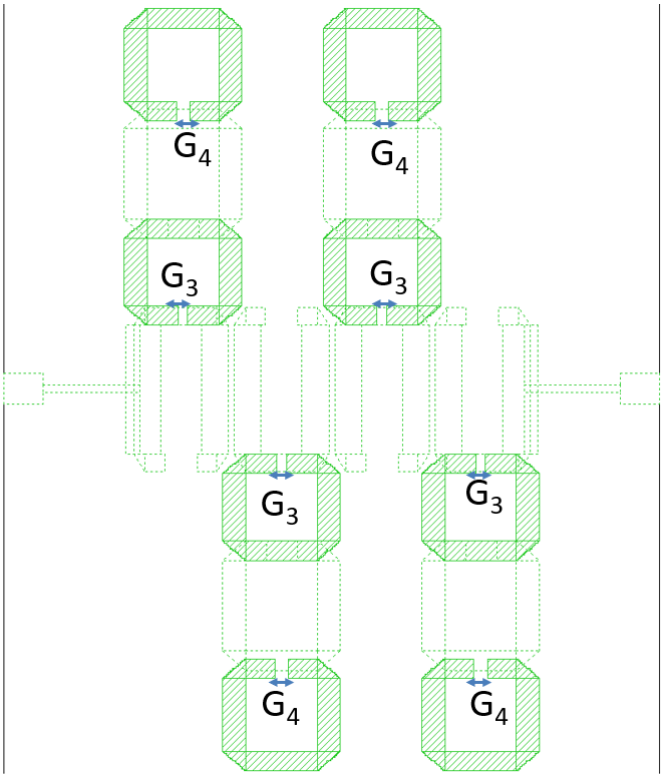

Fig. A.26 Gaps of resonators 5 to 8 and resonators 13 to 16: filter D

Appendix B

Dimensions of the coupled switchable filter

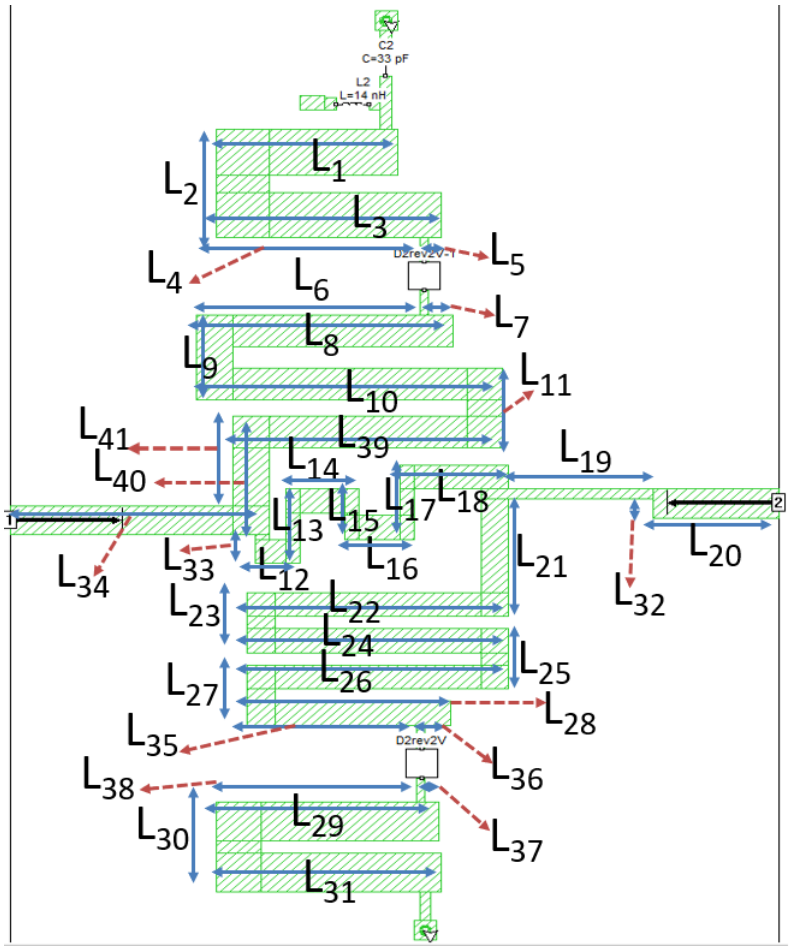

Fig. B.1 Length of one stage non-resonant circuit

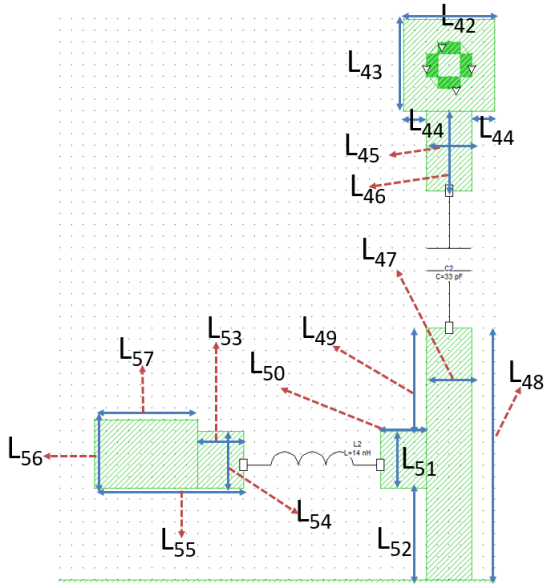

Fig. B.2 Length of one-stage non-resonant circuit

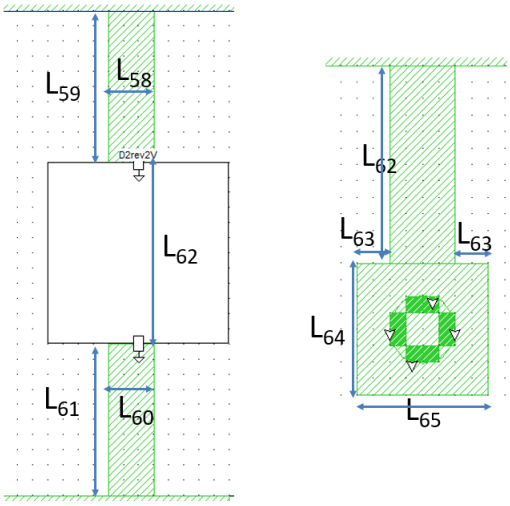

Fig. B.3 Length of one-stage non-resonant circuit

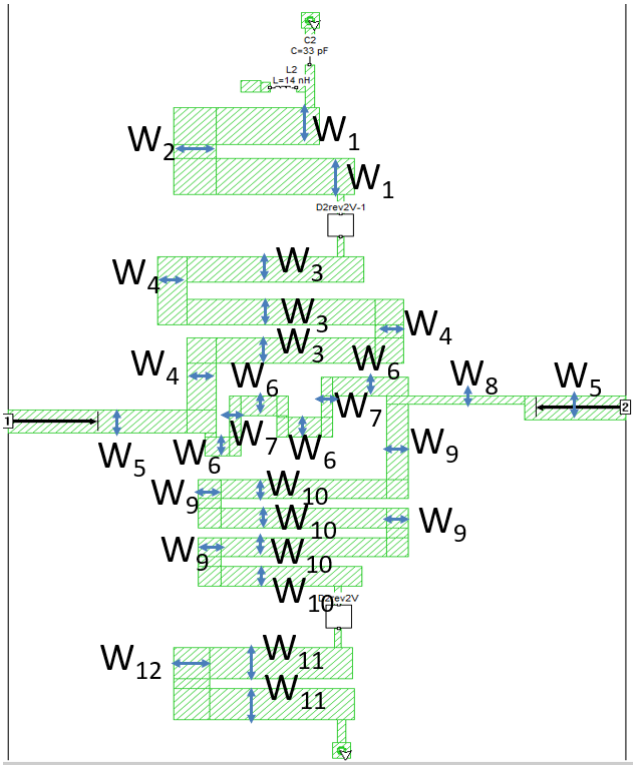

Fig. B.4 Width of one-stage non-resonat circuit

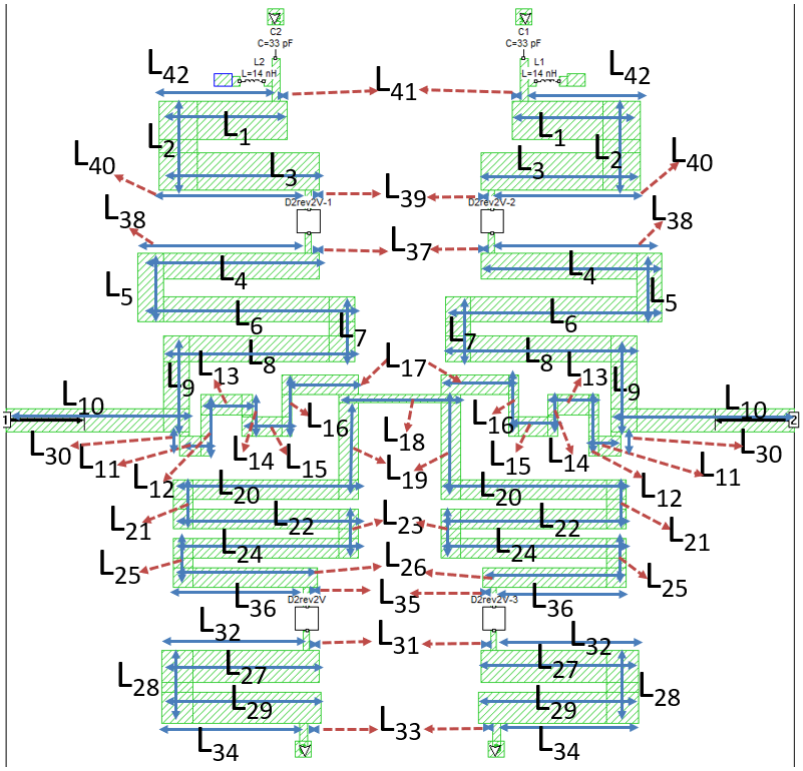

Fig. B.5 Length of two stages non-resonant circuit

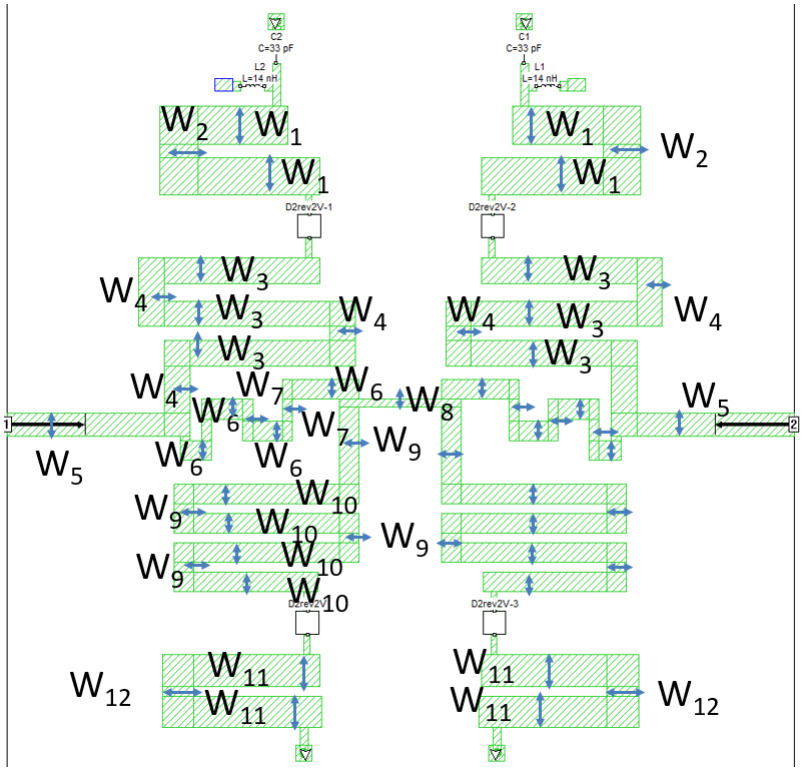

Fig. B.6 Width of two stages non-resonant circuit

Table B.1 Lengths of the one-stage non-resonant circuit in Fig B.1, Fig B.2 and Fig B.3.

L	mm	L	mm	L	mm	L	mm	L	mm	L	mm		
L_1	6.5	L_{11}	3.3	L_{21}	4.9	L_{31}	8.1	L_{41}	3.7	L_{51}	0.5	L_{61}	1.0
L_2	4.5	L_{12}	1.6	L_{22}	9.4	L_{32}	8.0	L_{42}	0.8	L_{52}	0.8	L_{62}	1.2
L_3	8.1	L_{13}	3.1	L_{23}	2,5	L_{33}	1.2	L_{43}	0.8	L_{53}	0.4	L_{63}	0.2
L_4	7.3	L_{14}	2.6	L_{24}	9.4	L_{34}	9.3	L_{44}	0.2	L_{54}	0.5	L_{64}	0.8
L_5	0.5	L_{15}	2.1	L_{25}	2.5	L_{35}	6.1	L_{45}	0.4	L_{55}	1.3	L_{65}	0.8
L_6	8.0	L_{16}	2.5	L_{26}	9.4	L_{36}	0.9	L_{46}	0.7	L_{56}	0.6		
L_7	0.9	L_{17}	3.1	L_{27}	2.5	L_{37}	0.5	L_{47}	0.4	L_{57}	0.9		
L_8	9.2	L_{18}	3.9	L_{28}	7.3	L_{38}	7.2	L_{48}	2.2	L_{58}	0.3		
L_9	3.5	L_{19}	5.2	L_{29}	8.0	L_{39}	9.7	L_{49}	0.9	L_{59}	1.0		
L_{10}	11	L_{20}	4.5	L_{30}	3.7	L_{40}	4.9	L_{50}	0.4	L_{60}	0.3		

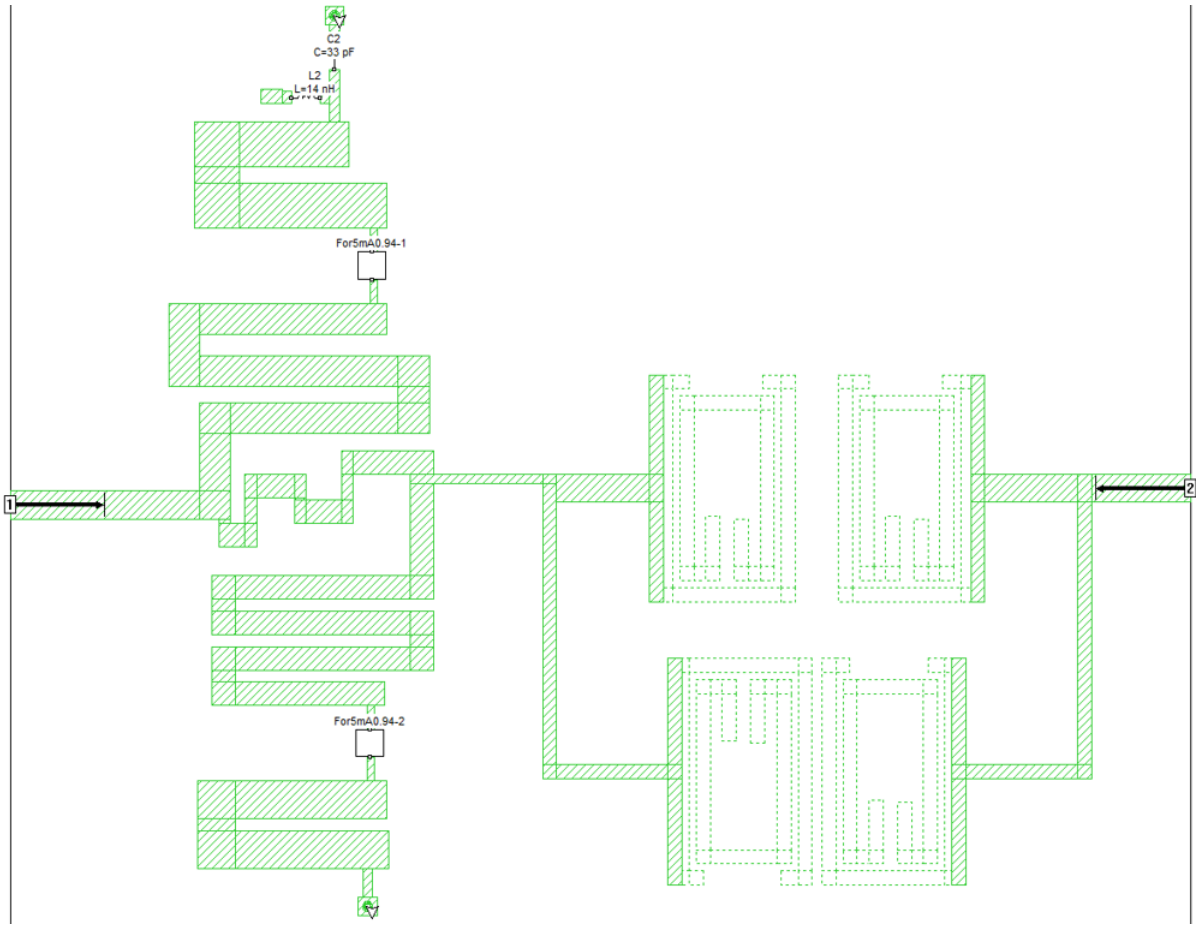

Fig. B.7 Length of one-stage switchable filter

Table B.2 Lengths of the two-stage non-resonant circuit in Fig B.5.

L	mm	L	mm	L	mm	L	mm	L	mm	L	mm
L_1	6.5	L_{11}	1.6	L_{21}	2.5	L_{31}	0.5	L_{41}	0.4	L_{51}	0.5
L_2	4.5	L_{12}	3.1	L_{22}	9.4	L_{32}	7.2	L_{42}	4.2	L_{52}	0.8
L_3	8.1	L_{13}	2.1	L_{23}	2.5	L_{33}	0.7				0.4
L_4	9.2	L_{14}	2.1	L_{24}	9.4	L_{34}	7.0				
L_5	3.5	L_{15}	2.5	L_{25}	2.5	L_{35}	0.4				
L_6	11	L_{16}	3.6	L_{26}	7.3	L_{36}	6.6				
L_7	3.3	L_{17}	3.9	L_{27}	8.0	L_{37}	0.4				
L_8	9.7	L_{18}	6.2	L_{28}	3.7	L_{38}	8.5				
L_9	4.9	L_{19}	4.9	L_{29}	8.1	L_{39}	0.4				
L_{10}	9.3	L_{20}	9.4	L_{30}	1.2	L_{40}	7.4				

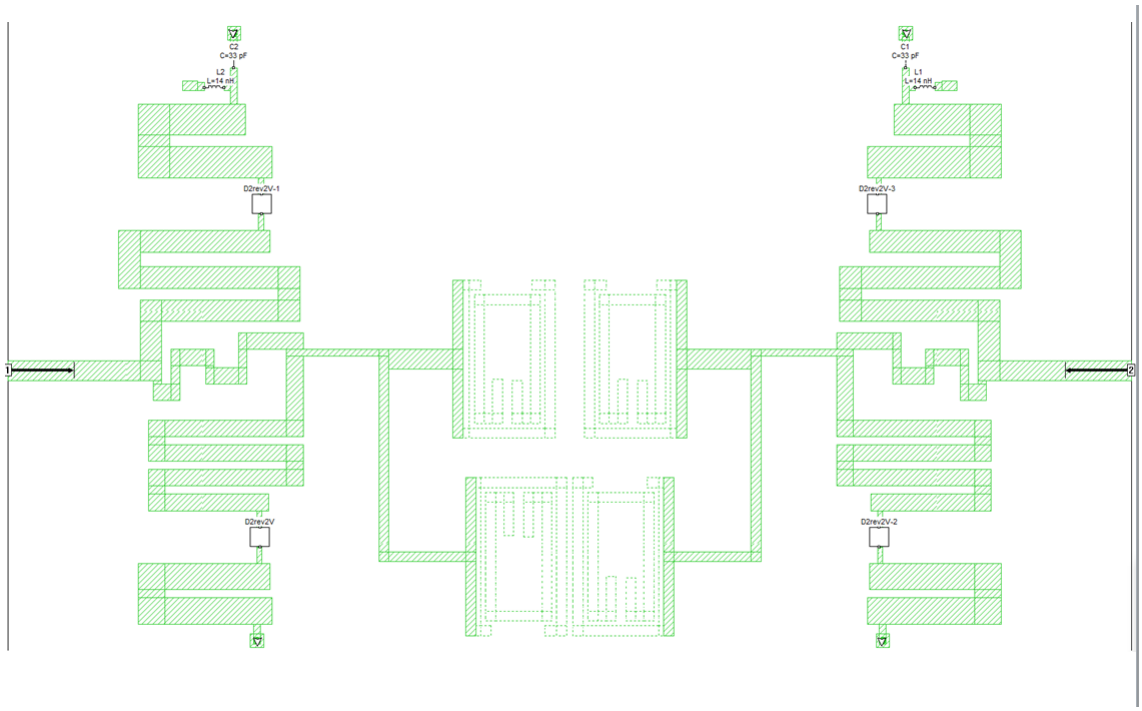

Fig. B.8 Length of the two-stages switchable

Appendix C

Dimensions of the dual band quasi lumped element filters

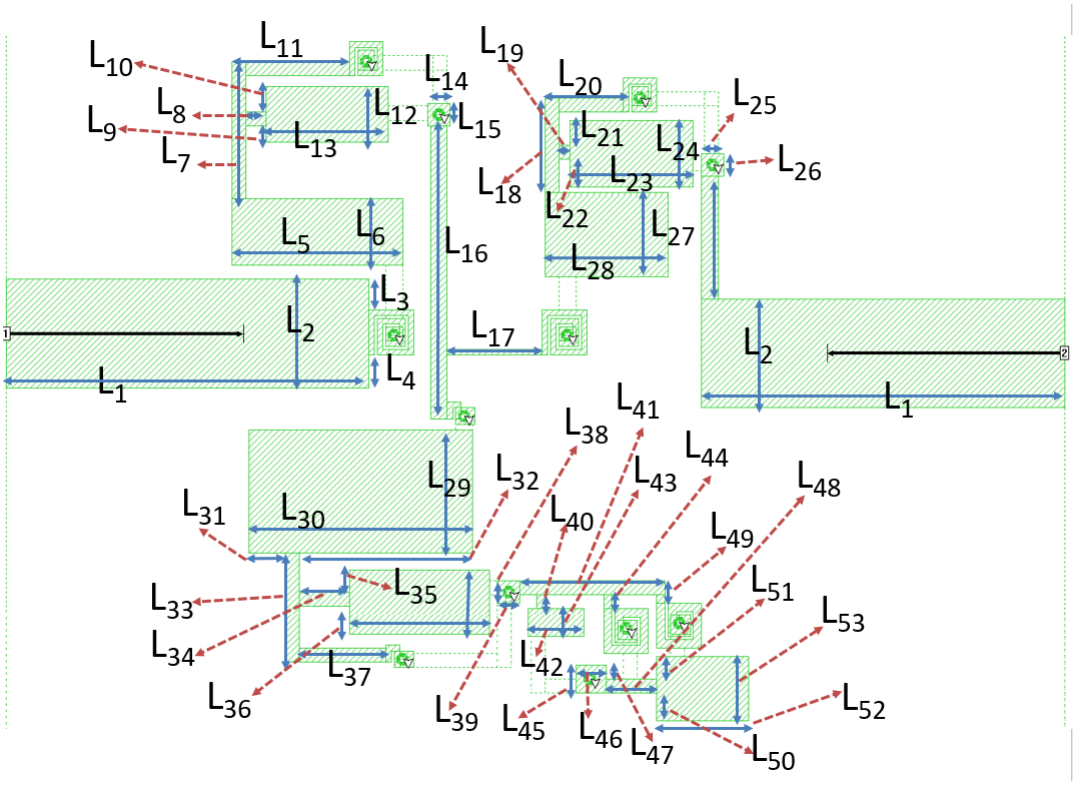

Fig. C.1 Length of Design B (Mixed cauer I and II) top layer

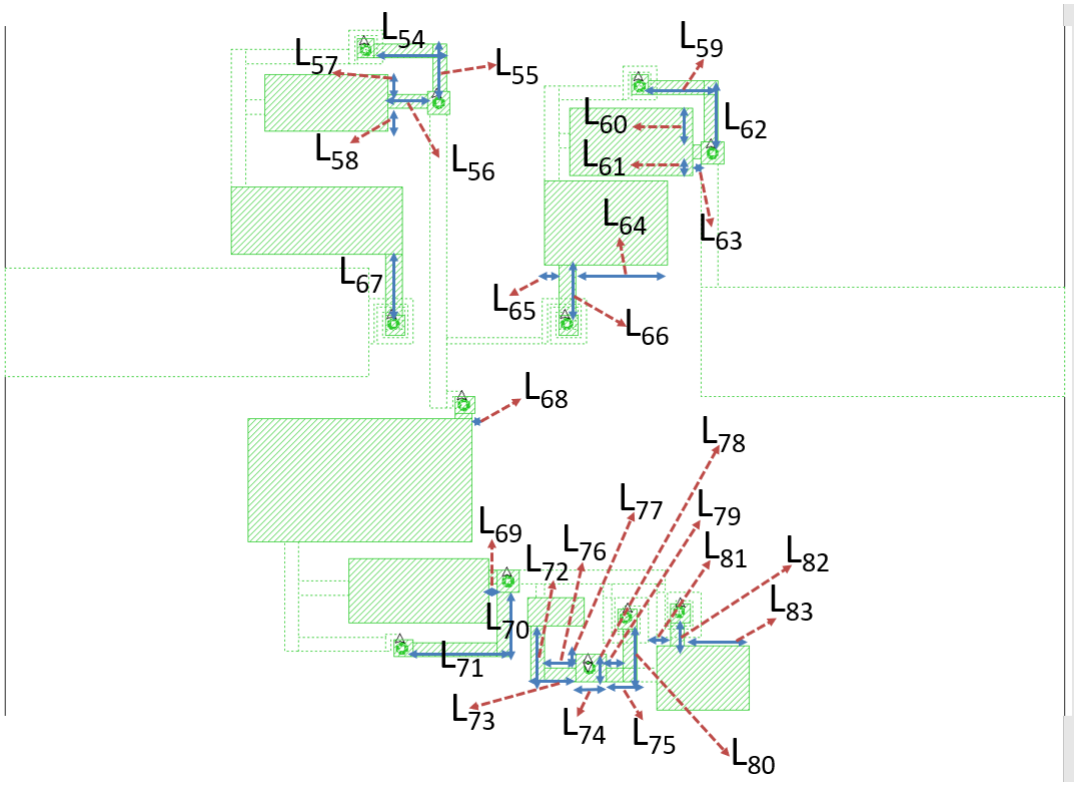

Fig. C.2 Length of Design B (Mixed cauer I and II) next layer

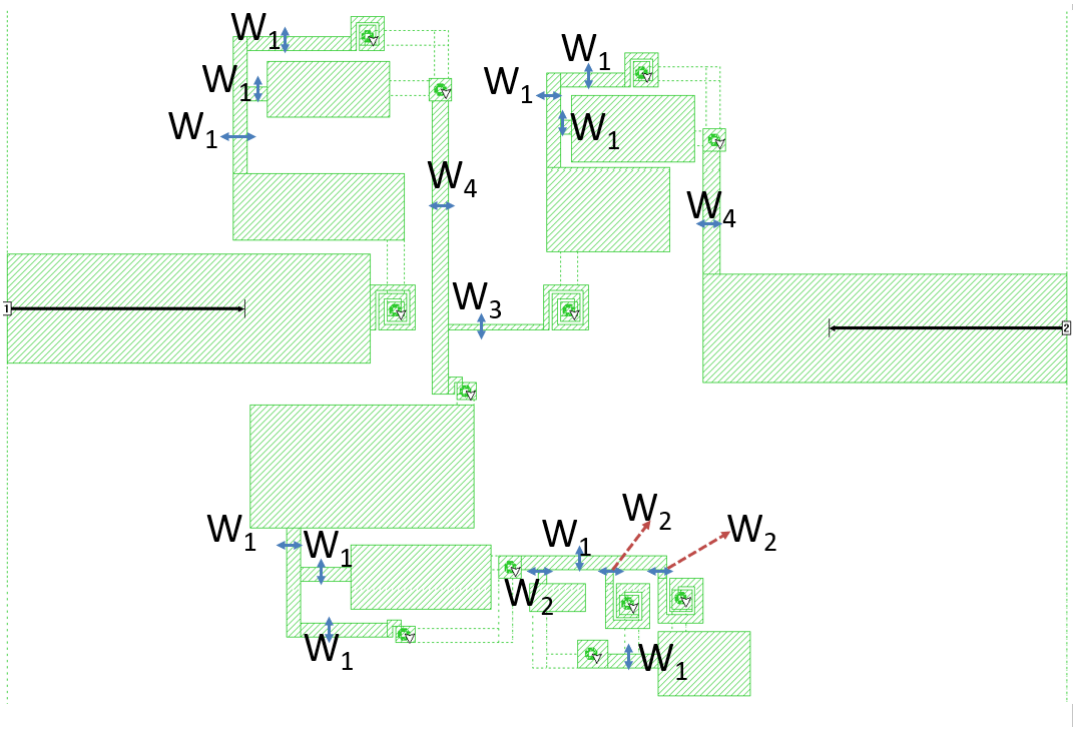

Fig. C.3 Width of Design B (Mixed cauer I and II) top layer

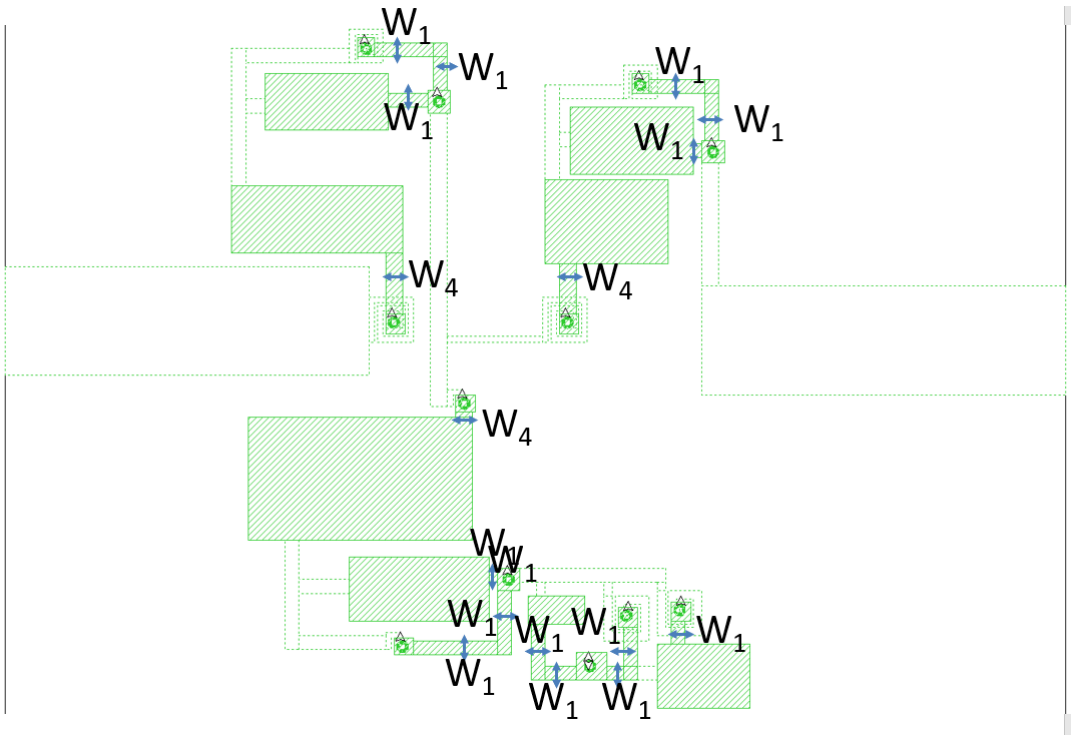

Fig. C.4 Width of Design B (Mixed cauer I and II) next layer

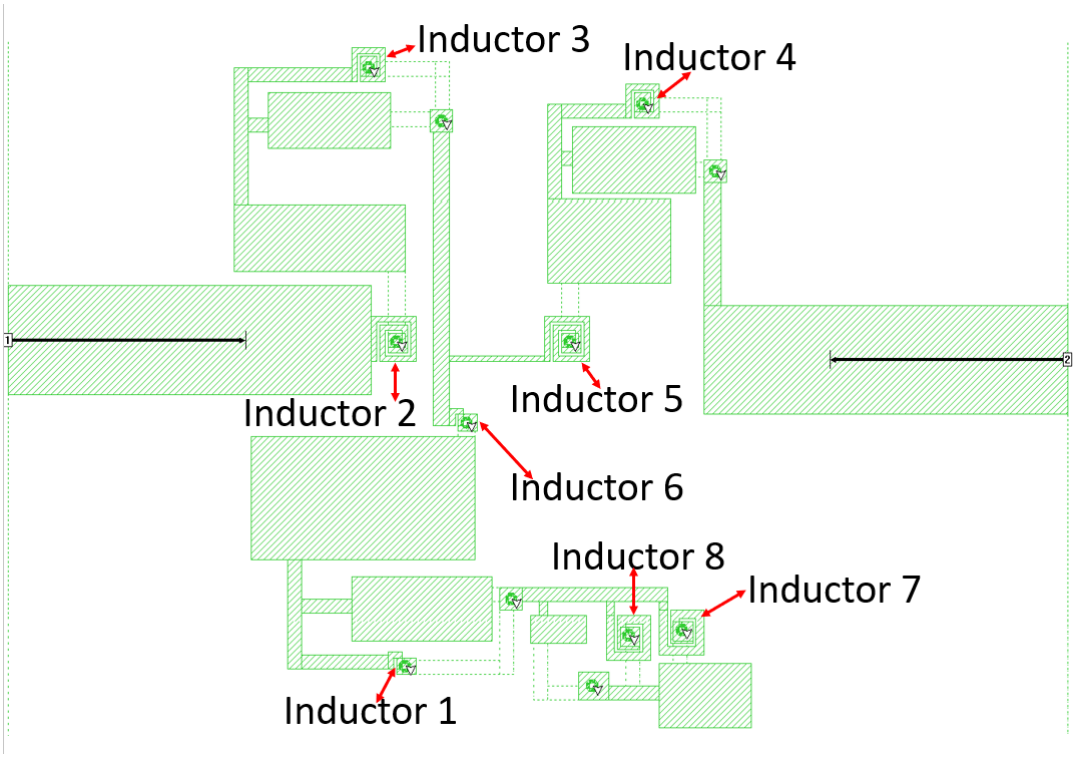

Fig. C.5 The numbered inductors are enlarge in Fig C.6 to C.9

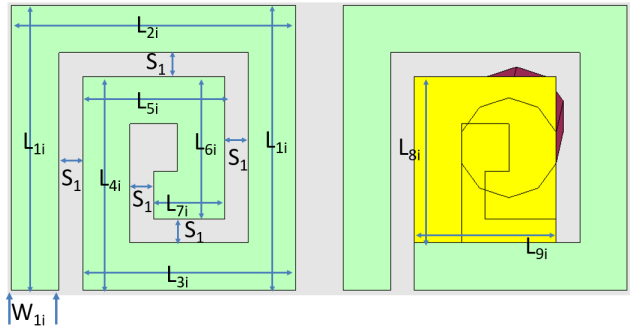

Fig. C.6 This inductor represent inductors number 3 and 4 in Fig C.5.

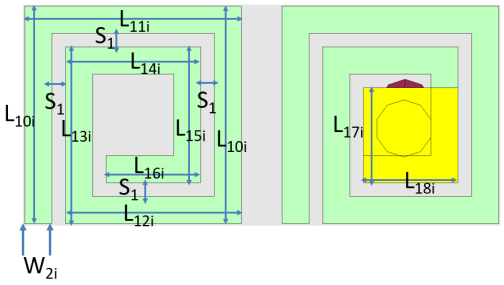

Fig. C.7 This inductor represent inductors number 2 and 5 in Fig C.5.

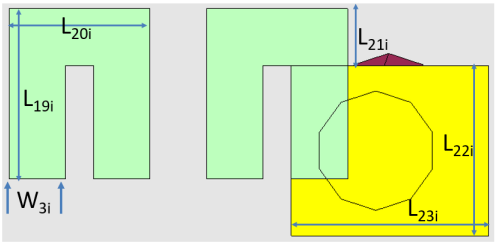

Fig. C.8 This inductor represent inductors number 1 and 6 in Fig C.5.

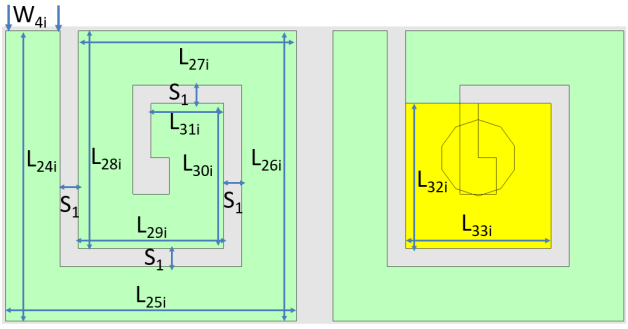

Fig. C.9 This inductor represent inductors number 7 and 8 in Fig C.5.

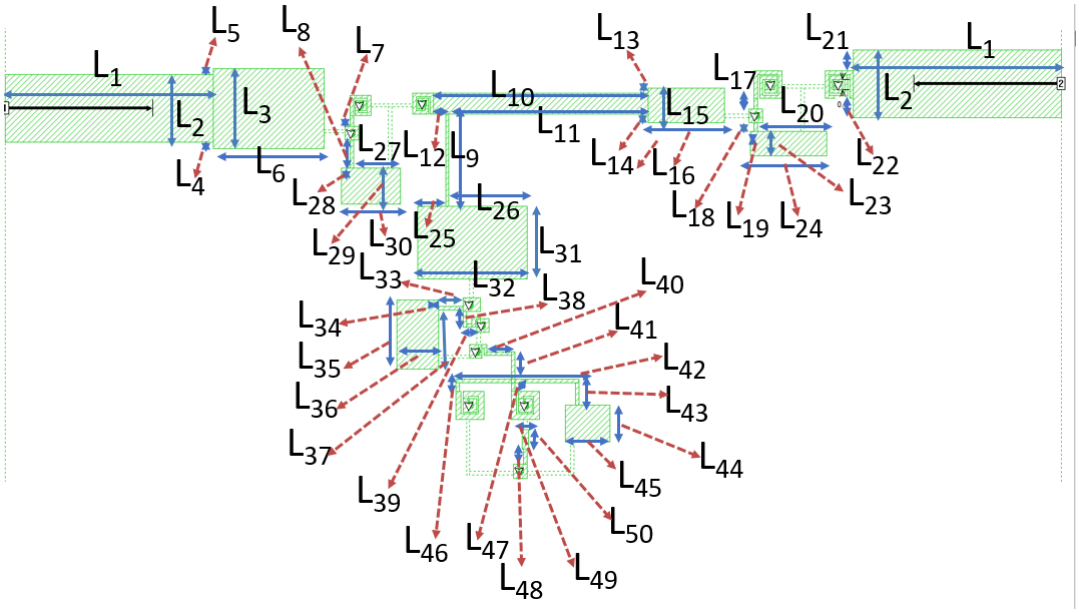

Fig. C.10 Length of Design A (Foster topology) top layer.

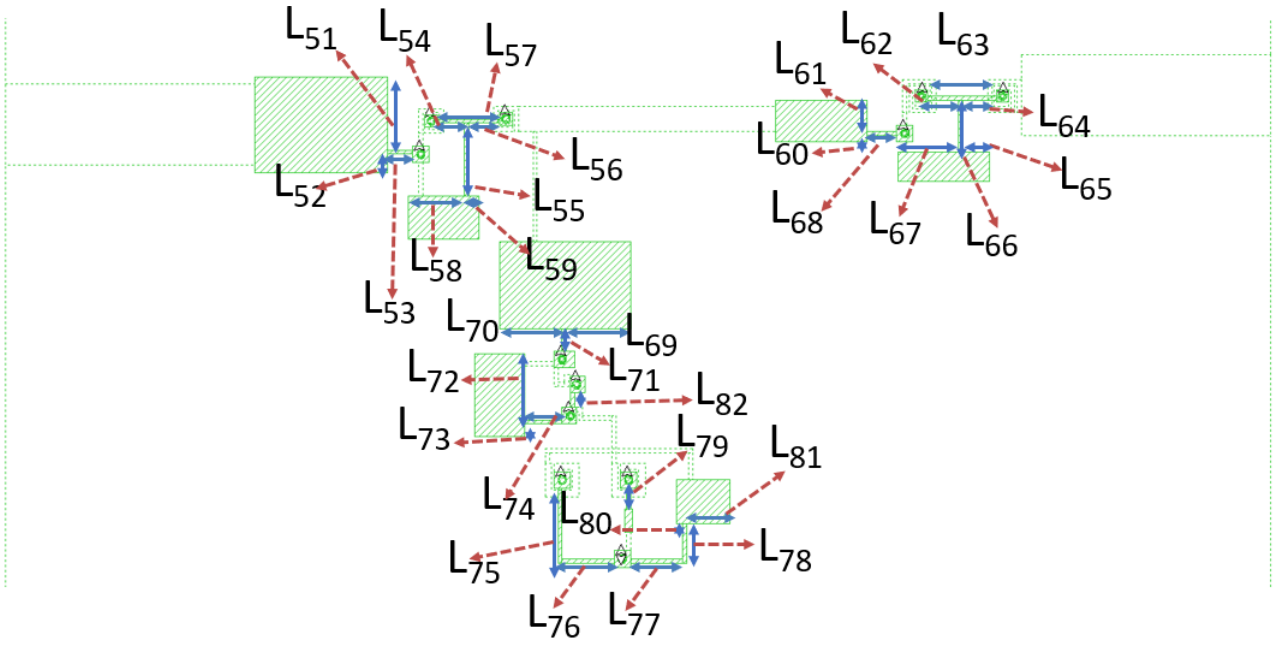

Fig. C.11 Length of Design A (Foster topology) next layer.

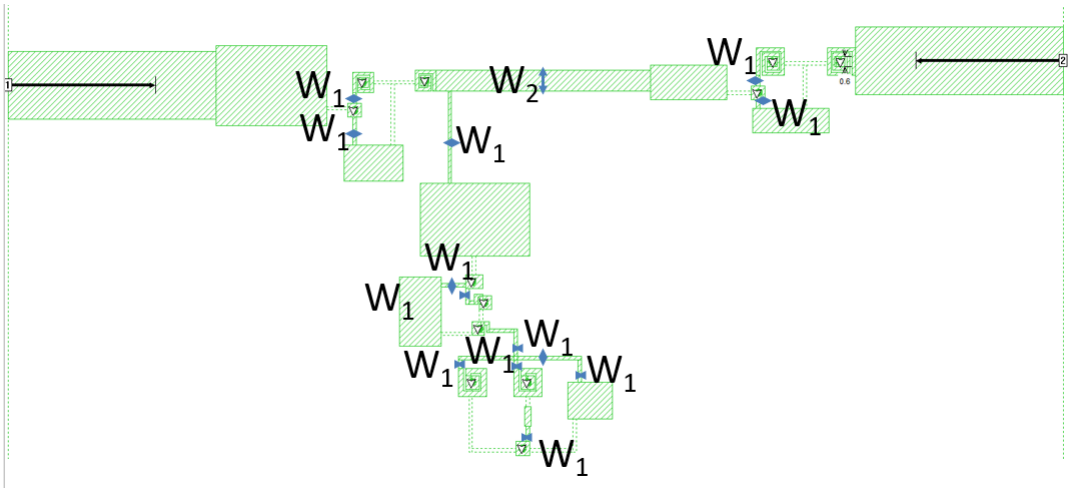

Fig. C.12 Width of Design A (Foster topology) top layer.

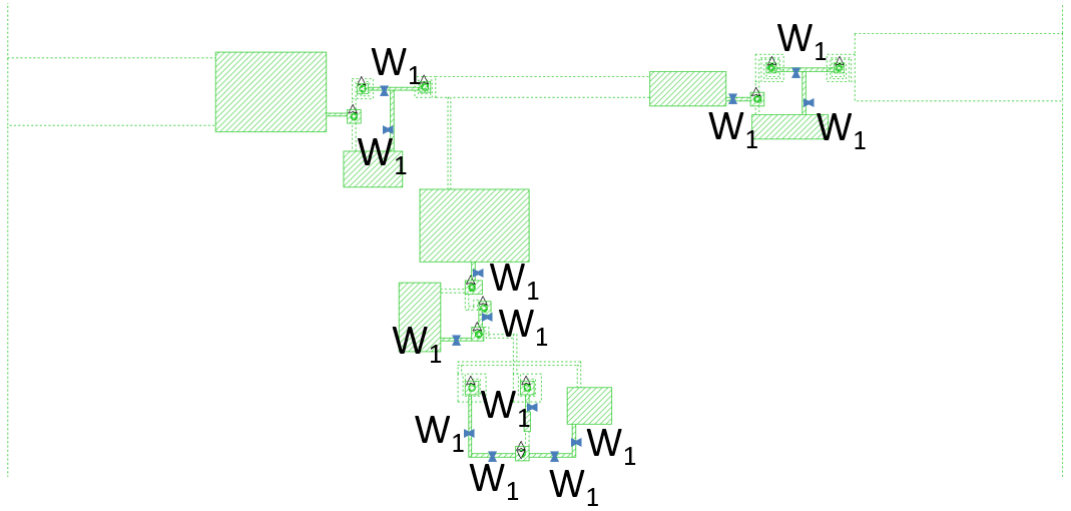

Fig. C.13 Width of Design A (Foster topology) next layer.

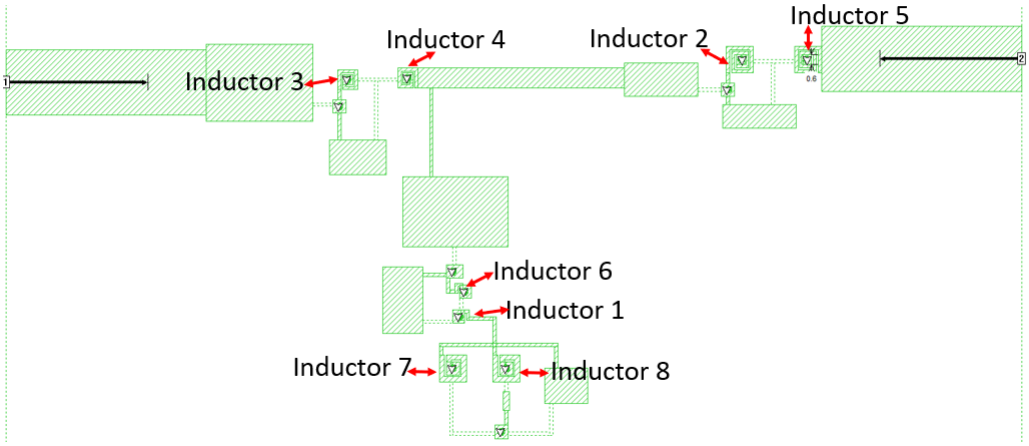

Fig. C.14 The numbered inductors are enlarge in Fig C.6 to C.9

Table C.1 Lengths of Design B (mixed Cauer I and II) for Fig C.1, and Fig C.2

L	mm	L	mm	L	mm	L	mm	L	mm	L	mm				
L_1	13	L_{11}	4.2	L_{21}	0.9	L_{31}	1.3	L_{41}	5.2	L_{51}	0.8	L_{61}	0.6	L_{71}	3.5
L_2	3.9	L_{12}	2.0	L_{22}	1.0	L_{32}	6.2	L_{42}	2.0	L_{52}	3.3	L_{62}	2.2	L_{72}	2.0
L_3	1.1	L_{13}	4.4	L_{23}	4.4	L_{33}	3.9	L_{43}	1.0	L_{53}	2.3	L_{63}	0.3	L_{73}	1.6
L_4	1.2	L_{14}	0.7	L_{24}	2.4	L_{34}	1.8	L_{44}	0.5	L_{54}	2.6	L_{64}	3.3	L_{74}	1.1
L_5	6.1	L_{15}	0.8	L_{25}	0.8	L_{35}	0.8	L_{45}	1.0	L_{55}	1.7	L_{65}	0.5	L_{75}	1.1
L_6	2.4	L_{16}	10.5	L_{26}	0.8	L_{36}	1.0	L_{46}	1.1	L_{56}	1.4	L_{66}	1.8	L_{76}	1.1
L_7	4.9	L_{17}	3.4	L_{27}	3.0	L_{37}	3.6	L_{47}	0.5	L_{57}	0.7	L_{67}	2.2	L_{77}	0.5
L_8	0.7	L_{18}	3.4	L_{28}	4.4	L_{38}	0.8	L_{48}	1.8	L_{58}	0.8	L_{68}	0.2	L_{78}	1.0
L_9	0.6	L_{19}	1.4	L_{29}	4.4	L_{39}	0.8	L_{49}	0.8	L_{59}	2.5	L_{69}	0.3	L_{79}	0.6
L_{10}	0.9	L_{20}	2.8	L_{30}	8.0	L_{40}	0.5	L_{50}	1.0	L_{60}	1.3	L_{70}	2.3	L_{80}	1.9
														L_{81}	0.5
														L_{82}	0.8
														L_{83}	2.3

Table C.2 Lengths of the inductors indicated in Fig C.5, are represented by enlarge inductors where inductor in Fig C.6 represents inductor 3 and 4, and inductor in Fig C.7 represents inductor 2 and 5, inductor in Fig C.8 represents inductor 1 and 6, and inductor in Fig C.9 represents inductor 7 and 8.

L	mm	L	mm	L	mm
L_{1i}	1.2	L_{11i}	1.6	L_{21i}	0.2
L_{2i}	1.2	L_{12i}	1.3	L_{22i}	0.6
L_{3i}	0.9	L_{13i}	1.3	L_{23i}	0.7
L_{4i}	0.9	L_{14i}	1.0	L_{24i}	1.6
L_{5i}	0.6	L_{15i}	1.0	L_{25i}	1.6
L_{6i}	0.6	L_{16i}	0.7	L_{26i}	1.6
L_{7i}	0.3	L_{17i}	0.5	L_{27i}	1.2
L_{8i}	0.7	L_{18i}	0.5	L_{28i}	1.2
L_{9i}	0.6	L_{19i}	0.6	L_{29i}	0.8
L_{10i}	1.6	L_{20i}	0.5	L_{30i}	0.8
				L_{31i}	0.4
				L_{32i}	0.8
				L_{33i}	0.8

Table C.3 Width of the lines of design B in Fig C.3 and Fig C.4. Width of the enlarged inductors and spacing between turns.

G & S	mm
W_1	0.5
W_2	0.3
W_3	0.2
W_4	0.6
W_{1i}	0.2
W_{2i}	0.2
W_{3i}	0.2
W_{4i}	0.3
S_1	0.1

Table C.4 Lengths and widths of the lines) of Design A (Foster topology) for Fig C.10, and Fig C.11

L	mm	L	mm	L	mm	L	mm	L	mm	L	mm				
L_1	12.0	L_{11}	11.5	L_{21}	1.2	L_{31}	4.2	L_{41}	1.6	L_{51}	5.3	L_{61}	1.5	L_{71}	1.1
L_2	3.9	L_{12}	0,7	L_{22}	1.1	L_{32}	6.3	L_{42}	7.1	L_{52}	0.9	L_{62}	1.5	L_{72}	3.2
L_3	4.6	L_{13}	0.3	L_{23}	1.4	L_{33}	1.4	L_{43}	1.5	L_{53}	1.2	L_{63}	3.3	L_{73}	0.6
L_4	0.4	L_{14}	0.5	L_{24}	4.4	L_{34}	0.4	L_{44}	2.1	L_{54}	1.3	L_{64}	1.6	L_{74}	1.8
L_5	0.3	L_{15}	2.0	L_{25}	1.6	L_{35}	4.0	L_{45}	2.6	L_{55}	3.5	L_{65}	1.3	L_{75}	3.6
L_6	6.4	L_{16}	4.4	L_{26}	4.5	L_{36}	2.4	L_{46}	0.7	L_{56}	1.5	L_{66}	2.5	L_{76}	2.7
L_7	0.6	L_{17}	0.6	L_{27}	2.7	L_{37}	3.4	L_{47}	0.5	L_{57}	3.0	L_{67}	2.9	L_{77}	2.7
L_8	1.6	L_{18}	0.5	L_{28}	0.5	L_{38}	0.9	L_{48}	0.9	L_{58}	2.7	L_{68}	1.4	L_{78}	1.9
L_9	5.3	L_{19}	0.2	L_{29}	2.1	L_{39}	0.2	L_{49}	0.4	L_{59}	0.5	L_{69}	3.1	L_{79}	1.0
L_{10}	12.4	L_{20}	4.0	L_{30}	3.4	L_{40}	1.6	L_{50}	1.1	L_{60}	0.3	L_{70}	3.0	L_{80}	0.3
														L_{81}	2.1
														L_{82}	0.7
														W_1	0.2
														W_1	1.2